

**Selective Laser Sintering of PMMA and
PMMA plus β -Tricalcium Phosphate Polymer
Composites**

Rajkumar Velu

A thesis submitted to Auckland University of Technology in
fulfilment of the requirement for the degree of
Doctor of Philosophy

May 2017

School of Engineering, Computer and Mathematical
Sciences

Table of Contents

List of Figures	vi
List of Tables	x
List of Publications from this research	xi
List of Terms and Abbreviations	xiii
Attestation of Authorship	xvi
Acknowledgements	xvii
Abstract	xviii
Chapter 1 Introduction	1
1.1 Bio-polymers and composites	1
1.2 Traditional manufacturing methods and new developments	3
1.3 The materials	4
1.4 Research gaps, questions, methods and implementation	6
Chapter 2 Literature review, research gaps, questions, and objectives	9
2.1 Poly (methyl methacrylate) (PMMA)	9
2.2 Industrial uses	11
2.3 Medical applications	13
2.4 Processing methods	14
2.5 Limitations and enhancements	17
2.6 Additive processing	21
2.7 PMMA-Ceramic composites and processing	23
2.8 Research gaps, questions, and hypotheses	27
2.9 Thesis structure	34
Chapter 3 Materials and methods	36

3.1 Evaluation of a new bio-polymer for selective laser sintering	36
3.2 Experimental Materials	38
3.3 Critical material and process attributes	40
<i>Laser type</i>	40
<i>Emissivity, Absorptivity, Reflectivity, and Transmissivity</i>	44
<i>Thermal Conductivity</i>	46
<i>Specific Heat</i>	48
<i>Density</i>	49
3.4 Material Processing	51
<i>Polymer dissolution process</i>	52
<i>Extrusion method</i>	54
<i>Manual mortar mixing</i>	55
3.5 The laser sintering setup	57
<i>The laser</i>	57
<i>Powder feeding</i>	61
3.6 Laser sintering parameters and trials	63
<i>Critical SLS parameters</i>	63
<i>Laser Beam Velocity</i>	66
<i>Scan Spacing and Vector Length</i>	67
<i>Layer thickness</i>	68
<i>Temperature settings</i>	70
<i>Single and multi-layer sintering</i>	71
3.7 SEM for Microstructural characterisation	72
3.8 Fourier Transform Infra-Red (FT-IR)	74
3.9 Mechanical and physical properties	76
<i>Tensile Tests</i>	76

<i>Three-point bending Tests</i>	77
3.10 Thermal characterisation	78
<i>Differential scanning calorimetry</i>	78
<i>Thermo-gravimetric analysis</i>	80
<i>Thermal imaging and online temperature measurement</i>	81
3.11 Biological responses	84
3.11.1 <i>Cell culture</i>	84
3.11.2 <i>Cell Proliferation Studies</i>	85
<i>MTT Assay</i>	85
<i>Alkaline Phosphatase assay and staining</i>	86
<i>Alizarin Red S staining</i>	87
<i>Field Emission Scanning Electron Microscopy (FE-SEM) Analysis</i>	88
3.12 Summary of materials and methods	89
Chapter 4 Selective Laser Sintering of Poly (methyl methacrylate) (PMMA)	90
4.1 Laser sintering materials and conditions	90
4.2 DSC results of neat PMMA powders and initial sintering parameters	94
4.3 Initial experiments and results	97
4.4 Further sintering trials and evaluation of influences of critical process parameters	104
4.5 Summary of the sintering trials with PMMA	113
Chapter 5 Laser Sintering PMMA+β-TCP Composites	114
5.1 Additive processing of PMMA composites	114
5.2 DSC of PMMA- β -TCP polymer composites	115

5.3 Initial experiments and results	119
5.4 Further experimental trials and surface morphologies	123
5.5 Evaluation of influences of critical process parameters	127
5.6 Morphology of β -TCP particles in laser sintered PMMA matrix	136
5.7 Cross-sections of the sintered samples	138
5.8 Tensile Test	141
5.9 Thermal Analysis of PMMA+ β -TCP composites	142
5.9.1 <i>Thermo-gravimetric analysis</i>	142
5.9.2 <i>Temperature variation along laser scan lines</i>	144
<i>Finite element simulation</i>	144
<i>Experimental temperature measurement</i>	147
5.10 Summary of laser sintering responses of PMMA plus β -TCP composites	150
Chapter 6 Laser sintering after effects; polymer degradation, biological, and mechanical responses	152
6.1 Post-sintering polymer characterisation	152
6.2 Porosity	153
6.3 Polymer Degradation	156
6.4 Biological Characterisation	159
<i>MTT Assay</i>	161
<i>ALP Assay</i>	163
<i>Alizarin-red S staining</i>	164
<i>Field Emission Scanning Electron Microscopy (FE-SEM) Analysis</i>	166
6.5 Multilayer Laser Sintering	169

<i>Multilayer Laser Sintering Conditions</i>	173
<i>Morphologies of multi-layer sintered specimens</i>	176
<i>Density and Porosity analysis</i>	182
<i>Mechanical Properties</i>	186
6.6 Summary of post-sintering analyses	190
Chapter 7 Conclusions	192
7.1 Research Undertaken and overall observations	192
7.2 General conclusions	194
7.3 More specific and quantitative conclusions	199
7.4 Future course	208
References	211

List of Figures

Figure 2.1 The chronology of PMMA development	10
Figure 2.2 The polymer-ceramic composite realm	24
Figure 2.3 β -TCP as a bone-repair and replacement option	27
Figure 2.4 The current polymer-ceramic composite	27
Figure. 3.1 Physical (a & b) and SEM (c & d) image of PMMA and β -TCP powder respectively	39
Figure. 3.2 Laser absorption of plain solid materials (Polycarbonate and copper) versus wavelength	42
Figure. 3.3 Powder in-coupling	42
Figure. 3.4 Material and thermal properties compound to influence the sintering attributes	44
Figure 3.5. The cubical orthorhombic arrangements of uniform spherical particles	50
Figure 3.6 Schematic view of the first stage of sintering	51
Figure. 3.7 Polymer Dissolution Process	53
Figure 3.8 (a) Powder and (b) Sintered samples of extruded PMMA and β - TCP composite material	55
Figure 3.9 PMMA and β -TCP composite powders	56
Figure 3.10 Block diagram of SLS test bed	58
Figure 3.11 Changes in laser spot diameter at different positions on the powder bed	60
Fig. 3.12 Laser sintering setup	61
Figure 3.13 CAD models of the powder-feed system	62
Figure 3.14 The fabricated powder-feed system	63
Figure 3.15 SLS Scanning Strategy	64
Figure 3.16 Laser Scanning Parameters	64
Figure 3.17 Critical laser parameters and settings	65
Figure 3.18 The layer thickness control system; stepper motor, drive elements, motion card, and the software interface	69

Figure 3.19 Powder Bed temperature control	71
Figure 3.20 Scanning Electron Microscopy	73
Figure 3.21 FT-IR Spectrometer	75
Figure 3.22 Procedural steps of the FT-IR analysis	75
Figure 3.23 Tensile testing Machine	76
Figure 3.24 (a) Tensile testing system, (b) Close-up view of the three-point bending sample and loading arrangement	78
Figure 3.25 Simultaneous Thermal Analyser for DSC and TGA	80
Figure. 3.26 Thermo-vision system and vario-capture interface	83
Figure 3.27 4 MG 63 cells captured using a Micros Lotus MCX51 microscope	85
Figure 4.1 DSC results based on the neat PMMA powder	94
Figure 4.2 Ozawa plot for neat PMMA	96
Figure 4.3 SEM Photographs of sintered PMMA: initial trials	100
Figure 4.4 SEM Photographs of sintered PMMA single layers with varying process parameters	102
Figure 4.5 No of pores per area vs. laser power at different energy densities	103
Figure 4.6 SEM photographs of single layer samples sintered at relatively higher laser power settings	105
Figure 4.7 Percent porosity vs laser power at different energy density settings ...	107
Figure 4.8 No of pores vs laser power (20 W to 35W) at two different energy densities.....	108
Figure 4.9 Causes of porosity	108
Figure 4.10 single layer sintered specimens	110
Figure 4.11 Mechanical properties of thin film PMMA tensile specimens	111
Figure 5.1 DSC results based on PMMA and PMMA/ β -TCP powders	116
Figure 5.2 Ozawa Plot based on the 5% β -TCP /95% PMMA	116
Figure 5.3 SEM Photographs of the sintered single layer with 80% PMMA and 10% β -TCP composite	120
Figure 5.4 Effects of process parameters on critical responses (10% β -TCP composite powder)	122

Figure 5.5 SEM Photographs of the sintered single layer with PMMA+20% β -TCP composite powders	123
Figure 5.6 SEM Photographs of sintered PMMA- β TCP composite single layer samples with varying process parameters	126
Figure 5.7 SEM Photographs of sintered 5% β -TCP/ 95% PMMA composite single layer samples with varying process parameters	129
Figure 5.8 SEM Photographs of sintered 10% β -TCP/ 90% PMMA composite single layer samples with varying process parameters	130
Figure 5.9 SEM Photographs of sintered 15% β -TCP/ 85% PMMA composite single layer samples with varying process parameters	131
Figure 5.10 SEM Photographs of sintered 20% β -TCP/ 80% PMMA composite single layer samples with varying process parameters	132
Figure 5.11 Percent porosity variation with varying amounts of β -TCP	135
Fig. 5.12 Uncontrolled porosity in sintered samples	136
Figure 5.13 SEM photo graphs of sintered layer with (a) 10 % β -TCP and (b) 20 % β -TCP particles	138
Figure 5.14 SEM micrograph of the cross- section of sintered layer (a) 10 % β -TCP and (b) 20 % β -TCP composites	140
Figure 5.15 Variation in the Young's Modulus with varying amounts of β -TCP	142
Figure 5.16 TGA results of PMMA and PMMA/ β -TCP composites powders	144
Figure 5.17 Temperature distribution at a specific time P =38W, speed = 780mm/s	147
Figure 5.18 Time dependent temperature variation at 20mm with varying compositions	147
Figure 5.19 Thermal imaging of laser movement	148
Figure 5.20 Infrared thermal imaging results of the time dependent variation in temperature at different locations for varying compositions	149
Figure 6.1 SEM photomicrographs of single layer sintered specimens (accelerating voltage 15kV)	155
Figure 6.2 Percent porosity with varying PMMA/ β -TCP compositions	155
Figure 6.3 FTIR results of neat PMMA powders	158
Figure 6.4 FTIR results of sintered specimens	159

Figure 6.5 Results of the MTT assay with varying compositions	163
Figure 6.6 Results of the ALP assay	165
Figure 6.7 Alizarin red staining results with varying composition	165
Figure 6.8 Morphology of MG-63 cells cultured on PMMA and β-TCP/ PMMA specimen	168
Figure 6.9 Multi-layer sintering stages	171
Figure 6.10 Initial trials on multi-layer samples	174
Figure 6.11 Selective laser sintering of Multi-layer specimens	176
Figure 6.12 Multilayer neat PMMA fractured surfaces	177
Figure 6.13 SEM Images of cross sections of 95% PMMA and 5% β-TCP samples	179
Figure 6.14 SEM images of cross sections of 90% PMMA and 10% β-TCP samples ...	180
Figure 6.15 Density and porosity vs laser power at different energy densities (5% β-TCP/95% PPMA case)	184
Figure 6.16 Pore size measurement at different locations (5% β-TCP/95% PMMA case sintered at 0.15 j/mm^2)	185
Figure 6.17 Optical photomicrographs of cross-sections of (a) 5% β-TCP/ 95% PMMA and (b) 10% β-TCP/ 90% PMMA samples sintered at 0.15 J/mm^2	186
Figure 6.18 Flexural Modulus of PMMA and PMM/βTCP composites	188
Figure 6.19 Fractured specimen and surfaces	189
Figure 6.20 Fractured surface of a laser sintered PMM/β-TCP composite sample	189

List of Tables

Tale 2.1 Conventional fabrication methods, applications and limitations	19
Table 3.1 Materials and properties	40
Table 3.2 Incoupling (Absorption) of powder Materials for Nd: YAG and CO ₂ Laser ...	43
Table 3.3 PMMA and β -TCP Composite mixing ratio	56
Table 3. 4 Specifications of the components of the SLS system	59
Table 4.1 Kinetic and thermodynamic parameters of neat PMMA derived from the DSC curve	96
Table 4.2 Experimental condition with specific energy densities and general observations	101
Table 4.3 Surface morphologies of single layer samples sintered with higher power settings	103
Table 4.4 Density and Porosity of single layer sintered PMMA at two different energy density settings	107
Table 4.5 Mechanical properties of single layer sintered samples	109
Table 5.1 Kinetic and thermodynamic parameters of PMMA and PMMA/ β -TCP composites derived from the DSC curves	117
Table 5.2 Experimental condition with specific energy densities and general observations	125
Table 5.3 Critical laser parameter	133
Table 6.1 Material and process parameter combinations used for the printed test pieces	154
Table 6. 2 Critical process parameters for Multi-layer sintering	175
Table 6.3 Density of Multilayer sintering of PMMA and PMMA/ β -TCP composites	183
Table 6.4 Mechanical properties of Multi-layer sintered PMMA and PMMA/ β -TCP composite	188

List of publications from this research

Journal Publications

1. Velu, R., & Singamneni, S. (2014). Selective laser sintering of polymer biocomposites based on polymethyl methacrylate. *Journal of Materials Research, 29*(17), 1883.
2. Velu, R., & Singamneni, S. (2014). Evaluation of the influences of process parameters while selective laser sintering PMMA powders. *Proceedings of the Institution of Mechanical Engineers, Part C: Journal of Mechanical Engineering Science, 0954406214538012*.
3. R. Velu, A. Fernyhough, D.A. Smith, M. Joo Le Guen and S. Singamneni. Selective laser sintering of biocomposite materials. *Journal of Laser in Engineering, Old city publishing, LIE 35.14*, p. 173186

Communicated

4. Rajkumar Velu, Banu Pradheepa Kamarajan, Muthusamy Ananthasubramanian, Truc Ngo, and Sarat Singamneni. Post-process composition and biological response of laser sintered PMMA and β -TCP composites. *Journal of bioactive and compatible polymers*.

Conference Publications

1. Rajkumar Velu and Sarat Singamneni, "Thermal Aspects of Selective laser sintering of PMMA/ β -TCP composite materials", *Proceedings of International Conference of Additive Manufacturing – Solid Free fabrication symposium*, University of Texas at Austin, USA, August 2015. pp 1738-1749.
2. Rajkumar Velu and Sarat Singamneni, "A Review of Finite Element Method in Selective Laser Sintering (SLS) Process", *Proceedings of International Conference on Systems Engineering and Emerging systems (ICSEES 2014)* @ PSG Tech, India. pp 61-68.
3. Rajkumar Velu and Sarat Singamneni, "Finite Element Modelling of Selective Laser Sintering Process", *Proceedings of International conference on GCMM2012* November 28-30 2012, School of Engineering, AUT University, Auckland, New Zealand

List of terms and abbreviations

PMMA	Poly(methyl methacrylate)
MMA	Methyl Methacrylate
MA	Methacrylic acid
DMI	Di-methyl itaconate
DBI	Di-n-butyl itaconate
BPO	Benzoyl peroxide
Ca-P	Calcium Phosphate
BCP	Biphasic Calcium Phosphate
OCP	Octacalcium Phosphate
TCP	Tricalcium Phosphate
α -TCP	Alpha- Tricalcium Phosphate
β -TCP	Beta- Tricalcium Phosphate
HA	Hydroxyapatite
PE	Polyethylene
PA	Polyamide
PCL	Poly(ϵ -caprolactone)
PLA	Poly(lactic acid)
PGA	Poly(glycolic acid)

PLGA	Poly(lactic-co-glycolic acid)
PEEK	Poly(ether-ether-ketone)
PLLA	Poly(L-lactic acid)
HDPE	High Density Polyethylene
POM	Polyoxymethylene
PHBV	Poly Hydroxybutyrate-Co-Hydroxyvalerate
HIPS	High Impact Polystyrene
PS	Polystyrene
PC	Polycarbonate
3DP	3D Printing
FDM	Fused Deposition Modelling
SLM	Selective Laser Melting
SLS	Selective Laser Sintering
ED	Energy Density (J/mm ²)
P	Laser power (W)
V	Lase scan speed
ED	Energy Density
FTIR	Fourier Transform Infrared Spectroscopy
SEM	Scanning Electron Microscopy
DSC	Differential Scanning Calorimetry

TGA	Thermo-gravimetric Analysis
EDS	Energy Dispersive Spectrometry
IR	Infrared
CT	Computed Tomography
CAD	Computer Aided Design
MRI	Magnetic Resonance Imaging
DNA	Deoxyribonucleic Acid
RNA	Ribonucleic Acid
ASTM	American Society for Testing and Materials
MTT	3-(4, 5-dimethylthiazol-2-yl)-2, 5-diphenyltetrazolium bromide
ALP	Alkaline Phosphatase
pNPP	p-Nitrophenyl phosphate
FE-SEM	Field Emission Scanning Electron Microscopy
MRad	Milliradian
AUT	Auckland University of Technology
CW	Continuous Wave
PID	Proportional–Integral–Derivative Controller
PWM	Pulse Width Modulation

Attestation of Authorship

I hereby declare that this submission is my own work and that, to the best of my knowledge and belief, it contains no material previously published or written by another person (except where explicitly defined in the acknowledgement), nor material which to a substantial extent has been submitted for the award of any other degree or diploma of a University or any other Institution of higher learning.

Acknowledgements

There are number of people, to whom I'm greatly indebted and without whose help, this thesis would not have been completed. I would like to express my grateful thanks to Assoc. Prof Sarat Singamneni, AUT University, who in spite of being extraordinary busy with his duties, took time out to hear, support and steer me on the right direction. I don't know where I would have been without him. I'm also thankful to Prof Thomas Neitzert, AUT University, for being the second supervisor during the course of this research.

I'm also grateful to AUT Additive Manufacturing Research Centre and the School of Engineering, Computer and Mathematical Sciences for providing me with all the experimental and computational facilities. In particular, special thanks are due to the University for funding this research, which provided the financial support for me and also allowed the necessary equipment to be procured.

I wish to express my sincere thanks to the entire Bio-technology team of the Department of Bio-Technology, PSG College of Technology, India for their support in biological studies. No sentence can express the gratitude to my parents, Mr K Velu and Mrs. Subbulakshmi and my wife Mrs. Hemalatha Rajkumar, who have been constant sources of moral support all through. I'm also thankful to Mrs. Afrose Begum and my sisters who guided me giving proper direction to my studies. Moreover, my sincere thanks to my friends, who continuously motivated and supported me. Last but not the least, thankful to the almighty and dedicating to my beloved daughter.

Rajkumar Velu

Abstract

Certain material systems are currently playing significant roles in the medical application areas. Classified as bio-polymers, polyethylene (PE), polyamide (PA), Poly(ϵ -caprolactone) (PCL), poly (lactic acid) (PLA), poly (glycolic acid) (PGA), and poly (lactic-co-glycolic acid) (PLGA), poly (methyl methacrylate) (PMMA) are notable examples. While these materials are known for their bio-compatibility characteristics, the bio-conductive nature promoting further growth and repairing the damaged parts is often lacking. Natural coral derived HA/calcium carbonate composites and synthetic calcium phosphates are known for bio-conductivity. As a natural consequence, medical materials used in particular for bone repair and replacement needs are a mixture of a biopolymer composite and a bio ceramic. The resulting bio-polymer composites loaded with bio-ceramics such as hydroxyapatite and calcium phosphate into different bio-polymer matrices combine the properties both phases and serve the purpose of the specific medical application.

Several processing methods such as solvent casting or leaching, phase separation, foaming, gas saturation etc., are applied to put these polymer composites to service. However, most methods fail due to several drawbacks such as time and cost involved and more importantly, lack of flexibility to exactly reproduce complex shapes. In particular, achieving a complex shape is often a prerequisite condition in many medical applications. During the past two decades, the layered processing methods rapidly evolved from mere prototyping solutions to the more advanced technologies, commonly referred to as additive manufacturing. Considering the freedom these techniques offer to manufacture

complex forms without any specific tooling or the alteration of the materials and processes, it became important to revisit the current processing techniques as applied to different biopolymers used for varying medical needs. The current research is an attempt in this direction, evaluating a selected combination of a bio-material and an additive processing technology.

The specific medical application area targeted is in the bone repair and replacement tasks. Poly (methyl methacrylate) (PMMA) is selected as the base polymer considering its wider use in bone related applications. The β -form of the tri-calcium phosphate (β -TCP) is the bio-ceramic component to impart the bio-conductivity to the polymer composite. Selective laser sintering is the process, considering the ease of working with powder raw materials and the ultimate control over the micro and meso structures of the sintered substrates. The material consolidation mechanism involves localized heating by a fast moving laser beam. The first task is to match the material combinations with the laser energy so that the substrates absorbs sufficient energy from the laser to achieve the particle melting, fusion, and consolidation.

Considering the absorptivity levels of the constituent powders, a CO₂ laser source is selected for the experimental investigations. Simulating the laser sintering process conditions required the development of both hardware and software systems and the integration of the same to achieve the overall experimental test bed. Powder feeding and envelope temperature control systems are added for further process controls. Establishing the viability of the material and process combination involved experimental evaluations in three significant stages. The neat PMMA powders are evaluated first for laser sintering with varying process

parameters. Working ranges of laser energy densities for initial laser sintering experiments are established by differential scanning calorimetric results. Morphologies of sintered surfaces and porosity analyses are used to evaluate the intra-layer coalescence. Critical process parameters, laser power and scan velocities are gradually adjusted towards more optimum combinations based on these initial results. Further sintering trials and evaluation of the morphological, physical and mechanical characterization results allowed to establish the best process conditions and the overall effectiveness of neat PMMA for selective laser sintering. The same procedure is repeated in the second stage based on varying compositions of PMMA plus β -TCP composites. The final stage involved evaluation of the possible after-effects if any on the biological and the multi-layer responses of the sintered polymer composites based on Fourier transform infrared spectroscopy (FTIR), in-vitro analyses, and mechanical testing.

Overall, the experimental results indicate the suitability of both neat PMMA and PMMA plus β -TCP polymeric materials for processing by selective laser sintering. Best combinations of critical process parameters, laser power and scan velocities could be established for both material systems. The laser interactions are proved to cause no detrimental effects either in the polymer chemistry or the biological nature of the materials further to sintering. Sufficient inter-layer coalescence is also evidenced, establishing the effectiveness of the material and process combination for manufacturing 3D forms. Considering the significant attributes of the constituent material systems and the unlimited design freedom allowed by the laser sintering approach, the findings reported in this thesis are expected to pave ways for wider research interest as well as potential medical applications in the future.

Chapter 1

Introduction

1.1 Bio-polymers and composites

Highly complex and hierarchically structured materials, together with abilities to spontaneously repair with minimal treatment or scarring are often needed for medical applications such as bone replacement and repair [1]. While allowing for the bone's geometry to adapt to the new loading conditions, the replacement material should also enhance the osteogenic healing process, when the defects are too large. Autograft, allograft, and xenograft techniques are common bone grafting methods, with specific shortcomings in each case; such as limited amount of extraction from the iliac crest, additional trauma and possible morbidity [2-4], immune rejection and inflammation possibilities [5-7], and high residual risk of disease transmission and immune rejection [8]. Bone replacement materials based on natural coral derived hydroxyapatite (HA) /calcium carbonate composites [9] and synthetic calcium phosphates [10] offer to resolve some or all of these issues and attract wider medical applications despite limitations such as shrinkage [11]. Consequently, the search for both material and process alternatives is never ending as new options are always investigated and established for use in the medical application areas.

Bio-polymers such as polyethylene (PE), polyamide (PA), Poly(ϵ -caprolactone) (PCL), poly (lactic acid) (PLA), poly (glycolic acid) (PGA), and poly (lactic-co-

glycolic acid) (PLGA), and poly (methyl methacrylate) (PMMA) are notable examples already added to the repertoire of biomedical materials. The mechanical strength and other attributes of some of these materials are noted to make them suitable for permanent and bio-resorbable implants [12 & 13]. Bio-polymer composites combining ceramic elements such as Hydroxyapatite (HA) and Tricalcium phosphate (TCP) with different base polymers have been used as bone replacement materials [14]. The biphasic composites of TCP and HA with varying compositions have also been used in dental applications [15].

While neat bio-polymer options lack bioactivity [16], bio-ceramics are weak and brittle; consequently, combinations of natural and synthetic polymer-ceramic composites became choice-materials, targeting both strength and bioactivity responses [17]. By combining biodegradable polymers and bioceramics such as HA and β -TCP it is possible to achieve biodegradable, osteoconductive, and bioactive materials [18]. Suitable manufacturing methods are then needed to achieve highly porous and interconnected structures with suitable surface chemistry and topography, for cell attachment, proliferation, and differentiation, together with sufficient mechanical properties [19 & 20]. The material and process combinations should also enable achieving controlled volume fractions and appropriate distribution of the bio-ceramic phases within the polymer/ceramic system to meet the mechanical and physiological requirements when used as implants [21]. Current manufacturing methods are often limited in capabilities to achieve all the essential attributes.

1.2 Traditional manufacturing methods and new developments

Solvent casting/salt leaching, phase separation, foaming, gas saturation, and use of textile meshes are common methods often used for processing bio-polymer composites, in particular for fabricating scaffolds for tissue engineering. Drying and sol-gel methods often result in shrinkage problems as noted by Goodridge *et al.* [13]. A powder material form was identified to be a better option to develop bone replacement solutions, but the lower mechanical strength and stiffness were limitations as well as the low fracture toughness of ceramics. Limitations associated with controlling the pore size, geometry, and the spatial distribution are further issues with these methods. In addition, complex re-entrant sections are difficult to be achieved, toxic organic solvents are used, and long fabrication times are often needed [22 & 23]. Most processes also depend largely on individual skills and pose serious limitations towards achieving consistent results and complex forms [24].

In recent years, layered manufacturing methods such as 3D printing (3DP), Fused Deposition Modelling (FDM), Selective Laser Sintering (SLS), and inkjet printing evolved as possible solutions to achieve complex shapes direct from computer generated data [25]. In biomedical research in particular, SLS has proved to play a greater role, as controlled micro-porosity could be achieved by varying the critical process parameters, laser power, scan speed, and part bed temperature considering composites of HA and other biopolymers. Naing *et al.* evaluated the surface morphologies of sintered HA/PEEK (Polyether ether ketone) composites and also fabricated scaffolds for evaluating the porosity levels and the effects of balling [20], while high density polyethylene (HDPE), with

HA as the filler was evaluated for laser sintering by Hao *et al.* and Savalani *et al.* [26 & 27].

Both material and process advances are evident in biopolymer applications for medical needs. In particular, the combination of additive processing and several bio-material alternatives appears to be the way forward in order to achieve most attributes finally required of materials and implants made of them for medical uses. Work is already in place applying the additive processing methods to specific polymer materials, but the overall progress is limited. Many aspects are yet to be investigated and explained, while new combinations of materials also offer further challenges and renewed opportunities. The current research is another step in this direction, evaluating one of the most promising additive technologies to process an equally promising material combination, with particular reference to bone repair and replacement tasks.

1.3 The Materials

Poly (methyl methacrylate) [(PMMA)-(C₅O₂H₈)] is a synthetic resin known for its toughness, rigidity, transparency, and stability in varied atmospheres. It has also been a popular choice for biomedical applications and offers potential compatibilities with the human tissue. The widely varying characteristics make PMMA a popular choice in quite different applications, including both industrial and medical uses. Further, the interconnected porosity characteristics allow PMMA to be used as a bone cement to fix implants and remodel lost bones [28]. In spite of all these attributes, neat PMMA suffers from a lack of bioactivity, which puts serious restrictions on its use in bone repair applications [29].

In order to develop strong bonds with the host bone, tricalcium phosphate $\text{Ca}_3(\text{PO}_4)_2$, and in particular the β -TCP form has been the choice as a bio-ceramic reinforcement for both organic and inorganic composites [30]. In view of this, the polymer composite based on PMMA and TCP appears to be the right combination to achieve both bio-compatibility and bio-activity attributes. Thermal forming techniques were applied to PMMA and β -TCP composites earlier, fabricating scaffold structures for tissue engineering [31]. The properties of the scaffolds were observed to be close to the native bone tissue, while growth of the neo-tissue was also evidenced. Polypropylene and TCP composites were also developed in filament forms and proved to be suitable for extrusion 3D printing, based on fused deposition modelling [32]. Ca-P and poly hydroxybutyrate-co-hydroxyvalerate (PHBV) nanocomposites were successfully processed by selective laser sintering achieving controlled structures and interconnected porosities targeting bone tissue engineering applications [30].

Combining different bio-polymers as base materials and bio-ceramics as filler materials, targeting better biological responses for the composites has been established in several cases. Progress is also evident in bringing the additive manufacturing and biopolymer composites together. However, the specific combination of PMMA and β -TCP, though evaluated by traditional methods, has not achieved much research attention yet for additive processing. In particular, the ability to process PMMA and β -TCP composites by SLS is not evaluated yet.

Further, evaluation of the after effects of SLS on the neat PMMA and the PMMA plus β -TCP composites need to be undertaken more systematically. Occasional attempts are evident evaluating the post-process biological responses of

polymers subjected to additive processing. Kalita *et al.* proved the matrices to be nontoxic while analyzing the polypropylene and tricalcium phosphate samples made of FDM [32]. Similar investigations on the laser sintered polymer nanocomposites showed improved cell proliferation and alkaline phosphate activity in the presence of Ca-P [33 & 34]. While these preliminary investigations indicate no obvious losses due to processing by additive methods, selective laser sintering of PMMA and PMMA plus β -TCP components are yet to be investigated to ascertain the same.

1.4 Research gaps, questions, methods and implementation

Evidently, the PMMA/ β -TCP polymer composites are potential candidates for medical applications such as bone repair and replacement. Selective laser sintering is also proved to be a potential processing route for bio-polymer composites to achieve application-specific micro and macro structures and overall forms. However, the PMMA based material systems and the SLS processing method are not evaluated together yet. Once the material and process combination is proved to work, the process parameters together with the material variations and their combined influences on the critical responses need to be established. Further, the polymer degradation possible due to the laser interaction and the variations in the biological responses should be ascertained.

These are the research gaps identified to formulate the overarching research question for the current work; How do neat PMMA and PMMA plus β -TCP composites respond to processing by selective laser sintering under varying material and process conditions and what after-effects do laser heating leave in the sintered substrates?

Initial working laser process parameters should be obtained by means of the thermal characterization of the material powders. Suitable experimental test facilities will have to be designed and developed considering the unavailability of viable commercial solutions. The optimum parameters for processing selected grades of PMMA and β -TCP powders mixed in different compositions have to be established next based on morphologies, physical, and mechanical characterization of single layer samples. Possible polymer degradation due to photonic interactions has to be evaluated. The biological responses of the sintered specimens need to be ascertained through evaluating the *in vitro* osteoblast functions. Considering the final applications of the materials to make complex 3D forms, laser sintering across multi-layers must be evaluated.

Literature relevant to the field of interest and more close to the actual topic is reviewed and the critical process and material parameters and settings are identified. A CO₂ laser sintering system is designed and developed together with other peripheral devices to control the envelope temperature and other process conditions. Initial sintering trials are done based on ballpark energy density calculations and more appropriate process conditions are established gradually working through the critical responses. Sintered single layer surface morphologies, porosity and tensile strength are specific responses used to establish the roles of critical process conditions. Numerical and experimental evaluation of the thermal fields allowed to understand the consequences of mixing powders of widely varying thermal attributes to sinter together. Post sintering performance is understood first ascertaining the absence of any polymer degradation based on the results of a FTIR analysis. *In vitro* studies detecting

attachment, spreading, proliferation, and osteogenic differentiation of MG-63 cells allowed to establish the bioactivity levels. Inter-layer coalescence and sintering responses are obtained and evaluated through multi-layer sintered samples.

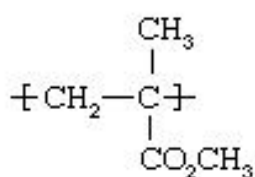
Overall, the neat and the composite forms of PMMA are proved to be suitable for processing by selective laser sintering. The morphologies, porosities and the mechanical responses are varied with varying process conditions, together with the material compositions. Results also indicate no loss of polymer quality and evidence of any degradation, while the biological responses are positive and varied with composition and process-dependent porosity levels. Multi-layer sintering is also successful, ascertaining the PMMA and SLS combination as a viable means to solving specific problems in the future bone repair and replacement applications.

Chapter 2

Literature review, research gaps, questions, and objectives

2.1 Poly (methyl methacrylate) (PMMA)

Poly (methyl methacrylate) (PMMA), a synthetic resin produced from the polymerization of methyl methacrylate, is a transparent and rigid polymer. Often used as a substitute for glass in products such as shatterproof windows, skylights, illuminated signs, and aircraft canopies, it is sold under the trademarks Plexiglas, Lucite, and Perspex. PMMA was first formulated in 1865 as an ester of methacrylic acid ($\text{CH}_2=\text{C}[\text{CH}_3]\text{CO}_2\text{H}$) and belongs to the important acrylic family of resins, created earlier as shown in Fig. 2.1. In modern production, it is obtained principally from propylene, a compound refined from the lighter fractions of crude oil. Propylene and benzene are reacted together to form cumene, or isopropylbenzene. The cumene is oxidized to cumene hydroperoxide, which is treated with acid to form acetone. Acetone is in turn converted in a three-step process to methyl methacrylate ($\text{CH}_2=\text{C}[\text{CH}_3]\text{CO}_2\text{CH}_3$), a flammable liquid. Methyl methacrylate, in bulk liquid form or suspended as fine droplets in water was polymerized (its molecules linked together in large numbers) under the influence of free-radical initiators to form solid PMMA in 1877 by the German chemist Wilhelm Rudolph Fittig [35]. The structure of the repeating unit of the polymer chain is:



The presence of the pendant methyl (CH₃) groups prevents the polymer chains from packing closely in a crystalline fashion and from rotating freely around the carbon-carbon bonds. As a result, PMMA is a tough and rigid plastic and was first made commercially viable as acrylic safety glass in 1936. In addition, it can also transmit visible light perfectly and retains these properties over years of exposure to ultraviolet radiation and other weathering conditions. These attributes qualify PMMA as an ideal substitute for glass. Generally, the plastic is drawn into sheets that are machined or thermoformed to shapes, but it is also injection-moulded to make automobile lenses and lighting-fixture covers. Because PMMA displays the unusual property of keeping a beam of light reflected within its surfaces, it is frequently made into optical fibres for telecommunication or endoscopy. Further qualities such as biocompatibility, reliability, relative ease of manipulation, and low toxicity soon qualified PMMA to be adopted by different medical specialties.

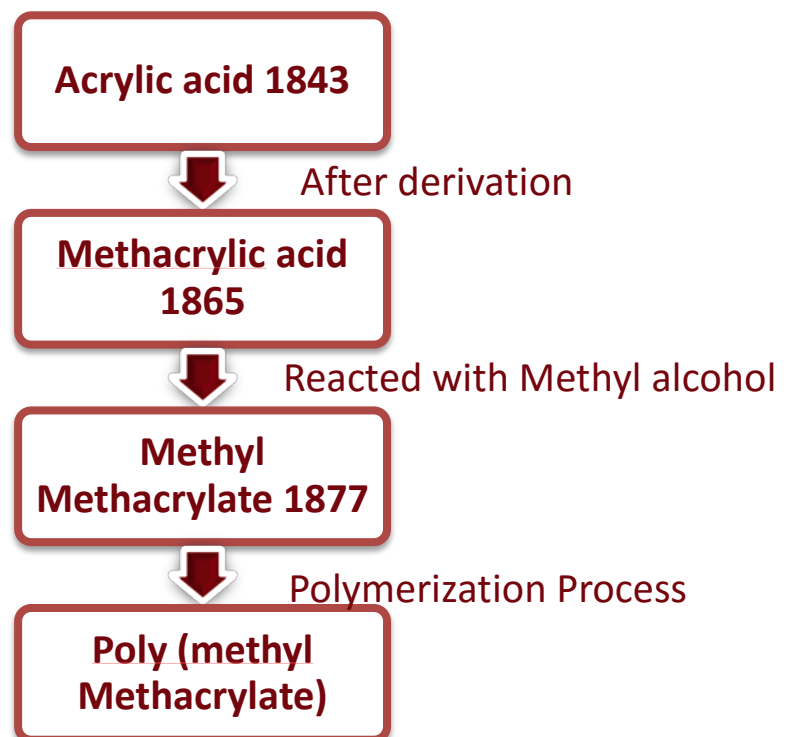


Figure 2.1 The chronology of PMMA development [35]

2.2 Industrial uses⁴⁸

The distinct features of PMMA compared to the other thermoplastic polymers allow it to find wider application in quite different areas such as architecture, construction, automotive, electronics, aerospace, and medical, to name a few. Door and window profiles, canopies and balustrades, sound barriers, aquaria, structural panels, carport and patio roofs, facades, etc., are common construction and architectural applications. Excellent chemical resistance including room temperature resistance to aliphatic hydrocarbons, mineral, vegetable, and animal oils, lye and weak forms of acids apart from the water absorption rate of 0.8% make them suitable for applications in aquaria [36]. The higher tensile, flexural, and pressure resistance compared to other thermoplastic polymers and the consistent mechanical performance within the temperature range from -40°C to +70°C and the superior resistance to UV radiation allow for PMMA to be extensively used in automotive and aviation industries; aircraft canopies and automotive glazing being notable examples. Attributes such as the chemistry to be in a clear water-white and transparent liquid monomer, the abilities to be polymerised into sheets, rods, tubes, moulding pellets, and additives and subsequent high formability allow PMMA to be used for multiple industrial applications [37].

PMMA sheets are often used in applications where electromagnetic radiation of specific wavelengths needs either to be passed or blocked. Depending on the thickness, PMMA sheets transmit infrared energy of wavelengths within the range 700 nm to 2800 nm. PMMA sheets of thickness 3mm and above are completely opaque to infrared radiation within the 2800 nm to 25000 nm wave length range

while a thickness less than 3 mm could result in partial transmission within this range [38]. Coloured PMMA sheets allow IR waves to pass through, while blocking visible light, which allows them to be used in remote control and heat sensor applications [39]. The U-factor and the overall heat transfer coefficient of PMMA are 10% lower than that of glass for the same thickness which impart better glass thermal shock and stress characteristics [40].

PMMA also finds extensive use in the electronics industry as display panels in equipment and infra-red transmitter/receiver windows. The high surface hardness has been the subject of substantial research and investigation evaluating the polymerisation mechanisms inducing the surface hardness through ionizing radiation such as e-beam and γ -rays. The material responses were identified to be widely different with high energy ion-beams induced by e-beam and γ -rays, while the cross-linking or the scission efficiency were found to depend on the polymer structure [41]. The aspect that PMMA degrades and dissolves in solvents when subjected to e-beam or γ -rays compared to other polymers qualifies it to be a photo-resist material in lithography and paves ways for the use in the semiconductor industry [42]. According to Lee *et al.*, massive increase in cross-linking and surface hardness can be achieved by subjecting PMMA to high energy ions such as 2 MeV Argon ions [43].

Settling and re-dispersion of dispersed magnetic particles can be achieved in industrial applications by dispersing PMMA on carbonyl iron based composites in magnetorheological fluids. Instead of using solid additives with carbonyl iron microspheres, Choi *et al.* observed that PMMA coatings based on in situ dispersion polymerisation exhibit decreased density and sustained yield

behaviour [44]. Further, PMMA is also proved to be the best material option for dairy equipment used for milking considering the high abilities to be cleaned and other surface attributes, compared to other competing alternatives such as stainless steel and polypropylene. Based on residual soiling infra-red spectroscopy studies on surfaces with adhering components dissolved into solvents, Wildbrett *et al.* observed that huge amounts of fat and proteins attached to polypropylene and stainless steel respectively, while PMMA was proved to be thoroughly clean [45].

2.3 Medical applications

PMMA exhibits excellent biocompatibility, which makes it a popular choice for different medical applications. Acrylic type materials in particular are used as intraocular lenses in cataract surgeries with recurrent ocular inflammations [46]. Sulcus-placed intraocular lens developed using PMMA is known for rigidity that contributes to enhanced concentration and resistance to tilt. PMMA is also used to develop anterior chamber intraocular lens and iris-fixated intraocular lens. Acrylate monomers containing one or more hydroxyl groups with hydrophilic, hydrophobic, and foldable characteristics are also used to develop soft contact lenses [47].

Acrylic resins are used to fabricate provisional restorations in dentistry for over five decades. These resins are typically PMMA or methyl methacrylate (MMA) based and have adequate strength and colour characteristics matching with the human dental support structures [48]. In fact, PMMA is one of the most unmodified acrylic materials for dental applications considering the absence of

tissue irritation, toxicity, and tooth adhesion [49]. Due to the high glass transition temperature (T_g), PMMA also tolerates heat while trimming, grinding, and finishing of the cured material without any distortion.

Certain compositions based on PMMA have been used as bone cements much before the actual application in dentistry. Specific examples include; bone cavity filling, rectifying skull defects and vertebrae stabilization in osteoporotic patients [50]. Structurally, PMMA based bone cements are formed of typical linear polymers, while they can also be modified in the form of a semi-IPN (Interpenetrating polymer network) structure by adding small amounts of cross-linking monomers (e.g. 2-30 wt% of ethylene glycol dimethacrylate, egdma) to the liquid phase [51]. Mousa *et al.* reported a dry method of producing bioactive cements through a salinization process to form bonds across the interface between mineral and organic components of apatite-wollastonite glass ceramic (AW-GC) with high molecular weight PMMA particles, but the properties of the cement appeared to be poor [52]. While investigating different combinations, Surgical Simplex and Palacos were mixed with MMA monomer to make PMMA-based cements and also Benzoyl peroxide (BPO) and N, N-dimethyl-p-toluidine were added to the cement improving the handling properties and dough setting times.

2.4 Processing Methods

Commercial manufacturing of PMMA in sheet, rod and other forms is essentially done either by extrusion or by casting. The extrusion method involves the liquid PMMA pushed by means of a roller and pressing into sheets while cooling. This

is simpler, cheaper, and easier compared to casting but prone to scratches and contamination. Domestic decoration items, artistic pieces, and kitchenware are often artefacts produced by this method [53]. Casting is done by pressing liquid PMMA between parts of a closed mould often made of glass and subjecting to a thermal cycle. Cast sheets are stronger than the extruded ones and are employed for applications such as aquariums and other products.

Seamless fabrication of PMMA structures is possible by means of chemical welding, based on solvents like chlorinated hydrocarbons; methylene chloride and carbon tetrachloride. PMMA can also be processed by emulsion polymerization, solution polymerization, and bulk polymerization [54]. All these processing methods propelled the applications of PMMA as it is made available in different forms, from moulding powders to flat sheets, rods, and tubes, for further processing into different shapes.

Injection moulding is commonly used to form shapes based on thermoplastic materials and is equally applicable to PMMA, in addition to the latter developments such as micro injection moulding used for the direct production of micro-parts [55, 56]. While comparing the performance of three different polymers, PMMA, PEEK, and POM, Michaeli *et al.* noted both PMMA and POM attaining better bonding in microinjection moulding compared to PEEK, due to better polymerisation [57]. Poitter *et al.* also noted the better reliability of PMMA for micro injection moulding in the context of manufacturing ribbon optical fibre connector [58].

Compression moulding was applied by park *et al.* targeting total hip replacement solutions based on PMMA [59]. Evaluation of physical, chemical and thermal properties revealed density levels indicative of complete sintering. PMMA loaded with different filler materials were also attempted successfully for compression moulding, identifying the diffusion-related behaviour across the interfaces as well as the curing of the monomer in the interstitial cavities as was the case with alumina tri-hydrate additions [60]. The exemplary optical properties and good formability attributes qualify PMMA for processing by thermo-forming, targeting optical products. Based on numerical simulations and experimental evaluations Taher *et al.* assessed both free- and plug-assisted forming characteristics of PMMA and reported equally good responses in terms of wall thickness and minimum mould marks [61]. Again, numerical and experimental evaluation led Dong *et al.* to believe that PMMA sheets can be thermo-formed into materials with isotropic structures [62]. Hot embossing and thermal nano-imprinting were combined to fabricate PMMA microchannel arrays and ascertained to result in fluid flow behaviour similar to the master stamps [63]. Lee *et al.* also used similar techniques to manufacture micro-fluidic devices and establish successful performance [64].

Emulsion, solution, and bulk polymerization methods are often used to produce flat sheets, elongated rod and tubular forms, and moulding powders of PMMA [54]. While moulding powders are made by suspension polymerization, flat sheets are formed by bulk polymerization based on the reactions between the monomer and the catalyst inside the mould [65]. Controlled environment and careful storage and handling of the chemicals are essential in order to prevent contamination and unsafe chemical reactions [66]. Nano-composites, monomers,

clays, and other fillers are also employed with polymerisation techniques in order to reinforce the polymer matrix [67]. Emulsion polymerisation of the monomer dispersed in water with a water soluble radical initiator in the presence of Na⁺ exchanged montmorillonite was reported to enhance both thermal stability and tensile properties of the polymer composite produced [68].

The polymerisation methods are more commonly used for medical applications. In dentistry, a two-component self-polymerising system is employed, consisting of a powder component PMMA polymer or related block copolymers and a liquid component made of methyl methacrylate (MMA) or related monomer liquids. Self-curing PMMA powders consisting of PMMA or related block copolymer beads (diameter 50 μm), an initiator, and radio-opaque substances are used as orthopaedic bone cements, combining the powder components which auto-polymerise within 10-15 minutes [69]. A mouldable viscous dough forms first after 3-7 minutes, followed by a very dense cured PMMA- based bone cement. The surgeon can judge the curing of the bone cement by pressing a thumb on it [69].

2.5 Limitations and enhancements

The foregoing discussion clearly elucidates the wider application of PMMA and the quite divergent processing methods employed. However, shortcomings are experienced due to both material and process limitations. Processing methods employed for industrial uses often suffer from delamination, embedded contaminates, stringiness, warping, and appearance of welding lines, apart from enormous material wastes in some cases. Further, high process costs, need for skilled workforces, excessive processing times and unavoidable internal stresses

are other significant bottlenecks. Long cycle and dwell times often also lead to polymer degradation.

Though a popular choice, the medical use of PMMA also suffers from limitations arising out of the processing methods, speed, time, and method of mixing, and composition of monomers and powders etc. In dentistry, during the material preparation stages, repeated mixing could lead to cytotoxic monomer formation that might lead to adverse effects on the oral tissues and some allergies. Irritation of oral mucosa may be exacerbated with changes in mixing proportions [70]. PMMA also suffers from shrinkage during polymerization and may lead to poorly fitting restorations. The cumulative effects of these shortcomings may lead to cracks, structural damages and consequent effects on adjacent oral tissues and possible formation of bacteria, yeasts, and moulds. Evidently, each of the PMMA processing methods as listed in Table 2.1 suffers from specific drawbacks, while polymerization techniques used for biomedical applications are restricted due to both extrinsic and intrinsic factors. The speed and time of mixing, mixing methods, pre-chilling of the monomer, and degree of porosity are the extrinsic factors, while composition of monomer and powder, powder particle size, shape and size distribution and powder-liquid ratio are the intrinsic factors affecting the mechanical properties of PMMA bone cements [71].

Ongoing research to overcome these deficiencies is mainly focussed on material enhancements. Modification of PMMA with di-methyl itaconate (DMI) and di-n-butyl itaconate (DBI) with varying concentrations based on a standard bath curing process led to the observations that the composition is less toxic and more environment and patient friendly [72]. Polymerization of mixtures of varying proportions of methyl methacrylate (MMA) and Methacrylic acid (MA) monomers

and subsequent mechanical characterisation showed that lower percentage of MA gives high transverse and flexural strength while higher percentage of MA results in the lowest modulus of elasticity and the greatest ionic charge [73]. However, the modification of PMMA with an acid resulted in a change of physical properties of the resin and allowed for achieving the desired biological responses by decreasing the candidal adhesion.

Tale 2.1 Conventional fabrication methods, applications and limitations

Conventional PMMA Fabrication method	Applications	Limitations
Injection Moulding [55-58]	Glazing (wind shields for boats, snow mobiles, airplanes)	Delamination Embedded contaminants Stringiness Weld line Warping
Compression Moulding Process [59&60]	Commercial signs, Solar panels, Bath housing and shower doors	Enormous Material waste High Labour cost High skill level required for larger part tools Slower processing time High part cost
Thermoforming [61&62]	Eye lenses, binoculars and fiber optics for light piping	Material waste Higher process cost Only one side of part is defined by the mould Causes Internal stresses
Hot Embossing [63&64]	Watch, clock and radio faces, motorcycle helmet visors	Difficulty in building up pressure, Long cycle time Long dwell time results polymer degradation
Synthesis and Polymerization [65-69]	Biomedical Applications like Bone cement for orthopaedic and dentistry. Paints and Artistic paint surfaces	Difficulties in Speed and time of mixing, Mixing methods, composition of monomers and powders

Shuichi Shinzato *et al*, developed PMMA-based composite bioactive bone cements consisting of bioactive MgO-CaO-SiO₂-P₂O₅-CaF₂ glass beads as

inorganic fillers and noted improvements in mechanical properties with varying proportions of the constituent phases together with possible variations in the degree of degradation [74]. The bone cement acts like a grout and not so much like a glue in arthroplasty and although sticky, it does not bond to either the bone or the implant, and primarily fills the spaces between the prosthesis and the bone, preventing motion. A big disadvantage to this bone cement is that it heats to quite a high temperature while setting and damages the bone in the surrounding area, and the additives need to be altered. There were other attempts also, to achieve a bioactive PMMA-based bone cement by adding Ceravita [75] and Bioglass [76] etc., but the results were not satisfactory due to the deterioration of the mechanical properties when the wt. % of the bioactive particles exceeds a certain limit, or a lack of bioactivity when the wt. % of the bioactive particles was too low.

Evidently, material enhancements achieved noteworthy research focus, targeting better utilisation of the multi-purpose PMMA material. The processing methods appear to have stagnated though, for a while. It is pertinent to note that both material and process enhancements are essential and more fruitful end results may be achieved through an integrated evolution of both. Indirect processing techniques do exist, but require more process steps, are less automated, have high material waste when machined subsequently, require special tooling, and also may cause aseptic loosening of the prosthesis in medical uses [77]. The mechanical weakness of the cement made by these conventional techniques may also lead to fractures [78], while production of wear debris by abrasion may result in prosthesis loosening [79]. Further, conventional process routes seriously limit the freedom to fabricate parts of complex shapes with re-entrant sections and considering that most biomedical applications require reproduction of very

complex shapes, alternative methods, including reverse engineering [80 & 81] and rapid prototyping [82 & 83] have attained much attention. This line of investigation is envisioned here encapsulating in particular, the developments occurring in the layered processing methods that are gradually evolving as additive manufacturing.

2.6 Additive processing

Rapid Prototyping (RP) refers to a set of allied technologies that can be used for building very complex physical models and prototype parts directly from computer data generated by Computer Aided Design (CAD) [84 & 85], Computed Tomography (CT) or Magnetic Resonance Imaging (MRI) data. With material and process improvements, some of these techniques have overcome the initial limitations and acquired abilities for the direct production of end use parts, and are being commonly referred to as rapid or additive manufacturing (AM) technologies. Selective Laser Sintering (SLS) [86 & 87], Selective Laser Melting (SLM) and Fused Deposition Modelling (FDM) [88 & 89], are noteworthy AM processes. Additive manufacturing offers certain unique characteristics for the end product, including unlimited design freedom and control over the macrostructures, where necessary. Specifically, selective laser sintering (SLS) scores the best in terms of processing biopolymers in powder form [80 & 81]. A CO₂ laser is commonly used considering the laser absorptivities of polymeric materials, and the powder material is converted into 3D forms based on the raster path data generated from CAD files. The interconnected porosity of the sintered part can be controlled through material selection, physical design, and processing parameters [90].

Considering the difficulties of processing PMMA and the numerous benefits of additive manufacturing, it becomes interesting to evaluate how the two approaches work together. The feasibility of using FDM to fabricate porous customized free form structures of medical-grade PMMA was investigated by Espalin *et al.* Evidently, PMMA was proved to be suitable for processing by FDM, allowing for medical applications such as custom fabrication of craniofacial implants from medical imaging data and paving way for better applications in medicine [91]. However, FDM suffers from certain inherent limitations such as poor part definition, insufficient surface qualities resulting from stair-step effects, and the need to build support structures.

On the other hand, Selective Laser Sintering (SLS) permits extremely complex shapes to be produced and enables the economic production of implants customized to size and functionality for individual patients. During SLS process, powders are subjected to low compaction forces, and the fabricated objects are inherently porous; a key property requirement for some in-vivo implantation devices. To date, medical applications of SLS have primarily been concerned with the production of physical models of human anatomy for surgical planning, training and design of customized implants [26]. While producing parts significantly closer to the expected levels of quality both in terms of dimensional tolerances and mechanical properties, SLS also allows processing of any material in powder form and with attributes to soften or melt and fuse when thermally treated by a laser. Berry *et al.* fabricated SLS models of two skulls and a normal femur using nylon, with the dimensions in virtuous agreement with the CT data [92]. Though selective laser sintered polymers were noted to possess

good biocompatibility and malleability attributes, the neat biopolymers generally lack bio-activity and show limited affinities to promote and interact with the surrounding tissues [93]. This necessitates the use of filler materials of suitable attributes to be employed, leading to bio-polymer composites, which will add further material and process complications as discussed in the next section.

2.7 PMMA-Ceramic composites and processing

Different types of biopolymers, including PMMA with both bio- stability and degradability have been studied largely for tissue engineering applications [94]. Linear, cross-linked, and interconnected polymer networks are the different structural forms, but the modulus of elasticity and deformation resistance properties are typically low. In particular, the neat bio-polymers severely lack bio-activity. Bio-ceramic materials are often used as fillers to enhance mechanical as well as bio-conductive attributes of composites employed for biomedical needs. Fig 2.2 is a graphical visualisation of the need, essential components, and target outcomes of the endeavours around bio-polymer-ceramic composite material developments.

Phosphorous is an essential element in all living systems as a key part of the phosphodiester bonds in Deoxyribonucleic Acid (DNA) and Ribonucleic Acid (RNA), and was identified to promote bio-activity in biopolymer applications through the augmentation of the tissue contact. Consequently, phosphorous-containing biopolymers are synthesized and developed as polymeric candidates for tissue engineering applications [95]. However, the polymer matrix containing the filler components results in complicated interactions between the constituent

phases of widely differing properties. Inorganic bio-ceramics are often the choice filler materials for bone replacement and repair applications. Highly complex and hierarchically structured materials with high mechanical performances are involved in the making of bones, while bone fracture defects are generally repaired spontaneously with minimal treatment or scarring [96]. When the defects are too large, as caused by trauma, tumor resection, osteomyelitis, and maxillofacial bone losses, a replacement material is often needed. This is to enhance the osteogenic healing process which is indispensable for the removal and replacement of the damaged parts. It also helps the bone's geometry to adapt to the new loading conditions. Autograft, allograft, and xenograft are common techniques used for bone grafting.

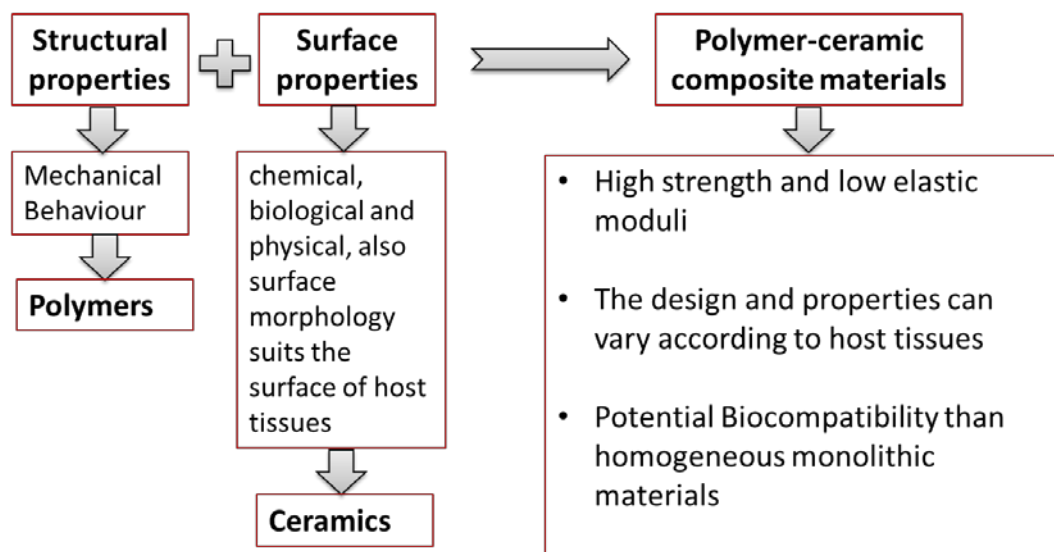


Figure 2.2 *The polymer-ceramic composite realm*

The autograft technique is quite successful in promoting osteoconductivity, bone formation and bone ingrowth, but is often associated with other difficulties such as the limited amount of extraction from the iliac crest and additional trauma and probable morbidity [2-4]. Allograft methods reduce risks of morbidity, but the

mechanical properties are inferior to autografts, and immune-rejection and inflammation possibilities are quite high [5 & 6]. Possible residual risk of disease transmission is also high [7]. Xenografts, though successfully employed for many years and offer impressive mechanical property results, the residual risk of disease transmission and immune rejection are still high [8]. Naturally derived bone replacement materials like HA/calcium carbonate composites and synthetic calcium phosphates offer to resolve some or all of these issues. These are excellent materials for bone replacement, as they have chemical affinity to the bone and when made as porous structures, facilitate effective interactions with the surrounding soft tissues and also invariably enable the exchange of nutrients and waste materials. It is feasible to fabricate the scaffolds with the pore sizes between 150-500 μm , which are in the range of the cancellous bones.

Calcium phosphates are shown to exhibit a variety of forms, but from the chemical perspective, hydroxyapatite (HA) [97], β -tricalcium phosphate (β -TCP) [98], multiphasic bioglass, biphasic calcium phosphate (BCP), and octacalcium phosphate (OCP) have evolved over time and been investigated both *in vitro* and *in vivo* [99]. Among these, TCP has better biodegradability and is most commonly used in bone surgery. It has two major distinct phases of anhydrous crystals as mentioned above: monoclinic α -TCP (low-temperature polymorph) and rhombohedral β -TCP (high-temperature polymorph). Further, considering better biocompatibility, osteoconductivity, and cell-mediated resorbability, β -TCP ($\text{Ca}_3(\text{PO}_4)_2$) and its derivatives and their combinations are most commonly used as bone substitutes as depicted in the chart of Fig 2.3. A Ca/P ratio of 1.5 is commonly used as it is within the physiological range of the human bone, which is 1.3–1.66, depending on the person's age and the state of well-being [100]. The

most stable phase is β -TCP, up to 1125 °C, and so its thermal stability and transformation behaviour are well under control.

The β -TCP ceramic possesses a high affinity for proteins and its porous structure acts as a filter to accumulate the growth factors from the surrounding body fluids. After implanting β -TCP particles as porous blocks in the bone, new lamellar cancellous bone forms within 4–8 weeks. It is also noteworthy that β -TCP is resorbed by osteoclast cells, whereas the much slower resorption of hydroxyapatite is affected mainly by foreign-body giant cells with limited resorbability. The processing methods often used with β -TCP are synthetic manufacturing approaches by mechanical-chemical means, but the mechanical strength and the fracture toughness are still low, restricting its use to low load-bearing applications [31]. Alternatively, the β -TCP ceramic needs to be processed together with specific biopolymer materials, targeting critical property improvements. Common biopolymer materials, and the bio-ceramic alternatives that are used to form composites are listed in Fig. 2.4, and considering the superior attributes as identified already, the PMMA and β -TCP combination is chosen as the possible material option for evaluating the research questions to be raised in the next section.

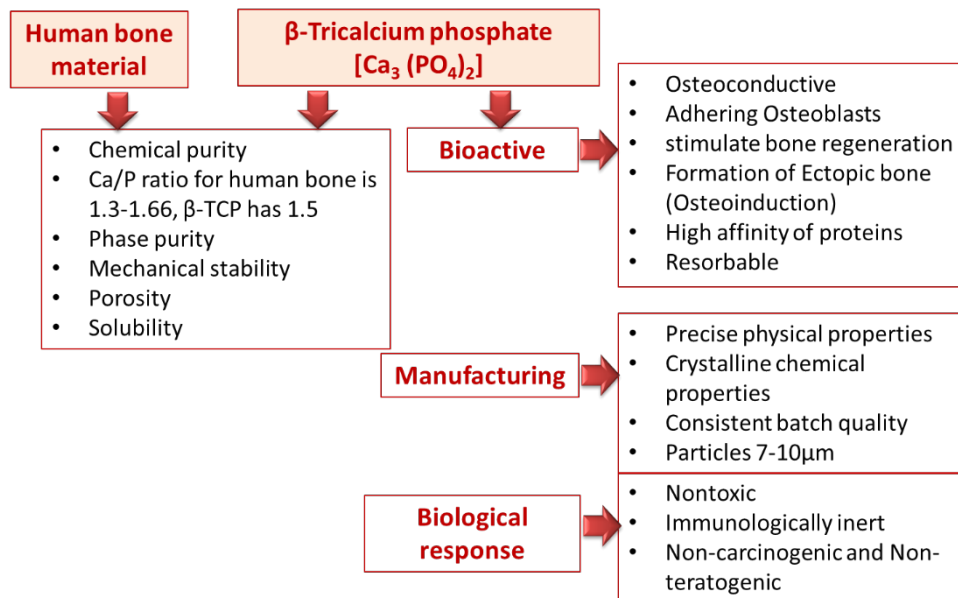


Figure 2.3 β -TCP as a bone-repair and replacement option

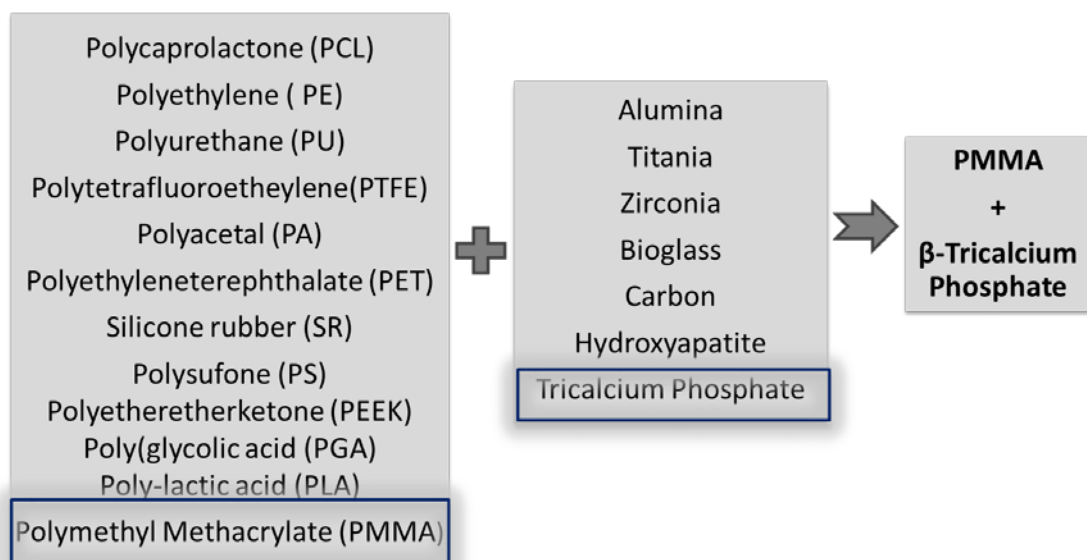


Figure 2.4 The current polymer-ceramic composite

2.8 Research gaps, questions, and hypotheses

The literature review presented above clearly identifies the widespread use of PMMA in both industrial [36-45], as well as medical [46-52] applications. Widely different processing methods including casting [53], injection [55-57] and

compression moulding [59], thermoforming [61] and hot embossing [63 & 64] techniques are applied conventionally. The bulk [65], solution [67], and emulsion [68] polymerisation methods are also equally applicable, in particular within the medical manufacturing needs [69]. In spite of these outstanding features, PMMA suffers from both material and process [70] limitations. Several attempts were made targeting better material attributes, mainly in terms of enhancing the polymerisation reactions [71-73]. However, the current methods are not allowing to fully utilise the benefits of PMMA, while an integrated material and process development scheme is the key to success.

With particular reference to the medical needs such as bone repair and replacement tasks, literature clearly elucidated the superior attributes of PMMA [51 & 52]. Considering the lack of bioactivity of PMMA in the as-processed state, significant improvements possible through use of additional filler materials is also envisioned [74-76]. Phosphorous is an essential element to impart the much needed bio-compatibility [95], but further research allowed identification of different variants of Calcium phosphate to score better as bio-ceramic fillers [97-99]. In particular, the β -TCP form is identified as the most suitable material substitute for bone replacement and repair [31 & 100]. In such applications, the resulting material structure should have specific attributes to match with the material properties of the native bone tissue and also allow for the sequential growth of the neo-tissue as the scaffold degrades with time. While several novel materials and processing techniques were investigated to address these requirements, [101] the search for better alternatives is never ending and the current research considers processing the PMMA and β -TCP composites based on the additive manufacturing methods.

Descamps *et al.* developed PMMA and β -TCP composites by means of a thermal forming technique and evaluated the resulting macro-porous structures. The mechanism of material consolidation involves a viscous flow and sintering of the PMMA coating over the relatively smaller TCP particles. While the control over the macro-porosity was reported to be good, the dimensional stability was still poor [102]. Additive processing methods were identified as possible new developments for medical needs [26, 92 & 93]. Significant growth and application with different other biopolymer materials, targeting different medical applications are already reviewed above [46-52]. There were also attempts applying additive processing specific combinations of polymer- β TCP composites.

Kalita *et al.* developed a polypropylene (PP) and TCP composite filament for extrusion 3D printing based on fused deposition modelling [29]. Scaffolds with different geometries were fabricated and the average pore size was noted to be in the range of 150–200 μm while the compressive strength was comparable to that of a cancellous bone. *In vitro* characterisation with immortalised human preosteoblastic cells (OPCI) revealed that the matrices were nontoxic and the cells were attached to the surfaces of the scaffolds. Though appears to be a viable alternative, FDM in general does not allow to control the porosity programmatically, while the meso structures lead to inherent weaknesses. Selective laser sintering is a better approach considering the possibility to achieve controlled porosity levels.

During the early stages, laser sintering was applied to fabricate implants with composites of HA and β -TCP materials [103]. This involved coating, reinforcing,

and blending of the ceramic powder with a secondary polymeric binder. Duan *et al.* processed Ca-P and poly hydroxybutyrate–co-hydroxyvalerate (PHBV) nanocomposites for bone tissue engineering via SLS and achieved controlled material microstructures, totally interconnected porous structures and high porosities. *In vitro* studies of the scaffolds showed that the presence of Ca-P improved cell proliferation and alkaline phosphate activity [104]. Williams *et al.* used SLS to process polycaprolactone to produce parts with controlled pore sizes in the range of 1.75–2.5 mm and designed porosities from 63.1% to 79%, however they met with limited success in terms of accurately achieving the required porosity levels. Particle size and thermodynamic variations were found to play critical roles [105].

Tan *et al.* and Chua *et al.* demonstrated the ability of SLS to fabricate physically blended hydroxyapatite (HA)–poly (ether–ether–ketone) (PEEK) and HA–poly (vinyl alcohol) composites for tissue scaffold development and observed micropores on the scaffold surface [106 & 107]. Das *et al.* investigated the production of HA–poly-(l-lactic acid) (PLLA) parts by SLS and noted the ultimate compressive strength and elastic modulus to be around lower limits of reported values for cancellous bones [108]. Evidently, past attempts were made applying SLS included HA and TCP combined with other biopolymer matrix options [26], but both PMMA and PMMA plus β -TCP composites received no attention so far in terms of processing by SLS and the possible after effects. This allows to identify the following two gaps in the current research:

Research gap 1:

Medical grade PMMA materials suitable for bone replacement and repair tasks have not yet been investigated systematically for processing by selective laser sintering

Research Gap 2:

The polymer ceramic composites constituted of PMMA and β -TCP also did not achieve any research attention in terms of being processed by selective laser sintering

The hypothesis

Based on the literature reviewed above and in view of the research gaps identified the following overarching hypothesis is proposed for the current research:

Both neat PMMA and PMMA plus β -TCP composites in powder forms can be processed by selective laser sintering, achieving controlled porosities, sufficient physical and mechanical properties, and the required biological responses, without the loss of the basic molecular or other attributes of the base materials of varying compositions.

Research Questions

A scientific proof of the above hypothesis involves development of experimental materials and methodologies, analysis, and integration of results in order to answer the significant research questions such as:

- How does a medical grade neat PMMA in powder form respond to consolidation by means of a laser energy selectively input into the substrate?
- What variations in the above responses occur if filler particles such as β -TCP are added forming bio-polymer-ceramic composites of varying compositions?
- With each material system, what are the process-structure relationships considering both micro- and meso-structures and morphological changes?
- What are the process-structure property relationships, considering critical physical and mechanical responses such as porosity and strength respectively?
- What are the post-process changes? Could the photon-bio-polymer interactions lead to loss of quality including polymer degradation or molecular alterations?
- Finally, could the violent thermal variations induced by the dynamic laser interactions cause any detrimental effects on the biological expectations of the polymer composites under investigation?

Objectives

Research work predominantly based on experimental investigations is undertaken and reported in this thesis searching for answers to the questions raised above. The following are the main objectives of the current research:

- Conduct further literature review, consolidating the material choice and identifying the experimental methods
- Develop the experimental methods and plans and identify the principal sources and systems
- Design, evaluate and develop the experimental systems
- Establish the material mixing methods
- Identify the critical responses allowing to establish the material-process combinations for processing by selective laser sintering
- Characterise the material consolidation mechanisms and mechanics of laser sintering neat PMMA powders with varying process conditions and identify the most promising process conditions
- Repeat the same with varying compositions of PMMA and β -TCP composites and identify the most promising material compositions and process conditions
- Evaluate and establish the after-effects of laser sintering if any, on the materials structures and compositions
- Establish the post-processing biological responses of both neat PMMA and PMMA plus β -TCP composites laser sintered to different conditions

2.9 Thesis structure

Research work is planned and undertaken achieving the objectives as listed above. The progress made and the critical body of knowledge generated is presented in the following chapters of this thesis. Chapter 3 is a consolidation of all the experimental methods developed and employed in the current research. It begins with a discussion of the critical aspects of laser sintering and the material-process relationships and identification of specific attributes of the material systems investigated here. The material mixing methods and the final choice are presented next. The experimental test facilities designed and developed are explained in detail including both hardware and software components. All experimental methods and systems used to characterise the materials for laser sintering, involving material consolidation and morphological studies, physical and mechanical response evaluation and establishing the post-sintering attributes are discussed next.

Chapter 4 covers the experimental investigations and observations made based on neat PMMA powders. Medical grade PMMA powders are sourced from commercial suppliers and laser sintering trials are done based on the experimental facilities designed and developed. Critical responses of the materials based on the evaluation schemes set are obtained, recorded and discussed in a chronological sequence, beginning with initial trials and gradually moving towards experiments involving more optimum process conditions. The overarching achievement from the research and results presented in Chapter 4 is the establishment of the PMMA powders to be suitable for processing by laser sintering.

Similar experimental investigations conducted based on the PMMA and β -TCP composites are discussed in Chapter 5. Again, beginning with the initial trials, the developments leading to the identification of the more appropriate material and process conditions are recorded sequentially. Evaluation of the critical responses including morphologies, physical, and mechanical responses are given due considerations. The presence of the finer β -TCP particles is noted to cause rheological changes due to differential thermal attributes. A thermal analysis is undertaken and reported in this chapter in order to further evaluate these differences through both numerical simulations and experimental measurements considering the laser track temperature variations. Overall, the PMMA plus β -TCP are proved to be suitable for processing by laser sintering based on the results presented in Chapter 5.

Chapter 6 is dedicated to the evaluation and assertion of the after effects of laser sintering both neat PMMA and PMMA plus β -TCP composites. First the possible effects of the laser heating on the chemical composition of the base polymer and composite materials as identified by FTIR results are discussed. A detailed discussion of the results of the *in vitro* trials is considered next, evaluating the possible loss of the biological properties due to the violent laser processing of the fine powder raw materials. Mechanical responses of multi-layer samples are discussed next as means of establishing the end-use attributes attainable from the material and process combinations investigated. Results indicated no process-related loss of material quality as well as evidence of any detrimental effects on the biological responses expected. Conclusions are drawn in Chapter 7.

Chapter 3

Materials and Methods

3.1 Evaluation of a new bio-polymer for selective laser sintering

Selective laser sintering involves point-by-point consolidation of powder raw materials through the controlled movement of a laser and transfer of calculated amounts of thermal energies into the substrate. Establishing a new bio-polymer material to be suitable for such a process needs first to evaluate the material attributes together with the process conditions. One of the key aspects is to match the material and the laser source as the energy absorption varies with varying material properties and wavelengths of the laser beam. Once this is done, a careful consideration of the other critical aspects such as the reflectivity, conductivity, and other thermal characteristics would become necessary. Once matching material and process attributes are ascertained, systematic experimental investigations should follow, identifying the most suitable process conditions, understanding the mechanisms and mechanics of material consolidation. Further to establishing the most suitable process conditions, critical responses of the sintered materials need to be established considering the specific application requirements.

Considering that PMMA and PMMA/ β -TCP composites are the subject material systems for the current research, a matching laser sintering scheme needs to be developed and implemented. A suitable mechanism of mixing the two components to form the polymer composite powders needs to be developed next. Both neat and the composite powders will require to be subjected to thermal

characterisation using methods such as differential scanning calorimetry [109] and thermo-gravimetric analyses [110]. The data generated would allow to establish the critical temperatures and other thermal properties and converge on the working laser settings to begin with. Once the working laser sintering parameters are established, the mechanisms and mechanics of sintering can be investigated initially through single layer sintered specimens subjected to microstructural and morphological studies. Porosity and density levels can be established and evaluated based on the surface morphologies of SEM images [111]. Comparative evaluation of the structure-property relations and responses will allow to identify the most suitable process conditions [112].

In order to evaluate the effectiveness of the mechanical properties tensile and three-point bending test samples can be fabricated using critical process parameter as per the ASTM standards [113]. Based on the results, the tensile strength, elongation at break, elastic modulus and flexural modulus of the samples can be established. Both single and multi-layer samples can then be made to the optimum conditions to evaluate the possible after effects as well as other critical responses such as the biological attributes. Polymer degradation and molecular alterations if any can be identified by means of the FTIR analysis [114]. Post-sintering biological responses are the most critical to be ascertained and a series of *in vitro* tests can be applied based on the human osteosarcoma cell line, MG-63 cells [30]. Cultured cells can be seeded on carefully prepared samples and analysed for the attachment and growth responses. MTT and ALP assays and Alizarin Red S staining tests can be used to establish the cell proliferation rates while the Field Emission Scanning Electron Microscopy (FE-SEM) allows observations on the cell morphologies. The materials, specific

process related attributes and the experimental methods are discussed in detail in the following sections.

3.2 Experimental Materials

The Poly(methyl methacrylate) (PMMA) and β -Tricalcium Phosphate (β -TCP) powders used in this research are sourced from Sigma-Aldrich and the manufacturer's specifications and property data are listed in Table 3.1. Photographs of the two powders and SEM images of the powder particles are presented in Fig. 3.1. As seen in Fig. 3.1 (c), the PMMA particles are larger (50 to 100 μm) and quite spherical in forms, while β -TCP is made up of finer (1 to 5 μm) grains of irregular forms as shown in Fig. 3.1 (d). It is important to note the large difference in the thermal conductivities of the constituents. Consequently, adding β -TCP as a filler material is likely to alter the overall mechanics of laser sintering, considering the predominant thermal nature of the process.

Suitability of any new material system for the selective laser sintering process depends on radiation properties such as absorptivity, surface emissivity and reflectivity. Evans *et al.* evaluated and identified several basic parameters to be considered while attempting new materials for laser sintering [115]. From physical considerations, the raw material must be in powder form and allow spreading by a roller or a sweeping system. Based on the mechanics of consolidation, thermal properties such as conductivity, density and specific heat are important. Eventually, the material should attain sufficient inter-particle and inter-layer coalescence when heated by a fast moving laser beam. In order to understand

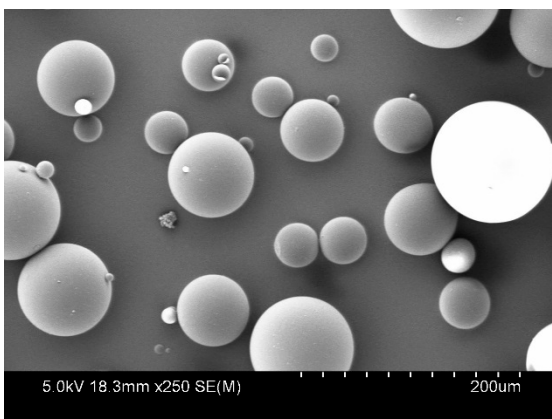
the material-process relations and develop appropriate experimental plans and process conditions, certain critical aspects need to be understood first.



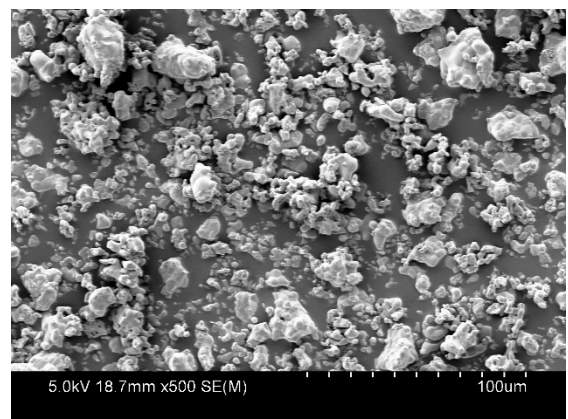
(a) PMMA Powder



(b) β -Tricalcium Powder



(c) PMMA Particle



(d) β -TCP particle

Figure. 3.1 Physical (a&b) and SEM (c&d) image of PMMA and β -TCP powder respectively

Table 3.1 Materials and properties

Material structure and Properties	Poly (methyl-methacrylate) (C₅O₂H₈)	β-Tricalcium Phosphate [Ca₃ (PO₄)₂]
Supplier	Sigma-Aldrich	Sigma-Aldrich
Material Type	Polymer powder	Ceramic powder
Particle Size	50 to 100 μm	1 to 5 μm
Molecular weight	100.12 g/mol	310.17 g/mol
Melting Temperature	160°C	1391°C
Thermal conductivity	0.2 W/m ⁰ K	3.605 W/m*K
Specific heat	1450 J/kg ⁰ K	-
Density	1180 kg/m ³	3140 kg/m ³

3.3 Critical material and process attributes

Laser type

Commercial SLS systems are commonly equipped with CO₂ lasers of power ratings varying from 50 to 200 W. Optimally, the laser wavelength should be adapted to the powder material to be sintered, since laser absorption greatly impacts the choice of the material and laser wavelength combination [116 & 117]. Fig. 3.2 is sourced from [118] and depicts how the absorption coefficients vary with the laser wavelength for a solid polymer and a metal. It may be noted that the absorptivity with metals is higher at lower laser wave lengths, while it is the other way with polymers. Polycarbonate shows almost 100% absorption with wave lengths at around 10 μm, typical of CO₂ lasers. Laser absorption in powders is usually larger than in solid materials, which is due to multiple reflections and absorption of the laser beam trapped in the pores of the powder known as powder

in-coupling as shown in Fig. 3.3 [118]. Percent absorptivity of different types of materials with varying laser wavelengths as reported by Tolochko *et al.* are reproduced in Table 3.2 [117]. Considering the trends in both Fig. 3.2 and Table 3.2, it is evident that the CO₂ laser with a wavelength of 10.6 μm is well suited for sintering polymer powders, due to the high absorption at the far infrared or long wavelength regions of the spectrum. Based on these facts, the final choice is a CO₂ laser for the sintering experiments to be conducted in the current research involving a polymer composite.

The nature of the powder flow together with the thermal and physical characteristics of the powder bed will eventually control the quality of sintering. Thermal radiation emitted in the form of electromagnetic waves plays a significant role in controlling the thermal fields. All materials emit and receive thermal radiation at rates primarily dependent on the temperature. The radiation properties of the materials such as emissivity, absorptivity, transmissivity and reflectivity will come into play influencing the effective heat transfer as the thermal responses of the material are compounded as depicted in Fig 3.4. Critical radiation properties and their relationships to the essential thermal nature and responses of the substrate material are briefly reviewed next as these will form the basis of the choice of experimental conditions

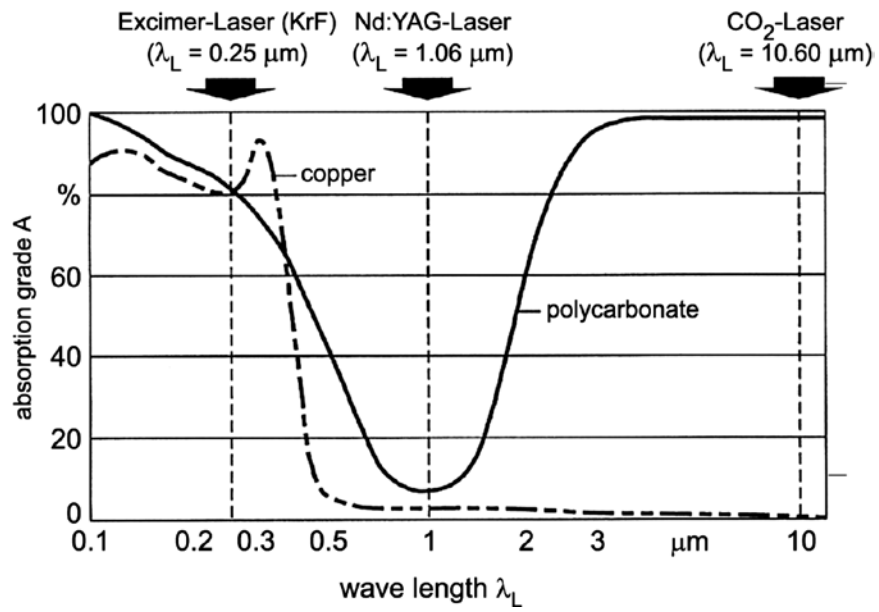


Figure. 3.2 Laser absorption of plain solid materials (Polycarbonate and copper) versus wavelength [117].

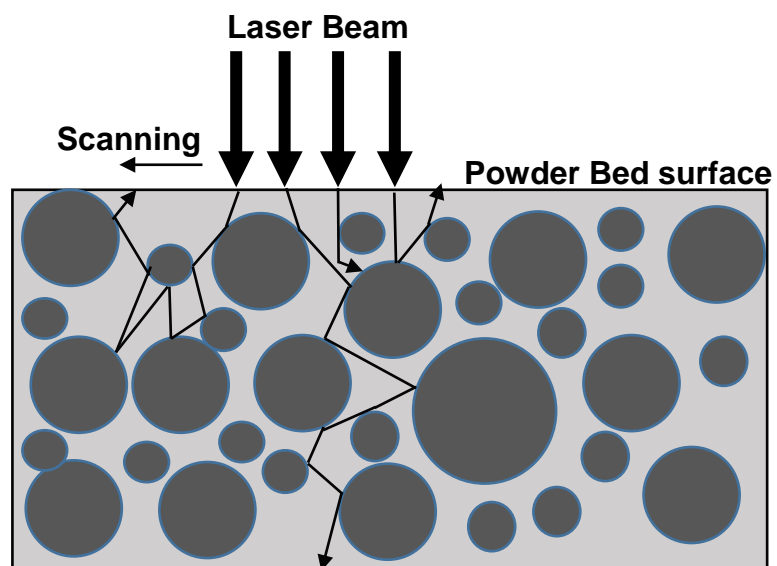


Figure. 3.3 Powder in-coupling

Table 3.2 Incoupling (Absorption) of powder Materials for Nd: YAG and CO₂ Laser

Powder Materials	Nd: YAG (1.06 μm)	CO₂ (10.6 μm)
Metals		
Cu (absorption in solid Cu)	59 percent (2-10 percent*)	26 percent (1 percent)
Fe (absorption in solid Fe)	64 percent (30 percent)	45 percent(4 percent)
Sn	66 percent	23 percent
Ti	77 percent	59 percent
Pb	79 percent	-
Co-alloy (1 percent C; 28 percent Cr; 4 percent W)	58 percent	25 percent
Cu-alloy (10 percent Al)	63 percent	32 percent
Ni-alloy 1 (13 Cr; 3 percent B; 4 percent Si; 0.6 percent C)	64 percent	42 percent
Ni-alloy 2 (15 percent Cr; 3.1 percent Si; 0.8 percent C)	72 percent	51 percent
Ceramics		
ZnO	2 percent	94 percent
Al ₂ O ₃	3 percent	96 percent
SiO ₂	4 percent	96 percent
SnO	5 percent	95 percent
CuO	11 percent	76 percent
SiC	78 percent	66 percent
Cr ₃ C ₂	81 percent	70 percent
TiC	82 percent	46 percent
WC	82 percent	48 percent
Polymers		
Polytetrafluoroethylene	5 percent	73 percent
Polymethylacrylate	6 percent	75 percent
Epoxypolyether-based polymer	9 percent	94 percent
Mixtures		
Fe-alloys (3 percent C; 3 percent Cr; 12 percent V) + 10 percent TiC	65 percent	39 percent
Fe-alloys (1 percent C; 14 percent Cr; 10 percent Mn; 10 percent Ti) + 66 percent TiC	79 percent	39 percent
Ni-alloy 2 (95 percent) + Epoxypolyether-based polymer (5 percent)	68 percent	54 percent
Ni-alloy 2 (25 percent) + Epoxypolyether-based polymer (75 percent)	23 percent	76 percent
Note: *Value varying with glass, surface roughness, surface oxidation, etc.		
Source: Tolochko et al [117]		

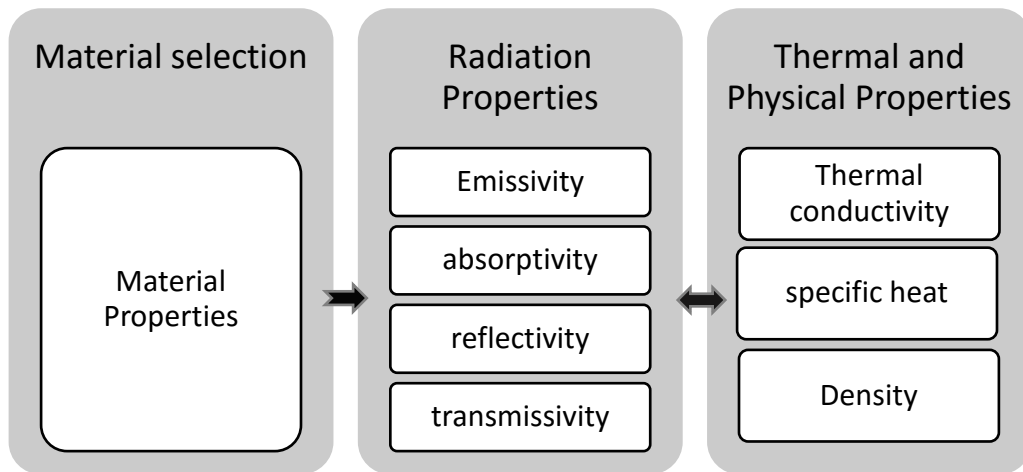


Figure. 3.4 Material and thermal properties compound to influence the sintering attributes

Emissivity, Absorptivity, Reflectivity, and Transmissivity

The emissivity ϵ , which is a surface property, is defined as the ratio of the radiation emitted by the surface to the radiation emitted by a black body at the same temperature and is expressed as follows:

$$\epsilon(T) = \frac{E_r(T)}{E_{br}(T)}$$

Where $E_r(T)$ is the total energy emitted from the surface and $E_{br}(T)$ is the total energy emitted from a black body at the same surface temperature. Additionally, $E_{br}(T)$ is defined as a function of the absolute temperature of the surface, T (K), and the Stefan-Boltzmann constant ($\sigma_R = 5.67 \times 10^{-8} \text{ W/M}^2 \text{ -K}^4$) as follows:

$$E_{br}(T) = \sigma_R \cdot T^4$$

When the radiation energy strikes a material surface, a fraction of the incident energy (I) is reflected, termed the reflectivity, ρ_R , a fraction is absorbed, termed the absorptivity α_R and a fraction is transmitted termed the transmissivity T_R . Nelson *et al.* experimentally measured the emissivity of polycarbonate powder using an integrating sphere [119]. The polycarbonate powder sample was placed in a holder positioned at the bottom of the sphere, and a laser beam was then projected normal to the sample. The amount of radiation reflected from the sample was measured as a voltage signal with a photo detector. The measurements gave a reflectivity (ρ_R) of 5% for the polycarbonate powder. As transmission of infrared radiation through polycarbonate is very poor, the absorptivity (α_R) could be estimated equal to 95%. Additionally, at thermal equilibrium, the emissivity (ϵ) and absorptivity (α_R) are the same, and thus the emissivity of the polycarbonate powder was assumed to be 0.95 [119]. Measurements were also performed on SLS fabricated polycarbonate samples and the results did not significantly vary from those measured for the powder samples.

While PMMA was noted to be discoloured when exposed to UV radiation, Donaldson *et al.* observed that this was only a temporary phenomenon and gradually disappears with time [120]. Hermon *et al.* also reported that PMMA shows significant discolouration after exposure to irradiation by a ^{60}Co gamma source at the rate of 10 MRad, but then recovers rapidly [121]. It was also observed that no polymerisation reactions occurred during the course of irradiation or subsequent recovery, indicating good optical and absorptivity properties for PMMA. More recently, Shashi *et al.* studied the absorptivity, reflectivity, and transmissivity responses of PMMA, based on CO_2 laser cutting

trials and spectrophotometry. The reflectivity and transmissivity were established to be 4.67% and 0.31 % for the 10.6 μm (943 cm^{-1} wave number) laser energy. Based on this it was concluded that the absorptivity of PMMA could be as high as 95% with a CO_2 laser [122]. This indicates that the material and laser combination choice is correct though the presence of the β -TCP particles is likely to alter the responses to varying degrees.

Thermal Conductivity

Thermal conductivity (k) is a physical property of a material and is a measure of the rate at which heat is transferred through a body. Thermal energy is conducted in polymeric materials by the vibration and molecular motion of the polymer chains and is understood to be anisotropic [123]. The reason being that the heat transferring along the backbone primary bond encounters less scattering than that transmitted from chain to chain along the secondary bonds. Consequently, an increase in the degree of polymerisation and the existence of extensive cross-links can allow higher thermal conductivity [124]. Amorphous polymers have low thermal conductivities compared to other polymers due to the loosely packed structure minimising the points at which the polymer chains contact one another. As the temperature of the polymer increases the atoms gain thermal energy and vibrate. The vibration of each atom is then transferred to the surrounding atoms. This causes rapid heat transfer, exhibited in an increase in the thermal conductivity, provided that the temperature of the polymer is below glass transition temperature T_g . At the glass transition temperature, the conductivity reaches a maximum value. However, at temperatures above T_g , bonding

between the polymer chains becomes weak, and thus scattering of the thermal energy is more pronounced, resulting in a decrease in the thermal conductivity.

Based on the photon conduction process Santos *et al.* studied the influence of thermal transition temperatures on the variation of the thermal conductivities of four amorphous materials; poly (methyl-methacrylate) (PMMA), high impact polystyrene (HIPS), crystal polystyrene (PS) and polycarbonate (PC). PC showed higher thermal conductivity values while HIPS and PS exhibited lower values. PMMA scored at medium levels measuring 0.25 W/mK. According to the material property data from Sigma Aldrich, the thermal conductivity of PMMA powders used in the current research is at 0.2 W/m⁰C. The moderate thermal conductivity value ascertains that laser sintering of PMMA could be effective as both rapid heat loss and lack of heating are likely to be avoided [125].

There is hardly any research evidence on the nature of variation of the thermal conductivity of β -TCP, however, based on the values obtained from Sigma Aldrich at 3.605 W/m⁰C, as listed in Table 3.1, it is evident that the filler particles are highly conductive compared to the matrix polymer material. This would mean controlled increase in the thermal conductivity levels of the powder bed with varying compositions of the composite. However, a polymer powder bed conducts heat far less readily than a homogenous solid of the same material. This is due to the interstitial spaces that exist in the powder bed, which is not the case in solids. In addition, the powder particles contact one another over a small area and at a few contact points. The conductivity of a powder bed is therefore highly influenced by the degree of compaction [126]. Several models were developed to formulate a mathematical expression for the effective thermal conductivity of a

powder bed. Yagi and Kunii [127] studied the influence of both temperature and packing characteristics of the powder bed on the effective thermal conductivity. They considered seven heat transfer modes to take place: (i) Heat transfer through solid (ii) Heat transfer through the contact surface of solid (iii) Radiation heat transfer between surfaces of solid (iv) Radiation heat transfer between adjacent voids (v) Heat transfer through the gas film near the contact surface (vi) Heat transfer by convection, solid-gas-solid, (vii) Heat transfer by lateral mixing of gas. The combined existence of both PMMA and β -TCP particles will further confound the heat transfer mechanisms considering wide differences in both size and thermal characteristics.

Specific Heat

Specific heat (C_p) is the amount of heat required to increase the temperature of a unit mass by one degree. It is expressed in the form,

$$C_p = \frac{dQ}{dT}$$

Where dT is the change in temperature experienced by a unit mass of the material when subjected to a quantity of heat dQ . There are no theoretical expressions for the specific heat of amorphous polymers. However, experimental observations showed the specific heat of amorphous polymers to increase as the temperature is increased, below and above the glass transition region. In the glass transition region, a step change in the specific heat is exhibited. Based on experimental measurements, for a powder bed, the specific heat is written as follows [124]:

$$C_p = \sum_n \omega_i C_{pi}$$

Where ω_i and C_{pi} are the weight fraction and specific heat of component i , respectively. The powder bed is made of two types of components; solid particles and the gas fillings in the interstitial spaces that exist in the powder bed. As the weight fraction of the gas is one thousandth of that of the solid, the product $\omega_i C_{pi}$ for the gas is extremely small when compared to that of the solid. Thus, the gas has very little influence on the overall specific heat of the powder bed, and the specific heat of a powder bed can be considered to be that of a solid particle [127].

Density

Considering the significant influence on the final mechanical properties, density achieved through sintering is often important together with the evaluation of the influences of constituent factors. One of the methods employed in increasing the density of fabricated parts is by increasing the density of packing of the powder bed, prior to laser sintering. The powder bed density is influenced by the density of the solid particles and their packing; particle shape, size and size distribution being the critical parameters [127]. An optimal packing density of a powder bed could be achieved if the voids among the largest particles in the bed are filled with smaller particles, which are in turn filled with further smaller particles and so forth. In principle, spherical uniform particles can be packed in different arrangements such as the cubical and the orthorhombic arrangements schematically illustrated in Fig. 3.5.

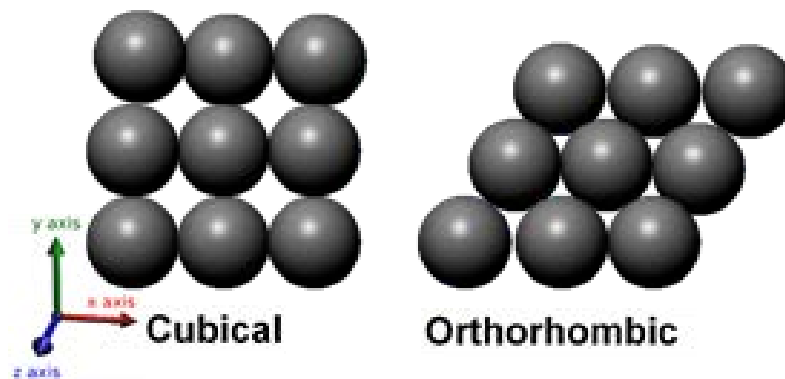


Figure 3.5. The cubical and orthorhombic arrangements of uniform spherical particles

The volume of the void space as a percentage of the total volume occupied by the arrangement of the spheres can be estimated as 47.6% for the cubical arrangement. Which means that the spheres occupy only 53.4% of the total volume of the powder bed. In a similar way, the percentage void volume of the orthorhombic packing of the bed can be found to be 39.5%. The cubical packing is unstable and does not occur in nature, whereas the orthorhombic is the most likely arrangement to exist in uniform-sized sphere beds [126]. In the current research both pure PMMA and PMMA+ β -TCP powders are sintered. Considering the mechanical dispersion of the powder, the orthorhombic arrangement is expected for the PMMA particles. The β -TCP particles being small will occupy the interstitial spaces in the powder composite. The average packing factor is expected to be at around 60%.

In selective laser sintering, a part is formed when the solid particles, in contact with each other in the powder bed, coalesce at elevated temperatures. It is accompanied by a decrease in the volume of the pore spaces between the particles, and thus reduction in the total surface area and volume of the sintered powder bed occurs. This phenomenon involves viscous flow between adjacent

particles, and its rate is therefore greatly affected by the local temperature. Sintering proceeds in two distinct stages. First, interfaces and bridges between adjacent particles are developed with very little change in density as shown in Fig. 3.6. This is then followed by a stage of densification in which inter-particle cavities are significantly reduced or eliminated. The density of the final sintered part will depend on the extent of inter-particle and inter-layer fusion and coalescence. Meso-structural evaluation of the morphologies of sintered surface will be considered to estimate the densities achieved in both material systems investigated here.

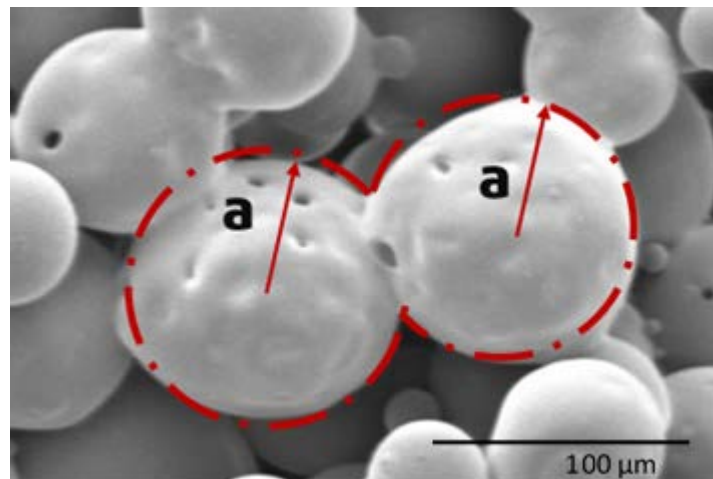


Figure 3.6 Schematic view of the first stage of sintering

3.4 Material Processing

The materials used in this research include both PMMA and PMMA+ β -TCP composite powder systems. The powder materials are used in the as-received state with no further treatment prior to sintering. Powder handling is kept at a minimum in all the experimental trials prior to sintering to limit the adsorption due to atmospheric contamination. Limiting particle segregation and exposure during

handling also allowed a reasonable degree of reproducibility of experimental data. Three methods are attempted for mixing the PMMA and β -TCP powder composites; polymer dissolution process, extrusion method and manual mixing using a mortar but resorted to the manual mixing by a mortar at the end, considering practical and time constraints as noted next.

Polymer dissolution process

Polymer dissolution method is attempted first with the 95% PMMA and 5% β -TCP powder composite. PMMA showed the normal dissolution behaviour as seen in Fig. 3.7a, as it is gradually consumed into the solution during the induction period. Due to plasticization of the polymer by the solvent, a gel-like swollen layer is formed along with two separate interfaces, one between the glassy polymer and the gel layer as shown in Fig. 3.7b and the other between the gel layer and the solvent. However, the β -TCP particles are not dissolved at this stage, and remained floating in the solution, giving it a characteristic white appearance.

The solvents evaporated in about two hours' time and the PMMA and β -TCP components are deposited back in the container as shown in Fig. 3.7c. A strong stone-like mass is created with cracks running across the polymer matrix probably due to large internal stresses generated in the polymer in the glass transition interval. The differences in the dissolution behaviour of the mass and the momentum transport in the swelling polymer matrix lead to cracking [128]. Thus, the polymer dissolves either by exhibiting a thick swollen layer or by undergoing extensive cracking, depending on how fast the osmotic pressure stress that builds up in the polymer matrix is relieved. The nature of the polymer

and the differences in the free volume and the segmental stiffness are responsible for behavioural variations from polymer to polymer [129]. On the other hand, the β -TCP particles are agglomerated in different zones within the polymer matrix based on the rheology of the evaporating solvent and the formation of the solid polymer component. The PMMA- β -TCP solid formed by the polymer dissolution method is then ground into finer particles. However, the solid is quite hard to grind and the resulting particles are quite crystalline and irregular in form. Further, the β -TCP particles are not well dispersed, leading to the decision that the polymer dissolution method is not very effective and so to be discarded.



(a) Hexane (Solvent), PMMA and β -TCP powder



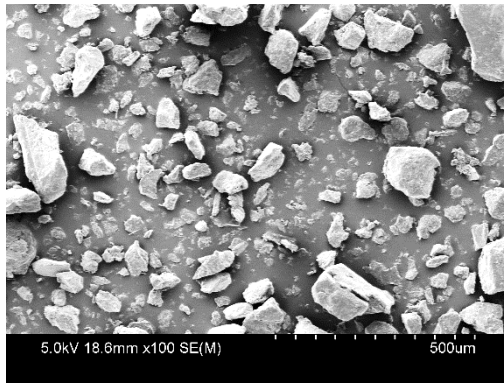
(b) Glassy stage

(c) After evaporation of Hexane

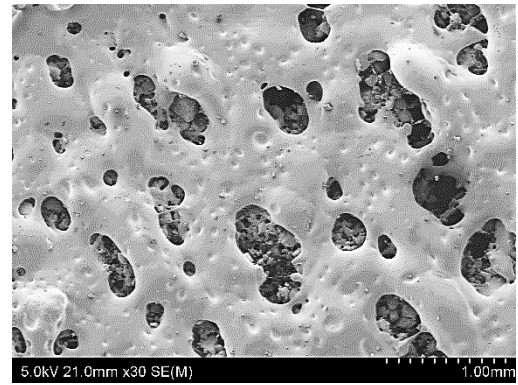
Figure. 3.7 Polymer Dissolution Process

Extrusion method

A single screw extruder was used next to extrude polymer composite pellets of 95% PMMA and 5% β -TCP powder. The PMMA and β -TCP powders are fed into the feed section of the screw to be conveyed through the barrel, heated up and extruded eventually in the form of pellets. The pellets are subsequently ground to produce the polymer composite powder. The resulting powder particles are again irregular in forms as shown in Fig. 3.8a, as against the uniform spherical forms of the base powder particles. Some preliminary sintering trials are attempted with the powder thus produced. The SEM photomicrograph showing the surface morphology of the sintered single layer is presented in Fig 3.8 b. It may be noted that the PMMA phase responds well with sufficient inter-particle sintering, leading to the formation of a continuous layer. However, two drawbacks are noticed from this. First, the β -TCP particles are fully covered under the blanket of the PMMA film, which will adversely affect the osteoconductivity as the ceramic particles are not exposed to the outer surface. It was noted earlier that for the growth of bone or to induce osseointegration, the surface of the implant must be conductive, providing direct structural and functional interactions between ordered living bone [130]. Further, the dispersion of the β -TCP particles within the polymer film led to probable thermal variations and surface tension forces which resulted in a wider porosity in the sintered single layer. Considering these defects, the extrusion method is also discarded.



(a) 95% PMMA & 5% β -TCP Powder



(b) Sintered Sample

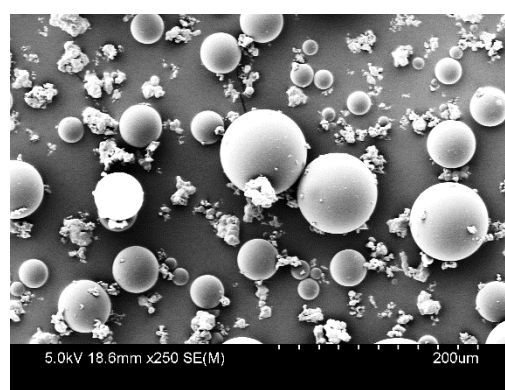
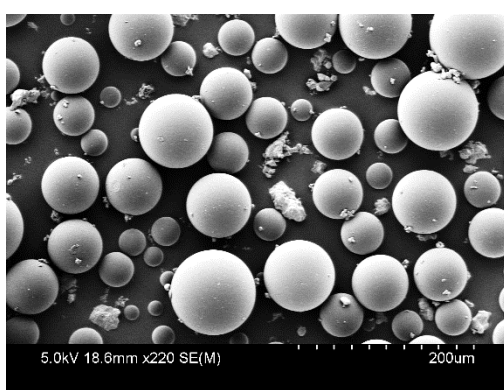
Figure 3.8 (a) Powder and (b) Sintered sample of extruded PMMA and β -TCP composite material

Manual mortar mixing

Considering the limitations of the equipment, time, and other constraints, mechanical mixing of powders in a mortar is finally employed for preparing the powder composites. Initial trials with mechanically mixed powders showed better dispersion as well as sintering characteristics and so powders in all compositions considered here are mixed using this method. The PMMA and β -TCP powder are weighed in ratios as shown in Table 3.3 and mixed thoroughly. The strokes and the pressure are so adjusted as not to crush the particles but to achieve homogeneous mixing of the two powders. The quality of mixing may be observed based on the SEM photographs taken on powder composites of different compositions as depicted in Fig 3.9. The smaller β -TCP particles are either dispersed in the inter-particle spaces or attached to the surfaces of the PMMA particles. This is not the most ideal dispersion, but it did not lead to any unwanted complications, and so the powders sintered reasonably well.

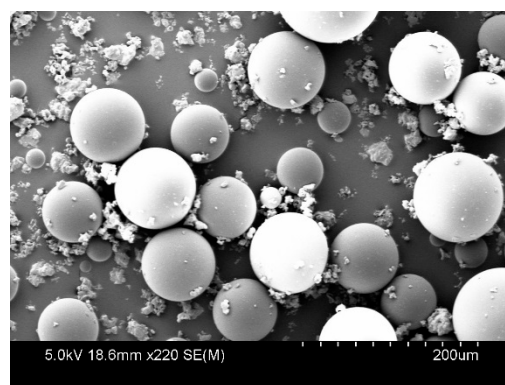
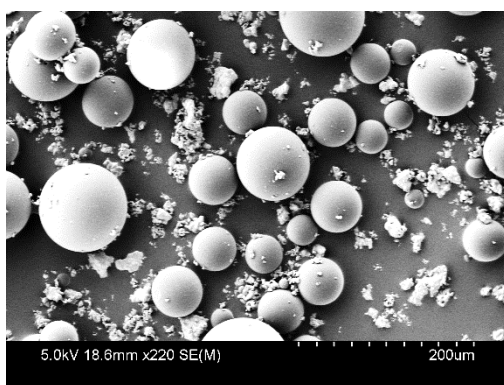
Table 3.3 PMMA and β -TCP Composite mixing ratio

SI No	PMMA Weight %	β -TCP Weight %
1	100	0
2	95	5
3	90	10
4	85	15
5	80	20



95% PMMA & 5% β -TCP

90% PMMA & 10% β -TCP



85% PMMA & 15% β -TCP

80% PMMA & 20% β -TCP

Figure 3.9 PMMA and β -TCP composite powders

3.5 The laser sintering setup

The laser

Commercial SLS systems are usually very expensive; for example, the EOS P100 currently available at AUT University 3D printing lab costs around NZ \$ 350,000, and also comes with serious restrictions on the freedom to play with materials systems and process conditions. Considering the need for complete freedom with the material choice and the full control of process variables, a make-shift SLS system is designed and fabricated for the purpose of this research. The essential building blocks of the laser sintering system are:

- Laser source
- Power source
- Laser beam scanning mechanism
- Control unit
- Software system

A block diagram showing the individual units and the integrated structure designed for the SLS test facility is presented in Fig.3.10. A CO₂ laser is selected based on the predicted absorptivity of PMMA powders. Normally, N₂ and He gases are mixed with CO₂ gas. The role of the N₂ gas is to facilitate the CO₂ pumping and population inversion by providing molecular collisions as pure CO₂ lases inadequately. The role of Helium (He) gas is to facilitate the removal of decayed molecules from their lower energy level to the ground level after the lasing process, in order to maintain the population inversion. Electric discharge

(generated by the use of high-voltage and low-current electrodes) is used as a pumping source. The wall plug efficiency of CO₂ lasers can reach up to 15% and the following are some of the other critical characteristics:

- Laser wavelength: 10.6 μm (for most CO₂ lasers) or 9.4μm, which are in the far infrared spectrum. The CO₂ laser beams are thus not visible for the naked eye.
- The laser can be operated in continuous wave (CW) mode where the output power is at constant level, or pulsed mode where the laser output power can be modulated.
- The laser beam is well absorbed by organic materials and ceramics but poorly absorbed by metallic materials.
- Mirrors rather than optical fibres are used for beam delivery, since normal glass or silica in optical fibres is opaque to the CO₂ laser beam.

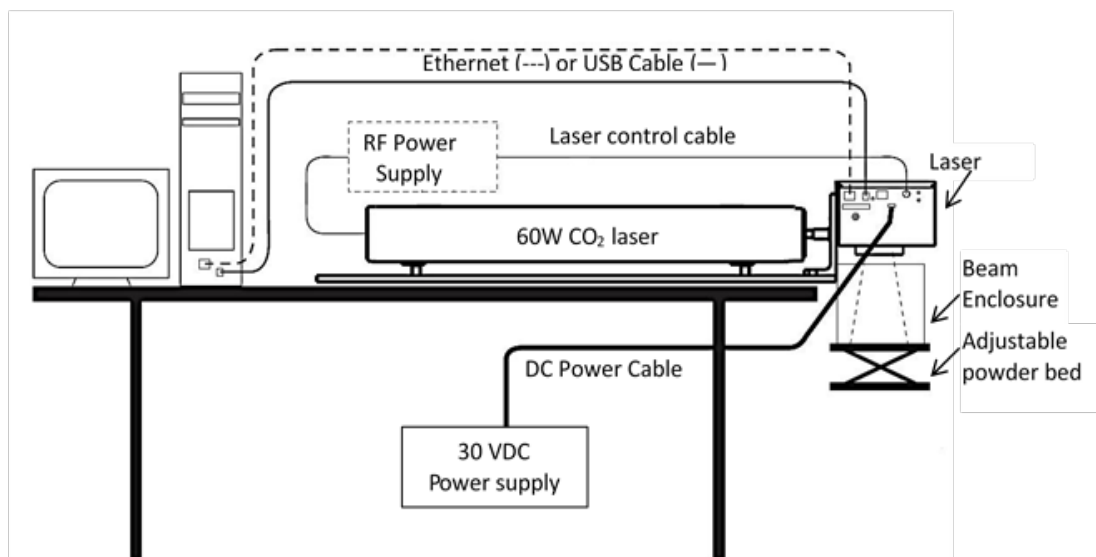


Figure 3.10 Block diagram of SLS test bed

Table 3. 4 Specifications of the components of the SLS system

CO₂ laser	
Maximum power	60 Watts
Mode quality	TEM ₀₀ 95% Purity M ² <1.1±0.1
Ellipticity	<1.2
Spot Size	0.54mm
Wave length	10.57-10.63µm
Radio frequency power supply	
RF	600
Deflection mirror system	
Lens focal length	370mm
Nominal field size	198X198 mm
Working distance	370±5 mm

A 60 W CO₂ laser manufactured by Synrad is procured to act as the primary energy source for the current sintering trials. The specifications of the laser and the RF power supply are listed in Table 3.4. Two options are studied for the laser scanning mechanism; a mirror deflection system mounted on a numerically controlled CNC gantry, and the galvanometer based motorised laser deflection mirror system. The former allows wider areas of the powder bed to be covered with the same spot size, but requires an elaborate design, construction of the precision XY gantry and the flying mirror deflection arrangement. The second option is more compact, but only covers a smaller area of the powder bed. Considering that the project is mainly intended for a fundamental research evaluating the suitability of the selected polymer composites for laser sintering, the maximum allowed size is not a vital constraint. A nominal field size of around 200mmx200 mm is sufficient, to produce standard test samples for common mechanical testing as per the ASTM specifications. After some search, an off-the-shelf laser head based on the tracking by a galvanometer is finally selected, whose specifications are also shown in Table 3.4.

A similar laser deflection system is used on all commercial SLS systems also and has an inherent drawback that the laser spot changes in diameter at extremities of the stroke length [131]. As shown in Fig. 3.11 the laser spot has the best focus and the smallest diameter (D) when $\alpha_p = 0$. An increase in the angle α_p leads the laser spot diameter to increase to $D' = D / \cos \alpha_p$. However, the increase in diameter can be calculated to be very small; approximately 5.7% at the maximum value of α_p (19°), and the detrimental effects can normally be neglected. A control unit and a software interface were procured prior to commencing this research and could be employed to complete the laser sintering system. After repeated trials and finer adjustments, the system became useful for the proposed SLS research and allowed complete control of all factors, including the orientation and location of each raster path. A closer view of the laser sintering the powder bed is presented in Fig. 3.12.

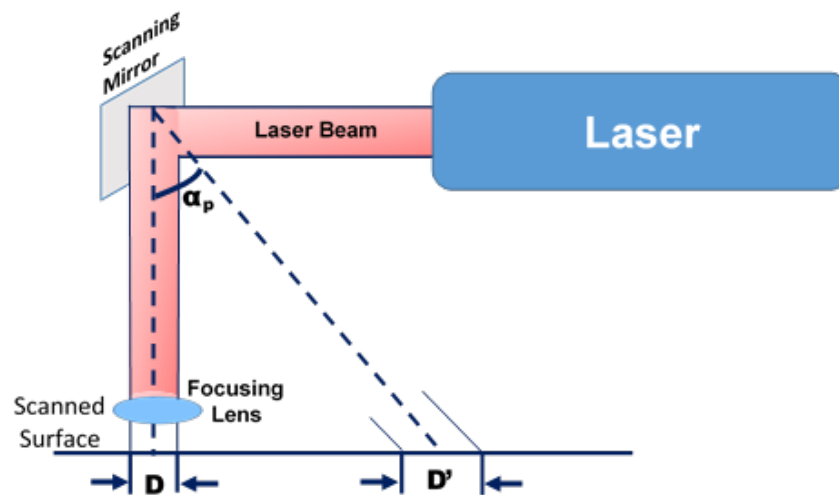


Figure 3.11 Changes in laser spot diameter at different positions on the powder bed

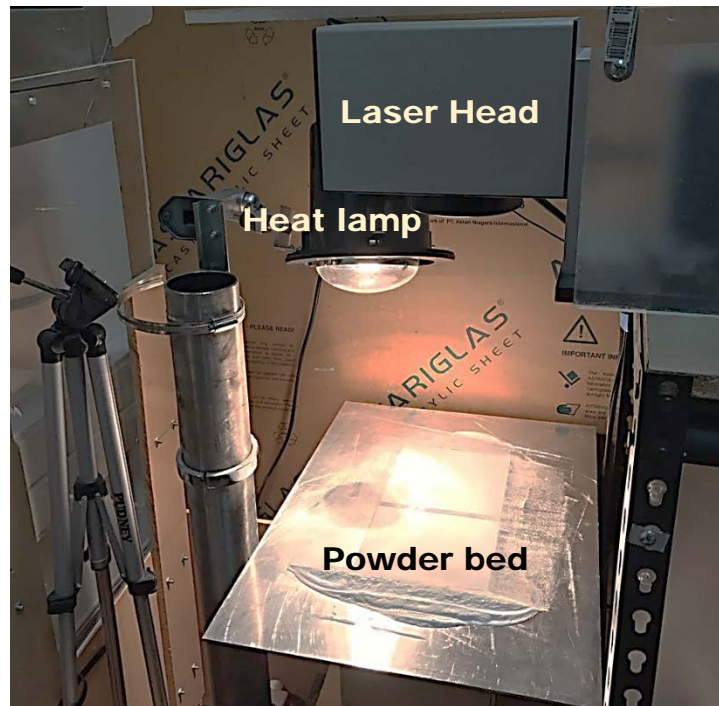


Fig. 3.12 Laser sintering setup

Powder feeding

The next setup necessary is the powder feeding system to enable sintering both single and multi-layer samples. This necessitated the design and fabrication of a twin chamber powder feeding mechanism similar to the powder feeding mechanisms employed in ceramic printers such as the Z-Corp systems. A miniature system with the overall dimensions as depicted in Fig. 3.13 is designed for this purpose. One chamber is used to store the powder, while the other chamber carries the build platform. As shown in Fig 3.14, the sliding platform in each chamber is connected to a stepper motor through drive screws. A nut and screw mechanism is employed to convert the rotation of the screw to the linear travel of the tables. The stepper motors are controlled using a xylotec driver and control unit which in turn is operated by the Mach 3 software.

For each pulse given to the control unit, the powder feeder table moves up and the build platform moves down by one step. The minimum step size which controls the minimum layer thickness possible is at around 0.1mm. The powder sweeping from the storage bin to the build platform is currently done manually as the main purpose is to build test samples, but can easily be automated later. Considering the difficulties to develop a completely enclosed hot chamber, the envelope temperature control is achieved by using a hot plate over the build platform. A resistance heater and a temperature control unit are used for this purpose. The support structure is designed and fabricated by acrylic sheets laser cut to specification and assembled. The final powder feeding system fabricated is shown in Fig. 3.14 while a proportional–integral–derivative controller (PID controller) is used to control the base-plate temperature.

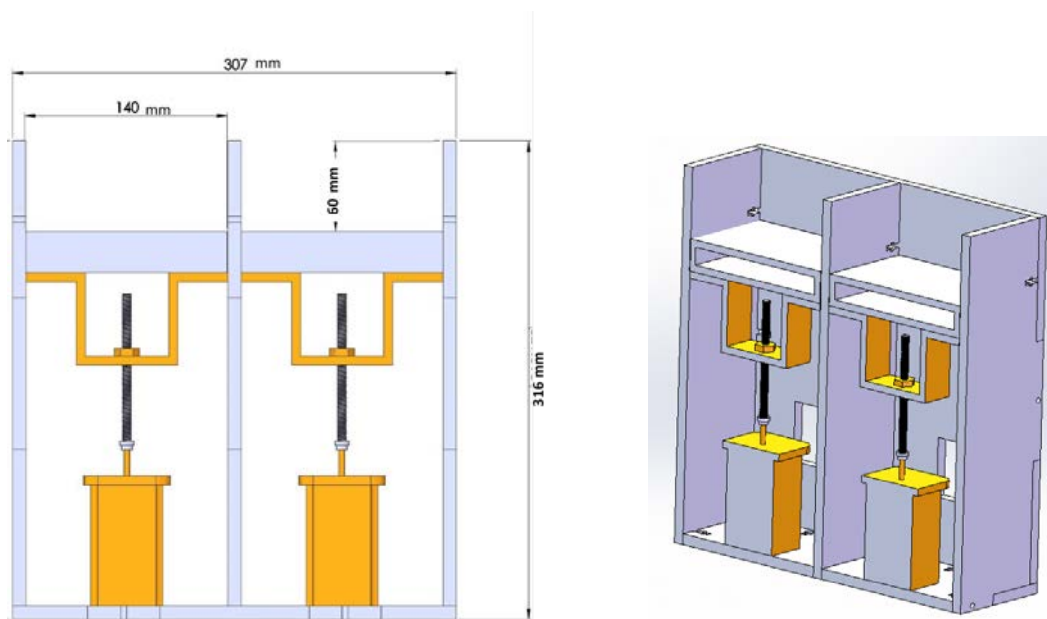


Figure 3.13 CAD models of the powder-feed system

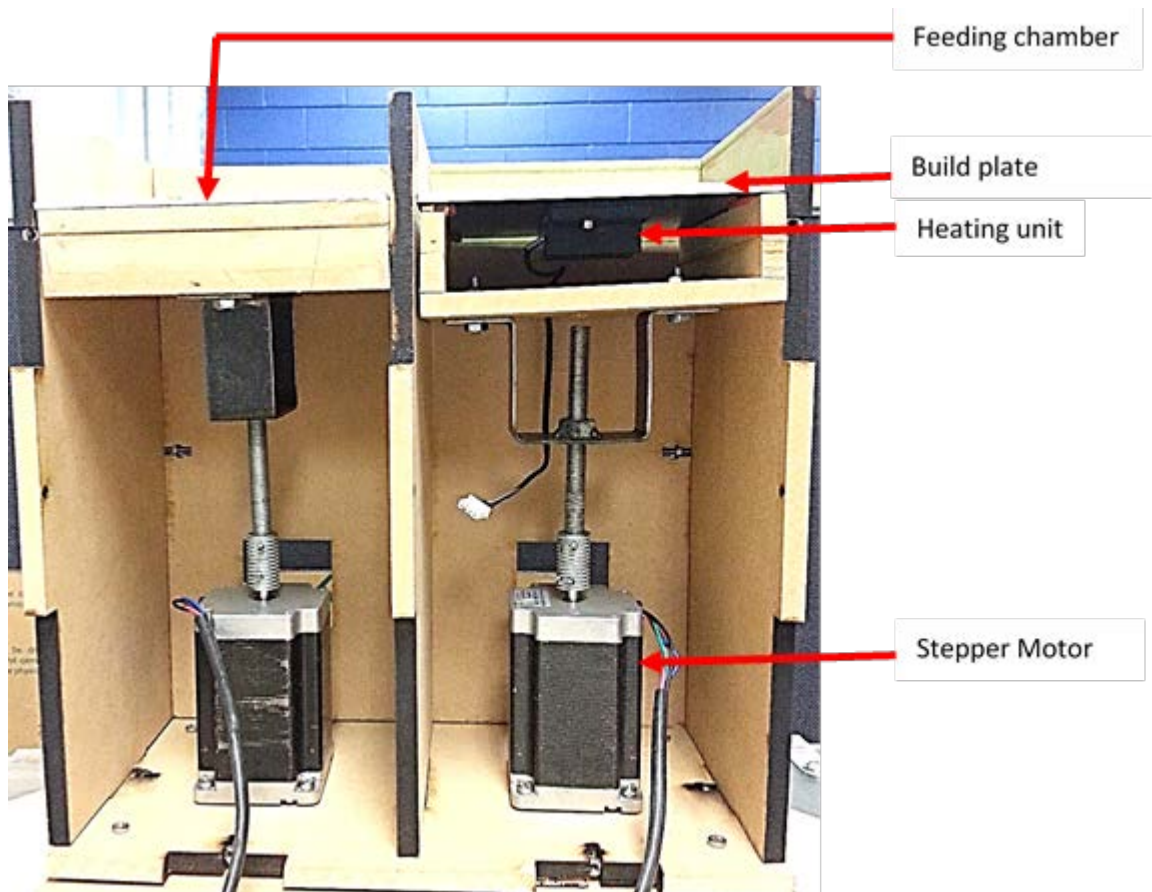


Figure 3.14 The fabricated powder-feed system

3.6 Laser sintering parameters and trials

Critical SLS parameters

The laser sintering system together with the powder feeding mechanism allows for the complete control of the sintering process, including the layer thickness, raster paths, laser power and scan speed and in turn the energy density settings.

The energy density is calculated using Eq. 3.1.

$$ED = \frac{P}{D*v} \quad \left(\frac{J}{mm^2} \right) \quad (3.1)$$

Where, P is the laser power, D is the beam diameter and v is the scan velocity

In SLS, the laser beam travels along the x-direction at different y-positions as illustrated schematically in Fig. 3.15. This scheme of energy input arises critical process parameters such as; the laser spot diameter (D), fill laser power (P), laser beam velocity (U), scan spacing (S), and the vector length (L) of the scans as depicted in Fig.3. 16.

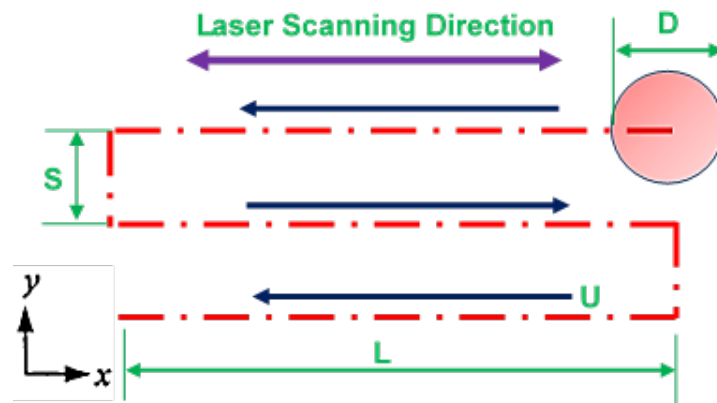


Figure 3.15 SLS Scanning Strategy

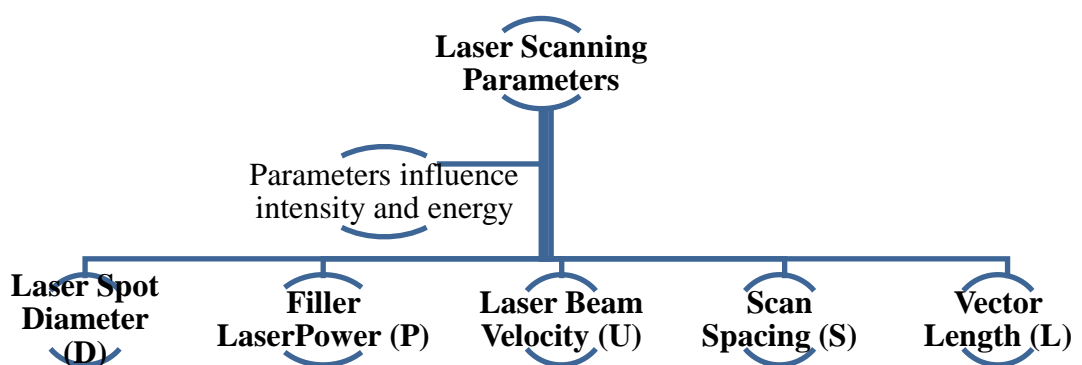


Figure 3.16 Laser Scanning Parameters

In commercial SLS systems, the laser beam diameter is generally fixed, but with the current experimental facility, it is possible to vary the beam diameter by varying the distance between the laser head and the build platform. This will leave the laser spot out of focus, but allows a wider dispersion of the energy where necessary. Some initial experiments are conducted with varying beam diameters, but the results are not indicative of any benefits achieved with the current material system and so, the beam diameter is fixed for all the subsequent sintering experiments done and reported in this thesis. Setting the height between the powder bed surface and the laser head equal to the focal length of the laser 370mm, the fixed beam diameter achieved is 540 μm . The control system allows to play with the pulse width modulation parameters (PWM) depicted in Fig. 3.17. Possible frequencies for the pulsated signal are 5, 10, and 20 kHz and in all the current trials the frequency is maintained the same at 5 kHz. Also the percentage maximum allowable duty cycle can be adjusted to either 95% or 99%. A 95% percent maximum allowable duty cycle is constantly employed considering the allowances for the plasma to cool slightly and increase the laser efficiency.

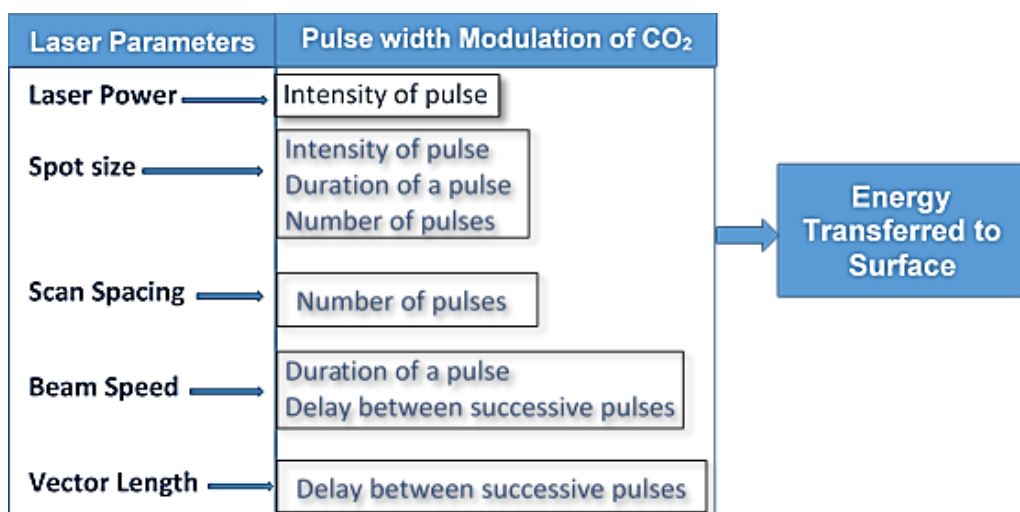


Figure 3.17 Critical laser parameters and settings

The fill laser power is an important and adjustable SLS parameter. It refers to the power available from the laser beam over the part bed surface. The laser intensity, I , (irradiance), i.e. the laser power incident on a unit area (W/m^2), is found to follow a Gaussian profile [4]. The Intensity Gaussian function has a peak at the centre of the laser beam spot and drops monotonically as the radial distance from the centre increases. The radius at which the beam intensity decreases to $1/e^2 = 0.135$ of its maximum value at the centre is termed the characteristic radius. The circle of the characteristic radius was reported to carry 86% of the total laser power [132]. The fill laser power setting varies with the material used for sintering. The aim of the laser application is to heat the powder to a temperature that exceeds its melting point to allow bonding between adjacent powder particles. It is necessary to determine the optimum laser power for the material used. For a given power, the effective energy density into the substrate will also vary with the scan speed.

Laser Beam Velocity

The laser beam velocity U is an adjustable machine parameter, which denotes the speed of the laser beam in the direction of scanning. This is another important experimental parameter as it controls the period a given spot on the part bed is allowed to extract energy from the laser beam. The effective energy input period can be expressed as the ratio of the diameter of the beam to the velocity of scanning [113]. However, the scan velocity of the laser beam varies along a given scan line.

Considering the simple forward and backward motion of the laser in successive scan lines as depicted in Fig 3.15, it may be noted that the laser starts with a zero velocity and then ends up with a zero velocity at the start and the end of each raster stroke. This results in a period of acceleration at the start, and deceleration at the end of each line, which will lead to over exposure for a while, outside the constant velocity zone [134]. This will be avoided by controlling the On/Off timing of the laser. The fill laser ON parameter allows a deliberate delay in turning on the laser during the period of acceleration. A suitable combination of the laser power and scan speed would require to be identified in order to satisfy the required energy density levels to achieve sufficient inter-particle and inter-layer coalescence while laser sintering a given material. Experiments are designed in the current research to establish the *a priori* data and then successively converge on the most suitable combinations of laser power and velocity settings for selective laser sintering of both pure PMMA and PMMA+ β -TCP composites.

Scan Spacing and Vector Length

The gap between adjacent scan lines is the scan spacing, as identified in Fig. 3.15. This setting will influence the number of exposures experienced by a point on the powder bed. A scan spacing greater than the beam diameter would result in a lack of the inter-strand coalescence, while a gap smaller the beam diameter would lead to over exposure, decomposition, and charring in some cases. The length of the scan line is geometry dependent, but the time lapse between successive passes at a given point is the time it takes the laser to complete the scanning of the length traversed to reach the same point along the two successive raster lines [133]. The optimum value of the line spacing varies from

material to material, depending on the thermal nature of the substrate powder. However, this becomes more significant at a later stage when a material already established for SLS is fine-tuned to achieve better internal quality. Considering that the current material-process combinations are still in the initial stages of investigation, the scan spacing is kept equal to the diameter of the laser beam, so that the laser beam passes tangential to the spot in successive tracks.

Layer thickness

Layer thickness is another important experimental parameter, but becomes more significant when an established material is actually implemented to fabricate specific forms. In reality, the layer thickness will control the quality depending on the profile and orientation of the external surfaces as stair-step effects become more prominent with inclined surfaces. Considering the objective to mainly evaluate and establish the new biomaterial combination for processing by selective laser sintering, it is too early to be concerned about the layer thickness in this research. Selective laser sintering of single and multilayer test pieces are the only parts to be produced and the stair-step effects are not significant in these applications.

As a result, the layer thickness is set based on the limitations of the make-shift powder-feed system described earlier, in which the layer thickness is controlled by a stepper motor through the Mach 3 software interface. All the components of the layer thickness control mechanisms are depicted in Fig. 3.18. The default layer thickness on most commercial systems is 0.127mm, but can range from 0.076mm to 0.508mm [135]. The powder feed and build chamber platforms are

operated as the X- and Y- axes from the Mach-3 software using appropriate G code commands. The long screw and nut mechanisms drive the platforms and the directions of motion are controlled by selecting the clock-wise and counter-clock-wise options based on the M-codes. While any size of the step is possible by selecting appropriate increments for the stepper motor steps, it is noticed that a layer thickness of 0.1 mm could be consistently maintained and is employed for all the trials that followed.

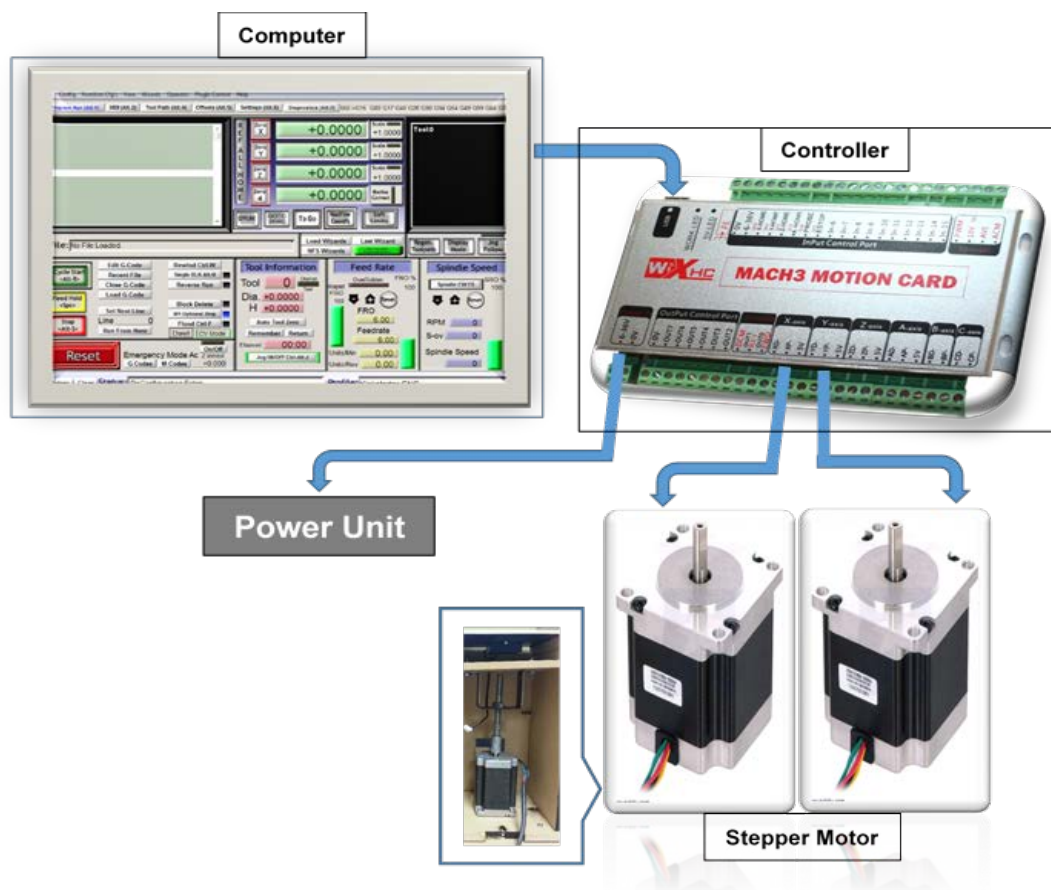


Figure 3.18 The layer thickness control system; stepper motor, drive elements, motion card, and the software interface

Temperature settings

The SLS process consists of three stages; "warm up", "build" and "cool down". In the "warm up" stage, the powder in the feed cartridges is initially heated to an initial pre-set temperature. In the "build" stage, the system maintains the temperature of the powder at the feed heater and part heater set points. The feed heater set point generally represents the highest possible temperature at which the powder can flow freely when spread by the roller. The part heater set point is a temperature generally adjusted just below the glass transition temperature of amorphous polymers, or the melting temperature of crystalline polymers. The temperature is set to reduce additional laser energy needed to heat the powder to the fusing temperature. In the "cool down" stage, the heaters are switched off and the part bed is allowed to cool in the process chamber.

In the current make-shift experimental setup it is difficult to control all these parameters accurately as the whole process is not automated. Further, the chamber is not closed and so a complete control of the envelope temperature is difficult. All these limitations are overcome through the use of the hotplate build platform described above. The build platform is made up of an aluminium plate, which is heated continuously by an electric resistor and controlled by means of a thermocouple and PID controller as depicted in Fig. 3.19. A Farnell Instrument L30-5 stabilised power supply is employed to operate the heating mechanism. A thermocouple connects to the Omron E5CB PID temperature controller which in turn operates the power supply to the heating coil. The hot-plate method of heating is usually effective up to 2 or 3 layers, but fails to keep the surface temperature beyond that. A table-mounted heat lamp is individually operated and

focussed on the powder bed as shown in Fig. 3.19 to maintain the surface temperature while sintering multi-layer samples.

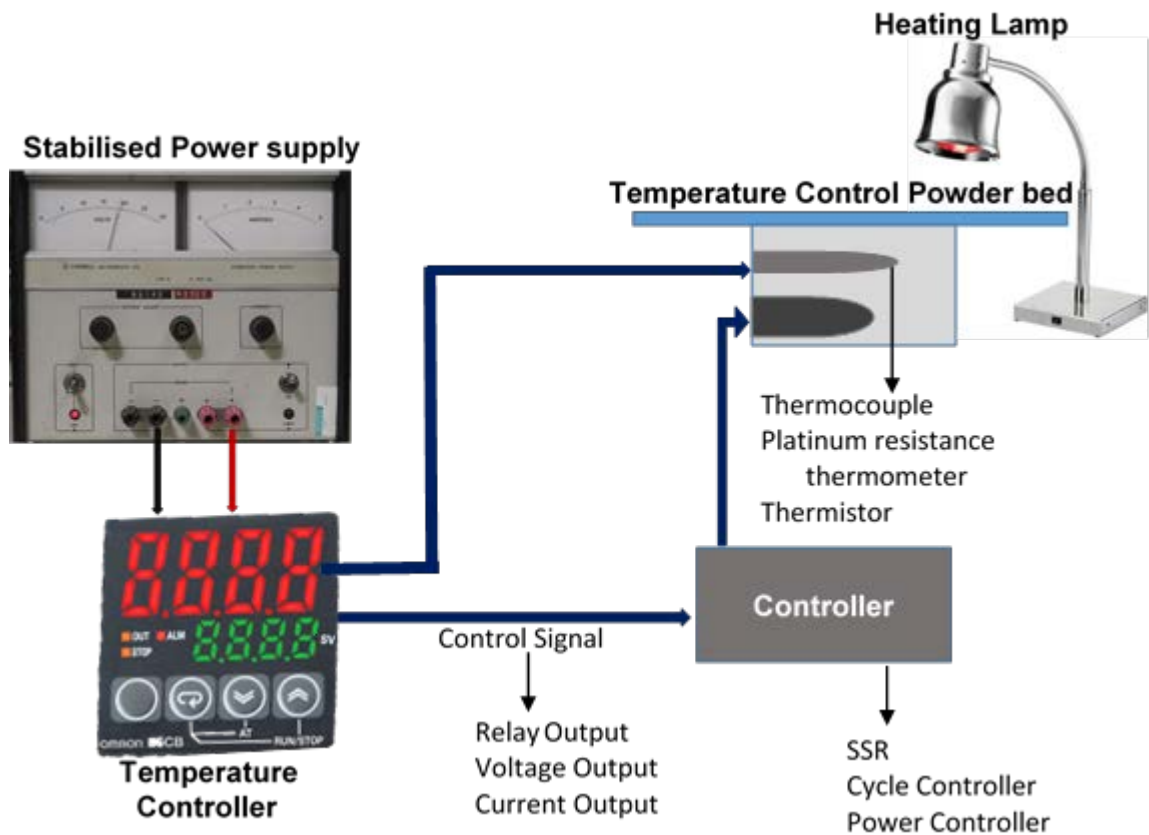


Figure 3.19 Powder Bed temperature control

Single and multi-layer sintering

In the absence of any *a priori* data, it is often difficult to establish the working ranges of critical process parameters whenever a new material is tried with any process and it is true even with SLS. The initial experimental trials with each material combination attempted are designed to sinter single layer samples in order to eliminate the complexity of achieving inter-layer coalescence. Single layer formation only involves intra-layer sintering, which is typically controlled by the inter-particle coalescence. Considering the 2D nature of this, it becomes

relatively simple to converge on the working ranges of process parameters. This method is used to establish the ranges of critical laser process parameters with both pure PMMA and PMMA+ β -TCP powders investigated in this research.

Initial experiments are designed with process conditions estimated based on single scan line responses. Single layer sintered samples in each material case are subjected to morphological, physical and mechanical testing. The final working ranges of the parameters are established based on these initial responses. Further experimental trials are then conducted with process parameters varied in the narrow ranges and critical responses are again established based on single layer sintered samples. The more promising process parameter combinations are then used to produce both single and multi-layer samples for evaluating the after effects of laser sintering as well as the post-process biological responses. The actual experimental conditions and the process parameter ranges are presented and discussed in later chapters.

3.7 SEM for Microstructural characterisation

The sintering responses of both neat and composite versions of the polymers investigated can primarily be established through morphological studies based on Scanning Electron Microscopy (SEM), as was also the method used by numerous other researchers [86-89]. A Hitachi SU-70 field emission scanning electron microscope shown in Fig. 3.20 is used at a voltage of 5-15kV, and with magnifications up to 800,000 times. The SEM images are obtained with a very small electron probe (or electron spot), scanned over the surface of the specimens, and by mapping the electron signals detected from each specimen

pixel onto the corresponding pixel of the cathode ray tube (CRT), or charge coupled device (CCD), i.e. the screen. All samples are coated with gold/platinum to provide a conductive surface for imaging. Topological and surface features of the coated samples and powders are captured through SEM imaging. Apart from shape, size, and arrangement of the fused particles, images are also captured on cross sections of single and multi-layer samples to evaluate aspects of inter-particle and inter-layer coalescence.

SEM images of neat PMMA and mechanically mixed PMMA+ β -TCP powders of different compositions are presented earlier in this chapter. The differences in the particle sizes may be reiterated, while the dispersion and the nature of attachment of the β -TCP particles vary with the composition. SEM imaging of the sputter coated samples is also combined with advanced analytical options like energy dispersive spectrometry (EDS) for elemental analysis to establish the composition of the sample using both mapping and spot analysis modes.



Figure 3.20 Scanning Electron Microscopy

3.8 Fourier Transform Infrared (FTIR)

Fourier Transform Infrared (FTIR) method allows evaluation of molecular changes occurring in the polymer before and after processing. In infrared spectroscopy, IR radiation is passed through the sample, where some of the infrared radiation is absorbed by the sample while the rest passes through (transmitted). The resulting spectrum represents the molecular absorption and transmission, creating a molecular fingerprint of the sample for several factors as shown in Fig. 3.22. As is the case with fingerprints, each molecular structure produces a unique infrared spectrum. This technique becomes quite useful in establishing the possible changes occurring in neat PMMA and PMMA+ β -TCP samples sintered with varying process conditions as was also employed by other researchers [137 & 138]. Unwanted changes in the compositions if any can be understood, while also establishing the quality and consistency levels of the sintered material.

The Thermo-Scientific FTIR spectrometer shown in Fig. 3.21 is employed in the current work for establishing the consequences of laser sintering on the polymers under investigation. The process steps in the FTIR spectroscopic evaluation are depicted in Fig. 3.22. The black-body source emits the infrared energy, the intensity of which is controlled by the aperture through which the beam passes. The interferometer receives the beam energy for spectral coding and generation of the interferogram. When the sample segment is in place, the IR beam is reflected off the surface of the sample, while specific frequencies of energy characteristic of the sample are absorbed. The beam energy finally falling on the detector allows to develop the special interferogram signal. The digitised signal

is then passed on to the computer for Fourier transformation and development of the infrared spectrum to interpret the molecular composition based on standard commercial tables. Both neat PMMA and PMMA+ β -TCP composite polymer compositions sintered in the current study are subjected to FTIR analysis and the results are presented and discussed in Chapter 6.



Figure 3.21 FTIR Spectrometer

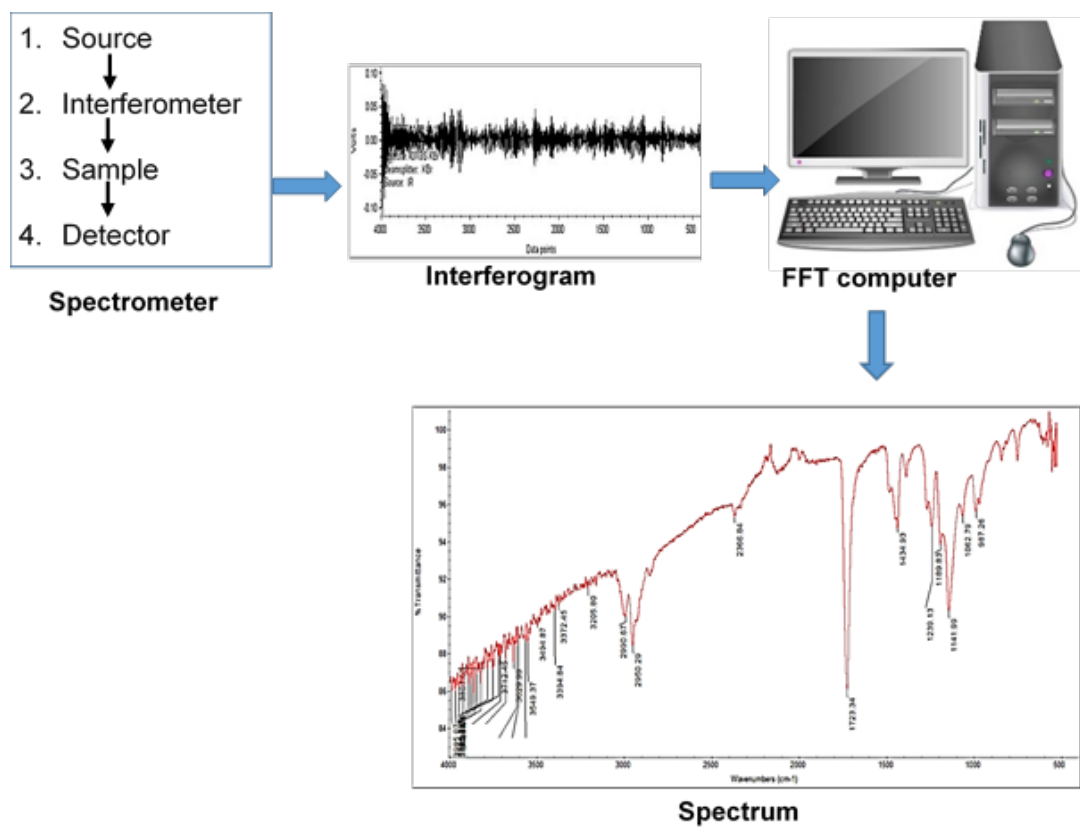


Figure 3.22 Procedural steps of the FTIR analysis

3.9 Mechanical and physical properties

Tensile Tests

The initial evaluation of the mechanical property responses is undertaken through tensile testing of thin-film single layer sintered samples as per the ASTM D882 standard. An Instron 5567 system shown in Fig. 3.23 with 0-200 N load range, 50 mm gauge length, 12.50 mm/min speed and a 125 mm maximum distance between grips is used for the thin-film tensile testing. The control unit and the software interface are used to adjust the test parameters while the load and strain data generated allows the software to establish the tensile test results. Both neat and composite polymer compositions are evaluated for the tensile test responses including the ultimate strength and modulus of elasticity values based on the thin-film single layer samples printed to the standard dimensions. The results are presented in Chapters 4 and 5.



Figure 3.23 Tensile testing Machine

Three-point bending Tests

Mechanical property characterisation of multi-layer samples is undertaken by means of three-point bending tests conducted as per the ASTM D7264 standards. This is due to the fact that the sample size is relatively small, which is essential considering the limitations of the make-shift powder feeding and sintering mechanisms available for the research. The Tinius Olsen tensile testing system shown in Fig. 3.24 (a) available at the materials testing laboratory of Auckland University of Technology is employed for these tests. The test samples are 50mmx10mmx3mm in size, with 20 layers each. Some variation in thickness is attained due to the heat affected zones, but is measured and factored into the stress calculations in order to normalise the final flexural strength values established. Fig. 3.24 (b) shows the close-up view of the arrangement of the specimen mounting and loading and a loading rate of 2 mm/min is employed. The load and deflection data generated by testing standard specimens made of all critical polymer compositions used in the current research are used to calculate the flexural stress and strain as per the following expressions and the final results are discussed in Chapter 7.

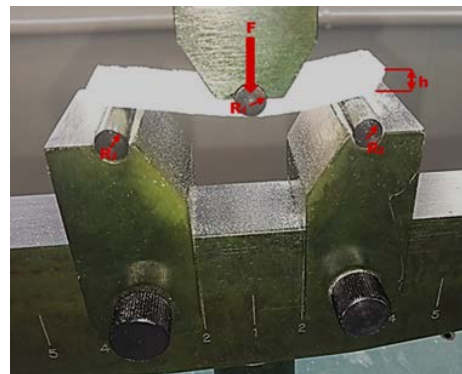
$$\text{Flexural stress } (\sigma_f) = \frac{3FL}{2bh^2}$$

$$\text{Flexural Strain } (\varepsilon_f) = \frac{6Dh}{L^2}$$

Where σ_f is the Flexural stress, F the load (N), L the span (m), h is the thickness of the specimen (mm), b the width of the specimen (mm), and D the maximum deflection of the centre of the beam (mm).



(a)



Where F = load,
 R_1 = indenter radius,
 R_2 = fixed support radius,
 h = thickness of the specimen

(b)

Figure 3.24 (a) Tensile testing system, (b) Close-up view of the three-point bending sample and loading arrangement

3.10 Thermal characterisation

Differential scanning calorimetry

Laser sintering is typically a thermally driven polymer processing technique and quantities such as glass transition, melting, and decomposition temperatures become critical. It becomes essential to establish these temperature levels whenever a new polymer is attempted for laser sintering. Differential scanning

calorimetry (DSC) is a technique used to investigate the changes (thermal transitions) that take place in a polymer when exposed to different temperatures. DSC can be used to determine the melting temperature range T_m , the enthalpy or latent heat of melting, the recrystallization temperature range T_c , and the enthalpy of fusion for semi-crystalline polymers. It is one of the most common tools used in characterizing materials used for laser sintering [109 & 110] because it quantifies the melting and solidification temperatures, usually associated with the crystalline phase. It was suggested that a large super-cooling range (temperature difference between the melting and solidification points) is necessary for successful laser sintering [139]. DSC can also be used to determine the glass transition temperature, T_g for amorphous polymers, which in turn depends on the rate of heating. Considering that PMMA is an amorphous polymer, DSC can be used to establish the heat capacity, activation energy, enthalpy, and the glass transition temperature values.

The Simultaneous Thermal Analyzer-STA 449 F5 Jupiter DSC shown in Fig. 3.25 is used in the current study for the thermal characterisation. There are two aluminium crucibles on this instrument; one takes the polymer sample, while the other is an empty reference pan. The two pans are separately heated by two different heaters that are controlled by the software. Once the heaters are turned on, the sample and the empty pan are simultaneously heated at a rate of $10^\circ\text{C}/\text{min}$ in a nitrogen atmosphere. The heat absorbed at the sample pan varies as phase transitions occur in the solid polymer sample. Depending on whether an endothermic or an exothermic transformation is taking place, a differential heat flow arises between the two pans and the analyser records these differences in heat flows which can be used to establish the critical temperatures.

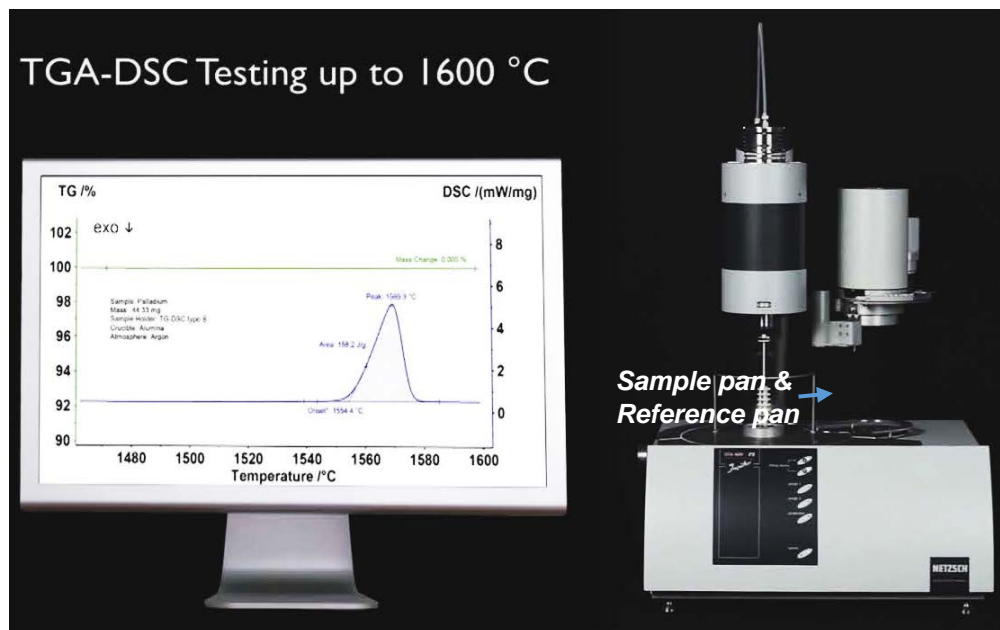


Figure 3.25 Simultaneous Thermal Analyser for DSC and TGA

Thermo-gravimetric analysis

Thermogravimetric analysis is done based on the same equipment as used for the DSC but involves heating to higher temperatures, close to the complete decomposition of the polymer sample. Both onset and final degradation temperatures are established by TGA curves. Laser sintering involves high

energy input into narrow areas in short timeframes which might result in sharp rise in the temperature. Evaporation of gases from the powder bed confirms the possible overheating to the critical temperature levels and the polymer degrading [140]. TGA curves allow quantifying both the onset and final degradation temperatures. Both free and sample pans are mounted on precision balancing systems allowing for the measurement of mass losses. A nitrogen atmosphere is maintained in the sample chamber in order to purge gases released and maintain a balanced atmosphere. Thermocouple and the mass-balance readings allow establishing the temperature vs mass loss curve. The so-called TGA curves eventually allow to determine the decomposition temperature of the polymer sample, which is found to be 400 °C for the neat PMMA powder.

Thermal imaging and online temperature measurement

The transient thermal fields of the sintering process need to be understood sufficiently, in order to explain and predict the mechanisms and mechanics of material bonding and the resulting meso-structures. Also, significant differences are already noted in the critical thermal attributes of the constituent phases used in the current polymer composites. This might lead to varying thermal behaviour of the powder substrates with varying compositions. An online thermal measurement system is essential in order to establish these changes and interpret the material consolidation responses.

An infrared measuring system IR-TCM 640 - detector size 640x480 pixels as shown in Fig. 3.26 is employed for recording the transient temperature variations at different points along the length of a single track laser sintered line on a

uniformly spread polymer composite powder substrate. The non-contact IR-camera system detects infrared energy (heat) and converts it into an electronic signal which can be processed to produce thermal images or perform temperature calculations. The ambient temperature range is from -20°C to 50°C , while the measured temperature could be from -40°C to 2000°C . The IR- camera is mounted on a tripod and is kept at a suitable distance so that it is not affected by the heat of the bed while the critical sintering areas could still be brought into focus. The vario capture software that talks to the camera is initiated with the camera turned on. The camera automatically focusses and levels the temperature range from room temperature to the powder bed temperature which also changes to the sintering temperature range when the laser is turned on.

With the vario capture software the frequency of measurements is set appropriately leading to the selection of either the number of readings within a given time span or the specific time intervals between successive measurements. These settings are adjusted so that readings at 10 equidistant points along a single laser scan of length 50 mm will be recorded. At each of the selected points, the software will continuously record temperature variations as the laser beam travels. A pre-set waiting time interval allowed synchronisation of the laser movement and temperature recording by the IR-system.

As the laser scans the complete length of the single strand, the Variocapture software records all the temperature variations at all experimental points. The final temperature distributions at experimental points are displayed as exclusive images at different points. The temperature data generated by the vario-capture module is then extracted and exported into another software module called

VarioAnalyse-Pro which allows to construct temperature vs time graphs at each and every experimental point. These graphs allow establishing the time-dependent temperature variations of the powder bed resulting from the dynamic movement of the laser beam.

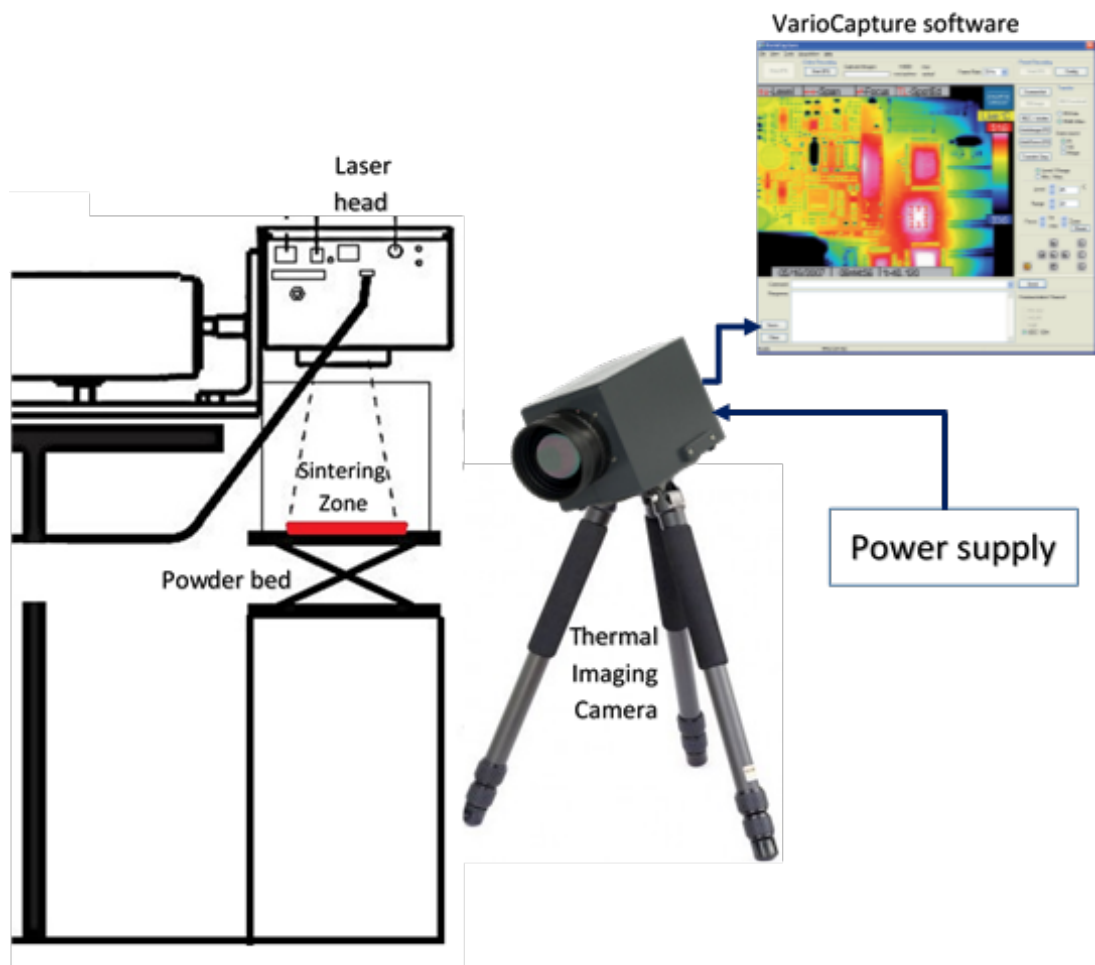


Figure. 3.26 Thermo-vision system and vario-capture interface

3.11 Biological responses

Both neat PMMA and PMMA+ β -TCP composites evaluated in the current study are mainly meant for bio-medical uses. Though both material systems were extensively studied further to processing by traditional processing methods earlier [53-69,], this is the first time selective laser sintering is applied to convert the powdered raw polymer compositions into 3D forms. It is important and essential to establish the possible after effects of the photon interactions on the biological responses of the sintered polymer and composite powders. *In-vitro* analysis methods are employed for this purpose and due to the lack of ready access to the experimental facilities all these tests are conducted at the Biotechnology Lab of the PSG College of Technology, Coimbatore, India, based on an ongoing overseas collaboration. Both single and multi-layer samples trimmed down to 10mmx10mm size are printed with varying compositions and process conditions in order to establish the in-vitro responses. Basic procedures of different tests done are discussed next, while the results are collated and evaluated in Chapter 6.

3.11.1 Cell culture

The human osteosarcoma cell line, MG-63, obtained from the National Centre for Cell Science NCCS Pune, India is cultured in Dulbecco's Modified Eagle's Medium (DMEM) supplemented with 200mM L-glutamine, 10% Fetal bovine serum, and 1X of Antibiotic Antimycotic Solution (A002 from Himedia, India). The cells are humidified with 5% CO₂ at 37°C and trypsinized with trypsin-EDTA after attaining 80-90% confluency. MG 63 cells cultured in the T-flask are captured

using a Micros Lotus MCX51 microscope (20X objective lens) and the infinity capture software as shown in the image of Fig. 3.27.

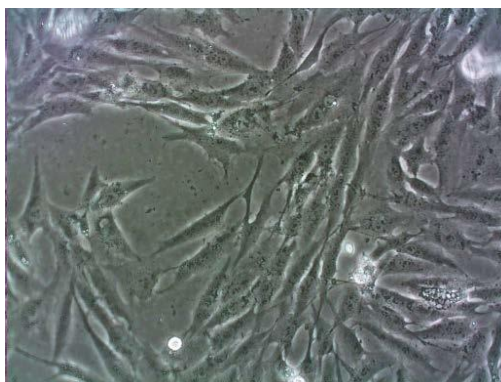


Figure 3.27 4 MG 63 cells captured using a Micros Lotus MCX51 microscope

3.11.2 Cell Proliferation Studies

MTT Assay

The 3-(4, 5-dimethylthiazol-2-yl)-2, 5-diphenyltetrazolium bromide (MTT) colorimetric assay measuring the reduction of yellow 3-(4, 5-dimethylthiazol-2-yl)-2, 5-diphenyl tetrazolium bromide (MTT) by mitochondrial succinate dehydrogenase is employed to assess the cell viability and proliferation within the laser sintered material. The MTT enters the cells and passes into the mitochondria where it gets reduced to an insoluble, coloured (dark purple) formazan product. The insoluble product is then solubilised with an organic solvent (Dimethylsulphoxide), and the released solubilised purple colored formazan is measured spectrophotometrically at 570 nm. Since reduction of MTT can only occur in metabolically active cells the level of activity is a measure of the

viability of the cells. The intensity of the purple color is proportional to the number of live cells.

Each well containing a UV sterilized scaffold is seeded with 1000 μL of medium containing approximately 1×10^4 cells in a 48 well plate, and incubated for 1, 3 and 5 days. After the incubation, 5mg/ml of freshly prepared MTT (HiMedia, India) solution is added to each well and incubated for 3.5 h at 37°C. After the incubation time, the solution is discarded and the scaffolds are air dried, followed by addition of 200 μl of Dimethyl sulphoxide (SD Fine Chemicals, India) to dissolve the insoluble formazan crystals formed. The plate is left shaking for 10-15 min in a dark room. The absorbance is then measured at 570 nm in a multi-well plate reader (Thermo Multiscan Labsystems, Model 352) [141].

Alkaline Phosphatase assay and staining

In humans, alkaline phosphatase (ALP) is present in all tissues throughout the entire body, but is particularly concentrated in liver, bile duct, kidney, bone, intestinal mucosa, and the placenta. ALP is a hydrolase enzyme responsible for removing phosphate groups from nucleotides, proteins, and alkaloids. It splits off a terminal phosphate group in the alkaline solution. Higher levels of ALP activity are observed during the active bone formation, as it is a by-product of the osteoblast activity and, also observed in elevated levels in the cell membrane of undifferentiated pluripotent cells. In the ALP staining, undifferentiated newly formed cells are stained, whilst the differentiated mature cells appear colorless. Hence, ALP staining is used to detect the pluripotency of the cells.

In the current research, the alkaline phosphatase assay is carried out using the p-nitrophenol pyrophosphate (N7653 Sigma Aldrich) as the substrate. According to the protocol specified by the manufacturer, ALP catalyses the hydrolysis of the colorless p-Nitrophenyl phosphate (pNPP) to a colored p-Nitrophenol. This product has a strong absorbance at 407 nm, which is a measure of the level of the enzyme activity. Each well containing a UV sterilized scaffold is seeded with 1000 μL of medium containing approximately 1×10^4 cells in a 48 well plate, and incubated for 4, 7 and 10 days. After the incubation, 200 μL of p-nitrophenol pyrophosphate solution is added to each well. The plates are then incubated in a dark atmosphere for 30 minutes at room temperature. After the incubation, 50 μL of 3M NaOH solution is added per 200 μL of the reaction mixture to stop the reaction. The absorbance is then read at 407 nm in a multi-well plate reader (Thermo Multiscan Labsystems, Model 352). The spectrophotometric values of both MTT and ALP assays are input into Microsoft excel sheets for plotting the results in the form of bar charts. The statistical significances are established using the MINITAB 15 software. Paired t-test is carried out at 95% confidence interval in order to establish the statistical significances of the biological responses.

Alizarin Red S staining

Alizarin Red S, an anthraquinone derivative is used to detect calcium depositions on the sample. The reaction is not strictly specific for calcium, since magnesium, manganese, barium, strontium, and iron may interfere, but these elements usually do not occur in sufficient concentrations to interfere with the staining. Calcium forms an Alizarin Red S-calcium complex in the chelation process. The test is carried out according to the protocol specified by Gregory *et al.* [142].

Alizarin Red S powder (A5533 Sigma Aldrich) is used to prepare the fresh solution (pH 4.1-4.2) each time as per the manufacturer's protocols.

Each well containing a UV sterilized scaffold is seeded with 1000 μ L of medium containing approximately 1×10^4 cells in a 48 well plate, and incubated for 25 and 28 days. The media in the 48 well plate is then removed and the wells are rinsed gently with 1 mL PBS. The cells are then fixed with 1.0 mL of 10% formalin in each well for 15 minutes at room temperature. Formalin solution is then removed and the wells are washed twice gently with double distilled water. To each well, 500 μ L of 40 mM Alizarin Red S solution is added and left at room temperature for 20 minutes with gentle shaking. After the incubation, the dye solution is removed; the wells are washed 4 times with 1.0 mL distilled water, replacing the water at each 5 minutes' interval. The specimens are then air dried, and images are taken to identify the mineralized areas that appear in red colour.

Field Emission Scanning Electron Microscopy (FE-SEM) Analysis

The cell growth is evaluated based on MG 63 cells cultured on the scaffolds and incubated for 5 and 10 days and subsequent SEM photomicrography. Further to the incubation periods, the media is removed, the samples are washed with PBS (pH 7.4), followed by fixing the samples with 2.5% gluteraldehyde for 15 min. The samples are then washed gently three times with a phosphate buffered saline solution of pH 7.4. The specimens are then dehydrated with 30%, 50%, 70%, 90%, and 100% ethanol, for 10 minutes each. The specimens are then air dried, sputter coated with gold and images are taken using a Carl Zeiss microscope (UK & SIGMA) [143].

3.12 Summary of materials and methods

Materials systems employed are introduced and characterised based on the laser sintering literature, in particular, attempting to identify the material-property relationships. Experimental systems designed and developed for the research are discussed. Methods of mixing material components and the scheme of converging on working process parameters are explained. Critical aspects to be evaluated are identified and the experimental methods to be followed to quantify the same are reviewed. The post-process material characterisation schemes are identified and discussed. Laser sintering trials involving neat PMMA powders, critical observations and discussions are the topics for the next chapter.

Chapter 4

Selective Laser Sintering of Poly (methyl methacrylate) (PMMA)

4.1 Laser sintering materials and conditions

Polymers are substances with high molecular weights as the molecular chains are made of many repeating smaller chemical units. Polymeric materials are by far the most successful material candidates for selective laser sintering. The molecular weight of a polymer to be processed by laser sintering should be above the critical entanglement molecular weight to impart good mechanical properties. It should also be low enough to provide the melt viscosity necessary to achieve sufficient inter-particle coalescence. Further, the consolidation must be achieved within limited laser heating, as excessive heating and temperatures might cause polymer degradation [145].

Laser sintering is applicable to both amorphous and semi-crystalline forms of thermoplastics. When heated from very low to the transition temperatures, both forms of thermoplastic materials change from hard (solid and glassy) to softer (tough leathery or rubbery) structures that will eventually turn into a viscous flowing melt. Semi-crystalline polymers have a first order melting transition which results in a drastic decrease in viscosity over a relatively small temperature range. This drastic decrease in viscosity might result in tighter tolerances in laser sintered parts based on semi-crystalline polymers [146]. However, a physical change in an amorphous polymer like PMMA occurs at the glass transition temperature, considering the quasi-second order phase transition. It may also be noted that polymers cannot be effectively coalesced purely based on solid state

sintering due to time constraints with the fast moving laser and rapid cooling rates. Either full or partial melting and subsequent liquid state sintering need to be achieved, while partial melting results in only the outer surfaces of the particles melting and fusing as the cores remain intact [147].

Establishing the appropriate material and process conditions with any new material system for SLS requires understanding the mechanisms and mechanics of consolidation. Past research in these lines was mainly centred around the laser sintering of Polyamide 12. Hague *et al.* reported both particles with un-molten cores surrounded by spherulites and fully melt particles resulting in spherulites without any cores due to partial and full melting of relatively larger and smaller particles respectively [148]. It was proposed that the inter-crystal form and, possibly, the inter-spherulite interfaces could have varying influences on the mechanical properties of laser sintered parts. While the inter-particle and inter-layer coalescence can be adjusted by altering the input energy, there is no mechanical pressure as in injection moulding, and so, the material consolidation progresses depending on the temperature, forces due to gravity, and the capillary action. According to Shi *et al.*, the crystallisation rate, which closely correlates to the crystallinity greatly affects the accuracy of the sintered part [149]. It was also noted that the particle size of the powder affects the precision as well as the density. A larger particle size will lead to a more obvious 'step effect' and a lower density. Considering the powder milling costs, the precision and density of the SLS part and the powder spreading issues, a particle size of 75–100 μm is thought to be more suitable for the SLS process.

Gibson and Shi. used tensile strength measurements on sintered fine nylon parts and established the relationships between the process conditions and the material attributes [150]. The porosity decreased and mechanical properties improved with increasing laser power and decreasing scan speed. Besides powder material properties, fabrication parameters, orientation and build-position also influenced the mechanical properties. The meso-structures and the consequent porosity lead to lesser compressive strengths as compared to the injection moulded counterparts [151]. The modulus of the laser sintered Nylon-12 was also found to be 10% less than that of the injection moulded part. Porous holes with no definite size, shape, and location arise as a result of uneven heat distribution within the build area, inadequate heat supply from the laser and insufficient process temperatures. Mechanical anisotropy is another critical aspect resulting from the build orientation and the end-of-vector effects [152]. Caulfield *et al.* investigated the influence of process parameters (such as energy density, distance between scan lines and the speed of the laser beam) on the physical and mechanical properties of polyamide 12 parts [140]. Based on tensile testing as per the ASTM D638 standards and SEM photomicrography it was observed that samples generated at lower energy densities were porous, weak and anisotropic, but became more isotropic, solid and stronger as the energy density levels increased.

Evidently, porosity is an issue with the laser sintered parts and it comes from the fact that the powders are dispersed under low compaction forces during the deposition into new layers. However, this interconnected porosity is a key property requirement in biomedical applications, including artificial bones and tissue engineering scaffolds. The nature and extent of this interconnected

porosity can be tailored and controlled effectively to meet different application criteria through material selection and physical design, and use of the additive nature of the SLS process. This brings laser sintering biocompatible materials and achieving controlled porosities into focus as the porosity also offers opportunities during post processing to introduce additional materials to achieve material variation as well as part stability.

Das *et al.* investigated the design and fabrication of scaffolds for periodic cellular and biomimetic architectures, but based on nylon [108]. Williams *et al.* designed and fabricated scaffolds of polycaprolactone, a bioresorbable polymer, with the smallest pores at 1.75 mm in diameter based on SLS [105]. Partee *et al.* investigated the development of optimal SLS processing parameters for CAPA®6501 polycaprolactone powder using factorial design of experiments [153]. The test scaffolds with designed porous channels were able to achieve a dimensional accuracy to within 3%–8% of design specifications and densities approximately 94% relative to full density. Schmidt *et al.* noted both relative density and porosity of Polyetheretherketone (PEEK) parts made of SLS to vary with the laser parameters, while these parts are typically produced by conventional manufacturing methods like injection moulding [154].

Apparently, the selective laser sintering research on polymeric materials paid significant attention to the porosity resulting from the point-by-point material consolidation. However, polyamide is the material option in most cases, probably due to the limited availability of the expensive commercial systems and the restrictions on the use of other material options. Occasional consideration of bio-material options such as Polycaprolactone [153] and Polyetherketone (PEEK)

[154] is evident, evaluating for selective laser sintering with varying process conditions. Considering the objective to expand this, selective laser sintering responses of PMMA are examined in this chapter based on the home-made sintering system presented in Chapter 3. The initial experiments, the *a priori* data generated and the results of the subsequent experiments based on laser sintering neat PMMA powders are presented next.

4.2 DSC results of neat PMMA powders and initial sintering parameters

Selective laser sintering was not applied to PMMA powders earlier and so there is no *a priori* data on the possible laser power and velocity settings to be employed and the consequent powder bed temperatures reached. Differential scanning calorimetry (DSC) is applied first to establish the critical temperatures such as the glass transition and melting temperatures. The procedure for conducting the DSC test was described in Chapter 3, while the measurements on neat polymer powders are plotted as shown in Fig. 4.1. Evidently, the DSC curve does not show any sharp variations in the differential energy absorbed, ascertaining the amorphous nature of the polymer [155].

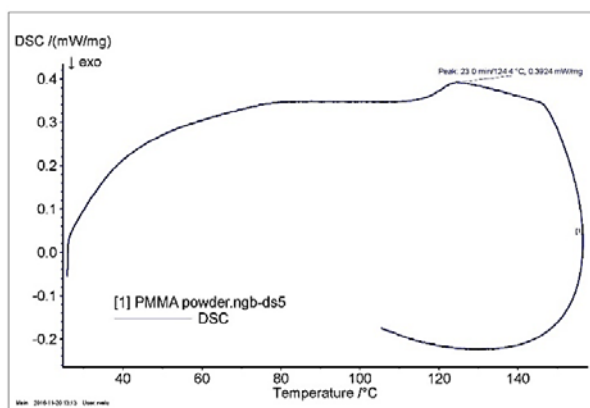


Figure 4.1 DSC results based on the neat PMMA powder

The DSC data generated is processed using the NETZSCH Proteus software and the thermodynamic and kinetic parameters; heat capacity (C_p) and glass transition temperature (T_g) are derived. The activation energy is obtained evaluating the slope of the Ozawa plot. The Ozawa plot method is a non-isothermal iso-conversional method which is based on the principle that reaction rate at a constant conversion is only a function of temperature [156]. The Ozawa equation is

$$\ln(\beta) = \text{const} - 1.052 \frac{E_a}{RT_p} \quad (4.1)$$

where, β is the heating rate ($2^\circ\text{C}/\text{min}$ to $10^\circ\text{C}/\text{min}$), E_a is the activation energy, R is the gas constant (8.314 J/ mol K), and T_p is the peak temperature.

To generate the Ozawa kinetics plot, the non-isothermal DSC values are measured at different heating rates with the same mass of samples. The heating rate varies from $2^\circ\text{C}/\text{min}$ to $10^\circ\text{C}/\text{min}$. Various heating rates and constant sample masses generate different peak temperatures. The Ozawa plot i.e. the heating rate β in logarithmic scale ($\ln(\beta)$) against the reciprocal of the peak temperature $1/T_p$ curve for neat PMMA is constructed as shown in Fig. 4.2. The R^2 value of the fit is 0.947. From the slope ($-E_a/R$) of the line, the activation energy E_a can be obtained using Eq. 4.2.

$$E_a = \frac{dR}{1.052} \quad (4.2)$$

where d represents the trend line slope.

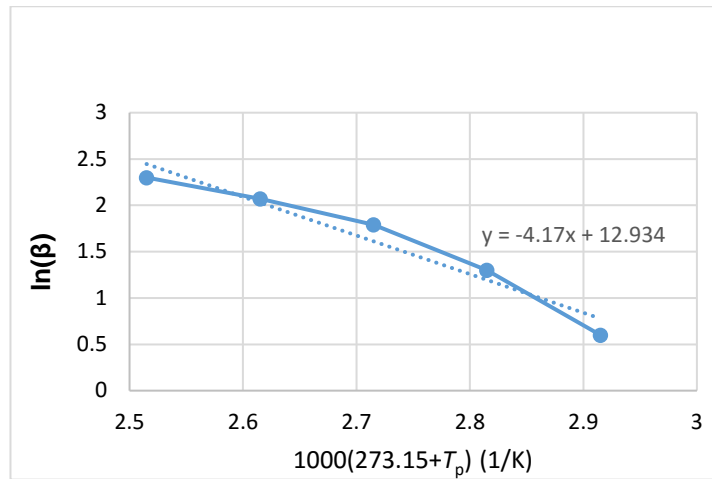


Figure 4.2 Ozawa plot for neat PMMA

Table 4.1 Kinetic and thermodynamic parameters of neat PMMA derived from the DSC curve.

Parameter	Values
Activation Energy E_a KJ/mol	32.955
Heat capacity C_p J/(g°C)	0.870
Glass transition Temperature T_g (°C)	125
Enthalpy H (J/g)	21.32

The kinetic and thermodynamic parameters established for neat PMMA from the DSC tests are listed in Table 4.1. Initial experiments involving single layered sintered samples are designed mainly to understand the effects of the critical process parameters on the inter-particle bonding and the overall consolidation of the powder material in a single layer. The *a priori* data thus generated will be used further in subsequent experimental evaluation in order to establish the overall responses of PMMA to selective laser sintering. Three critical parameters arise based on the mechanism of material consolidation; laser power (P), scan speed (v) and beam diameter (D). The laser and other parameter settings and

experimental methods are discussed in more detail in Chapter 3. The glass transition temperature value from Table 4.1 is used in Eq. 3.1, together with a selected laser scan velocity to establish the energy density required to achieve sufficient melting and inter-particle coalescence as equal to 0.06 J/mm^2 . This is the starting point for choosing working laser power and scan velocity settings for the initial trials sintering neat PMMA powders based on the CO_2 laser as described next.

4.3 Initial experiments and results

Considering the energy density level estimated above, the working energy density range is set from 0.04 J/mm^2 to 0.1 J/mm^2 and the laser power and scan velocities are varied as identified in Fig. 4.3 for the initial sintering trials. SEM photographs are generated based on the single-layer samples, mainly as to understand the influences of laser parameters on the melt-flow behaviour of powder particles, inter particle fusion and coalescence. Surface morphological analysis is also carried out evaluating the density of pores in the photomicrographs. While material properties, powder bed characteristics, and process parameters influence the properties of SLS parts, in particular, the laser power and scanning speed are found to play more significant roles. Alessandro and Luca [112] studied the sintering depth and height of polyamide and phenolic coated sand following single-pass laser scanning and showed that appropriate energy densities need to be employed for proper sintering. Initial experimental trials are conducted to produce single layer samples with the scanning speed and laser power varied from 30 to 5100 mm/s and 6 to 42 W respectively.

Fig. 4.3 (a) presents the SEM photographs of samples generated with the highest scan speed 5080 mm/s while the power varies from 24 W to 42 W. Evidently, the higher speeds employed did not allow enough time for inter-particle coalescence even though the power used is sufficiently high. This resulted in a sparsely connected network of the raw powder particles indicating insufficient sintering. Reducing the speed to 1524 mm/s and 1016 mm/s as shown in Fig. 4.3 (b) and (c) did not improve the result appreciably as there is still lack of energy absorption for significant inter-particle fusion. However, with the scanning speed reduced to 254 mm/s and 127 mm/s as shown in Fig. 4.3 (d) and (e), the inter-particle coalescence has improved as reflected by the plastered granular appearance of the layer, which is further enhanced as the laser power is gradually increased. As the scanning speed is reduced to 38 mm/s, there is a drastic reduction in the laser power required in order to achieve uniform and sufficient coalescence all across the single layer film as evident from the photomicrographs of Figure 4.3 (f).

These results clearly indicate the significant effects of the scanning speed on the surface morphology of the single sintered layer, while the sintered thickness also varies accordingly. Evidently, with lower scanning speeds, relatively longer interaction times lead to greater energy absorption and more time for particle interaction and fusion. With 38 mm/s speed, the powder bed started to change colour and degrade when the lesser power is increased to 9 W, indicating interacting effects between critical parameters and some clearly visible limits to the ranges of process parameters. At the other end, with higher laser scanning speeds, 1016 mm/s to 1524 mm/s the inter particle coalescence dropped to a minimum with the lower power settings; 6 W and 9 W, while a 12 W power setting resulted in a fragile single layer. The overall impression from the results of these

initial tests is that better sintering can be achieved with relatively moderate scanning speeds.

The initial results are used to narrow the ranges of speed and power further in order to converge on the more favourable experimental domain. The energy density expressed in Eq.3.1 is used again and the most successful combinations of speed and power based on the results presented in Fig. 4.4 yielded three possible energy densities as listed in Table 4.2. Keeping the effective energy densities at the three levels, several combinations are developed with laser scan speed and power varying in relatively narrow ranges as given in Table 4.2. Fig. 4.4 presents SEM photographs of the surface morphologies of sintered samples generated with these parametric combinations and the main observations are listed in Table 4.2. While all these trials gave good results, in general, for a given energy density, the higher the power, the better is the laser consolidation of powder particles. Complete fusion made the boundaries of particles indistinguishable when the power used is above 18 W, with any of the energy density settings employed. Porosity is observed in all samples, but with the intensities decreasing with increased coalescence across the thin layer.

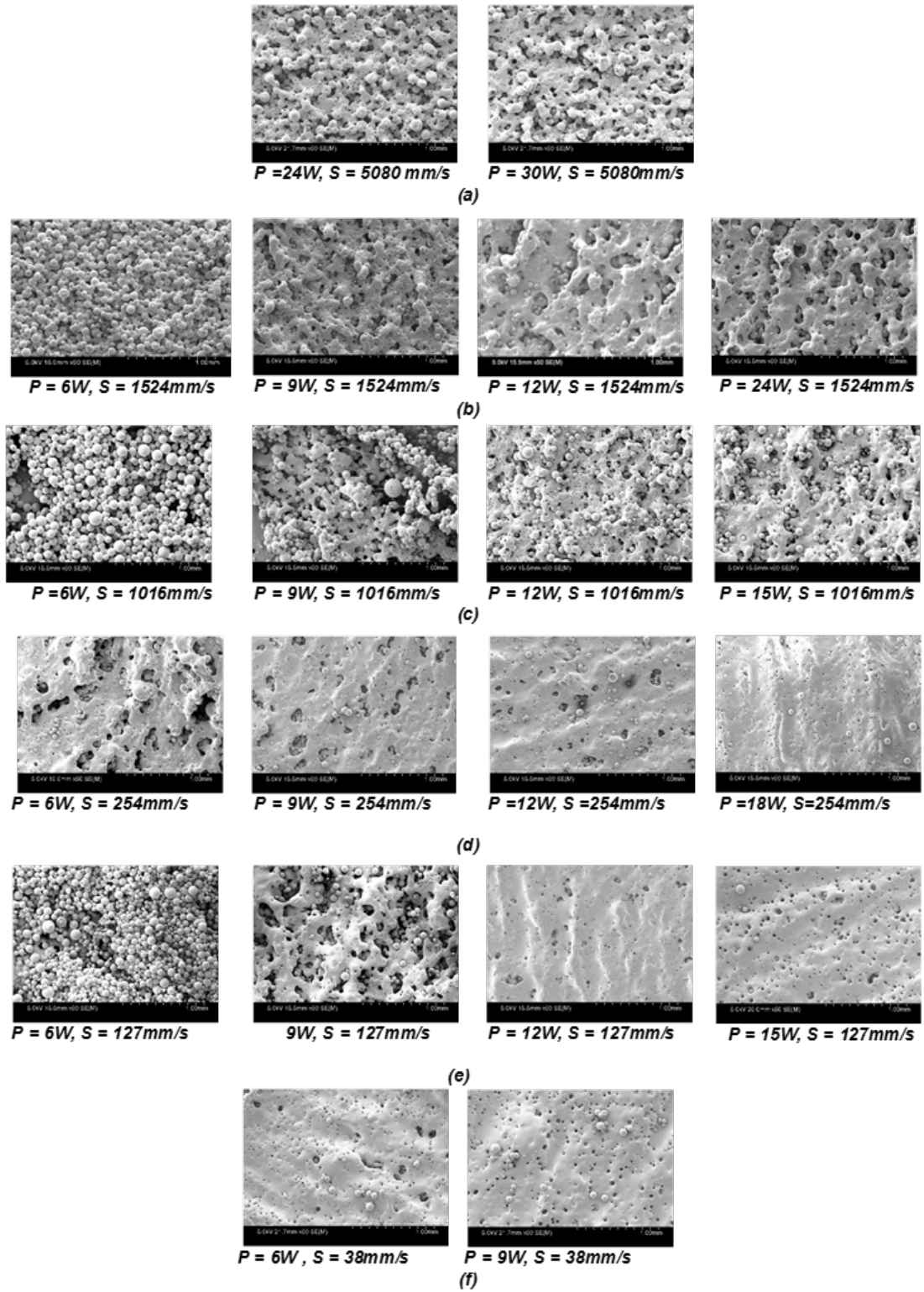
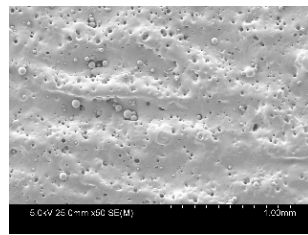


Figure 4.3 SEM Photographs of sintered PMMA: initial trials

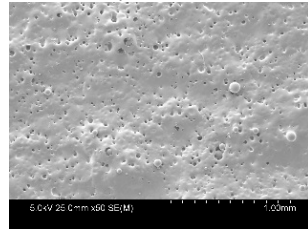
Table 4.2 Experimental condition with specific energy densities and general observations

Energy Density (J/mm ²)	Laser Power (W)	Scan speed (mm/s)	Surface morphology of sintered samples
0.15	9	95	<i>Individual particles could not be identified; all particles fused together; few pores were observed in low power.</i>
	12	127	
	18	190	
	24	254	
0.3	6	38	<i>Individual particles could not be identified; most of the particles fused together; boundaries between particles became indistinguishable; voids are evident.</i>
	12	76	
	18	114	
	24	152	
0.4	9	38	<i>Individual particles could not be identified; most of the particles fused together; boundaries between particles became indistinguishable; voids evident with low power, but reduced at high power</i>
	12	51	
	18	76	
	24	101	

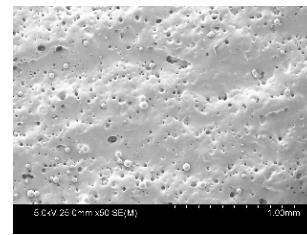
While complete fusion of individual particles resulting in a uniform sintered layer is an appreciable result, the porosity observed is an intriguing aspect and requires a quantitative evaluation. Image processing and statistical analysis tools in MATLAB are employed for this purpose. The method involves scanning the pixels and counting boxes of the fractal image using a built-in MATLAB function. The digital image in the form of a quantified two dimensional sampling array is converted into grey variation, which represents the roughness and the distribution of the surface pores. Photoshop is first used to process the SEM image and convert it into a black and white image with grey values varying from 0 to approximately 255. Image segmentation is done by the MATLAB Toolkit to develop a clear view between the background and the surface pores. For calibration and benchmarking, an image with a known number of pores is first tested with the software and the results are close.



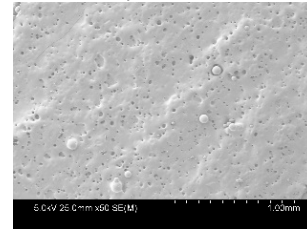
$P = 9W, S = 95mm/s$



$P = 18W, S = 190mm/s$

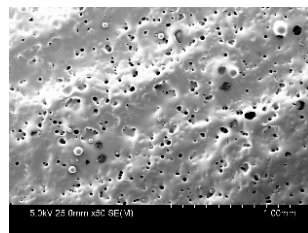


$P = 12W, S = 127mm/s$

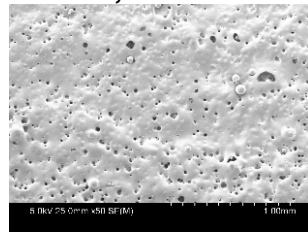


$P = 24W, S = 254mm/s$

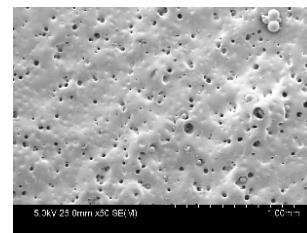
(a) Energy density = 0.15 J/mm²



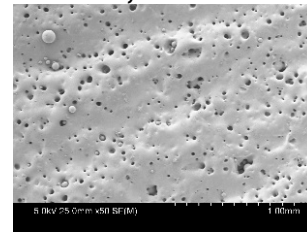
$P = 6W, S = 38 mm/s$



$P = 18W, S = 114mm/s$

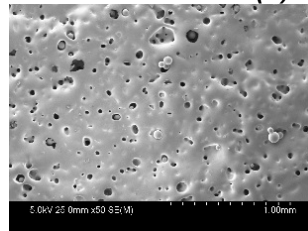


$P = 12W, S = 76 mm/s$

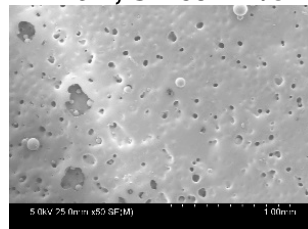


$P = 24W, S = 152mm/s$

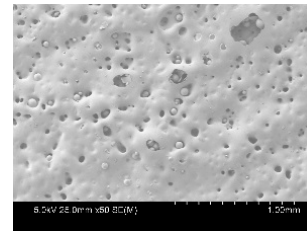
(b) Energy density = 0.3 J/mm²



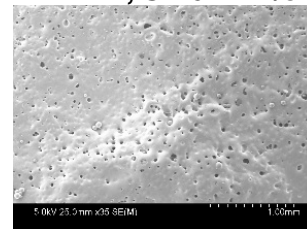
$P = 9W, S = 38 mm/s$



$P = 18W, S = 76mm/s$



$P = 12W, S = 51 mm/s$



$P = 24W, S = 101mm/s$

(c) Energy density = 0.4 J/mm²

Figure 4.4 SEM Photographs of sintered PMMA single layers with varying process parameters

The image processing results are presented in Fig. 4.5 as number of pores against laser power for different energy densities. It may be observed that for any energy density, the number of pores decreased with initial increase in the laser power. However, beyond a certain value, though all samples showed signs of number of pores increasing with power, there is again a second drop with the two lower energy density settings. With the energy density set at 0.4 J/mm², there has been a continuous rise in the number of pores as a result of excessive thermal energy deteriorating the powder consolidation mechanism. The other two energy density settings showed tendencies for the number of pores in the single layer to decrease with increasing laser power beyond certain limits, implying that the porosity of the PMMA parts could be controlled by the energy imparted to the powder surface.

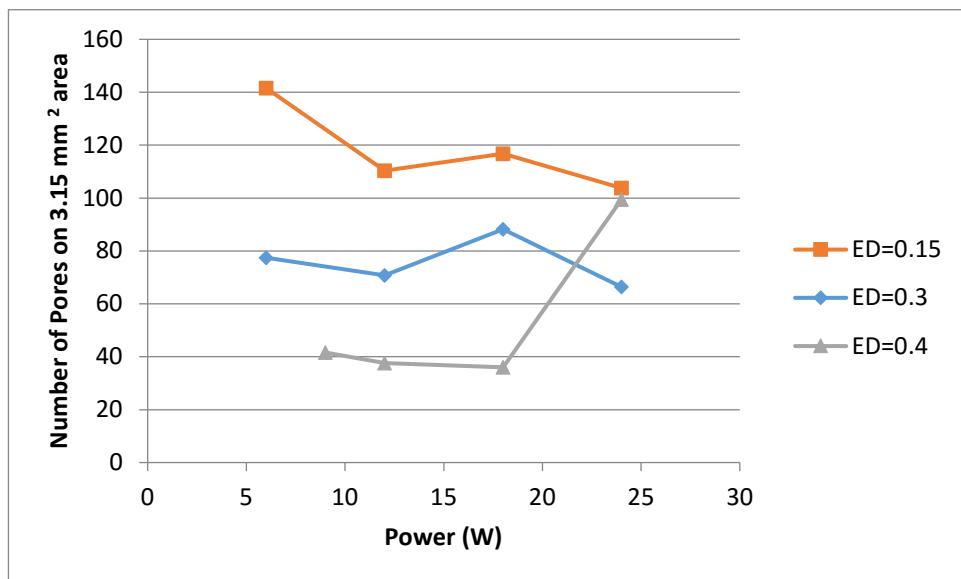


Figure 4.5 No of pores per area vs. laser power at different energy densities

4.4 Further sintering trials and evaluation of influences of critical process parameters

Considering the improved sintering and layer formation obtained with energy densities at 0.15 and 0.30 J/mm² as the laser power is increased beyond 20 W, further sintering trials are conducted shifting the laser power settings to the range 20 W to 35 W, as shown in Table 4.3. As evident from Fig. 4.6 and stated in Table 4.3, overheating and rapid degradation of the powder bed occurred when the laser power is increased beyond 35 W for ED 0.15 J/mm² and 30W for ED 0.3 J/mm². PMMA particles which are initially in spherical forms are fully coalesced after sintering, as shown in Fig. 4.6. However, when the power is increased beyond a certain limit, powder particles started to degrade and vaporise. With ED equal to 0.4 J/mm² or more, degrading occurred even at power settings as low as 20 W. It is pertinent to note from these results that laser sintered PMMA parts will exhibit porosity and the level and nature of this can be controlled through appropriate process evaluation. Ideally, bone repair and replacement devices must possess interconnected open-pore geometries and microstructures, permitting cell in-growth and reorganization during the in-vitro phase, providing the necessary space for neovascularization from the surrounding tissues [91].

Table 4.3 Surface morphologies of single layer samples sintered with higher power settings

Energy Density (J/mm ²)	Laser Power (W)	Scan speed (mm/s)	Surface morphology of single sintered layer
0.15	20	255	Sufficient inter-particle fusion but traces of inter-particle boundaries and melt flow lines are evident, fewer pores than those obtained with lower power settings
	25	309	
	30	370	
	35	432	
0.3	20	124	Particles are completely fused, there is a more integrated single layer, however relatively number of pores compared to the above case.
	25	154	
	30	185	
	35	216	

The percentage porosity of a specimen can also be calculated using the theoretical density together with the measured density and using Eq. 4.3.

$$\text{Porosity} = \frac{\rho(\text{theoretical}) - \rho(\text{sintered})}{\rho(\text{sintered})} * 100 \quad (4.3)$$

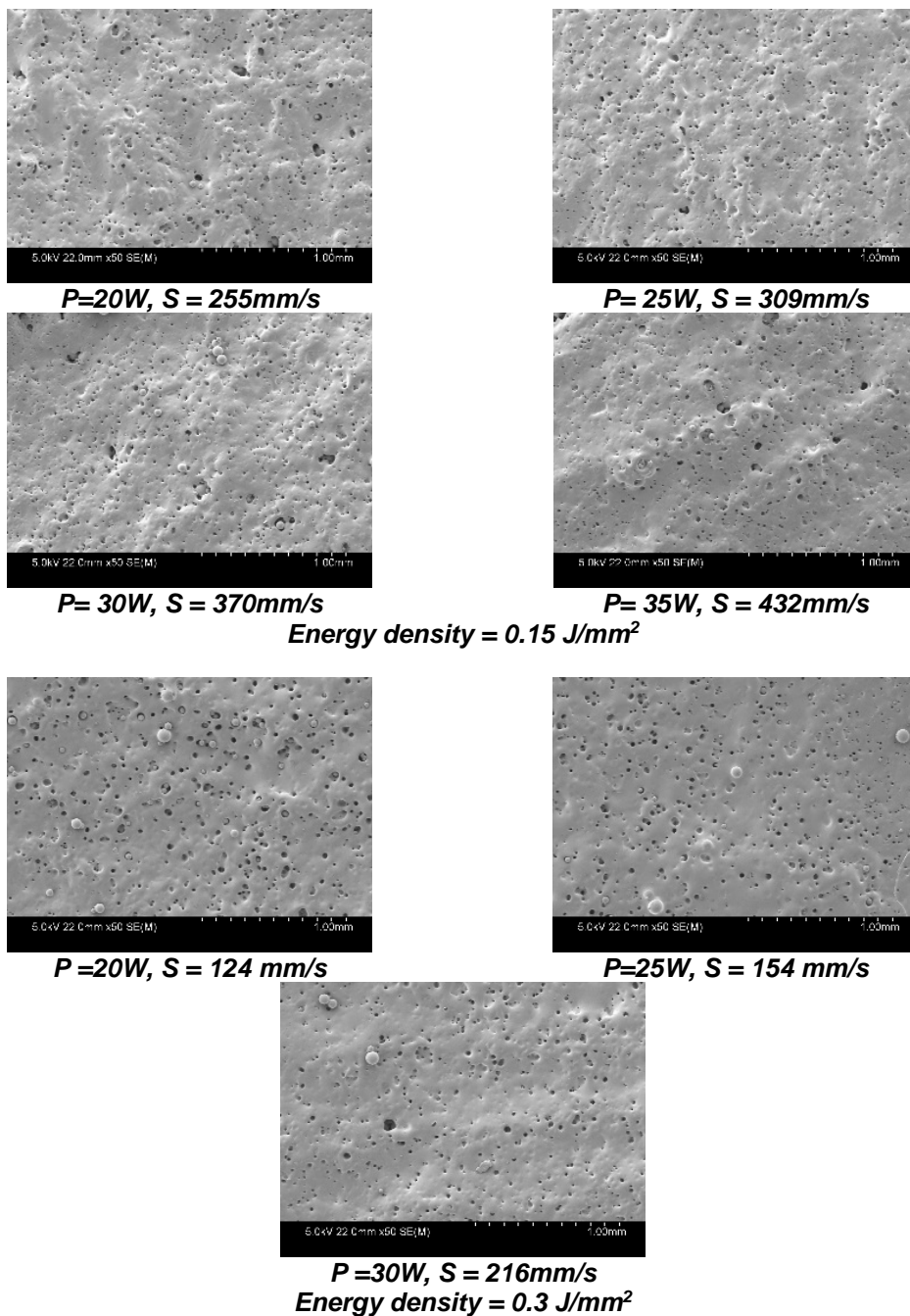


Figure 4.6 SEM photographs of single layer samples sintered at relatively higher laser power settings

Densities of the specimens are established by measuring the mass and the volume of each specimen, while the theoretical density is 1.18 g/cm^3 from table 3.1. Theoretical density and porosity values calculated are shown in Table 4.4. The variation of the percentage porosity is plotted against laser power in Fig. 4.7 at the two energy density levels. While the average pore size is at around $150 \text{ }\mu\text{m}$, the general trend is that the percentage porosity decreases with increase in laser power. Image processing results using the MATLAB program also gave similar results as shown in Fig. 4.8. The porosity arising at lower power settings is caused by partial melting of powder particles and the resulting inter-granular cavities as evident in Fig. 4.9 (a); an exploded view of one of the SEM photographs of Fig. 4.3. However, at sufficiently higher power and energy density settings, full melting and subsequent homogenisation of the sintered layer takes place as seen in all SEM photographs of Fig. 4.6, but porosity arises due to excessive heating, resulting gas pickup, and subsequent rupture due to thermodynamic variations, as shown in Fig. 4.9 (b), again an exploded view of one of the SEM photographs of Fig. 4.6.

During laser sintering, as more time is given, gases are trapped through the diffused material matrix, driven by the dissolution occurring under the Laplacian excess bubble pressures according to Henry's Law [157], especially as the viscosity of the matrix decreases. This is indeed seen in the regions around closed pore systems, as evident from Fig. 4.9 (b). Bubbles would tend to increase in size on heating, due to expansion taking place in order to maintain the pressure equilibrium. As the viscosity of the material decreases with temperature [92], the pressure opposing the surface tension drives the contraction of the pore. A dynamic balancing of the two effects eventually controls the size of the pore. The

process of gas pickup, bubbling, explosion and consequent porosity depend on both temperature and time variations. For example, with any of the two energy density settings, the lower power also requires lower scan speeds which necessitate the power source to be around a given point for longer, causing more porosity. With higher power settings, the scan speed also increases, in order to keep the energy density at the expected level, and this reduces the chances of porosity due to gas pickup and bubbling.

Table 4.4 Porosity of single layer sintered PMMA at two different energy density settings

Energy Density J/mm ²	Laser Power (W)	Scan speed mm/s	Trail 1	Trail 2	Trail 3	Mean Porosity %	Standard deviation	standard Error	Error 95% confidence
0.15	20	255	61	59	60	60	1	0.577	1.96
	25	309	58	56	59	57.66	1.527	0.88	2.99292
	30	370	56	55	58	56.33	1.527	0.88	2.99292
	35	432	55	53	56	54.66	1.527	0.88	2.99292
0.3	20	124	57	55	58	56.66	1.527	0.88	2.99292
	25	154	53.6	52	50	51.866	1.803	1.04	3.53388
	30	185	52	49	50	50.33	1.527	0.88	2.99292

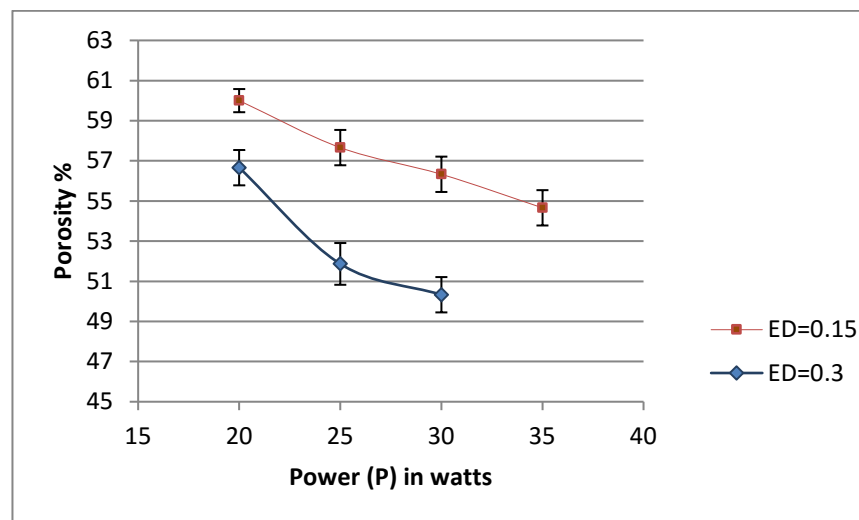


Figure 4.7 Percent porosity vs laser power at different energy density settings

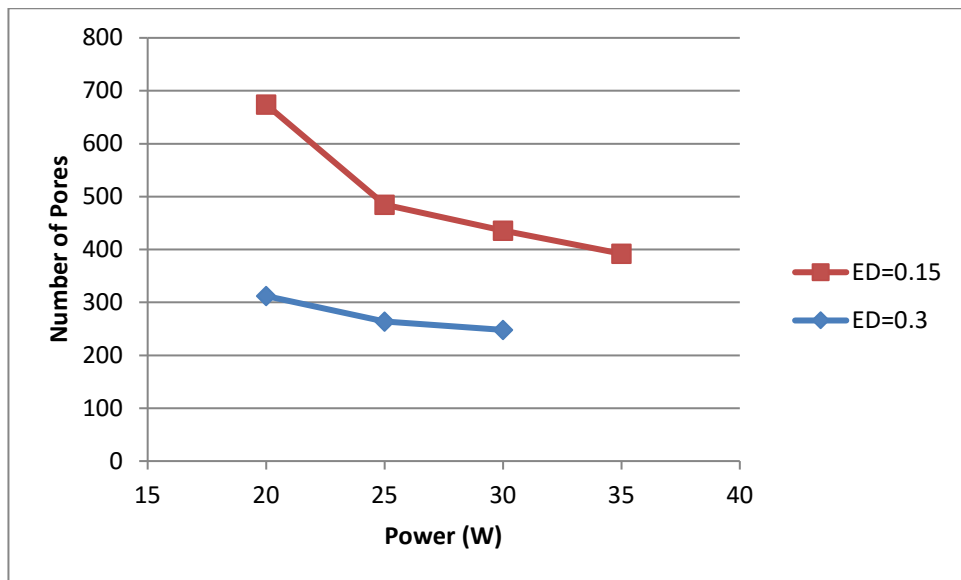


Figure 4.8 No of pores vs laser power (20 W to 35W) at two different energy densities.

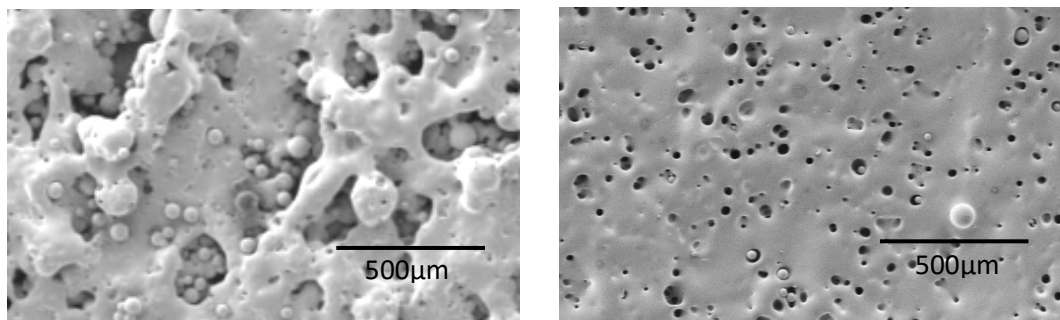


Figure 4.9 Causes of porosity

Thin film test specimens are prepared for tensile testing as per the ASTM D882 standards and the tests are conducted using the Instron 5567 Load frame with a cross head speed 12.50 mm/min, nominal gauge length 50mm and distance between the grips 125mm as explained in Chapter 3. The single layer sintered specimens printed as per the conditions listed in Table.4.5 and some of the samples are shown in the photograph of Fig. 4.10. Thicknesses of thin films are established as average values of micrometre measurements taken at three different locations. Table 4.5 lists values of elastic modulus, ultimate strength

and elongation at break, based on the results of the thin film tests on PMMA specimens.

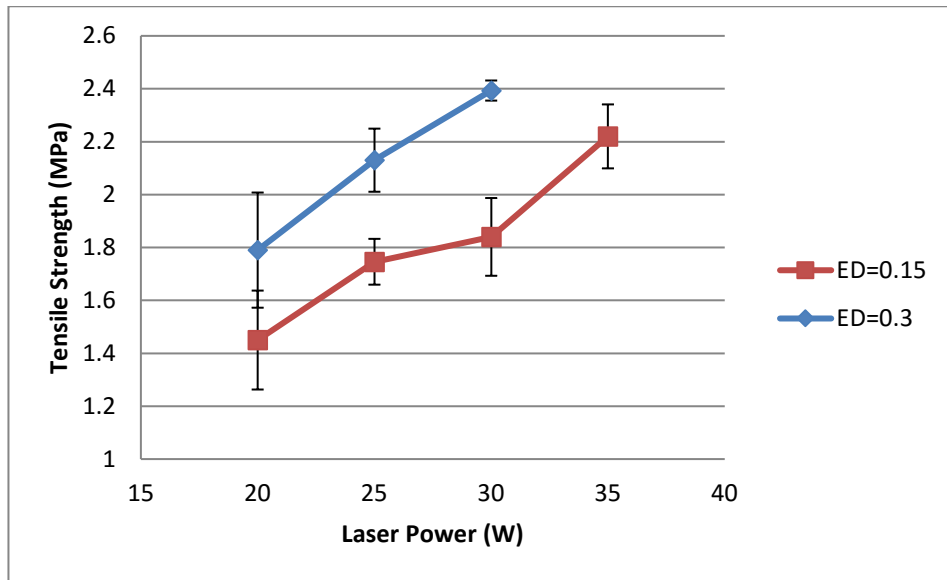
Table 4.5 Mechanical properties of single layer sintered samples

Energy Density J/mm ²	Laser Power (W)	Scan speed mm/s	Trial 1	Trial 2	Trail 3	Mean Ultimate Tensile Strength MPa	Standard deviation	standard error	Error 95% confidence
0.15	20	255	1.16	1.8	1.39	1.45	0.324	0.187	0.63504
	25	309	1.74	1.6	1.9	1.746	0.15	0.0866	0.294
	30	370	1.74	1.91	1.65	1.84	0.1266	0.073	0.248136
	35	432	2.27	1.98	2.4	2.22	0.209	0.1209	0.40964
0.3	20	124	1.37	1.89	2.1	1.79	0.377	0.2177	0.73892
	25	154	2.3	1.90	2.19	2.13	0.206	0.1193	0.40376
	30	185	2.41	2.32	2.45	2.3933	0.0665	0.038	0.13034
Energy Density J/mm ²	Laser Power (W)	Scan speed mm/s	Trial 1	Trial 2	Trail 3	Mean elastic modulus MPa	Standard deviation	standard error	Error 95% confidence
0.15	20	255	265	252	275	264	11.5325	6.65	22.6037
	25	309	282	310	300	297.33	14.189	8.19	27.81044
	30	370	300	315	305	311.66	7.6	4.409	14.896
	35	432	343	333	356	343.33	11.53	6.65	22.5988
0.3	20	124	303	290	310	302.66	10.14	5.859	19.8744
	25	154	316	321	325	320.66	4.509	2.6	8.83764
	30	185	357	360	349	355.33	5.686	3.2	11.14456

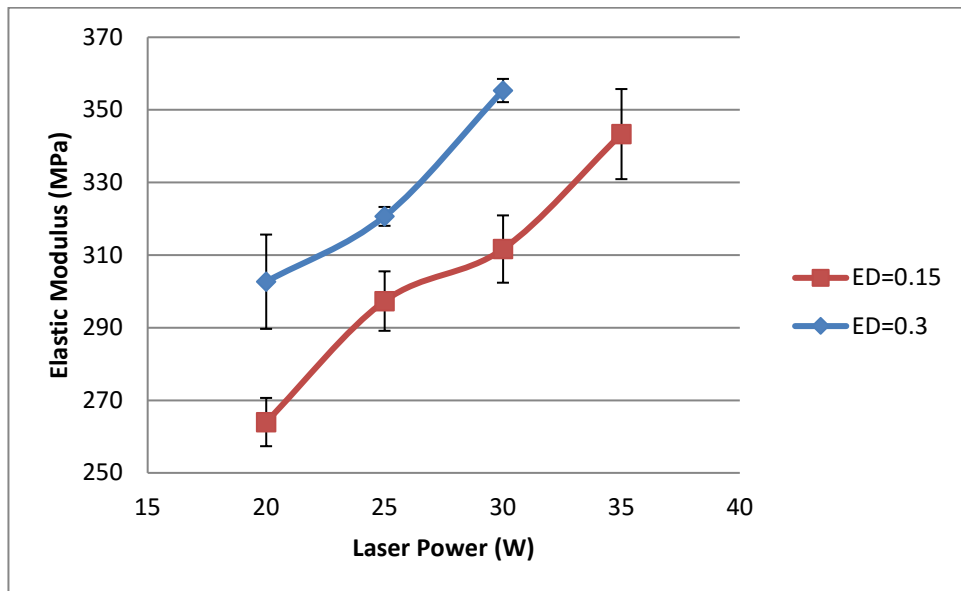


Figure 4.10 single layer sintered specimens

Fig. 4.11 is a graphical representation of the variation of tensile strength and elastic modulus with varying laser power at the two energy density levels considered. In general, both tensile strength and elastic modulus values increased with increasing energy density at all levels of the laser power. Also, with any given energy density, tensile strength and elastic modulus increased with increasing laser power. With energy density at 0.15, varying the power from 20 W to 30 W involves the laser scanning speed increased from 255 mm/s to 432 mm/s, and resulted in almost doubling the tensile strength from 1.16 MPa to 2.27 MPa, and about a 30% rise in the elastic modulus, from 265 MPa to 343 MPa. Similar trends are noticed with energy density 0.3 J/mm² also, as tensile strength and elastic modulus increased from 1.37 MPa to 2.4 MPa and 303 MPa to 353 MPa respectively while the variation in laser scanning speed in this case is 124 mm/s to 184 mm/s.



(a) Tensile strength vs laser power



(b) Elastic modulus vs laser power

Figure 4.11 Mechanical properties of thin film PMMA tensile specimens

Evidently, these results are in the reverse order to the variation in porosity levels with varying process parameters as depicted in Fig. 4.7 and Fig. 4.8. Overall, a lower power, lower speed setting is resulting in more porosity and consequent lower mechanical attributes compared to the higher power and speed setting. Evidently, with the laser heat source moving relatively slowly, there is more opportunity for the laminated powder substrate for gas pick-up and subsequent

porosity. However, across the two energy density settings, for any given laser power, a far lesser speed setting as with the higher energy density resulted in lower porosity and better mechanical properties indicating confounding effects of laser power and speed. The plausible explanation for this is that at far lesser scanning speeds, there is enough time for the power source to sufficiently reheat the already sintered zones, due to secondary heating as the raster scanning continues, and filling up of some of the voids created during the initial stages.

Eventually, the mechanical strength is governed by the thermal history and associated variations across the domain of the sintered sample. When the laser strikes the substrate at a point, the heat energy allows the polymer grains to be plasticised first, adjacent particles fuse into each other forming a neck, through which molecular diffusion and other processes take place, the neck grows to a certain extent and if sufficient energy is available, complete merging may take place, allowing a single continuous strand to be formed as the laser scanning continues [158]. If the laser stays longer at a particular place, due to slower speeds, there is the possibility of overheating, deterioration and subsequent formation of gas bubbles as pointed out earlier. However, during repeated laser scanning, the laser heat source also may revisit the affected zones and based on the diameter of the beam and the proximity to a cavity, reheating and subsequent re-filling of some of the existing pores is possible.

Overall, with a fixed energy density, and within the working ranges of laser power and scan speed, the results in terms of quality of sintering and coalescence are very similar for all combinations, from low power low speed to high power and speed settings (Fig. 4.6). However, the main constraints are the ranges of the two

parameters. For example, when the laser power used is beyond 35 W, the material immediately chars and degrades, no matter what scan speed is used, which also applies to the limits of the scan speed. These ranges are typically material dependent and for neat PMMA, the optimum settings are within the ranges identified from the current research.

4.5 Summary of the sintering trials with PMMA

Powder PMMA is processed by selective laser sintering and single layer specimens are successfully produced based on an experimental laser sintering test bed. Critical process parameters laser power and scanning speed are found to have significant effects on the inter-particle coalescence and the porosity levels in sintered single layers. The relationships between the degree of porosity and the process parameters are established and plausible means of effectively controlling the process are evidenced. The mechanical properties also varied in similar lines with varying process conditions. The use of energy density between 0.15-0.3 J/mm² appears to be the optimal range both from morphological and mechanical property considerations. While establishing the basic responses and critical aspects of laser sintering of PMMA, the results are indicative of a promising future for the approach in view of the specific needs of numerous medical applications. However, neat PMMA, though biocompatible, is not bio-active and requires to be loaded with a bio-ceramic component to complete the material attribute requirements. The laser sintering responses of the bio-polymer composite would then require further research attention, which is the focus for the next chapter.

Chapter 5

Laser Sintering PMMA+ β -TCP Composites

5.1 Additive processing of PMMA composites

The experimental results presented in Chapter 4 clearly elucidate the possible use of selective laser sintering to process neat PMMA powders into 3D forms. However, both materials and processes used for medical applications should have specific qualities. In the context of bone repair and re-construction, controlled open porosity and osteo-conductivity are essential apart from mechanical strength and bio-compatibility. While porosity is possible to be controlled by the process parameter combination as discussed in the previous chapter, the osteo-conductivity of laser sintered PMMA is an issue to be resolved. Several forms of calcium phosphates are often used for improving the bio-activity, considering properties similar to bone minerals, but often in combinations with other biopolymers. The next step in this research is to combine PMMA with a suitable bio-ceramic and evaluate the sintering responses in order to establish a bio-compatible and bio-active polymer composite for specific medical applications.

Ceramics and their composites are often used for bone repair and replacement applications as well as dental orthopaedics. Within the bio-ceramic subset, porous ceramics based on calcium phosphate are close to bone minerals and biologically responsive, and easily metabolised within the body. The materials commonly used to fabricate polymeric SLS parts are high strength thermoplastics. The chemical composition of the polymer, the presence and

concentration of the oxidation-prone groups, and the amount of plasticizers or additives have significant effects on the process. Consequently, it becomes important and interesting to investigate how any new bio-polymer composite responds to SLS. Generally, polymers are high-elastic and low-stiffness materials, while ceramics are rigid and brittle. Merging the two allows to combine both mechanical and bio-conductivity attributes in the polymer composite, but the differential thermal properties are likely to alter the sintering conditions and responses. Based on the literature reviewed in Chapter 2, β -TCP is already identified as the candidate filler material to be investigated for laser sintering with PMMA. The powder material mixtures are first subjected to the DSC analysis in order to establish the working laser process parameter levels.

5.2 DSC analysis of PMMA- β -TCP polymer composites

The procedure for conducting the differential scanning calorimetry on the powder samples used in the current study is detailed in Section 3.10 of Chapter 3. The DSC test results based on the PMMA + β -TCP composites are presented in Fig. 5.1. The thermodynamic and kinetic parameters of the material samples such as heat capacity (C_p), Glass transition temperature (T_g), and Enthalpy (H) are derived using the NETZSCH Proteus software. The activation energy (E_n) is determined from the slope of the Ozawa plot as shown in Table 5.1. The R2 value of the fit is 0.9373. As an illustration, the Ozawa plot i.e. the $\ln(\beta)$ against $1/T_p$ curve for the 5% β -TCP /95% PMMA sample is given in Fig.5.2.

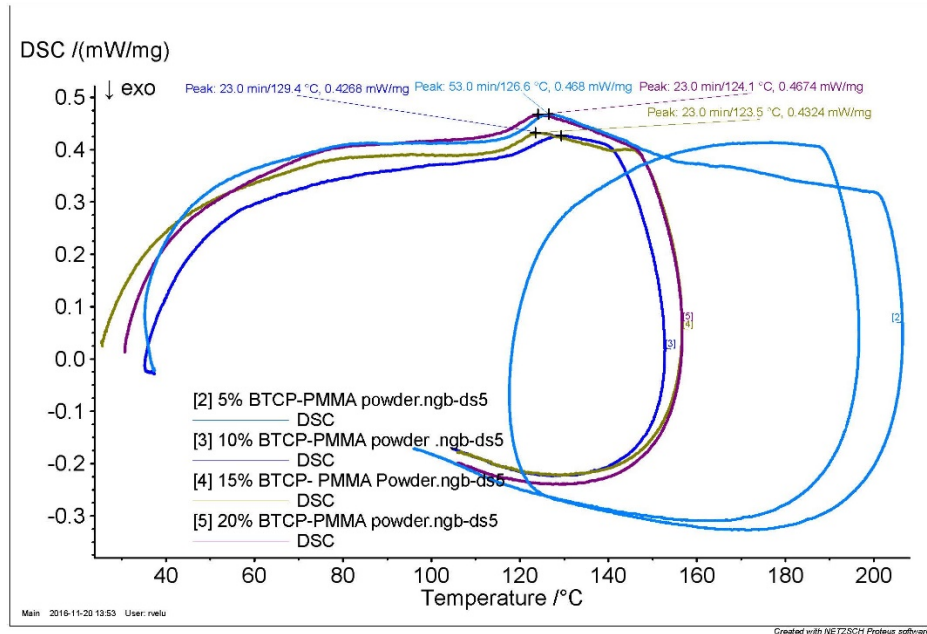


Figure 5.1 DSC results based on PMMA and PMMA/β-TCP powders

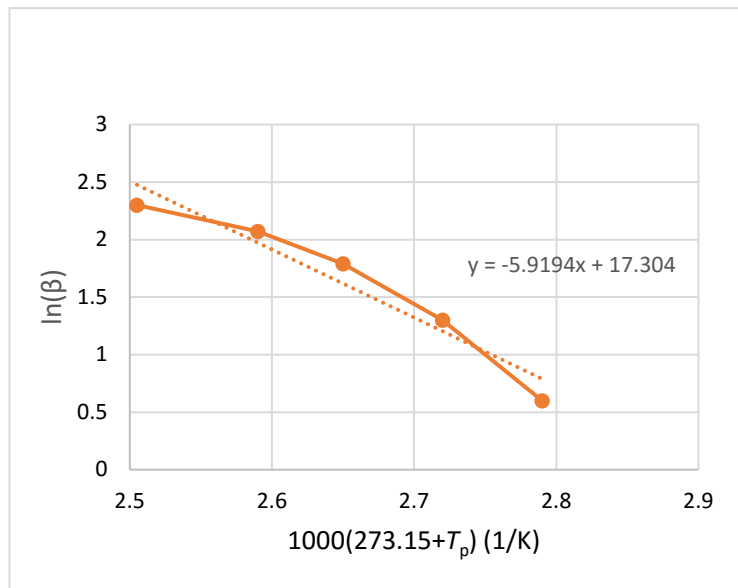


Figure 5.2 Ozawa Plot based on the 5% β-TCP /95% PMMA.

Table 5.1 Kinetic and thermodynamic parameters of PMMA and PMMA/ β -TCP composites derived from the DSC curves.

Sample	Activation Energy E_a (KJ/mol)	C_p Heat capacity J/(g $^{\circ}$ C)	Glass transition Temperature T_g mid ($^{\circ}$ C)	Enthalpy (H) (J/g)
100% PMMA	32.955	0.870	125	21.32
5% β-TCP/ 95% PMMA	31.6	0.9	118	27.17
10% β-TCP/ 90% PMMA	29.36	0.902	101.1	28.16
15% β-TCP/ 85% PMMA	27.45	0.937	93.8	29.71
20% β-TCP/ 80% PMMA	26.22	1.045	92.7	31.92

It may be observed that the activation energy gradually decreased with increasing β -TCP in PMMA, starting with a 32.955 J/mol for neat PMMA and ending up at 26.22 J/mol for the 20% β -TCP and 80% PMMA composite. This result is indicative of relatively lesser energy densities needed for the PMMA- β -TCP composites to achieve the inter-particle coalescence compared to neat PMMA, in a laser based consolidation process such as SLS. In fact, this is already noted from the results discussed in Chapter 4 and in sections 4.2 of this chapter.

On the other hand, the heat capacity increased from 0.870 J/g $^{\circ}$ C with neat PMMA to 1.045 J/g $^{\circ}$ C with the PMMA-20% β -TCP composite. This is probably due to a higher energy absorption capability resulting from the presence of the β -TCP particles [159]. This aspect can further be verified based on the thermogravimetric analysis as discussed next. The glass transition temperature as evaluated from the DSC curve indicates a reduction from 125 $^{\circ}$ C for neat PMMA to 92.7 $^{\circ}$ C with the 20% β -TCP case. Evidently, the higher the β -TCP content, the better is the heat absorption for every degree of temperature rise, while the

relative weight of the PMMA phase also decreases. The β -TCP phase allows for higher rate of heating as well as better preservation, which will be transferred to the actual melting phase (PMMA) to undergo phase transition at a lower temperature as compared to the case of the neat polymer.

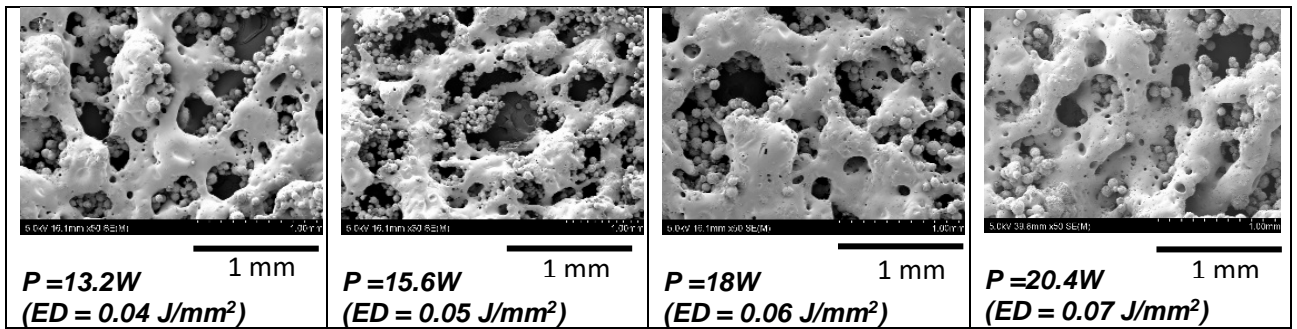
Heating a polymer up to the glass transition temperature T_g is associated with a linear thermal expansion and decrease in viscosity and elastic modulus values [160]. Beyond the glass transition temperature, the degree of conversion into monomers increases [161]. Naturally, the glass transition temperature varies with the composition of the polymer composite. In the present case, with increasing β -TCP, the heat capacity increases, leading to a reduction in the glass transition temperature levels [162]. This might lead to improvement in the coalescence when the polymer composites are sintered, but the presence of the loaded particles may also alter the viscosity and the rheology of the melt pool, thus adversely affecting the inter-particle consolidation. While pure PMMA powders resulted in better sintering as observed in Chapter 4, the porosity and other issues noted below in this chapter with the PMMA+ β -TCP composites are mainly due to the rheological changes in the plasticised polymer pools [163].

The enthalpy increased with increasing β -TCP as noted from the last column of Table 5.1, again clearly indicating the rise in the internal energy due to the presence of the β -TCP particles loaded into the base polymer. It was indicated in Chapter 2 that the enthalpy of fusion must be high for the selective laser sintering process to be more effective [109]. Following the same procedure as employed in the neat PMMA case, the DSC results, and in particular the glass transition temperature values are used again for a selected laser power and the

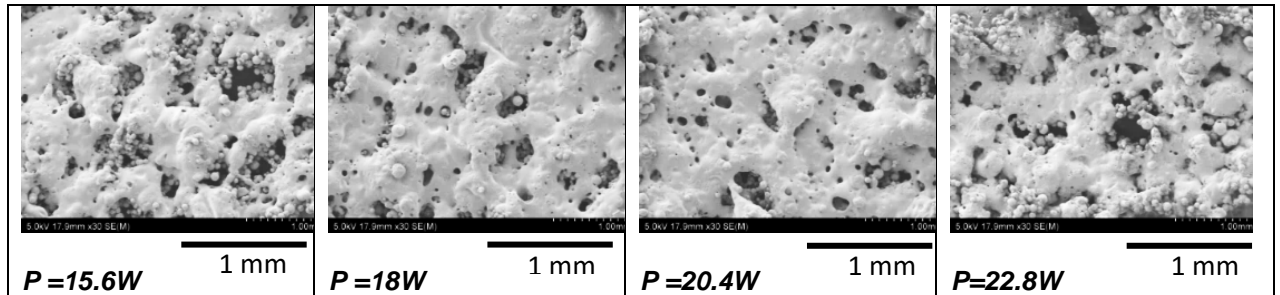
minimum energy densities necessary to achieve sufficient inter-particle coalescence in PMMA plus β -TCP powder composites are evaluated to be in the range from 0.03 J/mm² to 0.05 J/mm². The laser power and scan velocity levels for the initial trials reported next are selected satisfying this basic requirement.

5.3 Initial experiments and results

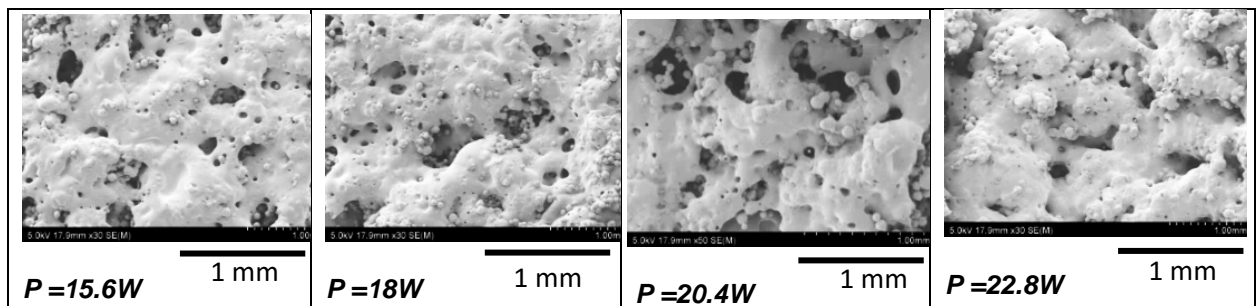
PMMA- β -TCP composite materials with varying compositions; 5% β -TCP/ 95% PMMA, 10% β -TCP/ 90% PMMA, 15% β -TCP/ 85% PMMA, 20% β -TCP/ 80% PMMA are evaluated, with particle sizes at 5 to 10 μ m (β -TCP) and 70 to 100 μ m (PMMA). Initial sintering trials on single layer test samples are produced for 10% β -TCP/ 90% PMMA with varying laser power and scan velocities from 250 to 500 mm/s and 13 to 24 W respectively. Franco and Luca. studied the sintering depth and height of polyamide and phenolic coated sand following single-pass laser scanning and showed that appropriate energy densities are to be employed for proper sintering [112]. Williams and Deckard. investigated the height and depth of the single pass sintered powders and ascertained that a certain minimum power is indispensable to induce sintering, while laser scan speeds exceeding certain limits result in poor sintering [133]. The energy density levels in these initial trials are based on the results of the thermal analyses of the previous section.



(a) Laser scan speed: 508 mm/s



(b) Laser scan speed: 381 mm/s



(c) Laser scan speed: 254 mm/s

Figure 5.3 SEM Photographs of the sintered single layer with 80% PMMA and 10% β -TCP composite

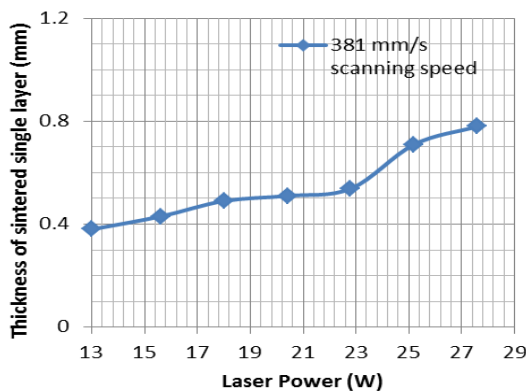
SEM photographs of single layer samples produced using 10% TCP+PMMA composite with varying laser power and scan speed settings are shown in Fig. 5.3. Variation in the density of pores as observed from the SEM photographs is used to evaluate the surface morphologies. While both blends of the composite are successfully sintered, the laser power and the scan speed are found to play significant roles, apart from the composition of the composite material. Each set

in Fig.5.3 corresponds to a specific scan speed setting, while the laser power increases from left to right. The effects of scan speed are similar to observations made by Williams and Deckard [133], indicating very poor inter-particle coalescence at higher speeds, as evident from the coarse structures of Fig.5.3(a). While the laser power interacts with the scan speed, there is however, hardly any improvement with the laser power even at 20.4 W, clearly elucidating the role of sintering time in achieving sufficient inter particle coalescence.

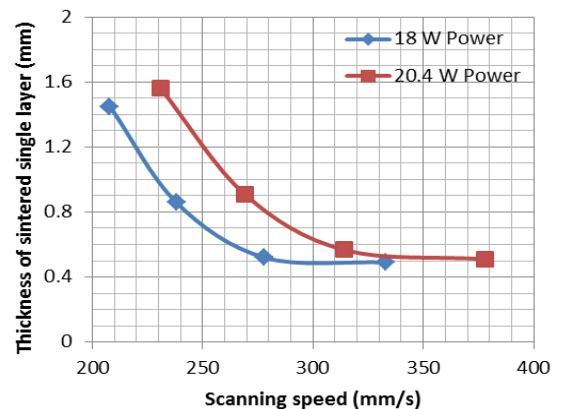
Improved inter particle coalescence is observed in the base matrix material, when the scan speed is reduced to 381 mm/s and 254 mm/s, depending on the laser power variation. With each speed setting, there is also a gradual improvement with increasing power, as the samples show wider areas of PMMA powder sufficiently coalesced to form continuous networks of the matrix holding the β -TCP particles. Again, with any given speed, the base polymer degrades and disintegrates when the power is increased beyond a certain limit. Considering the three cases presented in Fig. 5.3, there is a gradual improvement from case (a) to (c), while the sample with the lowest speed (254 mm/s) and the highest power (22.8 W) exhibited the best results with the PMMA phase coalesced significantly over wide areas. It is also evident that the optimum combination of laser power and scan speed are beyond the limits of these initial trials.

The thickness of the sintered layer also varies with laser power and scan speed settings. The variation of the thickness of single sintered layers is assessed with varying laser power with the scan speed set at 381 mm/s and the results are as shown in Fig. 5.4 (a). The thickness of the sintered layer increased with increasing laser power, as the energy absorption increases resulting in a wider

sintered zone. It is observed that the inter-strand coalescence is poor below 13 W, but the sintering results are good and the layer formation is uniform with laser power varying between 13 W to 35 W. Beyond 35 W, however, the material begins to char and discolour and degrade, emanating smoke and resulting in a disintegrated layer. Evidently, the process works only within certain ranges of constituent parameters. The effects of varying laser scan speed at two different laser power settings on the thickness of sintered samples are depicted in Fig. 5.4(b). Again the effective energy absorption controls the layer thickness, as increasing speed results in decreasing layer thickness for any given power.



(a) Laser power



(b) Laser scan speed

Figure 5.4 Effects of process parameters on critical responses (10% β -TCP composite powder)

Interestingly, the process attributes completely changed, with the material composition; 80% PMMA+ 20% β -TCP. Fig. 5.3 presents the SEM photographs of single layer samples produced with varying power and scan speed settings. It may be noted that the laser sintering behaviour of the material changed entirely with the increased amount of β -TCP. Though there is a certain improvement in the coalesced state from the higher speed case as in Fig 5.5 (a) to the lower scan speed case presented in Fig 5.5(b), in general, the material response to sintering

is poor, perhaps due to the rheological changes of PMMA with increased β -TCP content. With any given speed, the material shows signs of degrading and decolourisation when the laser power is increased beyond 18 W. Probably, the thermodynamics of the process is altered due to the excessive presence of β -TCP phase, in terms of higher energy absorption as the laser scans a given point and subsequent dissipation of the same, resulting in the overheating and degrading of the surrounding matrix phase.

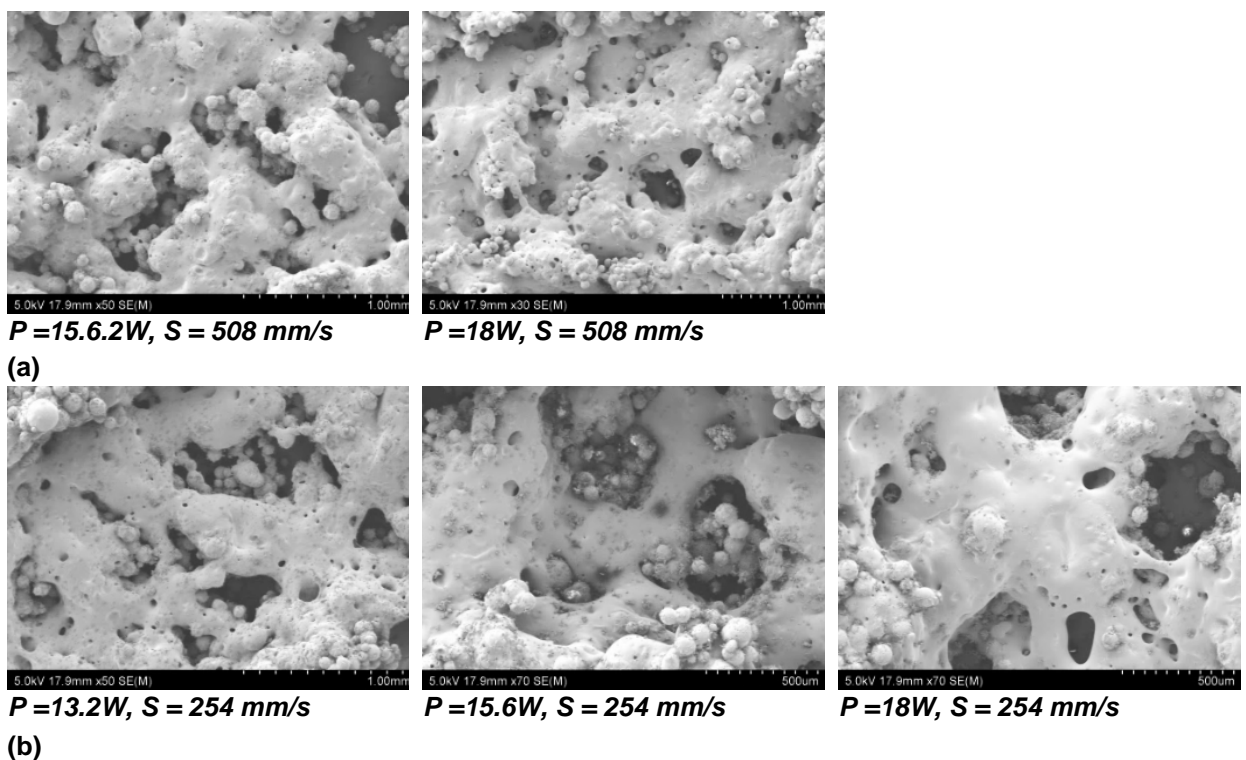


Figure 5.5 SEM Photographs of the sintered single layer with PMMA+20% β -TCP composite powders

5.4 Further experimental trials and surface morphologies

Based on the initial results, further experimental trials are designed considering laser power and scan speed settings closer to the optimum levels. Considering

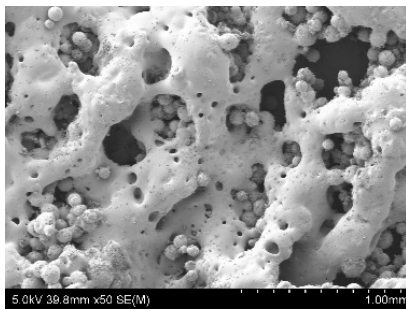
test cases with relatively better sintering results from Fig. 5.3, together with the energy density calculations based on equation 3.1 as mentioned in Chapter 3, four energy density levels are identified as possible conditions for achieving better sintering. Table 5.2 lists the energy density levels identified as the most suitable settings for the PMMA composite with 10% β -TCP.

Keeping the effective energy densities at these four levels, several combinations of laser scan speed and power settings varying within relatively narrow ranges are identified as given in Table 5.2. Experiments are conducted with these parameter settings and single layer samples are produced and SEM photographs of the surface morphologies of the samples are shown in Fig. 5.6. In general, it may be observed that all three samples show similar levels of coalescence and consolidation of the PMMA powder within any given energy density level. However, there is a gradual improvement when moving vertically downwards in any column, as the scan speed is reduced. Overall, the energy density levels 0.14 J/mm^2 and 0.16 J/mm^2 appear to give better sintering results. It was also noted that partial melting and neck formation are noted with the power set below 18 W, while complete fusion made the boundaries of particles indistinguishable when the power used is above 18W, with any of the energy density settings employed. Porosity is observed in all samples, but with the intensities decreasing with increased coalescence across the thin layer.

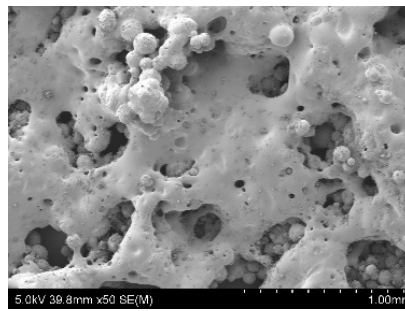
Table 5.2 Experimental condition with specific energy densities and general observations

Energy Density (J/mm²)	Laser Power (W)	Scan speed (mm/s)
0.1	18	333
	20.4	378
	22.8	422
0.12	18	278
	20.4	315
	22.8	352
0.14	18	238
	20.4	269
	22.8	300
0.16	18	208
	20.4	231
	22.8	263

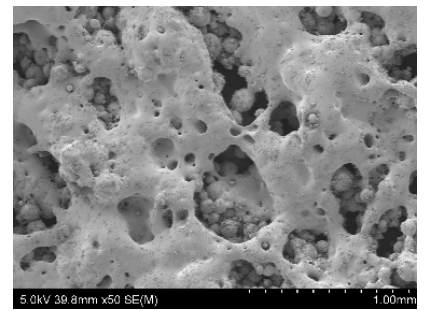
With energy density set at 0.16 J/mm², the particles are sufficiently fused and the normal pore size decreased considerably, indicating significant melting and subsequent inter-particle coalescence and bonding. However, large voids are randomly created probably due to the presence of β -TCP particles increasing the viscosity of the melt pool as well as offering resistance to the melt flow. Rimell and Marquis. observed that with still higher laser power settings, the polymer substrate is likely to go through a physical breakdown of polymer chains, resulting in a lighter material that eventually vaporises [164].



P=18 W, S= 333mm/s

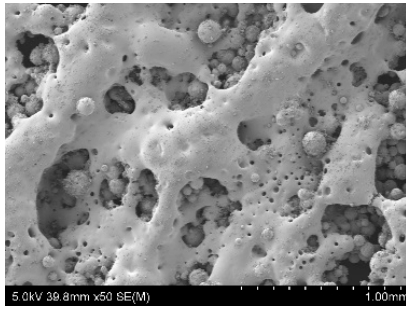


P=20.4 W, S= 378mm/s

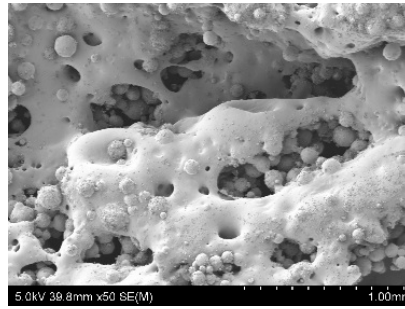


P=22.8 W, S= 422.17mm/s

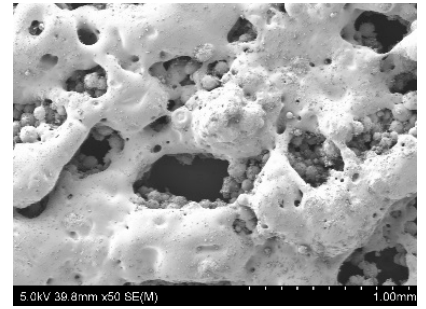
(a) Energy density = 0.1 J/mm²



P=18 W, S= 278 mm/s



P=20.4 W, S= 315mm/s

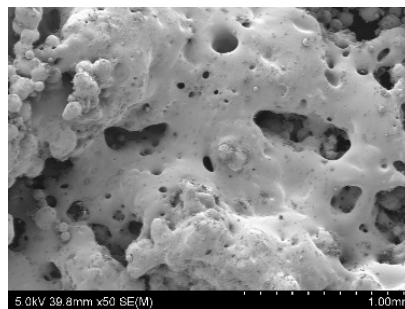


P=22.8 W, S= 352mm/s

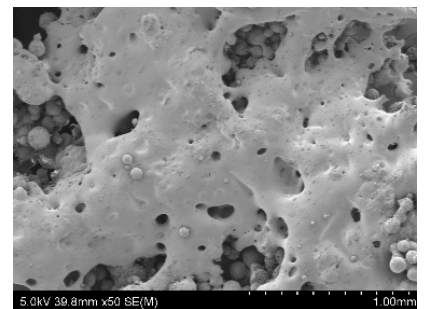
(b) Energy density = 0.12 J/mm²



P=18 W, S= 238 mm/s

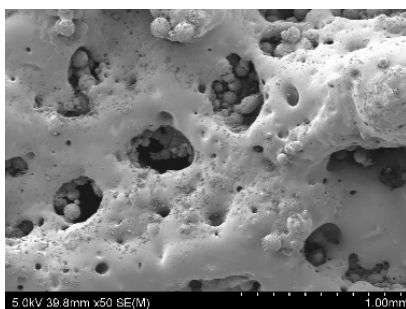


P=20.4 W, S= 269mm/s

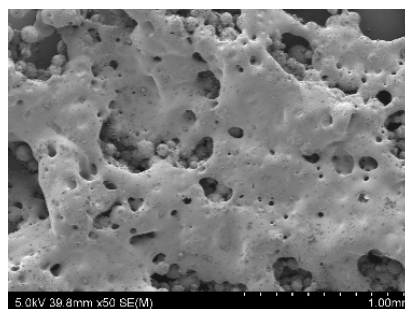


P=22.8 W, S= 300mm/s

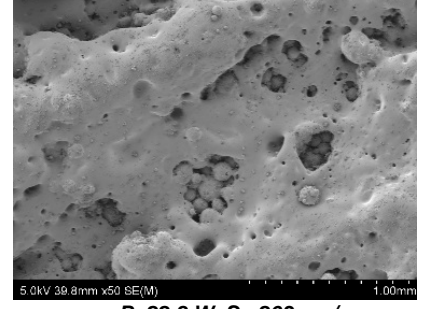
(c) Energy density = 0.14 J/mm²



P=18 W, S= 208 mm/s



P=20.4 W, S= 231mm/s



P=22.8 W, S= 263mm/s

(d) Energy density = 0.16 J/mm²

Figure 5.6 SEM Photographs of sintered PMMA- β TCP composite single layer samples with varying process parameters

5.5 Evaluation of the influences of critical process parameters

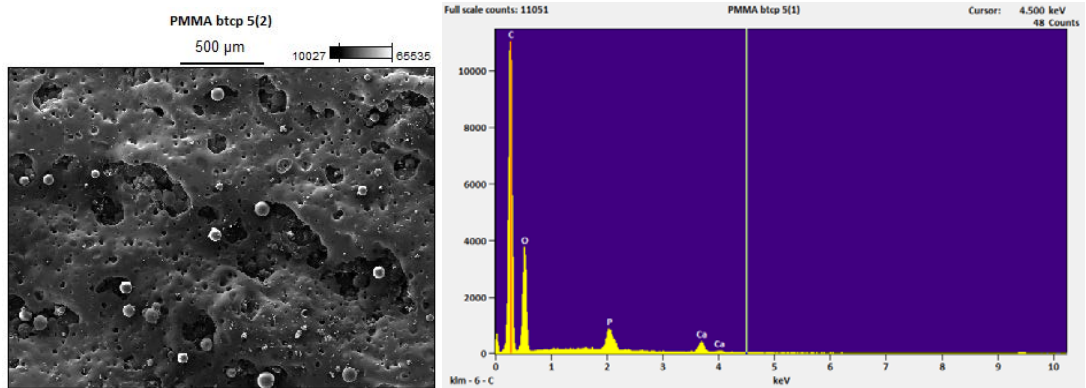
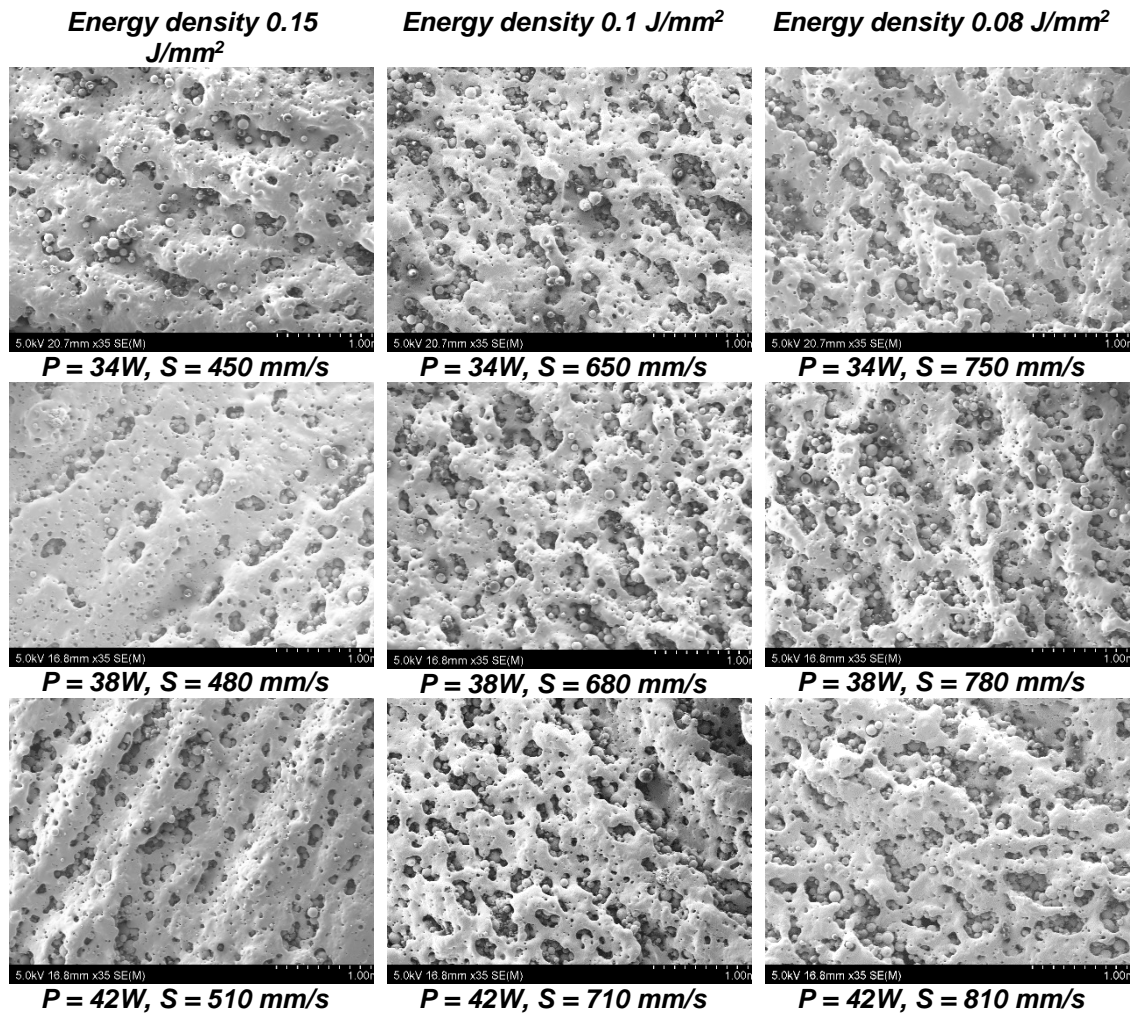
Considering the improvements evident as the laser power is increased with energy density values at 0.1, 0.12, 0.14, and 0.16 J/mm², further sintering trials are conducted shifting the laser power settings to the range 34 W to 42 W and for all PMMA- β -TCP composite materials with varying compositions like 5% β -TCP/ 95% PMMA, 10% β -TCP/ 90% PMMA, 15% β -TCP/ 85% PMMA, 20% β -TCP/ 80% PMMA as listed in Table 5.3. SEM results are presented in Fig 5.7, Fig 5.8, Fig 5.9, and Fig 5.10 respectively. With laser power and scan speed varied within these ranges, three specific energy densities are identified from the initial experiments listed in Table 5.2. Qualitative observations are made based on SEM photomicrographs of sintered single layer samples with process conditions as given in Table 5.3.

Referring to Fig. 5.7, the surface of the sintered sample of 5 % β -TCP/ 95% PMMA for energy density 0.08 J/mm² showed a much bigger heat affected zone when increasing the laser power from 34W to 42W. The samples gradually turned from brown to black and at the end dissipating a black smoke, indicating polymer decomposition. Apparently, the base polymer is carbonised in the presence of β -TCP, as the power input is gradually increased. However, the particle fusion and the inter-strand coalescence are better at relatively lower power settings. As in Fig. 5.8, when the β -TCP level is increased to 10%, drastic changes occurred in the sintered specimens as the porosity levels increased and at higher power, the surfaces looked quite irregularly shaped. With further increase in β -TCP to 15% and 20% as in Figs 5.9 and 5.10 respectively and processed at 0.08 J/mm², the pore sizes also increased clearly indicating lack of fusion between adjacent laser

scan lines and insufficient formation of the sintered layer. The presence of β -TCP makes the polymer to agglomerate in clusters, along each scan line. The 20% β -TCP sample actually caught fire at 42 W laser power, while the 34W and 450mm/s power and speed setting worked fine.

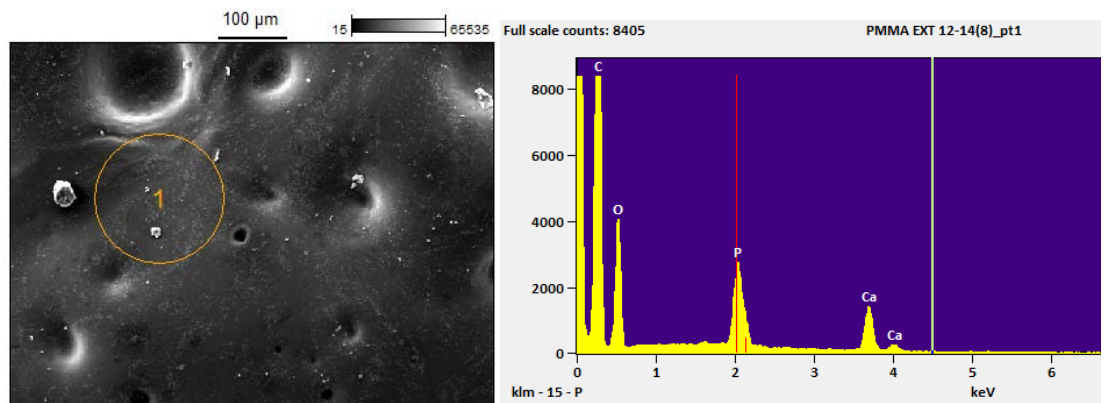
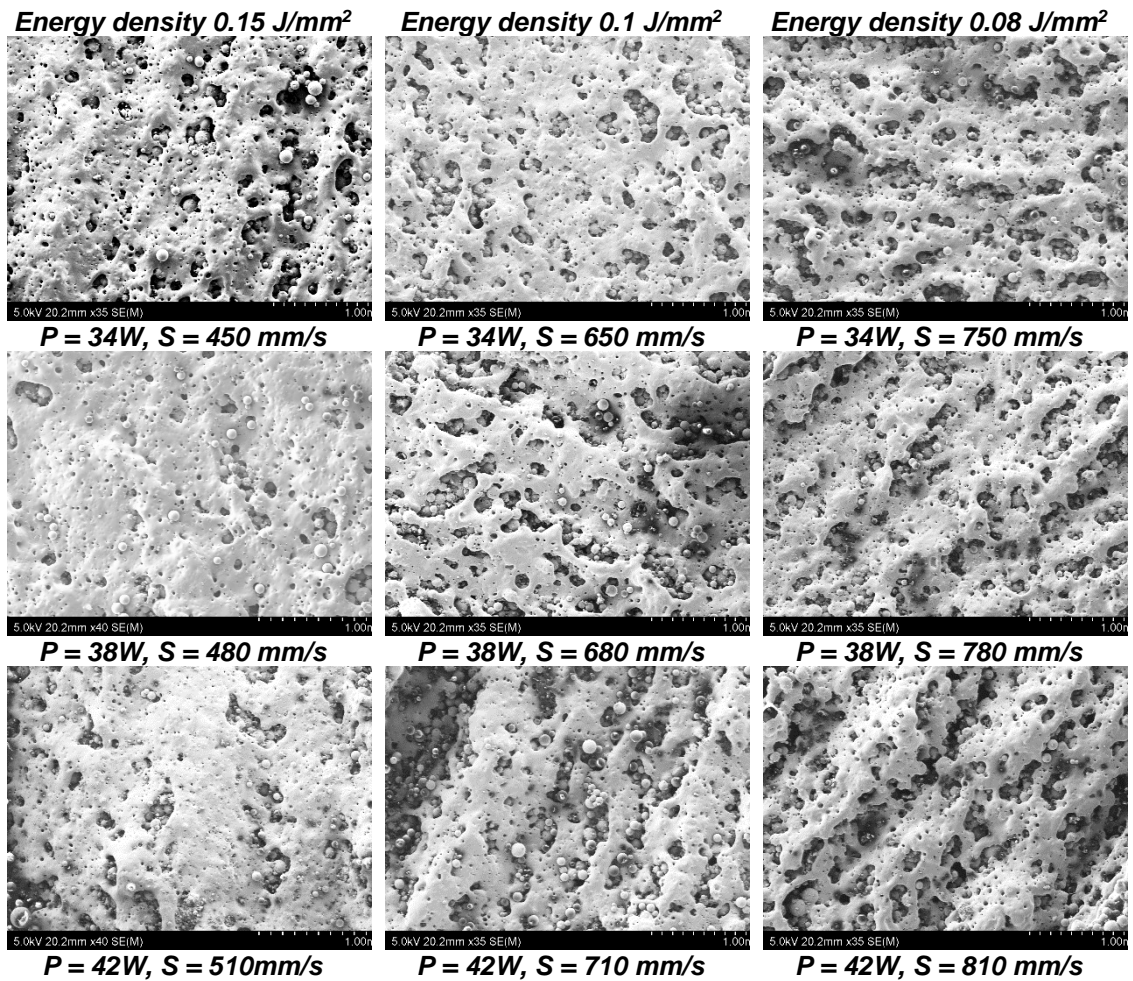
Similar observations were noted with the 0.1 J/mm² energy density as the heat affected zone increases with increasing energy density and the specimens begin to decompose at higher power settings, which is also much more pronounced at higher β -TCP levels. The surface colour of the sintered sample gradually becomes brown and the sizes of pores increase. Though inter particle sintering is reasonable at lower power settings, there is still lack of fusion between the lines though the results are better compared to specimens sintered at 0.08 J/mm² with 5% and 10% of β -TCP. With the energy density at 0.15 J/mm², the lower power range resulted in improper fusion between adjacent scan lines while higher laser power settings resulted in better inter-strand fusion. The porosity levels and surface irregularities increased with higher β -TCP contents, at above 15 % and 20%, while the 20% of β -TCP resulted in excessive particle agglomerations.

Apart from the surface morphologies, the selected specimens are also subjected to EDS analysis in order to have an initial impression of the possible changes in the polymer chemistry. The EDS results presented for selected cases in Figs 5.7 to 5.10 confirm the presence of elements as expected of the components of the polymer composites. For examples, the weight percent of calcium in each case is close to the actual amount of β -TCP added. These observations indicate no significant degradation occurring due to the thermal variations induced from laser sintering.



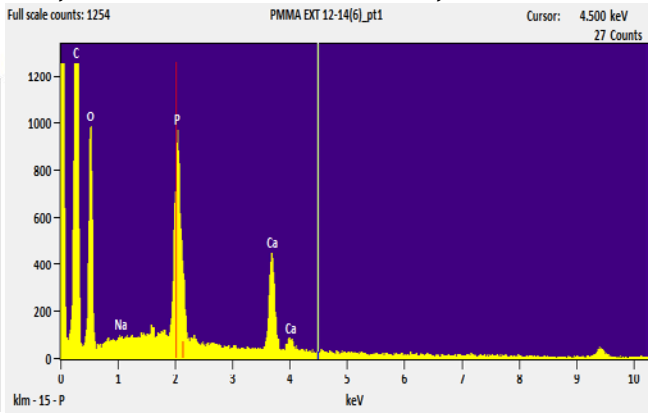
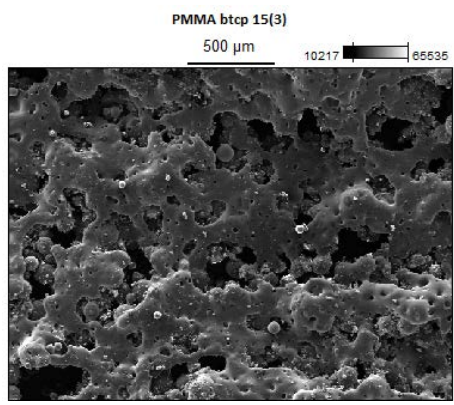
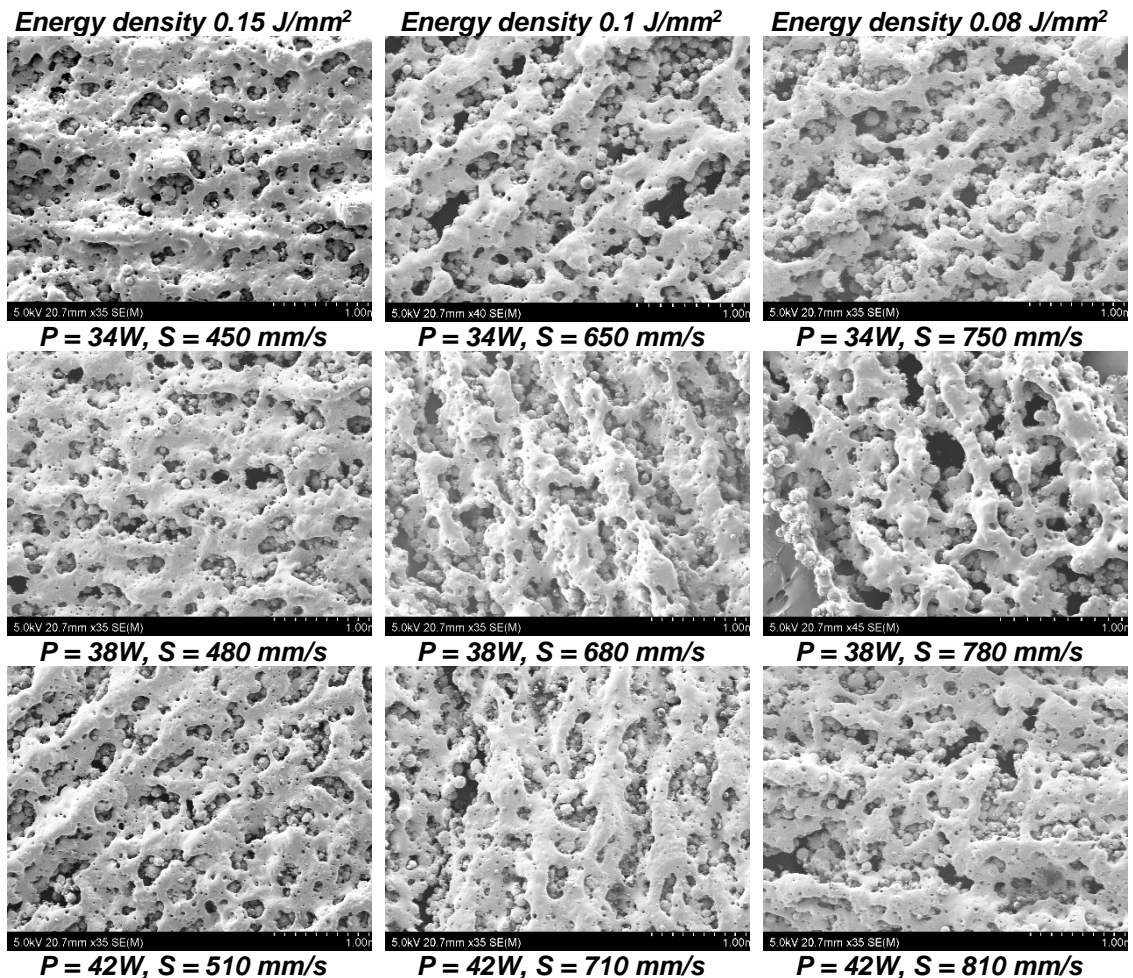
Element Line	Net Counts	Weight %	Atom %
CK	77960	59.80	69.41
OK	25210	30.79	26.83
PK	8792	4.76	2.14
Ca K	4517	4.65	1.62
Total		100.00	100.00

Figure 5.7 SEM Photographs of sintered 5% β -TCP/95% PMMA composite single layer samples with varying process parameters



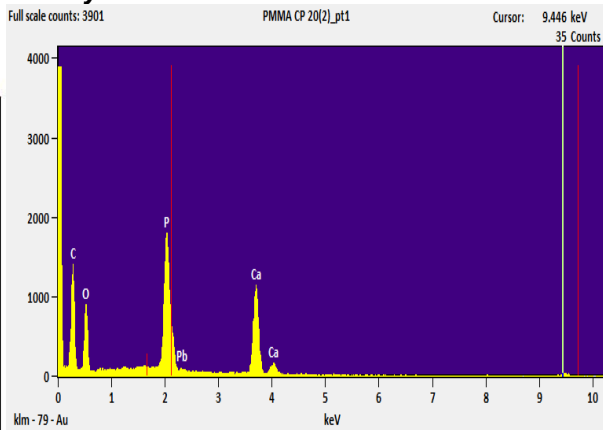
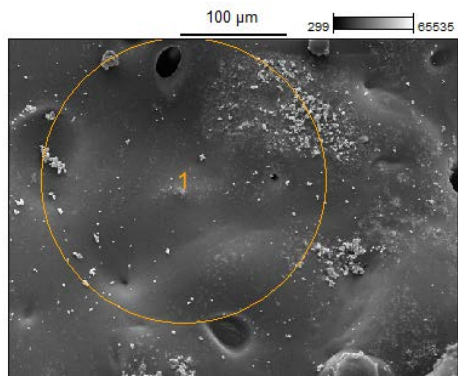
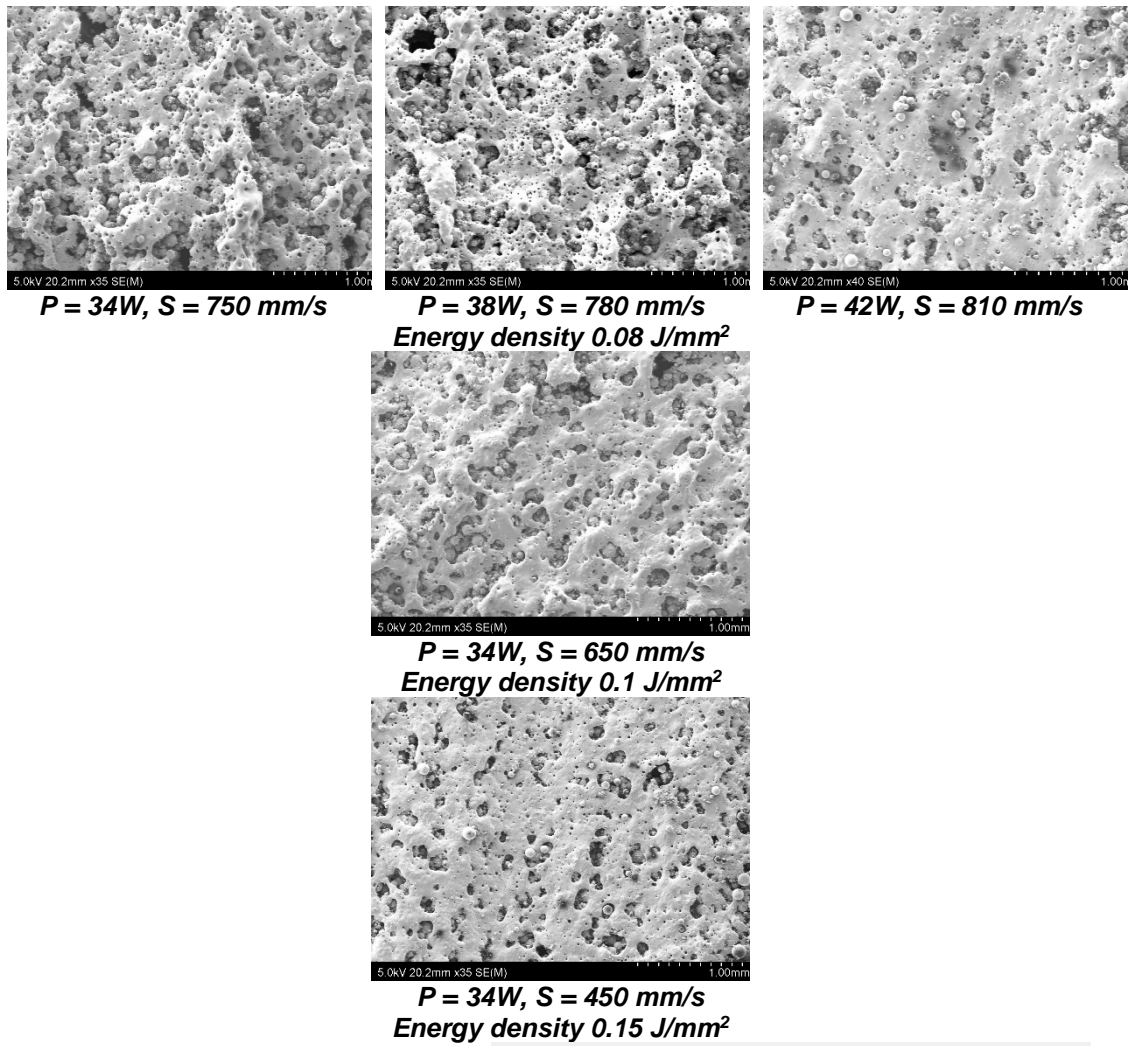
Element Line	Net Counts	Weight %	Atom %
C K	98970	54.65	68.30
O K	29412	24.12	22.63
P K	30348	10.12	4.90
Ca K	17504	11.12	4.16
Total		100.00	100.00

Figure 5.8 SEM Photographs of sintered 10% β -TCP/ 90% PMMA composite single layer samples with varying process parameters



Element Line	Net Counts	Weight %	Atom %
C K	46041	46.92	64.02
O K	16609	23.35	26.76
P K	11118	14.77	3.81
Ca K	10740	14.78	5.41
Total		100.00	100.00

Figure 5.9 SEM Photographs of sintered 15% β -TCP/ 85% PMMA composite single layer samples with varying process parameters



Element Line	Net Counts	Weight %	Atom %
C K	9122	43.03	59.85
O K	3897	20.46	23.45
P K	8919	18.89	10.19
Ca K	3864	17.62	6.51
Total		100.00	100.00

Figure 5.10 SEM Photographs of sintered 20% β -TCP/ 80% PMMA composite single layer samples with varying process parameters

Table 5.3 Critical laser parameter

Energy Density (J/mm ²)	Power (W)	Speed (mm/s)
0.08	34	750
	38	780
	42	810
0.1	34	650
	38	680
	42	710
0.15	34	450
	38	480
	42	510

Ideally, bone implants must possess an interconnected open-pore geometry and microstructure, permitting cell in-growth and reorganization during the in-vitro phase [92]. Evidently, the porosity levels of all sintered test pieces varied with laser power and scan speed settings implying that the porosity of β -TCP+PMMA composite parts can be controlled by using appropriate energy settings, while achieving the necessary other properties. A number of other parameters such as scan space, scan pattern, beam spot size, and layer thickness may also control the porosity levels in sintered specimens of the composite material, as these parameters will also influence the energy imparted to the powder surface as also observed with other material systems [140].

Based on these tests, the most promising laser power range is identified to be around 38 W, while the laser scan speed could be varied at 480 mm/s, 680 mm/s, and 780 mm/s, so as to achieve the three energy density settings as listed in Table 5.3. The surface morphologies indicate waviness, due to the interaction time between the laser beam and the powder particles. The presence of the relatively smaller β -TCP particles adversely affected the plastic flow and perhaps the liquid as well as the solid state sintering. While the level of sintering within the

layer deteriorates with increasing scan speed, the 5% and 10% β -TCP cases show better sintering compared to the 15% and 20% cases.

Further, the porosity level within the polymer matrix also increased with increasing β -TCP as shown in Fig. 5.11. The number of pores as well as their sizes increased with increasing β -TCP. While the physical size variations between the particles of the two constituents could be a plausible cause, it is mainly the thermally inactive β -TCP absorbed within the plasticised PMMA and the consequent reduction in the viscous flow of the plasticised material that could have caused this loss of coalescence. An optimum appears to exist at higher energy density levels, and within the lower levels of β -TCP, for which the intra-layer coalescence is improved as shown in Fig. 5.7 to Fig 5.10. These observations clearly elucidate that the surface morphology and the pore size can be modified by varying the laser parameters together with the composition, allowing for controlled biological responses required in bio-medical applications. This surface porosity will provide the required topology for cell ingrowth into implant and the β -TCP helps with the osteoconductivity.

However, uncontrolled porosity is also possible under certain conditions. First, inadequate energy levels resulting from either too low power or too high scan speed settings may lead to poor inter-particle coalescence and consequent sparsely connected grain structures resulting in uncontrolled porosity levels, as evident from Fig. 5.12 (a). Secondly, excessive laser energy levels can result in extremely high temperatures leading to polymer pyrolysis, which manifests itself in increased porosity levels [165]. Further, with excessive energy input, gases are trapped in the diffused material matrix, driven by the dissolution occurring under

the Laplacian excess bubble pressures according to Henry's Law [26], especially as the viscosity of the matrix decreases. This is evident in regions around closed pores on sectional areas of specimens as shown in Fig. 5.12 (b). With increasing temperature, bubbles also increase in size due to pressure and viscosity changes [92]. Eventually, gas pickup, bubble formation and growth and possible ruptures due to localised explosions give rise to uncontrolled porosity levels depending on laser power and scan velocity settings. As the PMMA matrix goes through these transformations, the β -TCP particles are in the middle of all this upheaval, generally retarding the freedom of movement, but specifically resulting in relatively lesser viscosity levels. Consequently, the uncontrolled porosity levels due to gas pickup and bubbling are relatively lesser in specimens sintered using PMMA+ β -TCP composites compared to pure PMMA samples for the same laser settings.

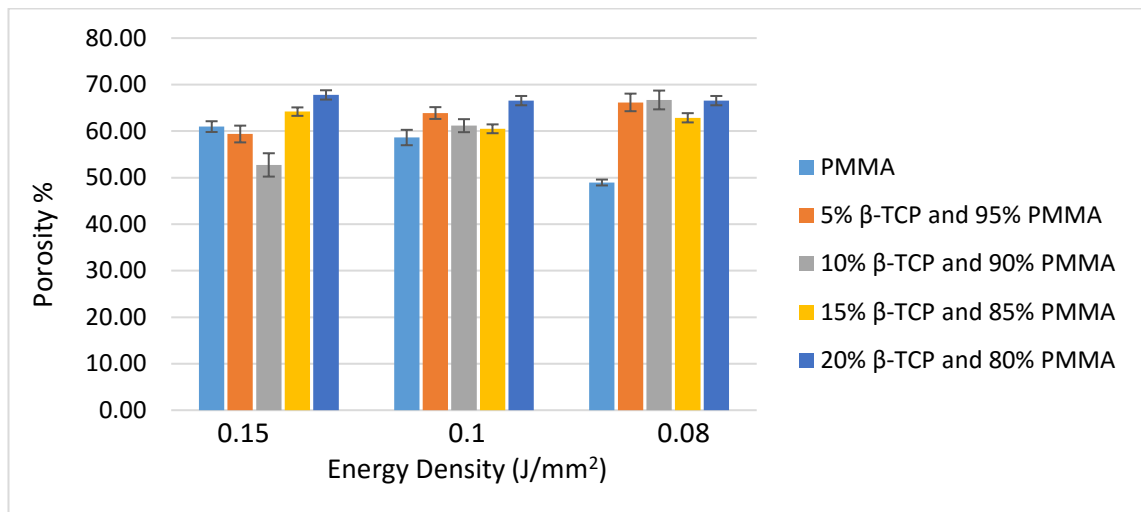
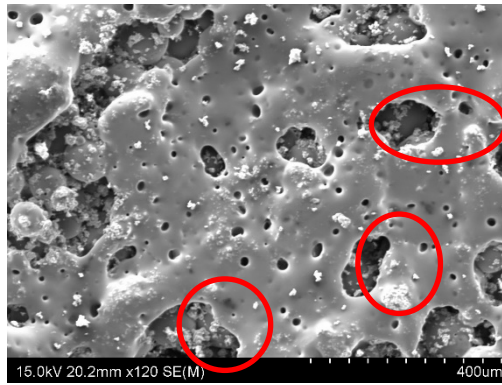
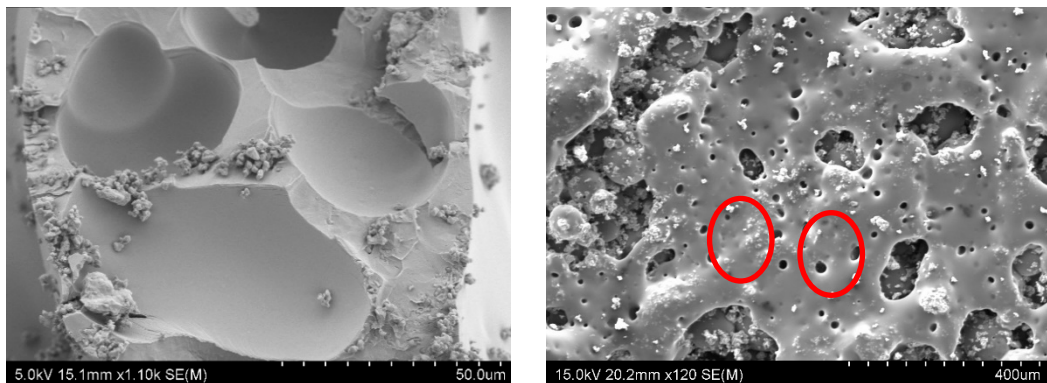


Figure 5.11 Percent porosity variation with varying amounts of β -TCP



(a) Uncontrolled porosity resulting from insufficient melting and fusion



(b) Porosity due to gas pickup

Fig. 5.12 Uncontrolled porosity in sintered samples

5.6 Dispersion of β -TCP particles in the laser sintered PMMA matrix

The dispersion of β -TCP particles and the consequent composite properties vary with particle size and the overall composition [166]. In this case, the PMMA serves as the biocompatible base matrix while β -TCP provides the required bioactivity. It is beneficial, if β -TCP particles are dispersed on the surface of the sintered samples to promote the biological tissue interaction when used as implants or scaffolds for tissue engineering. Fig. 5.13 presents the SEM photographs depicting the dispersion of β -TCP particles with varying process and material conditions.

As evident from Fig. 5.13(a), with 10% β -TCP composite, the formation of the base matrix layer improves as the laser power is increased with a given scan speed, reaching optimum quality levels at around 42 W. With this, the PMMA phase is uniformly sintered and fused into a smooth flat layer and the relatively light β -TCP particles float and segregate over the surface. When multi-layer samples are generated, this process is likely to continue, with β -TCP particles occupying the inter-layer regions. With further increase in power, at around 45 W, the PMMA layer appears to be bubbling and undulating, and often rupturing, but the β -TCP particles are still segregated over the surface. This dispersion of the β -TCP particles over the surface of the sintered part is expected to increase the bioactivity and the osseointegration [167]. According to Kasemo and Lausmaa. [130], biological tissues interact mainly with the outermost atomic layers of an implant. For bone growth or to induce osseointegration, the surface of the implant must be conductive, providing direct structural and functional connections between ordered living bone and the surface of a load carrying implant, regardless of implantation site, bone quantity and quality etc.

However, the situation is completely changed with the 20% β -TCP composite, as depicted in Fig. 5.13(b). While sintering and getting a reasonable sample is difficult, even with the few samples generated, the particle dispersion mechanism appears to have changed completely. The β -TCP particles are fully covered by the PMMA matrix, and the general structure of the layer is very irregular. Apparently, the thermal behaviour of the material system appears to have changed in the presence of excessive β -TCP, presumably due to increased absorption of energy as the laser scans a given point and subsequent release of the same eventually, resulting in plausible overheating of the PMMA powder.

Further, there is increased agglomeration of β -TCP particles with increased content as against a uniform dispersion of the particles several microns apart as in the case of the lower β -TCP case.

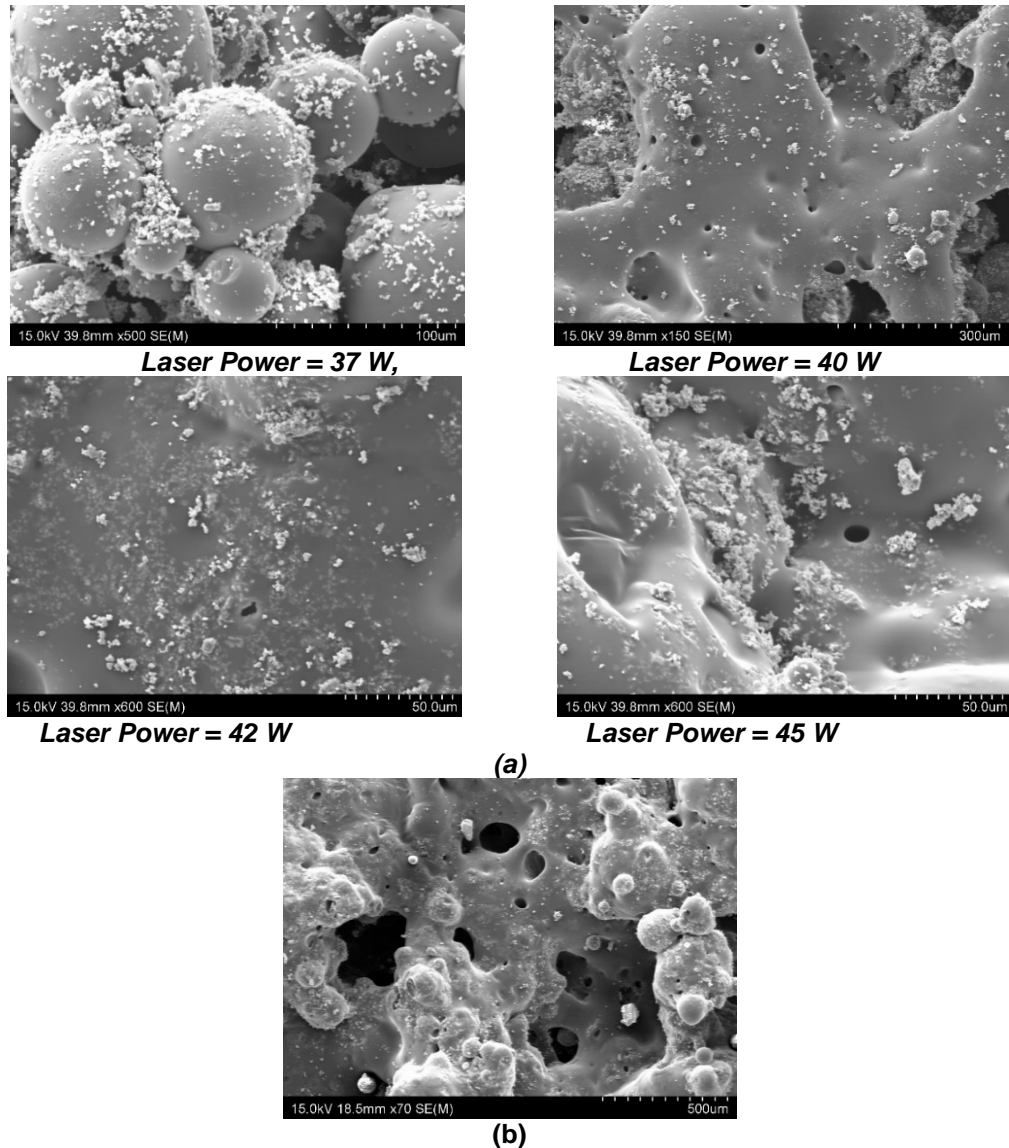


Figure 5.13 SEM photo graphs of sintered layer with (a) 10 % β -TCP and (b) 20 % β -TCP particles

5.7 Cross-sections of the sintered samples

The nature of dispersion of β -TCP particles and the possible agglomeration within the polymer matrix play major roles in determining the final properties of the

composite material resulting from laser sintering. Due to incomplete dispersion, a low content of relatively large, unbroken agglomerates can have destructive effects on certain mechanical properties such as tensile and impact strengths and elongation at break [168]. SEM images of the fractured surfaces of the sintered PMMA+ β -TCP composite layers presented in Fig. 5.14 show significant variations. The composite powder consisted of agglomerates of β -TCP adhering to PMMA powder. The SLS process, being solely driven by the reduction of surface energy of the base polymer, is unable to overcome the inter-agglomerate attractive forces and results in a mottled microstructure with alternating regions and random distribution of the polymer matrix and β -TCP for a given set of process parameters. Dispersion of the agglomerates depends on their initial dimensions and the mechanism by which they are incorporated into the polymer melt. In the current case, PMMA and β -TCP powders are mechanically mixed and sintered resulting in several agglomerates of β -TCP particles interspersed in the PMMA matrix. The cross-sections show large pores and the dispersion of the β -TCP particles along the boundaries. Comparing the results of Fig 5.14 (a) and (b), it is evident that the higher the β -TCP content, the more the agglomeration of the filler particles along the boundaries of pores, resulting in relatively weak structures.

Scaffolds must possess interconnected open pore geometries and microstructures permitting cell ingrowth and reorganization during the in-vitro phase, providing the necessary space for neovascularization from the surrounding tissues in-vivo [169-171]. Surface and cross-sectional morphologies of laser sintered PMMA+ β -TCP composite specimens evaluated in the current research ascertained the presence and controlled variations of porous structures

with composition and process parameters. While the presence of β -TCP altered the responses of PMMA to laser processing, detrimental effects are observed with excessive amounts. It is evident that controlled sintered structures and mechanical attributes can be obtained through laser sintering of PMMA+ β -TCP composites, but the process parameters and composition need to be optimised considering in-vitro and in-vivo studies.

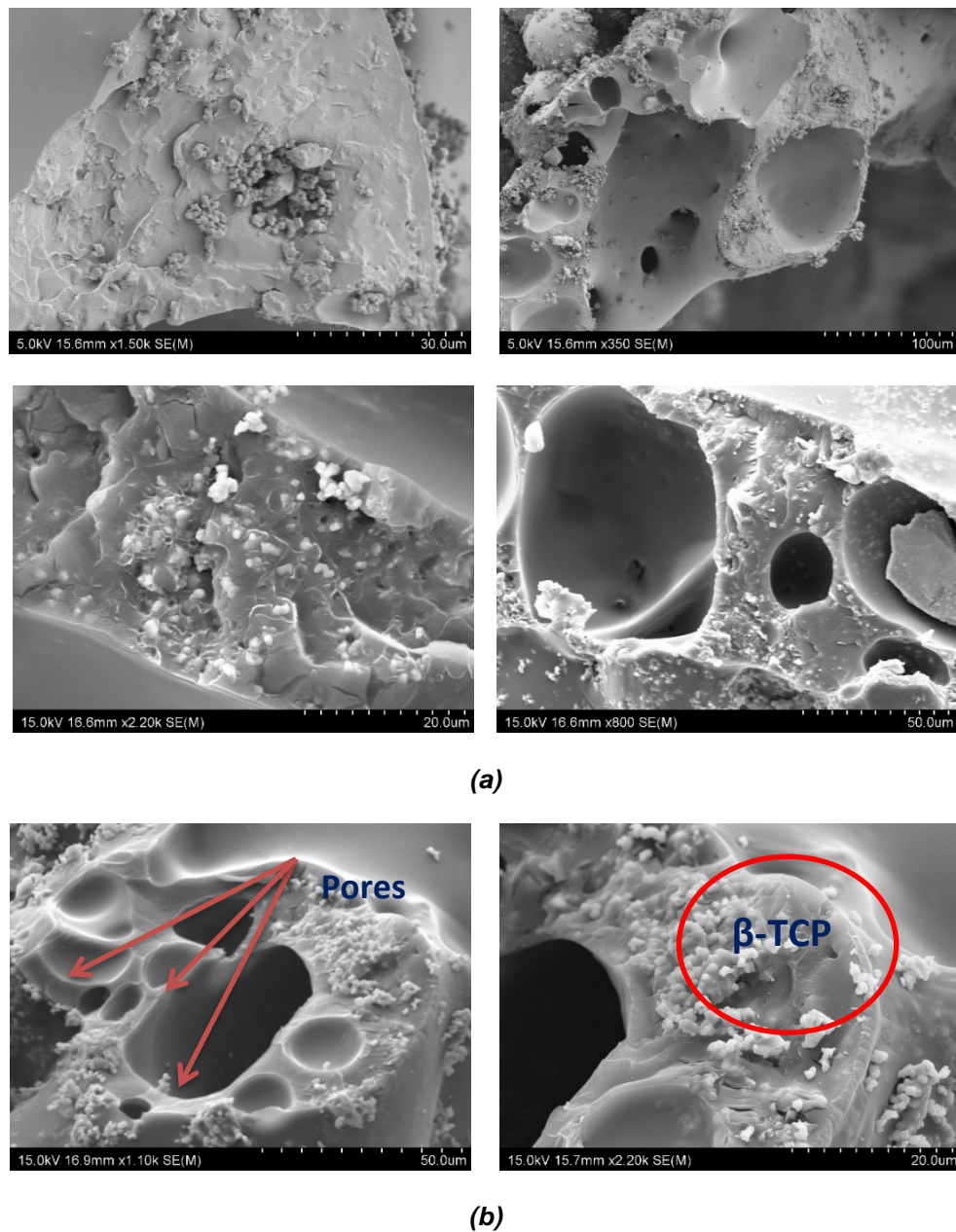


Figure 5.14 SEM micrograph of the cross- section of sintered layer (a) 10 % β -TCP and (b) 20 % β -TCP composites

5.8 Tensile testing

The Intron 5567 system is used for the tensile testing, with load range from 0 to 200N, gauge length 50mm, speed 12.50mm/min, and distance between the grips at 125mm. Thin film tensile tests are conducted as per the ASTM standards, based on the single layer samples sintered with varying process conditions and compositions. The variation in the Young's Modulus values is in similar lines to the porosity variation, as shown in Fig. 5.15. The 20% β -TCP case resulted in a lower elastic modulus, compared to the 5% β -TCP case, as the porosity levels increased resulting in insufficient consolidation within the layers. Similar results were noted by Beruto *et al.* [172] for TCP/PMMA composites, as the tensile strength significantly decreased with the presence of the bio ceramic component. From the specimens it is observed that the bio ceramic agglomerates during the sintering process, and there is a lack of fusion between adjacent laser scan lines. Considering the thermomechanical nature of consolidation, these changes are plausibly resulting from varying thermal conditions emanating from the varying amounts of β -TCP. This will be verified next considering the thermal evaluation of the powder materials based on TGA analysis and numerical and experimental assessment of temperatures along the laser scan lines.

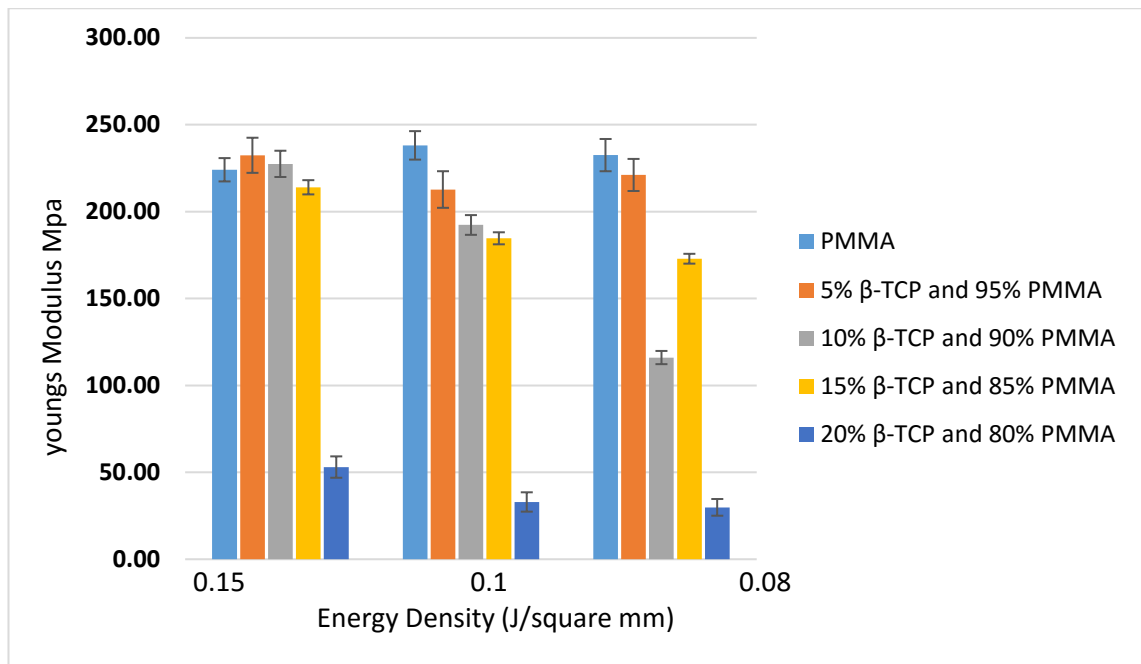


Figure 5.15 Variation in the Young's Modulus with varying amounts of β -TCP

5.9 Thermal Analysis of PMMA+ β -TCP composites

5.9.1 Thermo-gravimetric analysis

Thermo-gravimetric analyses of samples of pure PMMA and PMMA+ β -TCP composites of varying compositions are conducted using the same equipment as above as described in Chapter 3. The results in the form of thermo-gravimetric curves are presented in Fig. 5.16. The mass loss ratios are plotted against temperatures achieved through specific heating rates at 10⁰C per minute for samples of varying compositions. Evidently, pure PMMA begins to degrade at around 212 ⁰C. Pure PMMA continues to degrade with the increase in temperature almost through an uninterrupted smooth curve as depicted in Fig. 5.16 with 45% of degradation achieved in the temperature range from 300 to 350 ⁰C. Subsequent heating up to 400 ⁰C led to 100 % degradation. Three

degradation reactions were noted earlier; initiation due to scission of weak links and random chain scissions and final degradation due to propagation into monomers [163]. When thermally treated, PMMA degrades predominantly by the reverse of the polymerisation process, with a first order reaction rate over time [173].

With the addition of β -TCP, the temperature at which degradation initiates is slightly increased, though to varying degrees with the variation in the amount of β -TCP. Generally, the polymer composite powders began deteriorating at around 240 °C followed by a gradual loss of mass. However, in all the cases with β -TCP, there is a fluctuation in the mass loss vs temperature curve, which is probably due to the continuous variation in the composition of the residual sample. Apparently, it is the PMMA phase which is degrading and getting lost with heating beyond 240 °C, while the β -TCP remains undisturbed and begins to form the composite rich in the ceramic phase. This variation in composition together with the variations in the heat capacities probably caused the fluctuations in the thermo-gravimetric curves obtained with time-dependent variations in temperature. Variations in thermal stresses in the composite powders could have also contributed to these fluctuations [163]. These fluctuations in the temperature could have caused first order degradation mechanisms to be at play with relative ease, probably leading to lesser activation energies in the case of the polymer composite powders. Eventually, at around 400 °C, the pure PMMA sample has almost negligible mass, indicating complete degradation and loss of the polymer. However, the composite powders have residual masses almost close to the amounts of β -TCP contents present, indicating that the ceramic phase remains unaffected even after heating up to 400°C.

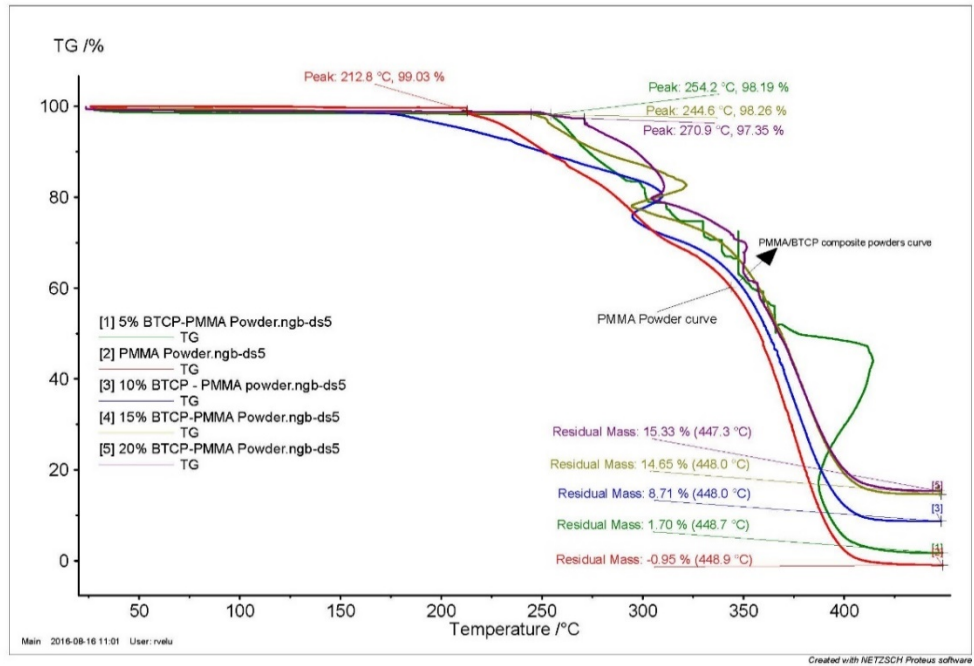


Figure 5.16 TGA results of PMMA and PMMA/β-TCP composites powders

5.9.2 Temperature variation along laser scan lines

Finite element simulation

Melting and re-solidification of powder particles leads to the formation of a layer and the inter-layer bonding, in order to create functional parts through the SLS process. Thermal phenomena play dynamic roles in achieving a desired sintering depth, while laser beam radius, laser intensity, scan velocity etc. become critical parameters. In the current case, the coexistence of two different material systems adds further complications and makes the thermal modelling more complicated together with other physical processes involved. The finite element method is used first to simulate the thermal field conditions for a single track laser scanning over the powder bed, evaluating the transient temperature variation at different points along the scan line.

Kolossov *et al.* considered the SLS transient temperature variation as a 3D non-linear heat transfer problem and the heat conduction model is expressed using the principle of conservation of energy [174]. This relates the local density of the powder bed during sintering, volume of the powder bed in relation to its surface, heat conduction relating specific heat capacity and position in the space and heat flux density of the laser per area. Thermal conditions such as local effective thermal conduction coefficient, convection heat exchange coefficient, pre-heat temperature and emissivity of powder are needed to achieve the conservation of energy. Considering a CO₂ laser beam as the heat source with a 10.6µm wavelength, the laser heat flux can be calculated using equation 5.1 [175].

$$I(r, w) = (1 - R_e) I_0 \exp\left(-\frac{2r^2}{w^2}\right) \quad (5.1)$$

Where r is radiation distance; R_e is the reflectivity of powder surface; w is the characteristic radius; I_0 is the maximum light intensity, which is decided by laser power and characteristic radius of laser.

The finite element simulation is carried out using the ANSYS academic research module, considering a 2D domain of 50mm X 20mm dimensions using the four-node quadratic element (PLANE55). The effective thermal conductivities and the densities of various compositions of PMMA+β-TCP are determined based on the weight percent ratios. The following are some of the other assumptions:

- The input heat flux is treated as internal heat generation within the powder layer. Gaussian distributed heat flux is adopted for the heat flux from the laser beam which is given over the powder layer.

- The finite element discretisation is done in such a way that the heat flux due to laser irradiation could be expressed per element, for each location, where the element size is equal to the laser beam diameter 540 μm
- The powder layer is considered to be homogeneous and continuous
- The powder bed temperature is maintained at 90°C and locations where the temperature goes beyond the melting temperature are considered to be sintered.
- The effective thermal conductivity of the powder layer is used for simulation, which incorporates solid thermal conductivity for various volume fractions of the composite material.

The temperature distribution at a particular location during the laser movement over the powder bed is shown in Fig. 5.17. The red spot denotes the laser sintering location, while the temperature distribution indicated the heat affected zone. The time dependent variation in the temperature at a location 20 mm from the start of the laser scan track is shown in Fig. 5.18, for different compositions of the PMMA+ β -TCP composite. Evidently, the higher the β -TCP content, the slower the temperature rise as well as the lower the peak temperature. The thermal conductivity of the bio-ceramic filler material being much higher, the absorbed heat is quickly transferred, resulting in a lower effective temperature. This will in turn affect the viscosity and the liquid and solid state sintering aspects of the powder bed.

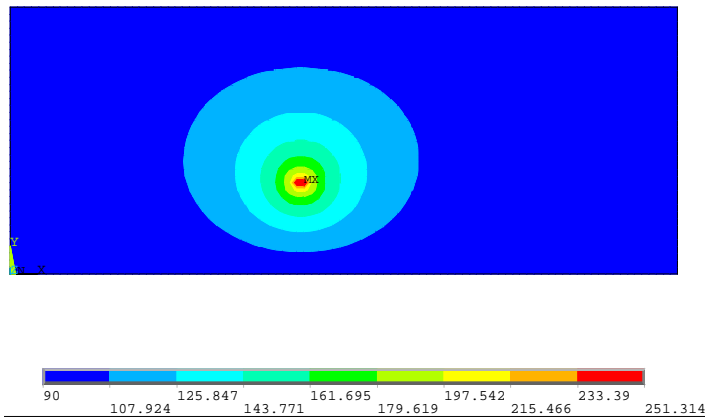


Figure 5.17 Temperature distribution at a specific time $P = 38W$, speed = 780mm/s

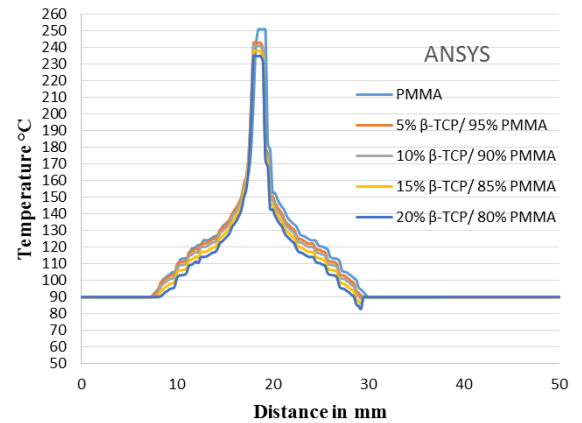


Figure 5.18 Time dependent temperature variation at 20mm with varying compositions

Experimental temperature measurements

An infrared thermal imaging camera is employed for recording the time-dependent temperature variations at different points along the length of a single laser scan line as shown in Fig.5.19. Fig. 5.20 presents the results of these measurements at 10 equidistant points between the limits 20 mm and 50 mm of the laser travel for three different compositions; pure PMMA, 5% β -TCP/ 95% PMMA and 10% β -TCP/ 90% PMMA. The blue line and the orange lines correspond to the locations at 20 mm and 50 mm from the start of the sintering line respectively, while the other lines correspond to the temperature variations at different intermediate points. Comparing the blue lines across the three cases presented in Fig. 5.20, it is clear that the temperature rise at the 20 mm location is considerably delayed with increasing β -TCP content, ascertaining the observations made from the numerical solution.

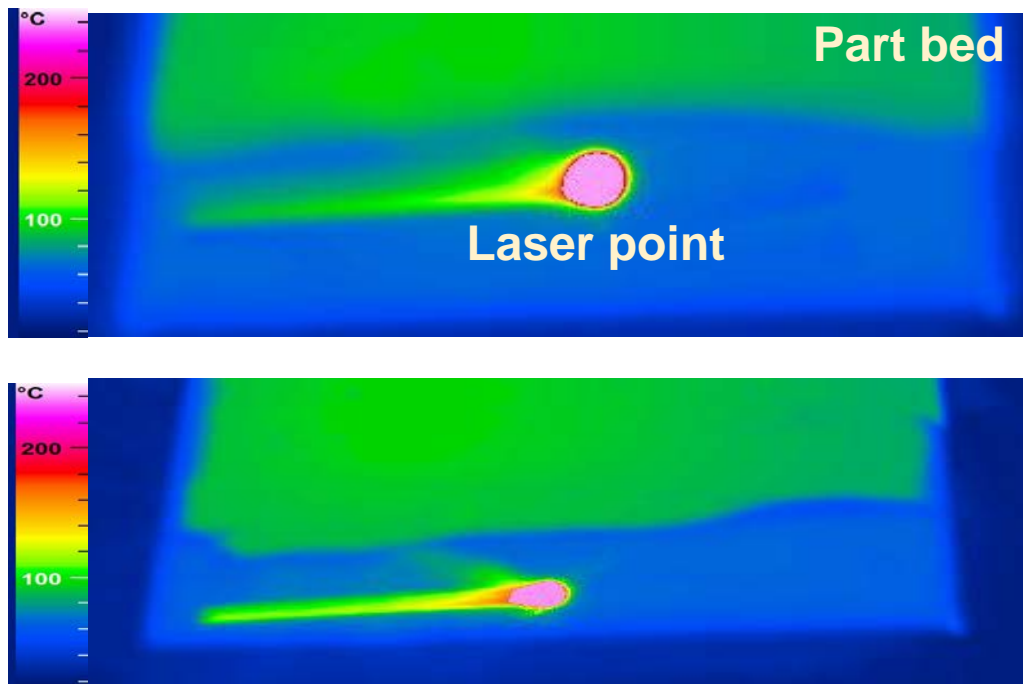


Figure 5.19 Thermal imaging of laser movement

However, a closer observation of the results presented in Figure 5.20 reveals the significant role of the ceramic filler in altering the temperature variations at different points. With the pure PMMA case, each point gets heated up to the maximum temperature at around 248 °C, with almost similar temperature-time profiles. The phase lag between adjacent lines is due to the time difference experienced by the laser, while passing through the successive points. As the β -TCP content is increased to 5% (Fig. 5.20 (b)) and then 10% (Fig 5.20 (c)), it may be noted that there is a significant delay in reaching the maximum temperature for the start point, while there is an accelerated temperature rise at later points. The time delay in raising the temperature at a specific location is in accordance with the numerical results, probably indicating a rapid loss of heat absorbed into the surrounding particles. It may also be due to a loss of heat apportioned into the PMMA phase, as most heat is actually absorbed by the ceramic component with increasing amounts of the loaded ceramic.

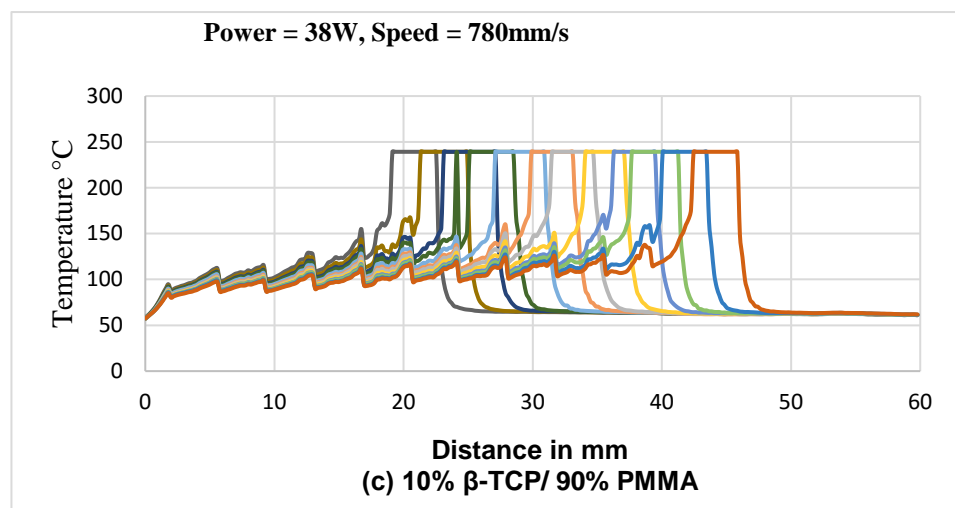
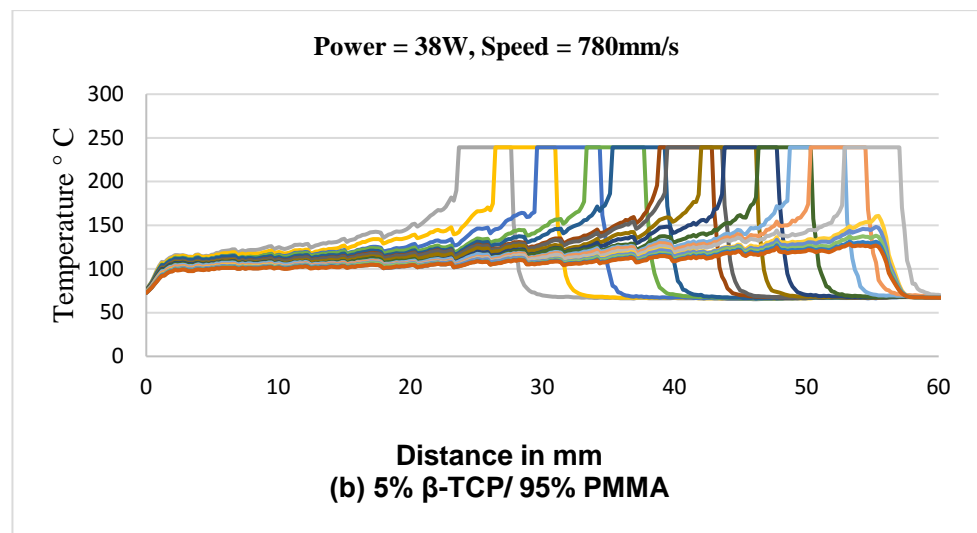
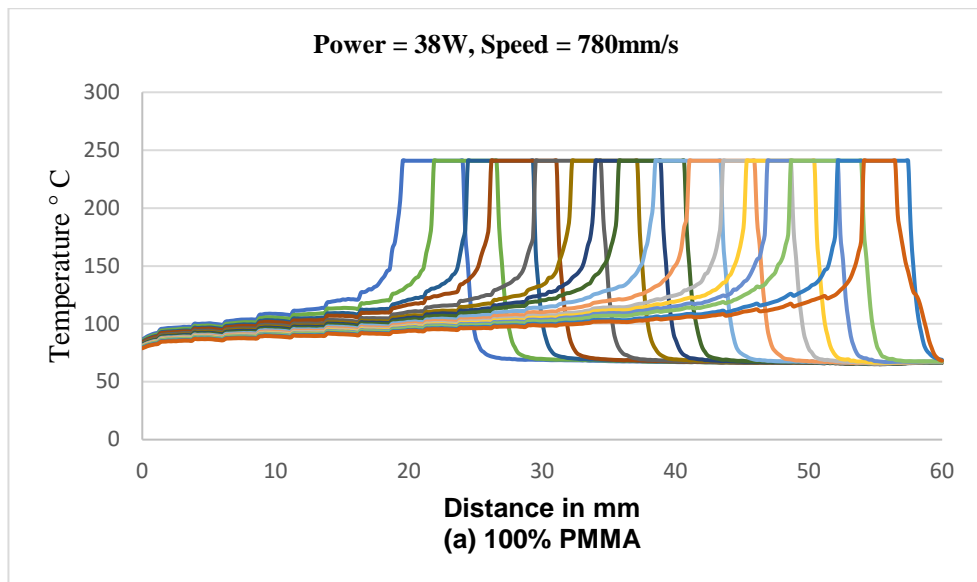


Figure 5.20 Infrared thermal imaging results of the time dependent variation in temperature at different locations for varying compositions

The accelerated temperature rises at subsequent locations and perhaps even before the laser actually reaches them are due to the increased conduction of heat through the powder bed at higher contents of β -TCP. These cycles are associated with corresponding thermal stress changes [176]. While the peak temperature varied from 235–251°C as predicted by the FE model for varying compositions, the experimental results did not show appreciable variation in the peak temperature with composition. However, it is clear from both the numerical simulation and the experimental observations that the β -TCP component absorbs the laser energy faster and results in a dominant thermal energy transfer through conduction and in fact, the 20% of β -TCP cases begin to burn, char and decompose with laser power at 38 W and above as evidenced from some of the photomicrographs of the initial trials.

5.10 Summary of laser sintering responses of PMMA plus β -TCP composites

The bio-polymer composites made by mixing PMMA plus β -TCP powders in different compositions are experimentally evaluated for selective laser sintering with varying process conditions. Evaluation of the surface morphologies of specimens sintered with initial process parameter combinations allowed to identify more promising levels of critical process parameters. The roles of the laser power and scan velocities together with the variation of the β -TCP content are ascertained based on evaluation of the intra-layer coalescence and thin-film tensile testing. The presence of β -TCP particles in the PMMA matrix is identified to cause rheological changes and consequent loss of quality of sintered layers. Both layer morphologies and subsequent thermal evaluations confirmed the role

of β -TCP in altering the thermal conductivity as well as the effective energy absorptivity of the powder substrate.

Chapter 6

Laser sintering after effects; polymer degradation, biological, and mechanical responses

6.1 Post-sintering polymer characterisation

Preliminary laser sintering responses and subsequent quality improvements with the more optimum process conditions are established in the previous chapters based on both neat PMMA and PMMA plus β -TCP composites. Morphological, physical, and mechanical analyses clearly established the suitability of processing these material systems based on the selective laser sintering process. However, the severe thermal stressing of the power substrates due to the dynamic energy flow from the laser source may result in the loss of specific qualities expected of the bio-polymer composites targeted for medical uses [177].

First, the photonic interactions may lead to alteration of the both molecular and polymer chain configurations [178]. Secondly, the biological responses such as bio-compatibility and bio-conductivity levels may have been altered adversely due to the thermal variations and stressing [153]. Also, considering that the material-process combination is so far characterised only based on single layer samples, the complications that may arise while sintering multiple layers need some attention [108]. The following sections present the results and discussions of the experimental work done finding answers to these questions.

The polymer degradation aspects are evaluated by means of the FTIR analyses, comparing the resulting infrared spectra with the standard patterns of the base-polymer [59]. In vitro studies involving MTT and ALP assays, Alizarin R staining and RNA evaluation are done together with the analysis of the cell morphologies to establish the possible biological changes [179-183]. Physical and mechanical property data is generated based on multi-layer samples sintered to specific conditions as identified in the previous chapters with different material compositions. Overall, no evidence of any adverse effects are noted due to the laser interactions with the biopolymer materials. While the actual experimental procedures are presented in Chapter 3, the results and discussion of different responses follow next.

6.2 Porosity

Based on the results discussed in Chapters 4 and 5, the laser power and scan speed settings as listed in Table 6.1 are employed to print the single layer specimens used to evaluate the sintering effects. While ensuring sufficient coalescence and mechanical strengths, these settings are also expected to provide the necessary porosity and pore sizes for the cells to adhere and proliferate during biological testing. The actual mechanisms and mechanics of inter-particle coalescence and consolidation of layers are discussed in greater detail in chapters 4 and 5. While the current focus is on the after effects of laser sintering, some attention is paid first on the porosity levels and their variation with process conditions considering the significance of controlling porosities also eventually. While the neat PMMA cases are already discussed in Chapter 4, SEM photomicrographs of single layer specimens of polymer composites of

different compositions printed as per the conditions in Table 6.1 are presented in Fig. 6.1. The formation of a continuous sintered layer is evident from these photomicrographs, while the porosity levels varied with varying compositions. Theoretical density is calculated based on the weight percentage and the density of the composite powder while the density of the sintered specimen is established by weighing the sample. Porosity levels of different samples are then estimated using Eq. 6.1 and plotted in Fig. 6.2. Evidently, the higher the β -TCP, the higher is the porosity.

$$Porosity = \frac{\rho(\text{theoretical}) - \rho(\text{sintered})}{\rho(\text{sintered})} \times 100 \quad \dots\dots(6.1)$$

Table 6.1 Material and process parameter combinations used for the printed test pieces

Composition	Energy Density (J/mm ²)	Power (W)	Speed (mm/s)
Pure PMMA Powder	0.15	35	432
5% β -TCP/ 95% PMMA	0.15	38	480
10% β -TCP/ 90% PMMA	0.15	38	480
15% β -TCP/ 85% PMMA	0.15	38	480
20% β -TCP/ 80% PMMA	0.15	34	450

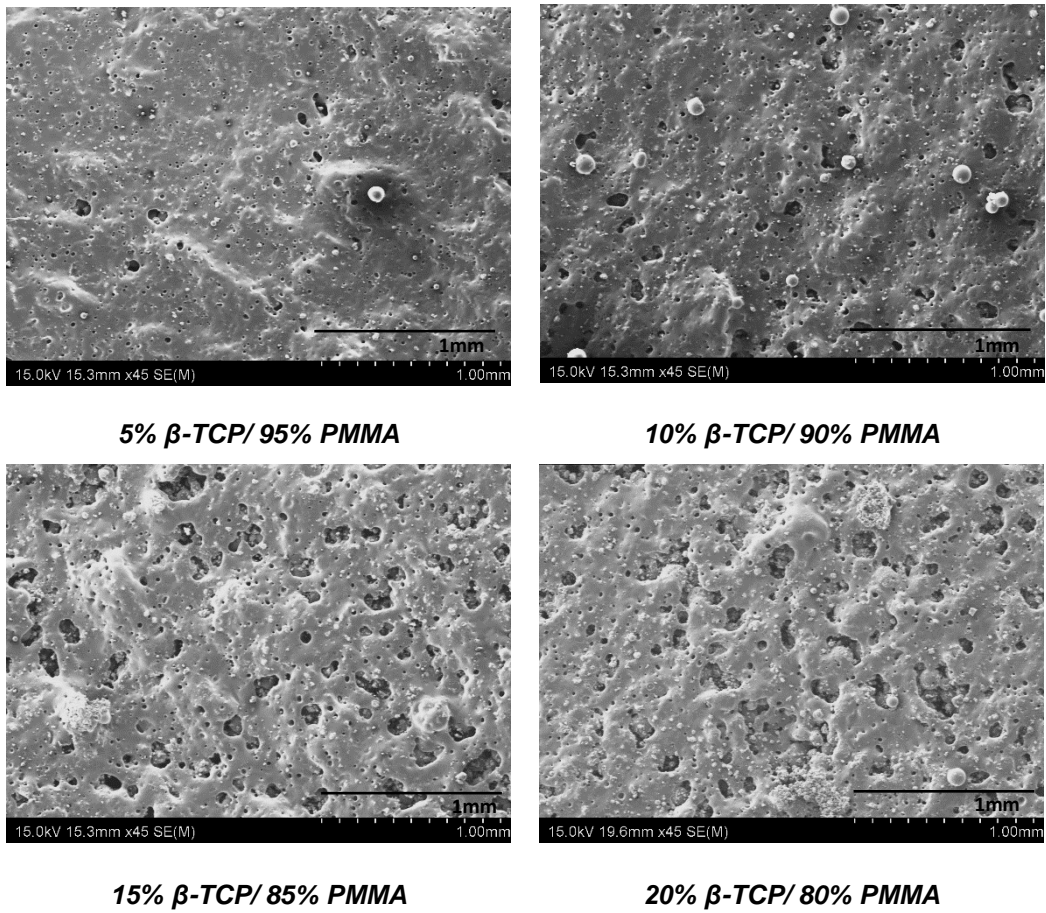


Figure 6.1 SEM photomicrographs of single layer sintered specimens (accelerating voltage 15kV)

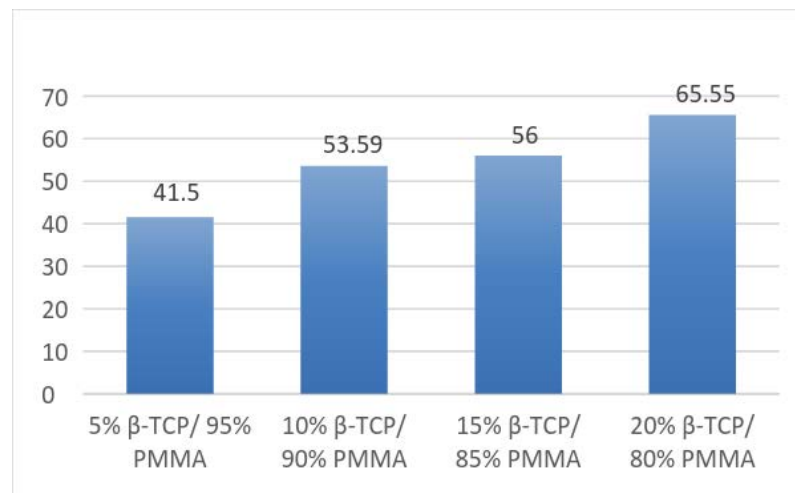


Figure 6.2 Percent porosity with varying PMMA/ β -TCP compositions

The pore size and the extent of porosity have significant roles to play in controlling the bioactivity of the sintered samples, possibly leading to increased cell proliferation and bone ingrowth in specific applications [184]. In general, the pore sizes may be observed to vary from 5 μm to 100 μm which are similar to the pores in natural bone [185]. It is expected that the porosity allows cells to attach and initiate growth forming a local micro-environment that presents potential biochemical, cellular, and physical stimuli orchestrating cellular processes such as proliferation, differentiation, migration, and apoptosis [186].

6.3 Polymer degradation

Polymer degradation may occur due to changes in chemical structures and physical properties emanating from chemical reactions triggered by external physical or chemical stresses [177]. Exposure to heat, UV light, irradiation ozone, mechanical forces, microbes and ablation can cause polymer degradation leading to pyrolysis, oxidation, mechanical, photo, catalytic and bio-degradation [178]. Thermal effects can often lead to complete degradation of polymers through breaking of the main chains, rupture of side fragments, and formation of volatile products and char residues [114]. Considering the highly thermodynamic nature of the laser sintering process, it is essential to evaluate and establish the possible occurrence of polymer degradation if any due to the dynamic thermal fields.

It is pertinent to note that thermal effects are the main causes of degradation in this case, rather than chemical reactions. As the temperature of the powder substrate increases due to sintering, and may lead to polymer degradation when

a certain limit is crossed. The mechanisms of degradation are often the alterations to the polymeric chains by chain scission, crosslinking, and formation of new functional groups and may significantly alter the properties [187]. While evaluating polyamide at elevated temperatures and in the absence of oxygen, wuddy *et al.* noted cross linking caused by thermal degradation and variation in the molecular weight of the polymer [188]. Literature suggests the use of infrared spectroscopy to establish the possible polymer degradation effects of processes such as SLS [189]. This will allow to locate the spectral position (frequency) and intensity of absorbed or emitted radiation arising from molecular transitions between quantum states associated with the vibrations and rotations of specific chemical groups before and after sintering. The resulting FTIR spectra will allow to identify possible changes if any in both neat PMMA and PMMA- β -TCP composites before and after laser sintering. The actual experimental conditions, methods, and equipment are discussed in Chapter 3, but the results and discussion follow next.

Fig.6.3 presents the infrared spectrum obtained based on the pure PMMA powder and is exactly similar to the patterns reported in the literature [59]. In comparison with the spectra reported, the C-O bonds dominate the majority of the vibrational peaks and the presence of C=O ester carbonyl group stretching vibration appeared at 1723 cm^{-1} peak. The broad peak ranging from $3000\text{-}2900\text{ cm}^{-1}$ is due to the presence of C-H stretch vibration and the $1385\text{-}1450\text{ cm}^{-1}$ band can be assigned to the CH_3 and CH_2 deformation vibration [190].

The spectrum thus established for the pure PMMA powder sample is then used to evaluate the spectra obtained with the sintered samples of varying

compositions presented in Fig. 6.4. It may be noted that the spectra in all the cases have similar patterns and peaks as in the case of the raw PMMA powder. This indicates that the polymer chemistry has not changed due to the interaction with the laser induced energy. Further, the presence of β -TCP particles also did not have any significant effects on the spectral results other than very minor variations. This clearly indicates that the laser sintering at 0.15 J/mm^2 energy density and the selected combinations of laser power and scan speeds do not alter the basic chemistry of the polymer. The infrared spectra presented in Figs 6.4 and 6.5 range from wave numbers 600 to 4000 cm^{-1} , which is equivalent to the wavelength range from $2.5 \text{ }\mu\text{m}$ to $20 \text{ }\mu\text{m}$. An absorption band is observed in the spectrum at $10.6 \text{ }\mu\text{m}$ (wave number 943.40 cm^{-1}) which confirms the assumption that PMMA has a 90% absorption at laser energy of $10.6 \text{ }\mu\text{m}$ wave length.

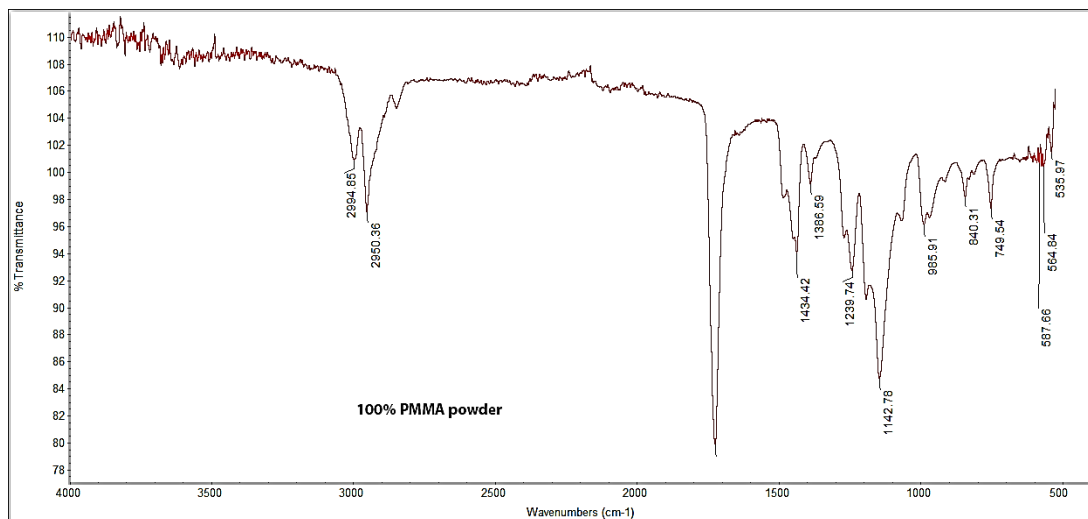


Figure 6.3 FTIR results of neat PMMA powders

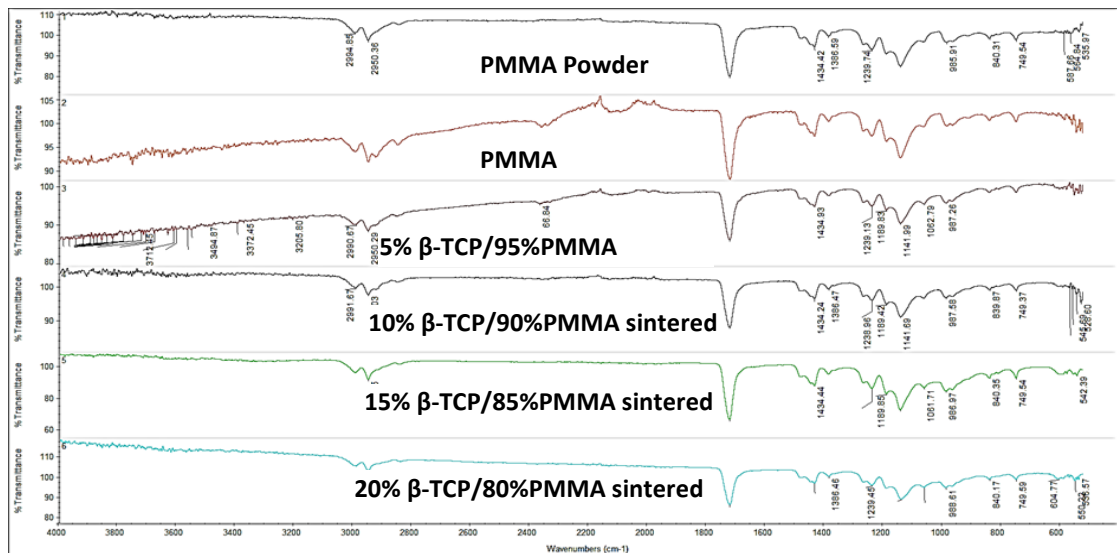


Figure 6.4 FTIR results of sintered specimens

6.4 Biological characterisation

The PMMA/ β -TCP composites evaluated here for selective laser sintering are mainly targeted for use in bone repair and replacement tasks. This needs certain biological responses to be exhibited by the sintered material specimens. Biocompatibility elucidates the molecular and cellular responses and reactions between the implant and the host systems [191]. Bio-conductivity refers to the promotion of the interactions with the surrounding tissue and other elements leading to the actual growth, repair, and healing of bone defects [192]. Both these aspects need to be checked understanding the toxicological profiles in order to establish the sintered materials as suitable for bio-medical applications [193]. *In vitro* tests are done for this purpose on the samples sintered as per the conditions in Table 6.1.

The cytotoxicity of the material to a specified cell type can be studied either by directly seeding the cells on the surface of the material, or by exposing the cells to the extraction fluid, which is an indirect toxicity evaluation [194]. Selection of the appropriate assays will always signify the evaluation of the cytotoxicity of the materials [195]. The other crucial parameters to be considered are cell lines, controls, biochemical assay types and culturing times. Different types of cells are in use to evaluate the *in vitro* cytotoxicity of varying material systems [196]. Schwann cells and neuroblastoma cell lines for nerve regeneration, human fetal osteoblast or osteosarcoma cell lines for orthopedic implant materials [197, 198], and keratinocytes or fibroblasts for establishing the cytotoxic potential of wound dressing materials [199] are some examples.

Human osteosarcoma cell line, MG-63 is employed in the current research for the *in vitro* analysis, as already noted in Chapter 3. These cells are derived from malignant bone tumours, and they have the osteoblastic (bone building cells) features [200]. Before undertaking the *in vitro* tests, the sintered material must be assured to have chemical stability to promote cell growth and sufficient porosity to allow for vascularization [201]. The porosity results presented above clearly ascertained the porous nature of the sintered specimens, while the FTIR analysis confirmed the chemical composition to be made up of PMMA and β -TCP, the two components known for biocompatibility and osteoconductivity respectively.

The purpose of the *in vitro* testing is to evaluate the critical biological responses of the sintered material in order to confirm that the severe thermal stressing due to laser sintering does not lead to adverse repercussions. Cell viability and metabolic activities can be monitored based on the MTT (3-(4,5-dimethylthiazol-

2-yl)-2,5-diphenyltetrazolium bromide) assay, which is essentially a colorimetric test [16]. The alkaline phosphatase (ALP) catalyses the hydrolysis of phosphate esters in an alkaline buffer producing an organic radical and inorganic phosphate and can be used to identify changes in the alkaline phosphatase levels and activity in a given material [179]. Increased ALP levels indicate increased bone cell activity. Calcium forms an alizarin Red S-calcium complex in a chelation process and the end product is birefringent [181]. This leads to the Alizarin Red S staining protocol which is an anthraquinone derivative and mineralization process and can assess mineral activity, predominantly by calcium. Field Emission Scanning Electron Microscopy (FE-SEM) is used to observe the cell-material interactions on the material surface, ascertaining the cell morphology, adhesion and spreading [182]. Amplification and detection of nucleic acids like DNA (deoxyribonucleic acid) and RNA (ribonucleic acid), is also important to ascertain the bone growth factors. The total RNA is isolated and analysed here to quantify gene dosage which is transformed at cell lines using a real-time polymerase chain reaction [183]. The actual methodologies of the *in vitro* studies are detailed in Chapter 3, and the results are discussed next.

MTT assay

Cell proliferation results using sintered specimens with pure PMMA, 5% β -TCP/95% PMMA, 10% β -TCP/90% PMMA, 15% β -TCP/85%PMMA, and 20% β -TCP/80% PMMA composites, quantified based on the MTT assay for 1, 3 and 5 days are presented in Fig. 6.5. All sintered specimens showed cytocompatibility and facilitated the growth and proliferation of MG-63 cells throughout the 12-day culture period. One-way ANOVA and paired t-test analyses indicate the

differences to be statistically significant ($p < 0.05$) with the 5% β -TCP/ 95% PMMA and 15% β -TCP/ 85% PMMA samples. It may be observed that on the first day, there was apparently no cell growth in the pure PMMA sample, while there is significant cell proliferation with both 5% and 10% β -TCP samples. This trend of rapid cell proliferation continued into the third day where the cell growth in general is higher for all samples including the pure PMMA sample. It may be noted that the symbols used in Fig. 6.5 denote; '*' significant difference compared to the control; '**' significant difference compared to PMMA; '#' significant difference compared to 5% β -TCP/95% PMMA; '##' significant difference compared to 10% β -TCP/90% PMMA; '&' significant difference compared to 15% β -TCP/85% PMMA. The 20% β -TCP/80% PMMA has no statistical significance compared to the remaining samples.

The fifth day saw a stabilization in most cases, while the 5% β -TCP case still shows an upward trend. Based on the statistical significance it may be noted that both 5% and 15% β -TCP samples scored higher than the normal expected levels in terms of cell proliferation. Besides β -TCP being osteoconductive, increasing its volume percentage in the composite did not show a linear increase in cellular proliferation and differentiation. These results are in similar lines to the observations made by Di Silvio *et al.* measuring the cell proliferation with varying compositions of HA within the HDPE matrix, and noting that the cellular proliferation and differentiation did not linearly increase with the increase in the volume percentage of bioactive HA in the HA/HDPE composite [202]. The Extra Cellular Matrix (ECM) formation is observed after about five days of culturing in the healthiest cases, and also the cells that grew into the porous holes are not visible. Similar results were also observed by Muhammad *et al.* after culturing the

bone marrow stromal cells for fourteen days on scaffolds [203].

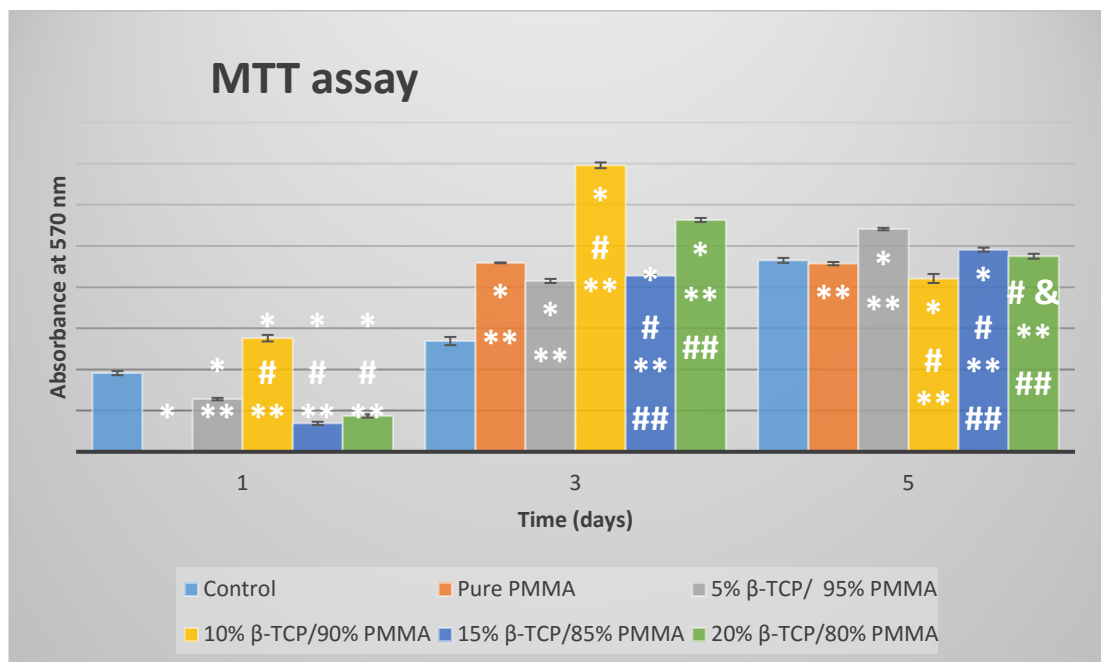


Figure 6.5 Results of the MTT assay with varying compositions.

ALP assay

The ALP assay results of MG 63 cells cultured on PMMA/β-TCP specimens for 4, 7 and 10 days are presented in Fig. 6.6. ALP enzyme is present in higher amounts in the actively bone forming cells, where it can catalyze the hydrolysis of the phosphate esters at alkaline pH and play an important role in the bone matrix mineralization process. Again, based on ANOVA and t-test, the difference observed for 5% β-TCP/95% PMMA and 15% β-TCP/85% PMMA are noted to be statistically significant ($p < 0.05$). The 5% β-TCP/95% PMMA, 15% β-TCP/85% PMMA, and 20% β-TCP/80% PMMA demonstrated increased ALP activity from day 4 to day 7. There is a relative decrease observed in the ALP activity on day 10. This could be due to the formation of the extracellular matrix (ECM) which

is later observed from the SEM images as presented in Fig. 6.8 and the consequent masking of the cells present. The specimens show ECM formation on day 10 which is evidently absent earlier, on day 4. Since, ALP is an enzymatic activity, only the cells interacting with the substrate, will contribute for the color formation indicating the initiation of the mineralization process [204]. Samples with 15% β -TCP/85% PMMA, and 20% β -TCP/80% PMMA did not show differences of statistical significance compared to the remaining samples.

Alizarin-red S staining

The Alizarin-red S staining test results with samples of varying compositions are presented in Fig. 6.7. The staining in the samples made of the polymer composites is evidently much greater than that of pure PMMA. Also, the higher the β -TCP content, the better is the staining. These results clearly indicate that the cellular attachment, proliferation, and calcium mineralization on the sintered polymer composite specimens is significantly more compared to that on pure PMMA samples, after 25 and 28 days. This means better mineralization with increasing β -TCP in laser sintered PMMA based composites.

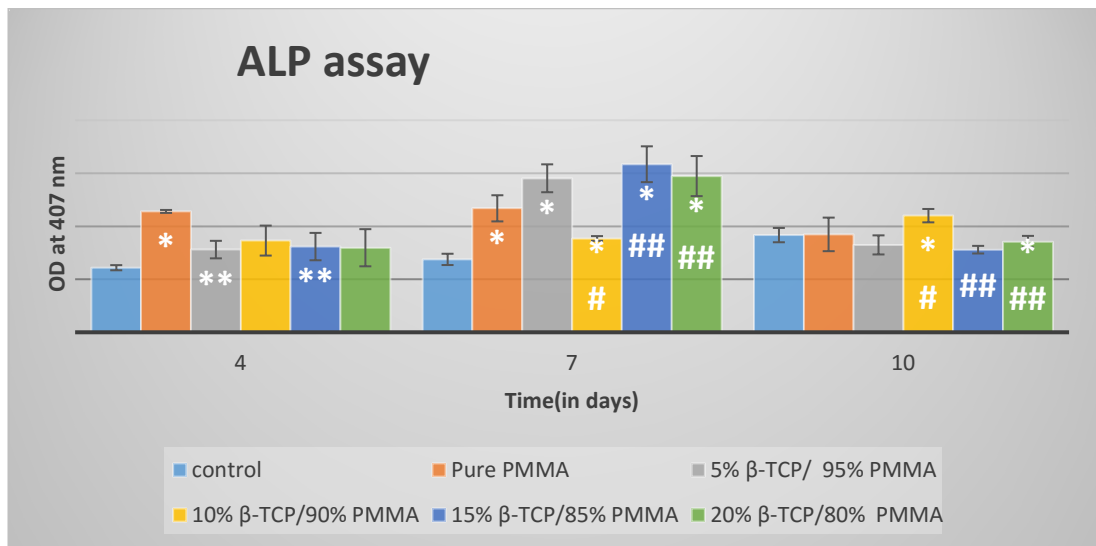


Figure 6.6 Results of the ALP assay

Sample / Day	PMMA	5% β -TCP/ 95% PMMA	10% β -TCP/ 90% PMMA	15% β -TCP/ 85% PMMA	20% β -TCP/ 80% PMMA
Day 7					
Day 12					

Figure 6.7 Alizarin red staining results with varying composition

FE-SEM imaging

FE-SEM images of sintered PMMA and β -TCP/ PMMA composite specimens cultured with MG 63 cells for 5 and 10 days are presented in Fig. 6.8. A marked difference may be noted between pure PMMA and the PMMA/ β -TCP composite samples in promoting cell proliferation comparing the photomicrographs taken on the fifth day. By the tenth day, the PMMA surface shows substantial improvement in the cell growth, while there are variations at different levels of β -TCP. The MG-63 cells are seen to spread varyingly over the surfaces of the sintered specimens, probably due to the relationship between the adhesion of osteosarcoma and the surface characteristics of specimens, such as topography, chemistry, and the surface energy [205]. Extra cellular matrix (ECM) formation is clearly evident in both 5% β -TCP/ 95% PMMA and the 15% β -TCP/ 85% PMMA samples, as noted in Fig. 6.8. Individual cells are bridged between adjacent microspheres on the surface, indicating strong interactions between cells.

However, the cells look diminished and probably unhealthy by the 10th day with the 10% β -TCP sample. This is probably due to the surface conditions and the porosity. The cells are likely to have grown into the porous holes. Again, when β -TCP is increased to 15% and 20 %, the cells are widespread and healthy and there is a clear evidence of the formation of ECM, in particular with the 15% β -TCP sample, indicating a higher bioactivity. Although the sample with 20% β -TCP allowed widespread cell proliferation, the formation of ECM is relatively less. Overall, the surface roughness and the nature and extent of porosity appear to control the adsorption of protein, in promoting the attachment and proliferation of the osteosarcoma cells [206]. It is likely that surface exposure of β -TCP caused

MG 63 cells to better interact with the β -TCP molecules on 5% and 15% β -TCP samples showing higher bioactivity. Earlier studies reported that PMMA is non-bioactive by itself, and modifications such as incorporating alkoxysilane and calcium salt [207], methacryloxypropyltrimethoxysilane and calcium acetate [143] silanation of apatite/wollastonite glass ceramic particles were found to increase the bioactivity.

MG 63 cells have fibroblast shapes when cultured in the T-flask, but, they look spherical on the FE-SEM images (Fig. 6.8). Cell attachments are characterized by numerous protrusions of filopodia that anchor the cells on the surfaces of the sintered specimens [208]. Khung *et al.* observed in similar lines and elucidated that the lack of rigid cell walls allows innate abilities to human cells to change shapes depending upon the surface topography and pore sizes of the scaffold materials [209]. It was also reported that neuroblastoma cells cannot adhere to the samples with pore diameters between 1000-3000 nm, as the pores were too large for the filopodia to find anchorage. Cells with greater number of protrusions were found to develop on samples with pore sizes from 100-1000 nm. Despite developing spherical morphologies, the cells regrouped to form clusters on samples with pore sizes in the range 50-100 nm. The current results as presented in Fig. 6.8 are similar to this. Evidently, samples with higher β -TCP allowed the cells to be healthier, bioactive, and resulted in the formation of the extra cellular matrix as identified in Fig. 6.8. After attachment and proliferation, the cells on the biomaterial surfaces further differentiate to synthesize collagen and other proteins and induce their own *in vitro* mineralization in certain culture medium conditions [210]. The spherical cell forms is further confirmed based on the discussions with the experts in the field at the Biotechnology lab of PSG Tech India.

Sample	Day 5	Day 10
PMMA		
5% β -TCP/ 95% PMMA		
10% β -TCP/ 90% PMMA		
15% β -TCP/ 85% PMMA		
20% β -TCP/ 80% PMMA		

Figure 6.8 Morphology of MG-63 cells cultured on PMMA and β -TCP/ PMMA specimen

While β -TCP is already known to promote biological activity, the current results indicate that this trend continues even with laser sintered β -TCP together with PMMA as the base matrix. Yang *et al.* suggested that PMMA/ β -TCP composites can be used as replacements ideally in the craniofacial and other non-load bearing regions of the body [211]. The results of the current study indicate the feasibility of achieving the relatively complex forms of such implants better by processing the composites using selective laser sintering.

6.5 Multilayer Laser sintering

All the experimental research done and reported so far is centred around laser sintering single layers of both neat PMMA and PMMA plus β -TCP powders. The results and analysis presented in Chapters 4 and 5 and in all the preceding sections in this chapter are based on the consolidation of the experimental powders into single layer thin samples. The results are positive so far, clearly establishing the suitability of the material-process combinations in terms of structural, physical, mechanical, and biological responses. Most of the objectives set for the current research are also achieved, but one aspect is yet to be ascertained; whether the current powder materials respond well to multi-layer sintering. This is quite important, considering that the real use of the materials involves multiple layers sintered, several hundreds or even more in many cases, in order to achieve the required forms. This section presents the experiments done and results generated quantifying the multi-layer sintering responses.

While the intra-layer material consolidation mechanisms still remain very similar, certain differences and some complications arise from the multi-layer sintering. A graphical representation of the sequence of events is developed as shown in Fig.6.9 in order to clearly elucidate these differences. The process stages after achieving the first layer are visualised as four significant steps for each successive layer. First, the build-platform with the already made previous layer descends by one-layer thickness and a new layer of powder is spread uniformly across. At this stage, the sintered substrate and the freshly dispersed powder layer are not at the same temperature. During the second stage, the sintered substrate gradually loses heat, while the new powder layer picks up some of this heat and gets active. For the best results, the temperature of the fresh powder layer must be brought to the glass transition level. This is achieved by means of both the heat conducted from the base plate through the existing layer or layers and also the heat flowing from the overhead heat-lamp and by properly controlling the dwell period between successive laser sintering steps.

The next step is the actual laser sintering of the freshly dispersed layer, achieving the next thin solid layer. The preheating of the powder layer actually helps in two different ways. The elevated temperature keeps the interface between the two successive layers active and ready for the inter-layer coalescence [212]. Further, the thermal energy necessary to achieve effective fusion and inter-particle coalescence in the new layer is kept at relatively lower levels, thereby allowing for a good balance between the laser power and scan speed settings as elaborated in Chapters 4 and 5. Once the formation of the new sintered layer is complete, the final stage involves achieving the much needed inter-layer coalescence and bonding. This requires the previously formed layer to be kept

active and alive through heating to an elevated temperature, ideally close to the glass transition level. As explained in Chapter 3, this is achieved by means of the hot plate build platform, whose temperature is controlled in such a way that the layers already formed will be warmed up to the extent that the interface between the two successively formed layers will have enough energy and time to achieve the inter-layer migration of molecules and solid state sintering. The process is repeated with each successive layer sintering [213].

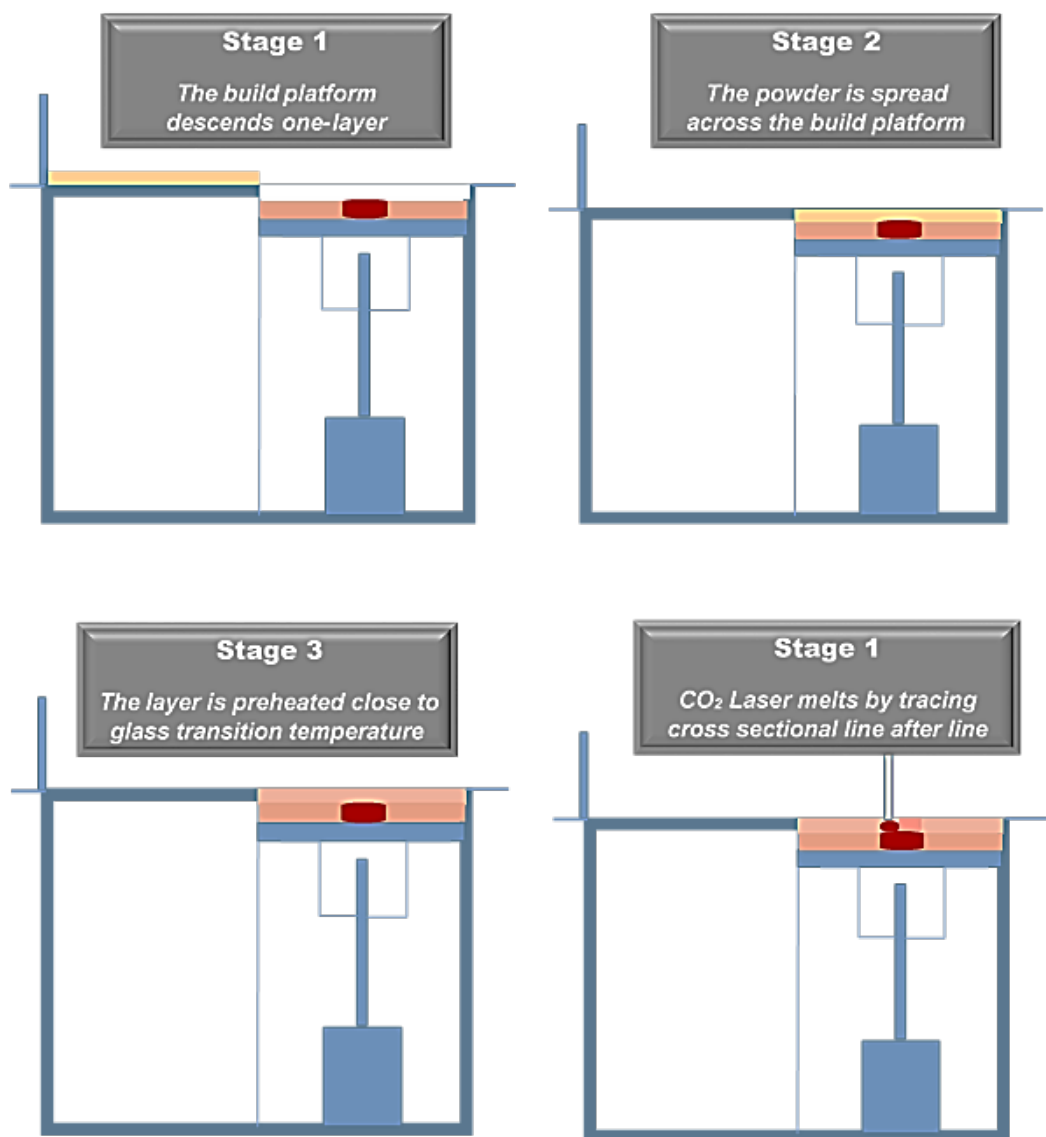


Figure 6.9 Multi-layer sintering stages

Critical process parameters such as the powder bed temperature, layer thickness, laser power and scan velocities and the energy density levels arise out of the process conditions in multi-layer sintering [140]. The part bed temperature is controlled by means of the base plate heating mechanism and set to achieve better fusion of the particles with relatively lesser energy absorption [212]. Normally, stair step effects are related to the choice of the layer thickness [214]. However, the layer thickness and the energy density levels interact and the actual laser power and scan speed settings will require to be altered together with the layer thickness levels. For a given thickness, the energy density level should be matched to achieve complete sintering of the layer. A lesser energy leads to insufficient fusion and trapping of loose powder particles between solid layers, while a higher than necessary energy level leads to excessive and repeated heating, resulting in probable loss of the polymer quality as well as warping and distortion of layers. Improper energy density settings may also lead to balling effects on the sintered surface with consequential loss of inter layer bonding [215]. The heat transfer and the temperature distribution are also affected by the shrinkage of the sintered layer [216]. All these factors are accounted for based on the experimental setup designed and developed as discussed in Chapter 3. While using the optimum combinations of parameters based on the single layer results discussed earlier as the *a priori* data, the experimental parameters are adjusted appropriately for multi-layer samples of specific powder compositions as follows.

Multi-layer laser sintering conditions

A complete new set of working conditions can be developed starting from the scratch but it is better and faster if the data already generated is used as the *a priori*. In particular, it is pertinent to note that the factors involved interact in multiple directions. For example, the interactions between laser energy density settings and the layer thickness are already noted. The layer thickness will also interact with the powder bed temperature as a larger thickness may need a higher bed temperature in order to achieve sufficient heat flow across the layer, achieving uniform heating of all particles to the glass transition level. Further, laser power and scan velocity settings will also interact with the layer thickness as the time, temperature, and heat flow rates vary with the thickness of the sintered layer. While achieving significant sintering within the layer is central to success, the optimum levels of energy densities established earlier for single layers of neat PMMA and PMMA plus β -TCP composites at 0.3 J/mm^2 and 0.15 J/mm^2 respectively are kept as the basis, while the other parameters are adjusted accordingly. Apart from neat PMMA, only the 5% β -TCP/ 95% PMMA and 10% β -TCP/ 90% PMMA options are evaluated for multilayer sintering based on the overall trends in other responses. Further, the layer thickness is fixed at 0.1 mm considering the ease of operation and also to reduce the overall level of complexity in the experimental conditions.

Initially, the part bed temperature is kept at around 85°C to 90°C , and the cross sections of the sintered multi-layer samples obtained as shown in Fig.6.10 (a) are evaluated. A serious lack of fusion in the intermediate particles and a consequent loss of inter layer bonding are evident. Any increase in the energy density beyond

the normal levels established in the previous chapters leads to decomposition and charring of the polymer resulting in deep trough-like layers are formed as shown in Fig. 6.10 (b). When layers are decomposed, excessive powder deposition occurs for the next layer. This escalates the problem further due to the insufficient energy density unable to sinter the largely accumulated powder particles with cumulative increase in the sintered volume in successive layers. The overall effect is a thin sintered top layer and around a 250 μm thick intermediate layer of loosely held powders as evident in Fig. 6.10 (b). Without altering the laser energy density settings, this problem is overcome by repeating the trials with varying powder bed temperature settings, together with the use of the overhead heat lamp at an appropriate distance as explained in Chapter 3. The optimum part bed temperature is identified to be 100°C, which when coupled together with the heating by the overhead lamp brings the surface temperature to be around 105 °C which is almost the glass transition temperature of the PMMA base polymer.

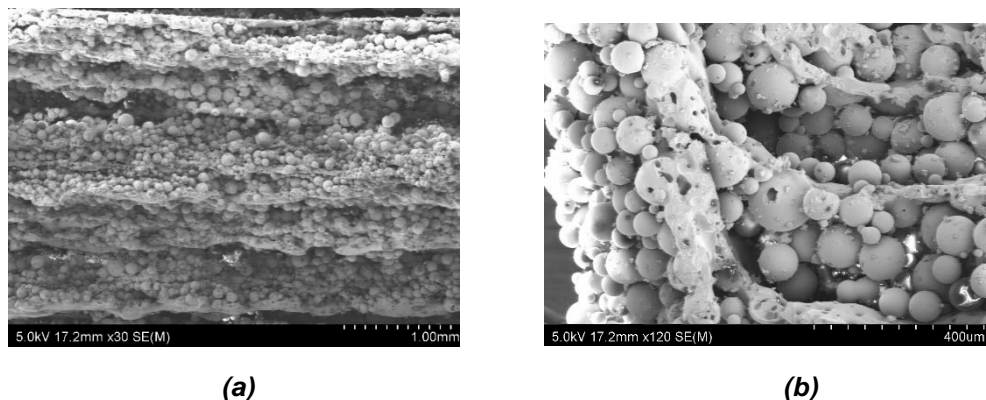


Figure 6.10 Initial trials on multi-layer samples

While keeping the energy density and other critical parameters at the levels as identified, different combinations of laser power and scan velocities are selected

in order to study the multi-layer sintering responses. The final critical laser process parameter combinations as used for further multi-layer sintering trials are listed in Table 6.2. Including the two energy density levels for the neat PMMA and the three energy density levels for the polymer composite options, a total of twenty-four rectangle specimens of 60mm X 10mm X 4.5mm are printed for mechanical characterisation based on three-point bending tests as per the ASTM standards. Images of some of the printed samples are shown in Fig.6.11 and no visible traces of loss of surface finish, colour or geometrical form are noticed. The powder deposition for each layer is at 0.10 mm and each sample is made up of 20 printed layers. Morphological and mechanical responses are discussed next.

Table 6. 2 Critical process parameters for Multi-layer sintering

Neat PMMA		
Energy Density (J/mm²)	Laser Power (W)	Scan speed (mm/s)
0.15	20	255
	25	309
	30	370
	35	432
0.3	20	124
	25	154
	30	185
	35	216

5% β-TCP/ 95% PMMA, 10% β-TCP/ 90% PMMA		
Energy density (J/mm²)	Laser power (W)	Laser speed (mm/s)
0.08	34	750
	38	780
	42	810
0.1	34	650
	38	680
	42	710
0.15	34	450
	38	480
	42	510

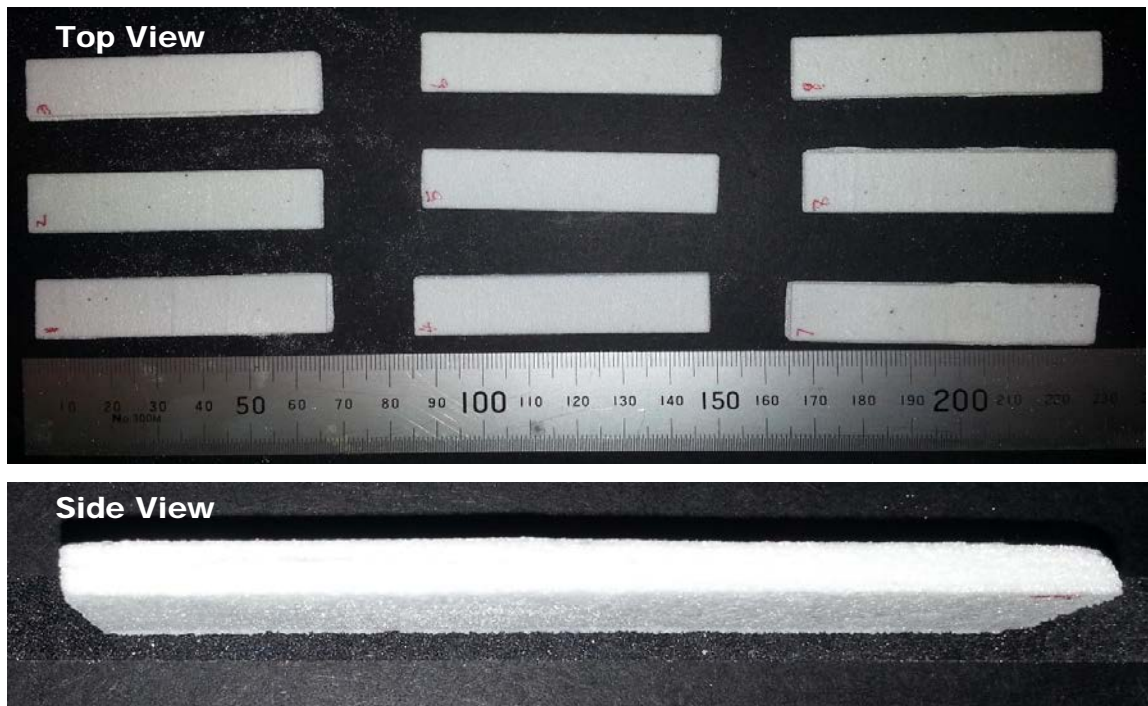


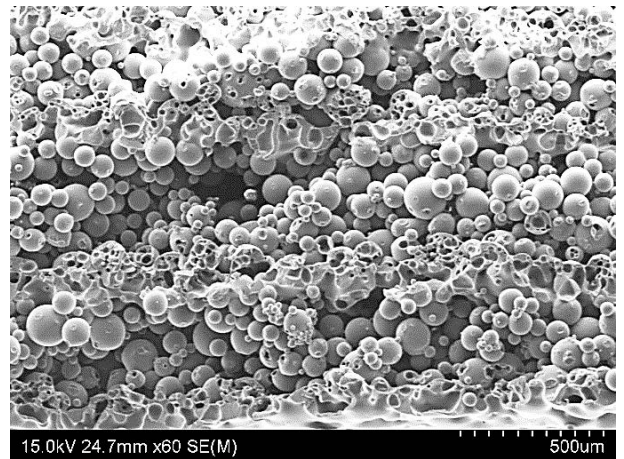
Figure 6.11 Selective laser sintering of Multi-layer specimens

Morphologies of multi-layer sintered specimens

Morphologies of single layer sintered neat PMMA and PMMA plus β -TCP composite samples are presented and discussed earlier in Chapters 4 and 5. Similar evaluation will be undertaken here with the multi-layer counterparts, but considering SEM images of cross-sections so that inter-layer coalescence can be understood. SEM images of cross sections of samples sintered at different energy densities using neat PMMA, 5% β -TCP/95% PMMA, and 10% β -TCP/90% PMMA are presented in Figs 6.12, 6.13, and 6.14 respectively and discussed next.

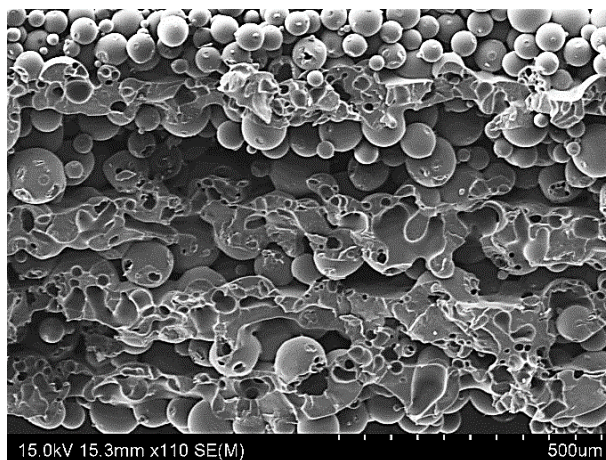


Power = 30 W, Speed = 370 mm/s

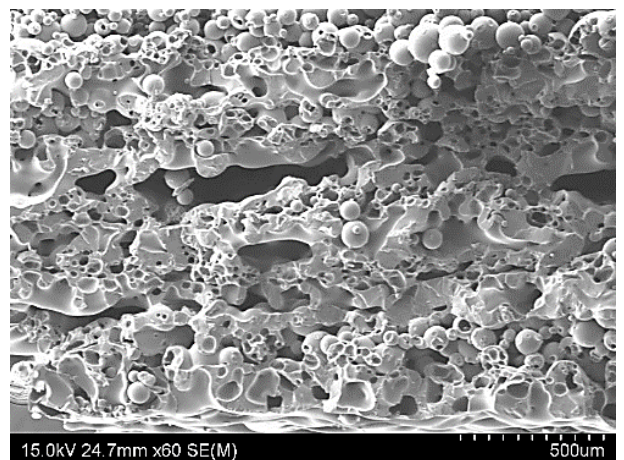


Power = 35 W, Speed = 432 mm/s

(a) Energy Density = 0.15 J/mm²



Power = 25 W, Speed = 154 mm/s



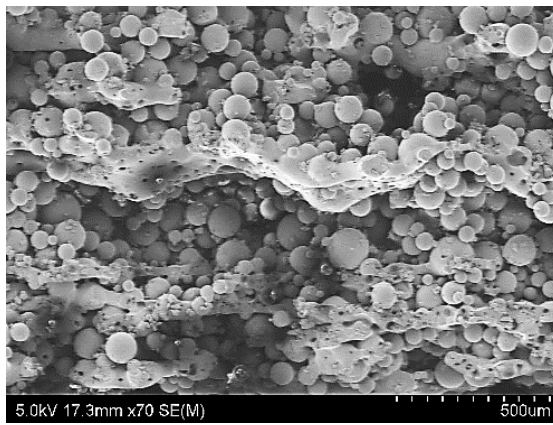
Power = 30 W, Speed = 185 mm/s

(b) Energy Density = 0.3 J/mm²

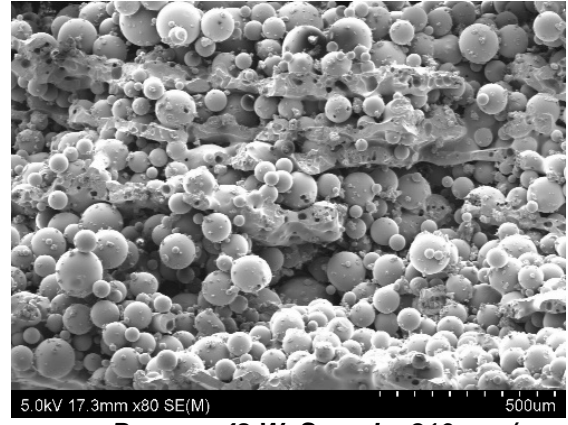
Figure 6.12 Multilayer neat PMMA fractured surfaces

Cross sections of neat PMMA samples sintered at 0.15 J/mm² energy density as seen in Fig 6.12 (a) show the spherical structures of most PMMA particles still intact. There is a small amount of inter-particle sintering, allowing the build-up of vertical columns of fused particles, but the overall level of inter-particle coalescence is limited. This has also led to the loss of inter-layer coalescence and probable delamination and poor mechanical responses. A higher degree of inter particle coalescence is evident in the SEM images of cross sections of neat PMMA specimens printed at 0.3 J/mm² energy density as shown in Fig.6.12 (b).

PMMA particles are clearly sintered to significant levels, forming a continuous solid layer. While most particles are consumed up during the melting and fusion into layers, porosity resulted from two sources. Thermal heating and inter-particle coalescence led to shrinkage and micro level separation leading to finer intra-layer gaps. Further, shrinkage of entire layers led to relatively larger inter-layer gaps. Overall, the cross sections look good and evident of the formation of a continuous network of solid polymer, surrounding the micro and macro porosities.

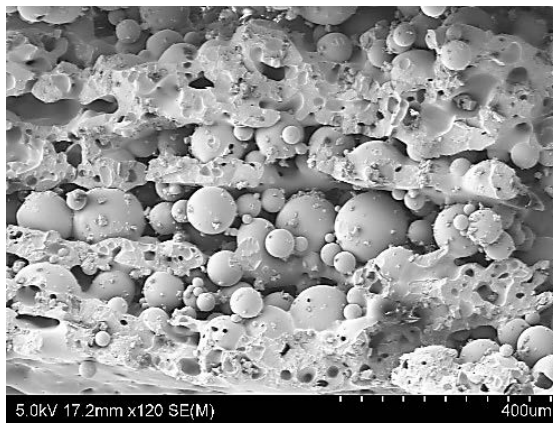


Power = 38 W, Speed = 780 mm/s

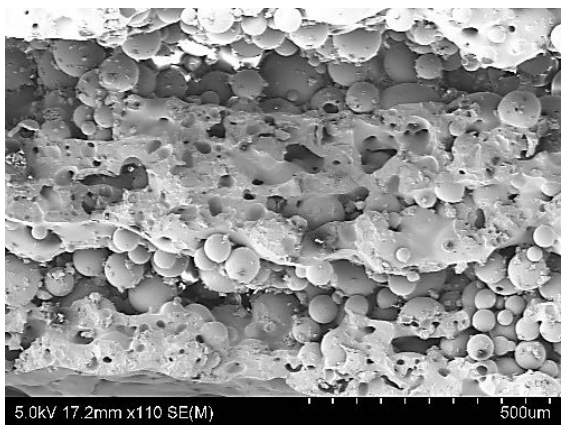


Power = 42 W, Speed = 810 mm/s

(a) Energy Density = 0.08 J/mm²

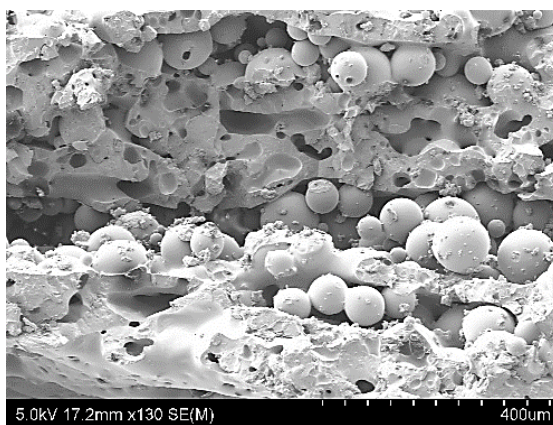


Power = 38 W, Speed = 680 mm/s

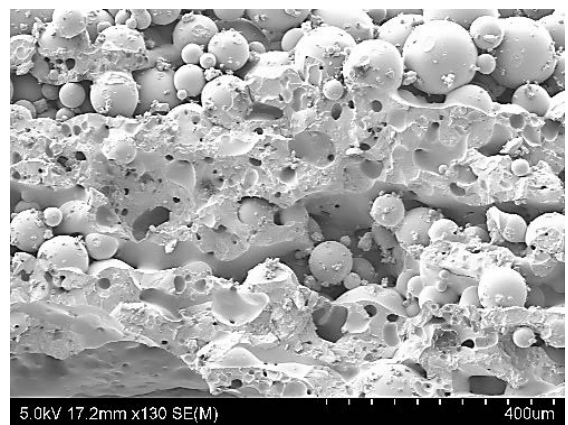


Power = 42 W, Speed = 710 mm/s

(b) Energy Density = 0.1 J/mm²



Power = 38 W, Speed = 480 mm/s

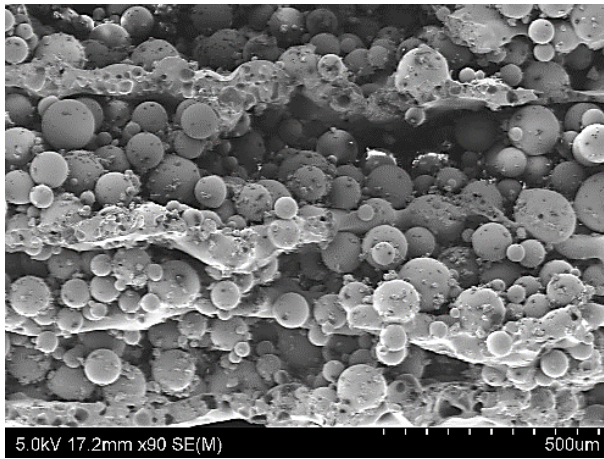


Power = 42 W, Speed = 510 mm/s

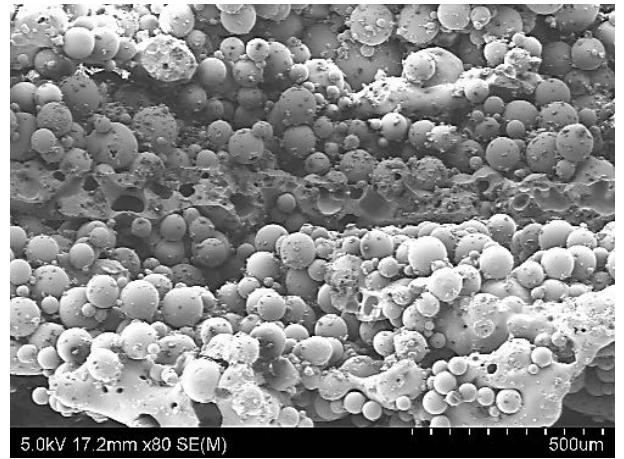
(c) Energy Density = 0.15 J/mm²

Figure 6.13 SEM Images of cross sections of 95% PMMA and 5% β -TCP

samples

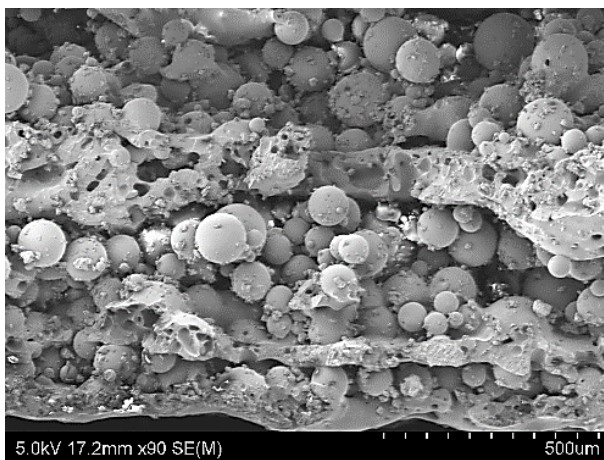


Power = 38 W, Speed = 780 mm/s

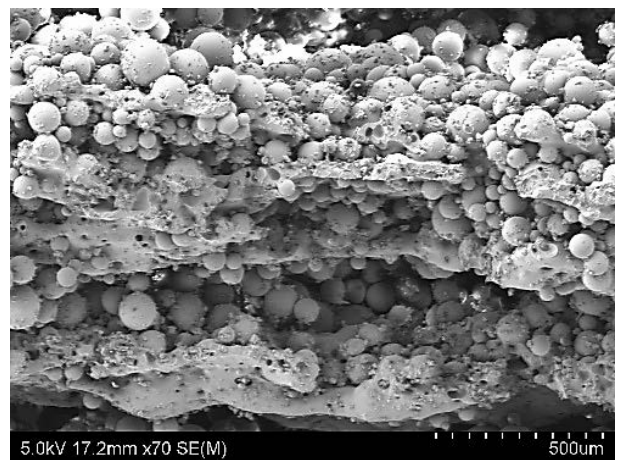


Power = 42 W, Speed = 810 mm/s

(a) Energy Density = 0.08 J/mm²

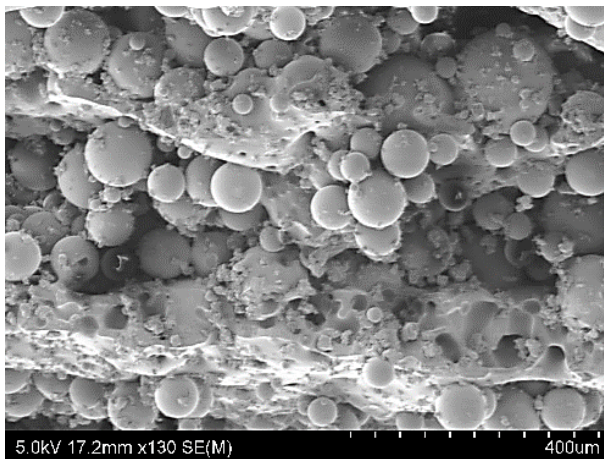


Power = 38 W, Speed = 680 mm/s

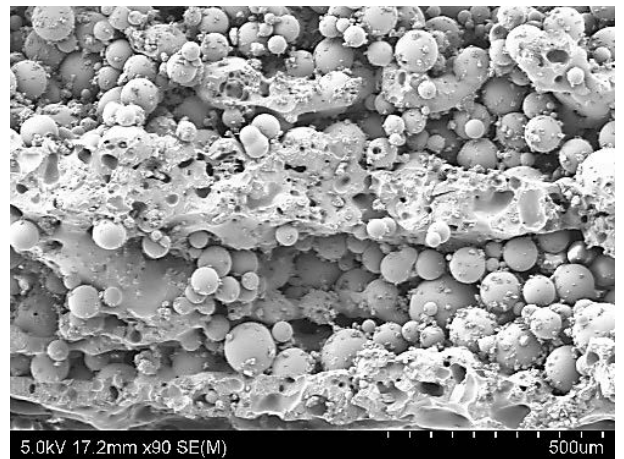


Power = 42 W, Speed = 710 mm/s

(b) Energy Density = 0.1 J/mm²



Power = 38 W, Speed = 480 mm/s



Power = 42 W, Speed = 510 mm/s

(c) Energy Density = 0.15 J/mm²

Figure 6.14 SEM images of cross sections of 90% PMMA and 10% β -TCP samples

SEM photomicrographs of the cross sections of 5% β -TCP/ 95% PMMA and 10% β -TCP/ 90% PMMA are presented in Figs 6.13 and 6.14 respectively. First looking at the 5% β -TCP cases, there is a gradual improvement with the increase in the energy density. The lowest energy density case at 0.08 J/mm² clearly indicates a lack of inter-particle consolidation. The layers formed are thin and the energy is insufficient to transfer across layers and there is hardly any evidence of inter-layer consolidation as loose PMMA particles seem to be floating in between the thin solid layers. There is an incremental improvement as the energy density is increased and thick sintered layers are clearly evident in samples sintered at 0.15 J/mm² as seen in Fig. 6.13 (c), with only an occasional particle remaining loose. Further, there is also improvement from the lower power lower velocity settings to the higher power and higher velocity settings, comparing the cases in the two columns in Fig. 6.13. The higher power cases scored better while the specimen produced at 42 W and 510 mm/s is the best in terms of achieving the most effective intra- and inter-layer coalescence and consolidation.

Similar observations could also be noted evaluating the photomicrographs of the 10% β -TCP cases presented in Fig. 6.14; a gradual improvement in sintering with increased energy density. However, the higher β -TCP content led to a loss of the quality of sintering compared to the 5% case. The actual reason for this loss of sintering quality is not very clear yet, but it is noted that thin continuous layers are rapidly formed in the cases with higher β -TCP content (10% and above) perhaps due to the much higher thermal conductivity. The substrate particles are blanketed from further heat flow and lacked consolidation. Further, comparing the photomicrographs of Figs 6.12 to 6.14, it is readily evident that the layer formation is more streamlined in the case of the neat PMMA samples. Most particles are

sintered, but the layers appear to have shrunk, leading to occasional inter-layer shrinkage cavities. The relatively higher temperature readings noted with the polymer composites from the thermal measurements reported in Chapter 5 and the thermogravimetric results indicate better heating and rapid formation of the layers, but the presence of the β -TCP particles appears to have caused rheological changes.

Density and Porosity analysis

Densities of sintered specimens are established by the weight-to-volume ratios, where the weights are measured using a sensitive balance and the volumes are calculated based on the sample measurements. Comparing the density values recorded in Table 6.3 considering the samples generated with the best process parameters, it is evident that neat PMMA samples sintered to better densities. This is also in accordance with the photomicrographs discussed above. Further, the density and porosity variations presented in Figs 6.15 show only slight variations with varying laser power at different energy densities. The reason for this is, though not sintered effectively, the powder particles are entrapped between solid layers and add to the density values measured based on the weights of the samples.

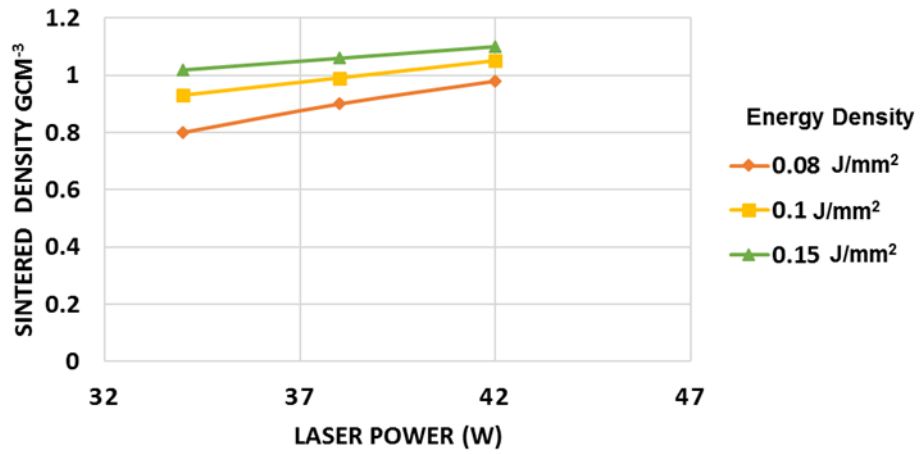
However, there is a slight but almost linear increase in the density and corresponding decrease in the porosity with increasing power at any given energy density as observed in Fig. 6.15 for the 5% β -TCP cases. The sintered specimens attained an average porosity of around 20% at 0.15 J/mm² and the pore sizes, as evident from the photomicrographs of Fig.6.16 vary from 10 μ m to 65 μ m. The

ability to control the internal porosities and meso-structures, based on process controls indicates better utilisation of the polymer composites for bone-related applications as also noted by Yang *et al* [217]. It was also observed earlier that the general pore size for the ingrowth of fibrous tissue is at around 5-11 μ m, while a pore size in the range of 20-60 μ m is ideal for cell spreading and proliferation [10].

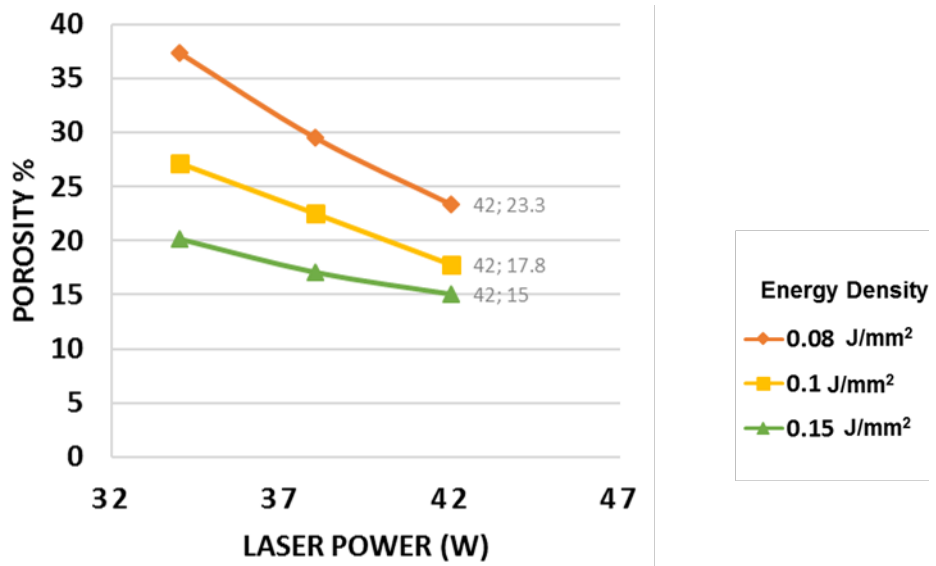
Fig. 6.17 illustrates the optical photomicrographs of cross sections of 5% β -TCP/ 95% PMMA and 10% β -TCP/ 90% PMMA samples sintered at 0.15 J/mm² energy density further to cold mounting and light polishing. The white areas represent the sintered polymer matrix while the spheres represent the semi-sintered or unsintered PMMA particles. The dark areas represent the porosities in the sintered samples. It may be noted that the 5% β -TCP case presents relatively larger porous holes, mainly segregated along the inter-layer boundaries. This is in lines similar to the neat PMMA behaviour, where the layers are noted to shrink upon sintering and create larger inter-layer shrinkage cavities. With the increase in the β -TCP content to 10%, the nature of porosity is converted to the predominantly intra-layer micro porous hole appearance.

Table 6.3 Density of Multilayer sintering of PMMA and PMMA/ β -TCP composites

Samples	Energy Density (J/mm ²)	Density (g/cm ⁻³)
Neat PMMA	0.3 (30 W and 185 mm/s)	1.96
5% β -TCP/ 95% PMMA,	0.15 (42 W and 510 mm/s)	1.12
10% β -TCP/ 90% PMMA	0.15 (42 W and 510 mm/s)	0.83



(a)



(b)

Figure 6.15 Density and porosity vs laser power at different energy densities (5% β -TCP/95% PPMA case)

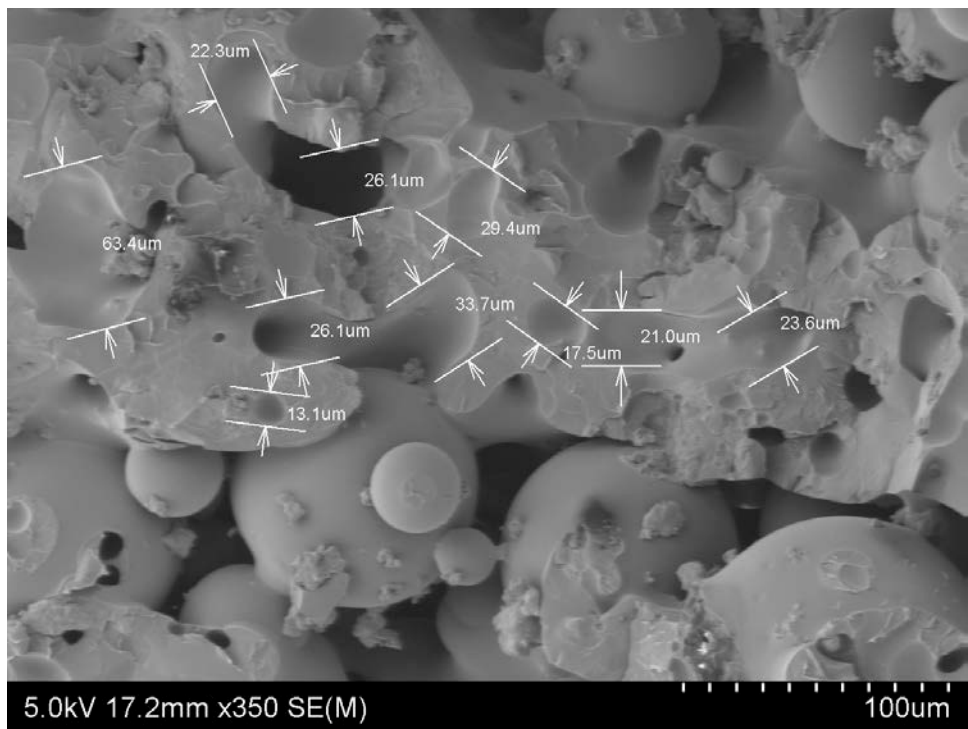
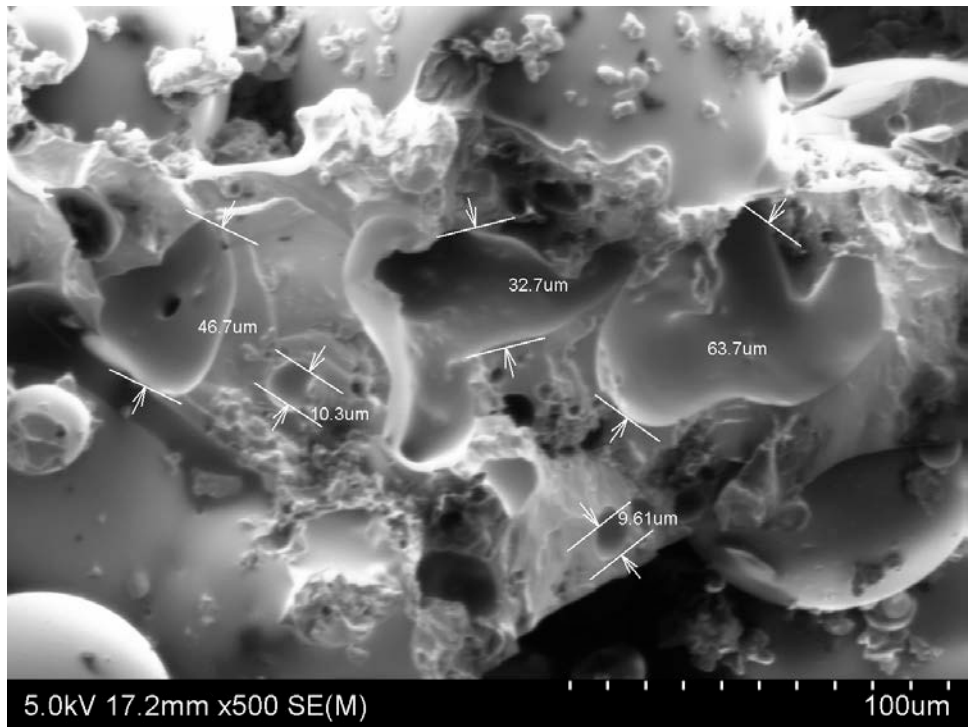


Figure 6.16 Pore size measurement at different locations (5% β -TCP/95% PMMA case sintered at 0.15 J/mm²).

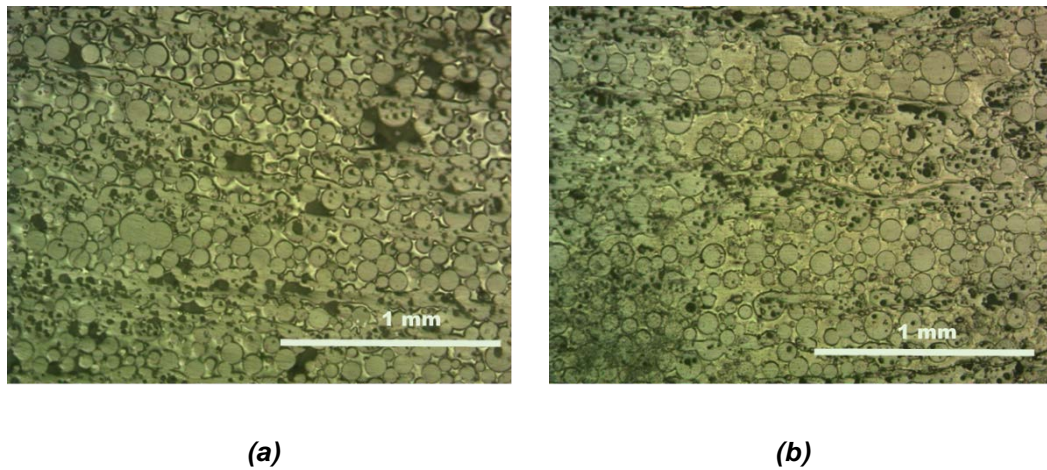


Figure 6.17 Optical photomicrographs of cross-sections of (a) 5% β -TCP/95% PMMA and (b) 10% β -TCP/90% PMMA samples sintered at 0.15 J/mm².

Mechanical Properties

Three-point bending samples of both PMMA and PMMA/ β -TCP composites are sintered as per the ASTM D7264 standards to quantify the mechanical responses. The actual bending tests on the printed samples are conducted as detailed in Chapter 3. The flexural moduli calculated based on the results are listed in Table 6.4 and also plotted in Fig. 6.18 for all the process parameter combinations. As evident from Fig. 6.18, for any given composition, the flexural moduli of samples increased with increasing energy densities. This is due to better intra and inter layer sintering as evidenced from the photomicrographs discussed above.

Overall, the flexural moduli decreased with the addition of the β -TCP particles as compared to the neat PMMA cases. Deshmane *et al.* noted that the incorporation of the ceramic component into the polymer changes the bulk crystallinity, adversely affecting the modulus of the material, apart from altering the

mechanism of plastic deformation [218]. However, these differences are relatively minor with the 5% β -TCP case. In the case of neat PMMA, the maximum flexural modulus 115 MPa is achieved at 0.3 J/mm² with laser power 30 W and scan speed 185 mm/s. For the 5% β -TCP/95% PMMA case, the maximum flexural modulus achieved is 101.4 MPa at 0.15 J/mm², power 42 W, and speed of 510 mm/s. This has been reduced to 83.2 MPa with the 10% β -TCP/90% PMMA case, at 0.15 J/mm², 42 W, and 510 mm/s settings.

The other lower energy densities yielded significantly lower flexural modulus values, due to the poor inter-layer coalescence as already noted in the above section 6.5 morphologies of multi-layer sintered specimens. Similar results were also reported by Chung *et al.*, while experimenting Nylon-11 loaded with 0–10% by volume of silica nanoparticles [219]. Better dispersion of the β -TCP particles is noted with the more uniformly sintered polymer composite specimens, while irregular meso-structures led to the agglomeration of the β -TCP particles. Understandably, the presence of the β -TCP particles alters the rheology of the base polymer, mostly increasing the viscosity levels. At relatively lower levels of the filler particles, the enhanced thermal attributes of the powder composite help improve the heating as well as the flow of the liquid polymer, leading to a more uniform sintering as well as dispersion of the particulate phase. With further increase in the β -TCP content, the rheology changes over to the more viscous flow, insufficient coalescence and adverse meso-structures, together with the agglomeration of the filler particles. The gradual loss of the flexural modulus as noted in Fig. 6.18, at 10% β -TCP content can be attributed to these structural changes.

Table 6.4 Mechanical properties of Multi-layer sintered PMMA and PMMA/ β -TCP composite

Materials	Energy Density (J/mm ²)	Flexural modulus (MPa)
PMMA	0.15	84
	0.3	115
5% β -TCP	0.08	89.2
	0.1	99.9
	0.15	101.4
10% β -TCP	0.08	52.6
	0.1	74.1
	0.15	83.2

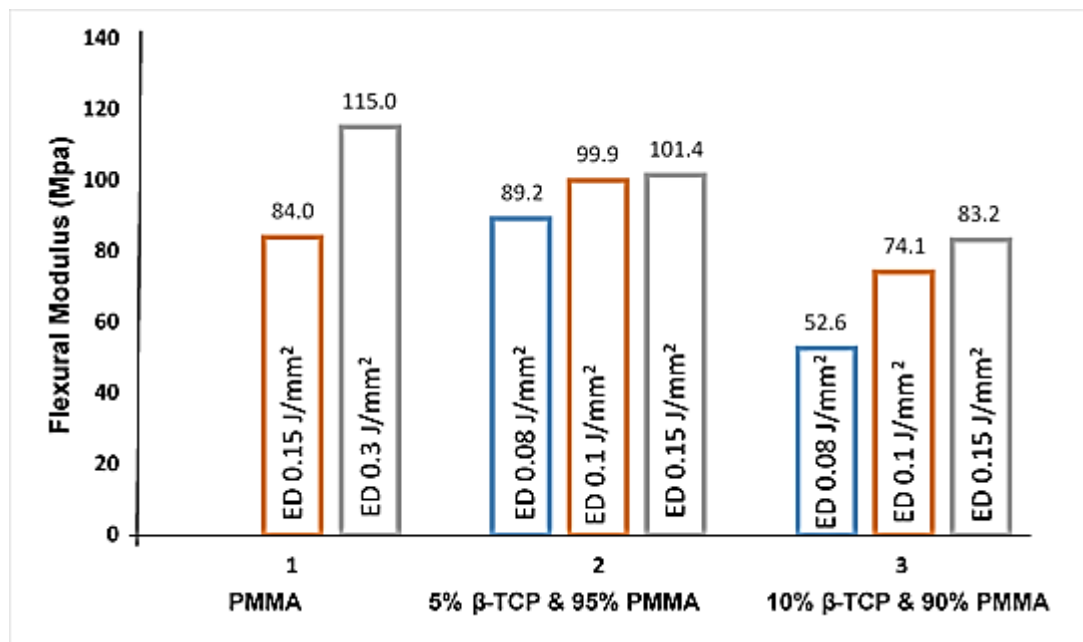
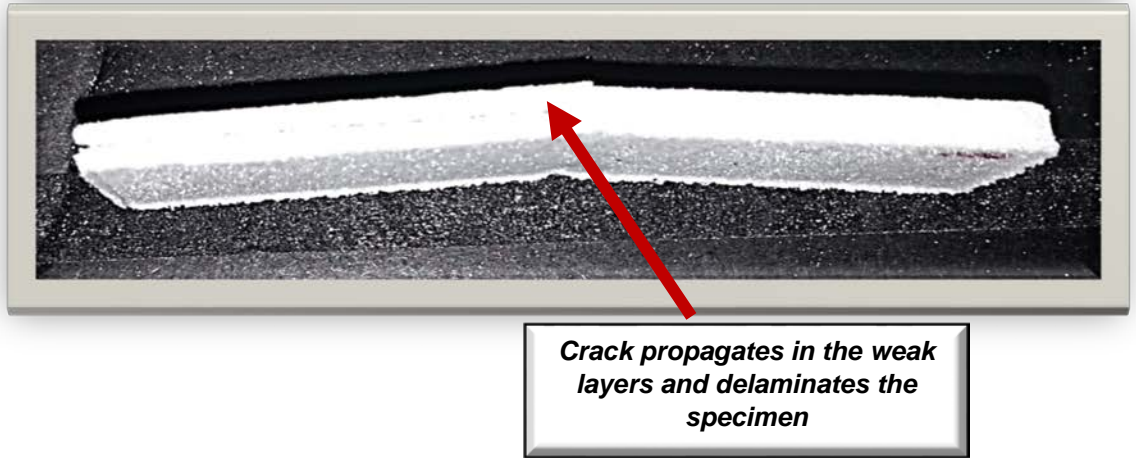
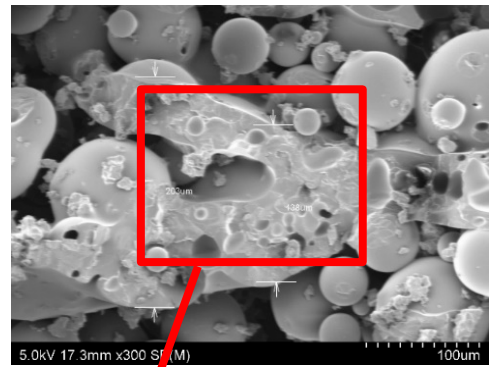
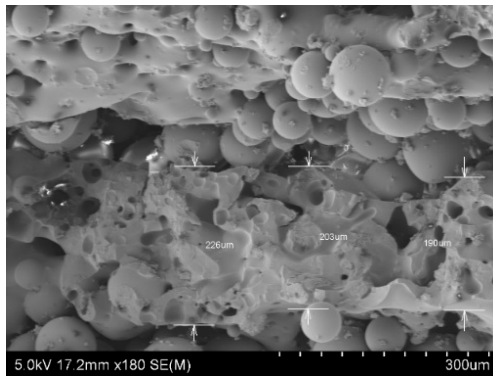


Figure 6.18 Flexural Modulus of PMMA and PMM/ β TCP composites



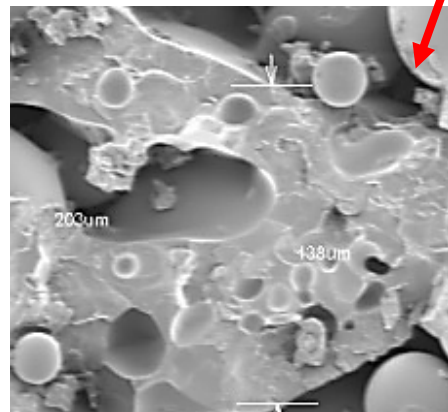
Crack propagates in the weak layers and delaminates the specimen

Figure 6.19 Fractured specimen and surfaces



(a)

(b)



(c)

Figure 6.20 Fractured surface of a laser sintered PMM/ β -TCP composite sample

A fractured polymer composite sample is presented in Fig. 6.19, indicating the fractured layers and subsequent delamination resulting from the shear sliding along the loosely sintered layers. SEM images of the fractured surface of a sintered PMMA plus β -TCP specimen subjected to three-point bending loads to failure are presented in Fig. 6.20. Each section of the sintered specimen is made up of several sintered layers and depending on the process conditions some loosely bound particles sandwiched in between. Under the compressive load, the bottom most layer is first stressed under tension while the upper most layer is under compression. The layers of insufficient coalescence act as cushioning zones. The sintered layers will begin to fail first due to the initiation and propagation of a randomly generated crack at points of stress concentration. Once this begins, the loosely packed powder layers allow the shear sliding of the sintered layers, leading to the final failure of the printed part. The images presented in Fig. 6.20 signify the fractured sintered layers, while the intermediate layers appear to be depleted of the loose particles. Considering the close up view of the fractured layer as in Fig. 6.20 (c) a brittle fracture mode is evident, probably due to the presence of the β -TCP particles in the polymer matrix [113i].

6.6 Summary of post-sintering analyses

The after-effects of laser sintering both neat PMMA and PMMA plus β -TCP material compositions are evaluated based on FTIR and in-vitro studies. The FTIR results indicated no loss of the polymer chemistry or composition due to the laser interactions and heating. *In vitro* studies based on MTT and ALP assays, Alizarin R staining, morphological studies and RNA quantification led to the

understanding that the biological attributes of both PMMA and β -TCP are preserved even after subjecting the powder substrates to severe thermal conditions during sintering. Morphological, physical, and mechanical evaluation of the multi-layer sintered samples of different compositions allowed to establish the expected attributes of the biopolymer materials investigated for selective laser sintering.

Chapter 7

Conclusions

7.1 Research undertaken and overall observations

Poly (methyl methacrylate) (PMMA) is reviewed to be a promising candidate material for numerous applications, including the medical needs; in particular, in the bone repair and replacement tasks. The beta form of tri-calcium phosphate (β -TCP) is the bio-ceramic option to impart the bio-conductive nature to base polymers such as PMMA. Both PMMA and the PMMA plus β -TCP composites are processed by different means but the literature review identified the gap in the understanding of the possible use of the more promising additive processing methods, in particular the selective laser sintering technology. The hypothesis that both these material options are suitable for processing by selective laser sintering is tested and proved to be correct in this thesis. The remainder of this chapter is a review of the significant systems developed, aspects investigated and critical conclusions drawn based on the results.

Experimentally evaluating the medical grade PMMA powders and the PMMA plus β -TCP composites for selective laser sintering is the primary objective of this work. An experimental setup is designed and developed based on a CO₂ laser including the hardware and software components and their integration. With the peripheral arrangements allowing to control the envelope temperature and powder feeding also added, the overall system led to laser sintering powder materials of varying compositions with complete control on the critical process

parameters. Powders of varying compositions are thermally characterised by differential scanning calorimetry. Laser sintering responses of different polymer compositions are established both qualitatively and quantitatively based on surface morphology, physical, and mechanical studies. FTIR analyses and in-vitro studies allowed to establish the post-sintering chemical and biological attributes.

Laser sintering trials with neat PMMA powders began with the DSC analysis, leading to the estimate of the minimum energy density requirements. The powder bed temperature and the focal distance for the heat-lamp are optimised by trial and error methods. Initial experiments are conducted varying both laser power and scan velocities but ensuring overall that the energy density levels are above the minimum required values and at 0.15 J/mm^2 , 0.3 J/mm^2 , and 0.4 J/mm^2 . Surface morphologies of sintered specimens allowed to identify the directions for the more optimum laser power and scan velocity settings, but with energy densities at 0.15 J/mm^2 and 0.3 J/mm^2 . Repeated sintering at the renewed process settings and evaluation of the critical responses allowed to complete the experimental trials and draw the conclusion that PMMA powders are suitable for selective laser sintering.

PMMA plus β -TCP composite powders are investigated in similar lines next, but mixing the powders manually. The DSC results led to establishing the minimum energy density requirement for the polymer composites at around 0.03 J/mm^2 to 0.05 J/mm^2 . Initial experimental results based on surface morphologies with energy densities varied above the minimum levels allowed to identify the significantly different responses by the polymer composite. Further sintering

experiments are conducted with the energy density levels and the constituent laser power and scan velocity settings better optimised based on the initial sintering results. Randomly created large voids are noticed in the single layer surface morphologies, indicating rheological variations with increasing β -TCP. This is presumably due to the variation in the thermal nature of the polymer composites further to adding the β -TCP component. Subsequent thermal analyses based on numerical and experimental methods confirmed this.

Infrared spectral results based on FTIR tests allowed to identify the polymer chemistry to be intact further to laser processing both neat PMMA and PMMA plus β -TCP powders. The *in vitro* behaviour evaluated based on MTT and ALP assays, Alizarin red S staining, and the FE-SEM imaging confirmed the biological responses to be positive even after the severe thermal loading on the sensitive polymer phases during the laser interaction stages. Sintering trials conducted based on multi-layer printed samples allowed assessment of the inter-layer coalescence. Overall, the methods identified and employed served to achieve the research objectives and the material systems under investigation could be characterised as possible candidates for selective laser sintering.

7.2 General conclusions

Experimental evaluations planned for a three-stage implementation are successfully completed allowing to draw several conclusions. The more general conclusions are listed in this section.

(a) Neat PMMA

The kinetic and thermodynamic parameters established based on DSC tests allowed to identify the baseline energy density levels for sintering with neat PMMA powders. Morphologies of single layer sintered PMMA specimens indicate 0.15 J/mm², 0.3 J/mm², and 0.4 J/mm² as the most promising energy density values. The corresponding working ranges of laser power and scan speed settings are identified as 9 W to 24 W and 38 mm/s to 254 mm/s respectively. Further morphological observations allowed to converge on 0.15 J/mm² and 0.3 J/mm² as the best energy density levels for neat PMMA powders, with the working laser power range amended to 20 - 35 W and corresponding changes in the scan velocity settings. Within the limits of these process parameters, the porosity generally decreased with increasing laser power, while the average pore size is at around 150 μm.

(b) PMMA-β-TCP polymer composites

DSC results confirmed the activation energy levels decreasing with increasing addition of β-TCP particles within the PMMA powder matrix, while the heat capacity levels increase. The glass transition temperature decreases and the enthalpy increases with increasing levels of β-TCP. The *a priori* minimum energy density levels for sufficient inter-particle coalescence are identified to range from 0.03 J/mm² to 0.05 J/mm² for the PMMA/β-TCP composite powders. Based on this and some basic laser sintering trials, the working ranges for laser power and

scan velocities 13 to 24 W and 250 to 500 mm/s respectively are established for the initial sintering trials involving PMMA/ β -TCP composite powders.

Material consolidation results based on surface morphologies of sintered layers indicated the higher power and lower velocity setting as the better process parameter combination, but optimum levels are evidently beyond the initial ranges of process parameters. Rheological changes are clearly evident in the polymer substrate further to adding the β -TCP component. Differential thermal attributes of the two material components and the mechanical resistance leading to changes in viscosities of the melt pools are identified to be the plausible causes. Consequently, the porosity levels are higher in the PMMA/ β -TCP single layers sintered.

Based on the results from the initial sintering trials, the more promising ranges for the energy density levels are identified to vary from 0.1 to 0.16 J/mm². The laser power and velocity ranges for these trials are at 18 to 22.8 W and 208 to 422 mm/s respectively. Morphologies of sintered surfaces and EDS analyses and further mechanical characterisation led to the understanding that slightly lower energy range from 0.08 to 0.15 J/mm² achieved through higher laser power and scan velocity ranges 34 to 42 W and 450 to 810 mm/s respectively as the better optimum parameter settings. Further analyses based on these parameter settings allowed to converge on the laser power 38 W and scan speeds from 480 mm/s to 780 mm/s as the best parameter settings for achieving the most favourable layer formation based on the polymer composites with the β -TCP content below 15%.

The 20% β -TCP case responded quite differently, as the higher β -TCP content caused detrimental effects on the consolidation of the layers plausibly due to the significant changes to the thermal characteristics of the powder substrates. The thermo-gravimetric results and the finite element and experimental measurements of the temperature variations along single laser scan lines confirmed these observations. The presence of the β -TCP particles increases the laser absorptivity levels, but most of the energy absorbed preferentially goes into the β -TCP phase, while the PMMA particles receive lesser energy apportionment, resulting in an overall reduction in the temperature at a given point.

(c) *Post sintering responses*

The infrared spectra from all sintered samples of all compositions closely matched with the raw PMMA powder results, indicating no loss of the polymer chemistry due to laser sintering. Porosity levels gradually increased with increasing β -TCP contents while the pore sizes also varied quite widely. The FTIR results and the porosity analysis confirm both the stability and the mesostructures of the sintered specimens to be amenable to promote cell proliferation and growth in the *in vitro* environment.

The *in vitro* results in general confirmed the biological responses of the sintered specimens to be good. All sintered specimens showed cytocompatibility, facilitating the growth of the MG-63 cells. The presence of β -TCP helped improve the cell proliferation and differentiation, but only up to a certain limit, which is around 15% β -TCP in the current cases. It is possible that the cells grow into the porous holes and do not show up in the tests, in particular at higher β -TCP levels

with which porosities are much higher. Evidence of the formation of the extra cellular matrix is noted. The Alizarin-red S staining results confirm better mineralisation with increasing β -TCP contents. Overall, the β -TCP content and the nature and the extent of porosity controlled the adsorption of protein, in promoting the attachment and proliferation of the osteosarcoma cells.

Multi-layer sintering trials are done using energy densities 0.15 J/mm² and 0.3 J/mm² for neat PMMA and 0.08 and 0.15 J/mm² for PMMA plus β -TCP composites, while the layer thickness is commonly maintained at 0.1 mm. Excessive heating and loss of the layer thickness and accumulation of excessive powder particles in successive layers are noted to be the major problems. Use of the optimum powder bed temperature together with the overhead heat-lamp system allowed resolving these shortcomings. The inter-layer coalescence is noted to improve with increasing laser power. A blanketing effect of the rapidly formed thin layers is noted to block heat flow across the layers in the polymer composite, resulting in loosely packed particles in the inter-layer spaces.

Sintered layers in neat PMMA powders are noted to shrink and lead to inter-layer shrinkage cavities and relatively macro porosities. The PMMA/ β -TCP cases tend to improve in this respect with increasing β -TCP content, but show predominantly intra-layer micro porosities. The flexural modulus values of multi-layer sintered specimens decrease with increasing β -TCP contents. More uniform dispersion of the β -TCP particles is noted with better sintered layers, while agglomeration of the filler particles occurs when the sintered layers are more porous.

7.3 More specific and quantitative conclusions

More specific and quantitative conclusions drawn from the results of the experimental investigations undertaken at three different stages are listed in this section:

Stage I: Selective laser sintering of neat PMMA

Initial sintering trials

- Very high scan speeds of the order of 5080 mm/s with power at 24 W and 42 W result in a sparsely connected network of the raw powder particles indicating insufficient sintering.
- Reducing scan speeds to 1524 mm/s and 1016 mm/s, (power 6 W to 24 W) still showed lack of energy absorption and significant inter-particle fusion.
- Scan speeds at 254 mm/s and 127 mm/s, and laser power 6 W to 24 W improve the inter-particle coalescence as reflected by the plastered granular appearance of layers.
- With laser scan speed reduced to as low as 38 mm/s, a drastic reduction in power to 6W and 9 W becomes necessary to achieve uniform and sufficient coalescence.
- Evidently, laser scan speed and power settings interact and significantly affect the sintering qualities

Further sintering trials

- Further sintering trials based on 0.15 J/mm², 0.3 J/mm² and 0.4 J/mm² energy density levels gave good results with several combinations of laser power and scan speed settings.
- The higher energy density 0.4 J/mm² and the higher power 18 W and 24 W levels resulted in better laser consolidation of powder particles and complete fusion, leading to almost indistinguishable inter particle boundaries.
- Porosities are observed in all samples, but with the intensities decreasing with increased coalescence across the thin layer.
- Further sintering trials with energy densities at 0.15 and 0.30 J/mm² and laser power settings ranging from 20 W to 35 W resulted in the average pore size at around 150 μm, as the percentage porosity decreased with increase in the laser power from 20 W to 35 W.
- With energy density at 0.15 J/mm², varying the power from 20 W to 30 W led to almost doubling the tensile strength from 1.16 MPa to 2.27 MPa and about a 30% rise in the elastic modulus, from 265 MPa to 343 MPa.
- Similar trends are noticed with the energy density at 0.3 J/mm² also, as tensile strength and elastic modulus increased from 1.37 MPa to 2.4 MPa and 303 MPa to 353 MPa respectively.
- The level of porosity is decreased from 61% to 55% with increase in the laser power from 20 W to 35 W at 0.15 J/mm².
- Similarly, percent porosity levels reduced from 57% to 52 % with increasing the laser power from 20 W to 30 W at 0.3 J/mm².

Stage II: Selective laser sintering PMMA/ β -TCP polymer composites

DSC analysis

- The activation energy gradually decreased with increasing β -TCP in PMMA starting with a 32.955 J/mol with neat PMMA and ending up at 26.22 J/mol with the 20% β -TCP composite.
- The heat capacity increased from 0.870 J/g⁰C as noted for the neat PMMA to 1.045 J/g⁰C with the 20% β -TCP composite.
- The glass transition temperature indicates a reduction from 125 °C with neat PMMA to 92.7 °C with the 20% β -TCP case.
- The enthalpy increased with increasing β -TCP from 21.32 J/g to 31.92 J/g.
- The overall DSC result shows that the β -TCP phase allows for a higher rate of heating, resulting in the melting phase (PMMA) to undergo phase transition at a lower temperature within the polymer composite, as compared to the neat PMMA.

Initial sintering trials

- From the initial sintering trials, gradual improvement in coalescence occurred with increasing power from 13W to 24 W at scan speeds 381 mm/s and 254 mm/s.
- The sample sintered with the lowest speed (254 mm/s) and the highest power (22.8 W) exhibited the best results with the PMMA phase coalescing significantly over wide areas.
- The thickness of the sintered layer increased from 0.4 mm to 0.8 mm with increasing laser power from 13 W to 27 W, as the energy absorption increases resulting in a wider sintered zone.

- While the process attributes significantly changed for the 20% β -TCP / 80 % PMMA case, overall, the laser sintering behaviour of the material changed with the increased amounts of β -TCP.
- At higher β -TCP contents, though some improvement is noted in the coalesced state from the higher speed 508 mm/s to the lower scan speed case 254 mm/s, the material response to sintering is generally poor due to the rheological changes in the PMMA melt pools.

Further sintering trials

- Further sintering trials at 0.1 J/mm², 0.12 J/mm², 0.14 J/mm², 0.16 J/mm² energy density settings showed similar levels of coalescence and consolidation of the PMMA powder in three samples repeated at each given energy density level.
- Overall, the energy density levels 0.14 J/mm² and 0.16 J/mm² appeared to give better sintering results.
- Partial melting and neck formation are also noted when the laser power is less than 18 W, while complete fusion made the boundaries of particles indistinguishable when the laser power is increased beyond 18 W and up to 22.8 W.
- Large voids are randomly created due to the presence of the β -TCP particles, increasing the viscosity of the melt pool as well as offering resistance to the melt flow.
- With further optimised energy density levels at 0.08 J/mm², 0.1 J/mm², 0.15 J/mm², the lower power settings gave good sintering results, but with the laser power increased from 34 W to 42 W, at 0.08 J/mm² the 5% β -TCP samples are thermally affected resulting in polymer degradation.

- With the 10% β -TCP case, the porosity level increased at 42 W laser power and the overall surfaces for all parameter settings at 0.08 J/mm² looked quite irregularly shaped.
- The 15% and 20% β -TCP cases also showed increased porosity levels due to insufficient fusion at 0.08 J/mm²
- The 20 % β -TCP sample actually caught fire at 42 W laser power, while the 34W and 450mm/s power and speed setting sintered fine.
- Similar observations are noted with the 0.1 J/mm², but with 0.15 J/mm² the lower power range resulted in insufficient fusion between adjacent scan lines while the higher laser power 42 W settings resulted in better inter-strand fusion.
- The porosity levels and surface irregularities increased with the higher β -TCP contents, at above 15 % and 20%, while the 20% of β -TCP also resulted in excessive particle agglomerations
- Based on these results, the most promising laser power range is identified to be around 38 W, while the laser scan speed could be varied at 480 mm/s, 680 mm/s, and 780 mm/s, achieving the three energy density levels identified.
- Further, the porosity level within the polymer matrix also increased from 50% to 70 % with increasing β -TCP from 5% to 20%.
- With the 10% β -TCP composite, the formation of the base polymer matrix layer improves as the laser power is increased with a given scan speed, reaching the optimum quality levels at around 42 W.
- With further increase in power, at around 45 W, the PMMA layer bubbles, undulates, and often ruptures, but the β -TCP particles will still be segregated over the surface

- Generally, the sintering responses of the 20% β -TCP composites are quite poor. The particle dispersion mechanisms change completely as the β -TCP particles are observed to be fully covered by the PMMA matrix, and the general structure of the layer becomes very irregular
- Overall, the 5%, 10 %, and 15 % of β -TCP combinations gave better young's modulus values from 6×10^6 MPa to 9.5×10^6 MPa but the 20% β -TCP case resulted in a lower elastic modulus at 2×10^6 MPa, as the porosity levels increased resulting in insufficient consolidation within the layers

Thermal evaluations

- Pure PMMA begins to degrade at around 212°C and continues to degrade with the increase in temperature and attains about 45% degradation in the temperature range from 300 to 350°C . Complete degradation is noted at around 400°C ,
- The β -TCP and PMMA composite powders begin deteriorating at around 240°C , followed by a gradual loss of mass but show characteristic fluctuations in the mass loss vs temperature curves.
- The PMMA phase degrades and gets lost with heating beyond 240°C , while the β -TCP remains undisturbed and begins to form the composite rich in the ceramic phase.
- Numerical simulations predicted that the higher the β -TCP content, the slower the temperatures rise as well as the lower the peak temperature.
- Results of the temperature measurements showed each experimental point reaching a maximum temperature of around 248°C with neat PMMA

sintering, while almost similar temperature-time profiles are also recorded for PMM/ β -TCP composites.

- As the β -TCP content is increased to 5% and then 10%, a significant delay in reaching the maximum temperature occurs at the start point, while each of the subsequent points experiences an accelerated temperature rise.
- The FE simulations predicted the peak temperature to vary from 235–251°C but the experimental results did not show any appreciable variation in the peak temperature with composition

Stage III Post-processing responses

FTIR analysis

- The infra-red spectra of all samples very closely matched with those of the original PMMA powder and the other reports in the literature.
- The absorption band observed in the spectrum at 10.6 μm (wave number 943.40 cm^{-1}) confirmed that 90% of the energy of the 10.6 μm wave length CO_2 laser is absorbed by the PMMA sample.

In vitro studies

- Based on the statistical significance of the MTT assay results, both 5% and 15% β -TCP samples are observed to exhibit more than normal levels of cell proliferation
- Three polymer-ceramic composites 5% β -TCP/ 95% PMMA, 15% β -TCP/ 85% PMMA, and 20% β -TCP/80% PMMA demonstrated increased ALP activity from day 4 to day 7

- Alizarin-red S tests indicate that the polymer composite samples stained much higher compared to the pure PMMA samples.
- Also, the higher the β -TCP content, the better is the Alizarin-red S staining.
- An extra cellular matrix (ECM) formed in both 5% β -TCP/ 95% PMMA and the 15% β -TCP/ 85% PMMA samples.
- The 10% β -TCP sample showed diminishing and unhealthy cells on the 10th day
- With the β -TCP content increased to 15% and 20 %, the cells are again widespread and healthy and a clear evidence of the formation of ECM is noted.

Multi-layer sintering

- The glass transition temperature of neat PMMA at around 105 °C is identified as the optimum powder bed temperature to achieve sufficient inter-layer coalescence in the multi-layer samples.
- Insufficient inter-particle coalescence is evidenced through almost spherical particles observed in the morphologies of cross sections of neat PMMA samples sintered at 0.15 J/mm² energy density
- A higher degree of inter particle coalescence is achieved for neat PMMA with the energy density increased to 0.3 J/mm²
- Overall, the cross sections look good and evident of the formation of a continuous network of solid polymer, surrounding the micro and macro porosities.

- Lower energy density levels such as 0.08 J/mm² and 0.1 J/mm² resulted in the lack of inter-particle consolidation for all combinations of the critical laser parameters.
- With the lower energy density levels, the layers formed are thin and the energy is insufficient to flow across layers and led to serious lack of inter-layer consolidation and the presence of loose PMMA particles floating in between the thin solid layers.
- Incremental improvements are evidenced as the energy density and other parameter settings are set to 0.15 J/mm², 42 W, and 510 mm/s. The layers formed are thicker, with substantial intra-layer consolidation
- The higher power cases scored even better. The specimen produced at 42 W and 510 mm/s is identified to be the best in terms of achieving the most effective intra- and inter-layer coalescence and consolidation.
- All the above observations are based on the 5% β -TCP case, but are noted to be equally true with the 10% β -TCP cases also.
- Still higher levels of the β -TCP resulted in a loss of inter-layer quality with multi-layer sintering.
- Evidently, the neat PMMA samples sintered to better densities at around 1.96 g/cm⁻³.
- Within the limits of the process conditions used, only slight variations in bulk density values are noted for both 5% and 10 % β -TCP combinations with varying laser power.
- The sintered specimens attained an average porosity of around 20% at 0.15 J/mm² while the pore sizes vary from 10 μ m to 65 μ m.
- Based on the 5% β -TCP/ 95% PMMA and the 10% β -TCP/ 90% PMMA samples sintered at 0.15 J/mm² energy density, the 5% β -TCP case

resulted in larger porous holes mainly segregated along the inter-layer boundaries, while the 10% β -TCP case showed predominantly intra-layer micro porous hole appearance.

- The flexural moduli values decreased with the addition of the β -TCP particles in the PMMA matrices.
- In the case of neat PMMA, the maximum flexural modulus 115 MPa is achieved at 0.3 J/mm² with laser power 30W and scan speed 185 mm/s.
- For the 5% β -TCP/95% PMMA case, the maximum flexural modulus achieved is 101.4 MPa with critical process parameters at 0.15 J/mm², 42 W, and 510 mm/s.
- The flexural modulus values reduced to 83.2 MPa with the 10% β -TCP/90% PMMA case, at 0.15 J/mm², 42 W, and 510 mm/s laser settings.
- Fractured surfaces of the sintered polymer composite samples indicate brittle fracture modes, probably due to the presence of the ceramic component and the polymer-ceramic interactions.

7.4 Future course

The Neat PMMA polymer and the PMMA plus β -TCP polymer composites in powder forms are analysed for their suitability to be processed by selective laser sintering. Both material components and their combinations are already well established for use in different medical applications. In particular, the bone repair and replacement uses are noteworthy. The selective laser sintering process is new and rapidly emerging as an alternative to other traditional methods in varied applications. The ability to convert raw materials in powder forms into ready to

use 3D forms and the scope of achieving unlimited design freedom make SLS a potential solution in many application areas, including the medical uses.

The current research is the first attempt towards bringing the two well-established medical material systems and the newly emerging SLS technology together. Considering the absence of any *a priori* data, the research is focussed on initial evaluation of the powder materials for a set of selected conditions, analysis of the material consolidation mechanisms, and converging on more promising combinations of material and process parameters. Considerable time is also spent identifying and developing the experimental methods and facilities. Overall, the experimental results and the inferences drawn prove the material and process combination to be successful. However, the main attention of this work is in the fundamental research ascertaining the material and process interactions and the absence of post-process residual adverse effects.

Overall, the results are very positive and both neat PMMA and PMMA plus β -TCP are proved to be candidate material systems for SLS. Optimum process parameters are established within the working ranges of material compositions and other process parameter settings. Both the basic chemistry and the biological attributes of the constituent material systems are proved to be intact even after the severe thermal stressing due to SLS. The next course of action is to undertake both material and process enhancements. The material composition can further be enhanced including specific other elements, targeting better mechanical and biological responses. Further research is also essential based on multi-layer sintering experiments leading to the fabrication of specific three

dimensional objects, real world bone replacement components, and implants. *In vivo* studies based on implants made of the optimised material and process conditions will eventually allow to complete the research tasks initiated through this thesis.

References

1. Logeart-Avramoglou, D., Anagnostou, F., Bizios, R., & Petite, H. (2005). Engineering bone: challenges and obstacles. *Journal of cellular and molecular medicine*, 9(1), 72-84.
2. Ben-Nissan, B. (2003). Natural bioceramics: from coral to bone and beyond. *Current opinion in solid state and materials science*, 7(4), 283-288.
3. Lane, J. M., Tomin, E., & Bostrom, M. P. (1999). Biosynthetic bone grafting. *Clinical orthopaedics and related research*, 367, S107-S117.
4. Pelker, R. R., & Friedlaender, G. E. (1987). Biomechanical aspects of bone autografts and allografts. *The Orthopedic clinics of North America*, 18(2), 235-239.
5. Mankin, H. J., Gebhardt, M. C., Jennings, L. C., Springfield, D. S., & Tomford, W. W. (1996). Long-term results of allograft replacement in the management of bone tumors. *Clinical orthopaedics and related research*, 324, 86-97.
6. Strong, D. M., Friedlaender, G. E., Tomford, W. W., Springfield, D. S., Shives, T. C., Burchardt, H., ... & Mankin, H. J. (1996). Immunologic responses in human recipients of osseous and osteochondral allografts. *Clinical orthopaedics and related research*, 326, 107-114.
7. Simonds, R. J., Holmberg, S. D., Hurwitz, R. L., Coleman, T. R., Bottenfield, S., Conley, L. J., ... & Rayfield, M. A. (1992). Transmission of human immunodeficiency virus type 1 from a seronegative organ and tissue donor. *New England Journal of Medicine*, 326(11), 726-732.
8. Jensen, S. S., Aaboe, M., Pinholt, E. M., Hjoerting-Hansen, E., Melsen, F., & Ruyter, I. E. (1996). Tissue reaction and material characteristics of four bone substitutes. *International Journal of Oral and Maxillofacial Implants*, 11(1), 55-66.
9. Moore, W. R., Graves, S. E., & Bain, G. I. (2001). Synthetic bone graft substitutes. *ANZ journal of surgery*, 71(6), 354-361.
10. Albee, F. H. (1920). Studies in bone growth: triple calcium phosphate as a stimulus to osteogenesis. *Annals of surgery*, 71(1), 32.
11. Goodridge, R. D., Dalgarno, K. W., & Wood, D. J. (2006). Indirect selective laser sintering of an apatite-mullite glass-ceramic for potential

- use in bone replacement applications. *Proceedings of the Institution of Mechanical Engineers, Part H: Journal of Engineering in Medicine*, 220(1), 57-68.
12. Asti, A., & Gioglio, L. (2014). Natural and synthetic biodegradable polymers: different scaffolds for cell expansion and tissue formation. *The International journal of artificial organs*, 37(3), 187-205.
 13. Vroman, I., & Tighzert, L. (2009). Biodegradable polymers. *Materials*, 2(2), 307-344.
 14. Tas, A. C., Korkusuz, F., Timucin, M., & Akkas, N. (1997). An investigation of the chemical synthesis and high-temperature sintering behaviour of calcium hydroxyapatite (HA) and tricalcium phosphate (TCP) bioceramics. *Journal of Materials Science: Materials in Medicine*, 8(2), 91-96.
 15. Gauthier, O., Goyenvalle, E., Bouler, J. M., Guicheux, J., Pilet, P., Weiss, P., & Daculsi, G. (2001). Macroporous biphasic calcium phosphate ceramics versus injectable bone substitute: a comparative study 3 and 8 weeks after implantation in rabbit bone. *Journal of materials science: materials in medicine*, 12(5), 385-390.
 16. Baxter, R. M., MacDonald, D. W., Kurtz, S. M., & Steinbeck, M. J. (2013). Severe impingement of lumbar disc replacements increases the functional biological activity of polyethylene wear debris. *The Journal of Bone & Joint Surgery*, 95(11), e75.
 17. Kim, H., Kim, H. M., Jang, J. E., Kim, C. M., Kim, E. Y., Lee, D., & Khang, G. (2013). Osteogenic differentiation of bone marrow stem cell in poly (lactic-co-glycolic acid) scaffold loaded various ratio of hydroxyapatite. *International journal of stem cells*, 6(1), 67.
 18. Seunarine, K., Gadegaard, N., Tormen, M., Meredith, D. O., Riehle, M. O., & Wilkinson, C. D. W. (2006). 3D polymer scaffolds for tissue engineering.
 19. Agrawal, C., & Ray, R. B. (2001). Biodegradable polymeric scaffolds for musculoskeletal tissue engineering. *Journal of biomedical materials research*, 55(2), 141-150.
 20. Naing, M. W., Chua, C. K., & Leong, K. F. (2008). Computer aided tissue engineering scaffold fabrication. In *Virtual Prototyping & Bio Manufacturing in Medical Applications* (pp. 67-85). Springer US.

21. Bonfield, W., Wang, M., & Tanner, K. E. (1998). Interfaces in analogue biomaterials. *Acta Materialia*, 46(7), 2509-2518.
22. Thomson, R. C., Shung, A. K., Yaszemski, M. J., & Mikos, A. G. (2000). Polymer scaffold processing. *Principles of tissue engineering*, 2, 251-62.
23. Niklason, L. E., & Langer, R. (2001). Prospects for organ and tissue replacement. *Jama*, 285(5), 573-576.
24. Leong, K. F., Cheah, C. M., & Chua, C. K. (2003). Solid freeform fabrication of three-dimensional scaffolds for engineering replacement tissues and organs. *Biomaterials*, 24(13), 2363-2378.
25. Chua, C. K., & Leong, K. F. (2003). *Rapid prototyping: principles and applications* (Vol. 1). World Scientific.
26. Hao, L., Savalani, M. M., Zhang, Y., Tanner, K. E., & Harris, R. A. (2006). Selective laser sintering of hydroxyapatite reinforced polyethylene composites for bioactive implants and tissue scaffold development. *Proceedings of the Institution of Mechanical Engineers, Part H: Journal of Engineering in Medicine*, 220(4), 521-531.
27. Savalani, M. M., Hao, L., & Harris, R. A. (2006). Evaluation of CO₂ and Nd: YAG lasers for the selective laser sintering of HAPEX®. *Proceedings of the Institution of Mechanical Engineers, Part B: Journal of Engineering Manufacture*, 220(2), 171-182.
28. Lewis, G. (2009). Properties of antibiotic-loaded acrylic bone cements for use in cemented arthroplasties: A state-of-the-art review. *Journal of Biomedical Materials Research Part B: Applied Biomaterials*, 89(2), 558-574.
29. Puska, M. A., Kokkari, A. K., Närhi, T. O., & Vallittu, P. K. (2003). Mechanical properties of oligomer-modified acrylic bone cement. *Biomaterials*, 24(3), 417-425.
30. Jarcho, M., Kay, J. F., Gumaer, K. I., Doremus, R. H., & Drobeck, H. P. (1977). Tissue, cellular and subcellular events at a bone-ceramic hydroxylapatite interface. *Journal of Bioengineering*, 1(2), 79-92.
31. Descamps, M., Richart, O., Hardouin, P., Hornez, J. C., & Leriche, A. (2008). Synthesis of macroporous β -tricalcium phosphate with controlled porous architectural. *Ceramics International*, 34(5), 1131-1137.
32. Kalita, S. J., Bose, S., Hosick, H. L., & Bandyopadhyay, A. (2003). Development of controlled porosity polymer-ceramic composite scaffolds

- via fused deposition modeling. *Materials Science and Engineering: C*, 23(5), 611-620.
33. Duan, B., Wang, M., Zhou, W. Y., Cheung, W. L., Li, Z. Y., & Lu, W. W. (2010). Three-dimensional nanocomposite scaffolds fabricated via selective laser sintering for bone tissue engineering. *Acta Biomaterialia*, 6(12), 4495-4505.
 34. Lee, G., & Barlow, J. W. (1994, September). Selective laser sintering of calcium phosphate powders. In *Proceedings of the Solid Freeform Fabrication Symposium, Austin, TX* (pp. 191-197).
 35. <http://www.britannica.com/science/polymethyl-methacrylate>.
 36. Mark, H. F. (2013). *Encyclopedia of polymer science and technology, concise*. John Wiley & Sons.
 37. Szeteiová, K. (2010). Automotive materials: plastics in automotive markets today. *Institute of Production Technologies, Machine Technologies and Materials, Faculty of Material Science and Technology in Trnava, Slovak University of Technology Bratislava*.
 38. Altuglas, 2014, Acrylic Optical and Transmission Characteristics.
 39. Sood, V. (2007). *An Experimental Study on Thermal Bonding Effects of PMMA Based Micro-Devices Using Hot Embossing*. ProQUEST
 40. Schwartz, M. (Ed.). (2008). *Smart materials*. CRC Press
 41. Graessley, W. W. (1974). The entanglement concept in polymer rheology. In *The Entanglement Concept in Polymer Rheology* (pp. 1-179). Springer Berlin Heidelberg.
 42. Randall, J. N., Flanders, D. C., Economou, N. P., Donnelly, J. P., & Bromley, E. I. (1983). High resolution ion beam lithography at large gaps using stencil masks. *Applied Physics Letters*, 42(5), 457-459.
 43. Lee, E. H., Rao, G. R., & Mansur, L. K. (1996). Super-hard-surfaced polymers by high-energy ion-beam irradiation. *Trends in Polymer Science*, 7(4), 229-237.
 44. Choi, J. S., Park, B. J., Cho, M. S., & Choi, H. J. (2006). Preparation and magnetorheological characteristics of polymer coated carbonyl iron suspensions. *Journal of Magnetism and Magnetic Materials*, 304(1), e374-e376.
 45. Wildbrett, G., & Sauerer, V. (1989). Cleanability of PMMA and PP compared with stainless steel. *Fouling and Cleaning in Food Processing. Proceedings ICFC*, 163-177.

46. Shah, A., Spalton, D. J., Gilbert, C., Vasavada, A., Boyce, J. F., Minassian, D., ... & Mabey, D. (2007). Effect of intraocular lens edge profile on posterior capsule opacification after extracapsular cataract surgery in a developing country. *Journal of Cataract & Refractive Surgery*, 33(7), 1259-1266.
47. Alió, J. L., Chipont, E., BenEzra, D., Fakhry, M. A., & Group, I. O. I. S. S. (2002). Comparative performance of intraocular lenses in eyes with cataract and uveitis. *Journal of Cataract & Refractive Surgery*, 28(12), 2096-2108.
48. Bayindir, F., Kürklü, D., & Yanikoğlu, N. D. (2012). The effect of staining solutions on the color stability of provisional prosthodontic materials. *Journal of dentistry*, 40, e41-e46.
49. Ratner, B. D., Hoffman, A. S., Schoen, F. J., & Lemons, J. E. (2004). *Biomaterials science: an introduction to materials in medicine*. Academic press.
50. Park, S. E., Chao, M., & Raj, P. A. (2009). Mechanical properties of surface-charged poly (methyl methacrylate) as denture resins. *International journal of dentistry*, 2009.
51. BomBač, D., Brojan, M., Fajfar, P., Kosel, F., & Turk, R. (2007). Review of materials in medical applications Pregled materialov v medicinskih aplikacijah. *RMZ–Materials and Geoenvironment*, 54(4), 471-499.
52. Mousa, W. F., Kobayashi, M., Shinzato, S., Kamimura, M., Neo, M., Yoshihara, S., & Nakamura, T. (2000). Biological and mechanical properties of PMMA-based bioactive bone cements. *Biomaterials*, 21(21), 2137-2146.
53. Ibeh, C. C. (2011). *Thermoplastic materials: properties, manufacturing methods, and applications*. CRC Press.
54. Whitaker III, W.A. *Acrylic polymers: A clear focus*, <http://www.devicelink.com/mpb/archive/96/01/001.html>
55. Michaeli, W., Spennemann, A., & Gärtner, R. (2002). New plastification concepts for micro injection moulding. *Microsystem technologies*, 8(1), 55-57.
56. Michaeli, W., & Spennemann, A. (2001). A new injection molding technology for micro parts. *Journal of polymer engineering*, 21(2-3), 87-98.

57. Michaeli, W., Opfermann, D., & Kamps, T. (2007). Advances in micro assembly injection moulding for use in medical systems. *The International Journal of Advanced Manufacturing Technology*, 33(1-2), 206-211.
58. Piotter, V., Mueller, K., Plewa, K., Ruprecht, R., & Hausselt, J. (2002). Performance and simulation of thermoplastic micro injection molding. *Microsystem Technologies*, 8(6), 387-390.
59. Park, K. D., Khang, G. S., Lee, H. B., & Park, J. B. (2001). Characterization of compression-molded UHMWPE, PMMA and PMMA/MMA treated UHMWPE: density measurement, FTIR-ATR, and DSC. *Bio-medical materials and engineering*, 11(4), 311-323.
60. Ebnesajjad, G. G. H. (1998). *U.S. Patent No. 5,817,710*. Washington, DC: U.S. Patent and Trademark Office.
61. Azdast, T., Doniavi, A., Ahmadi, S. R., & Amiri, E. (2013). Numerical and experimental analysis of wall thickness variation of a hemispherical PMMA sheet in thermoforming process. *The International Journal of Advanced Manufacturing Technology*, 64(1-4), 113-122.
62. Dong, Y., Lin, R. J. T., & Bhattacharyya, D. (2005). Determination of critical material parameters for numerical simulation of acrylic sheet forming. *Journal of materials science*, 40(2), 399-410.
63. Mathur, A., Roy, S. S., Tweedie, M., Mukhopadhyay, S., Mitra, S. K., & McLaughlin, J. A. (2009). Characterisation of PMMA microfluidic channels and devices fabricated by hot embossing and sealed by direct bonding. *Current Applied Physics*, 9(6), 1199-1202.
64. Lee, G. B., Chen, S. H., Huang, G. R., Sung, W. C., & Lin, Y. H. (2001). Microfabricated plastic chips by hot embossing methods and their applications for DNA separation and detection. *Sensors and Actuators B: Chemical*, 75(1), 142-148.
65. Baird, Ronald J. and David T. Baird. *Industrial Plastics*. The Goodheart-Willcox Company, 1986.
66. Cowie, J.M.G. *Polymers: Chemistry and Physics of Modern Materials*. Chapman and Hall, 1991.
67. Messersmith, P. B., & Giannelis, E. P. (1995). Synthesis and barrier properties of poly (ϵ -caprolactone)-layered silicate

- nanocomposites. *Journal of Polymer Science Part A: Polymer Chemistry*, 33(7), 1047-1057.
68. Lee, D. C., & Jang, L. W. (1996). Preparation and characterization of PMMA–Clay hybrid composite by emulsion polymerization. *Journal of Applied Polymer Science*, 61(7), 1117-1122.
69. Lewis, G. (2009). Properties of antibiotic-loaded acrylic bone cements for use in cemented arthroplasties: A state-of-the-art review. *Journal of Biomedical Materials Research Part B: Applied Biomaterials*, 89(2), 558-574.
70. Smith, D. C. (1958). The acrylic denture base, residual monomer. *Br Dent J*, 105(5).
71. Park, J. B., & Bronzino, J. D. (Eds.). (2002). *Biomaterials: principles and applications*. crc press.
72. Spasojevic, P., Zrilic, M., Panic, V., Stamenkovic, D., Seslija, S., & Velickovic, S. (2015). The Mechanical Properties of a Poly (methyl methacrylate) Denture Base Material Modified with Dimethyl Itaconate and Di-n-butyl Itaconate. *International Journal of Polymer Science*, 2015.
73. Park, S. E., Chao, M., & Raj, P. A. (2009). Mechanical properties of surface-charged poly (methyl methacrylate) as denture resins. *International journal of dentistry*, 2009.
74. Shinzato, S., Nakamura, T., Kokubo, T., & Kitamura, Y. (2002). PMMA-based bioactive cement: Effect of glass bead filler content and histological change with time. *Journal of biomedical materials research*, 59(2), 225-232.
75. Hennig, W., Blencke, B. A., Brömer, H., Deutscher, K. K., Gross, A., & Ege, W. (1979). Investigations with bioactivated polymethylmethacrylates. *Journal of biomedical materials research*, 13(1), 89-99.
76. Heikkilä, J. T., Aho, A. J., Kangasniemi, I., & Yli-Urpo, A. (1996). Polymethylmethacrylate composites: disturbed bone formation at the surface of bioactive glass and hydroxyapatite. *Biomaterials*, 17(18), 1755-1760.
77. Freeman, M. A., Bradley, G. W., & Revell, P. A. (1982). Observations upon the interface between bone and polymethylmethacrylate cement. *Bone & Joint Journal*, 64(4), 489-493.

78. Saha, S., & Pal, S. (1984). Mechanical properties of bone cement: a review. *Journal of biomedical materials research*, 18(4), 435-462.
79. Maloney, W. J., Jasty, M., Rosenberg, A., & Harris, W. H. (1990). Bone lysis in well-fixed cemented femoral components. *Bone & Joint Journal*, 72(6), 966-970.
80. Amato, I. (1999). Reverse engineering the ceramic art of algae. *Science*, 286(5442), 1059-1061.
81. Popister, F., Popescu, D., & Hurgoiu, D. (2012). A new method for using reverse engineering in case of ceramic tiles. *Calitatea*, 13(5).
82. Yang, S., Leong, K. F., Du, Z., & Chua, C. K. (2002). The design of scaffolds for use in tissue engineering. Part II. Rapid prototyping techniques. *Tissue engineering*, 8(1), 1-11.
83. Yeong, W. Y., Chua, C. K., Leong, K. F., & Chandrasekaran, M. (2004). Rapid prototyping in tissue engineering: challenges and potential. *Trends in biotechnology*, 22(12), 643-652.
84. Eufinger, H., Wehmöller, M., Machtens, E., Heuser, L., Harders, A., & Kruse, D. (1995). Reconstruction of craniofacial bone defects with individual alloplastic implants based on CAD/CAM-manipulated CT-data. *Journal of Cranio-Maxillofacial Surgery*, 23(3), 175-181.
85. Klein, M., & Glatzer, C. (2006). Individual CAD/CAM fabricated glass-bioceramic implants in reconstructive surgery of the bony orbital floor. *Plastic and reconstructive surgery*, 117(2), 565-570.
86. Tan, K. H., Chua, C. K., Leong, K. F., Cheah, C. M., Cheang, P., Bakar, M. A., & Cha, S. W. (2003). Scaffold development using selective laser sintering of polyetheretherketone–hydroxyapatite biocomposite blends. *Biomaterials*, 24(18), 3115-3123.
87. Wiria, F. E., Leong, K. F., Chua, C. K., & Liu, Y. (2007). Poly- ϵ -caprolactone/hydroxyapatite for tissue engineering scaffold fabrication via selective laser sintering. *Acta biomaterialia*, 3(1), 1-12.
88. Deckers, J., Vleugels, J., & Kruth, J. P. (2014). Additive manufacturing of ceramics: A review. *J. Ceram. Sci. Technol*, 5(4), 245-260.
89. Bellini, A., Shor, L., & Guceri, S. I. (2005). New developments in fused deposition modeling of ceramics. *Rapid Prototyping Journal*, 11(4), 214-220.

90. Zaman, H. A., Sharif, S., Idris, M. H., & Kamarudin, A. (2014). Metallic Biomaterials for Medical Implant Applications: A Review. *Applied Mechanics & Materials*, 735.
91. Espalin, D., Arcaute, K., Rodriguez, D., Medina, F., Posner, M., & Wicker, R. (2010). Fused deposition modeling of patient-specific polymethylmethacrylate implants. *Rapid Prototyping Journal*, 16(3), 164-173.
92. Berry, E., Brown, J. M., Connell, M., Craven, C. M., Efford, N. D., Radjenovic, A., & Smith, M. A. (1997). Preliminary experience with medical applications of rapid prototyping by selective laser sintering. *Medical engineering & physics*, 19(1), 90-96.
93. Baxter, R. M., MacDonald, D. W., Kurtz, S. M., & Steinbeck, M. J. (2013). Severe impingement of lumbar disc replacements increases the functional biological activity of polyethylene wear debris. *The Journal of Bone & Joint Surgery*, 95(11), e75.
94. Aho, A. J., Tirri, T., Kukkonen, J., Strandberg, N., Rich, J., Seppälä, J., & Yli-Urpo, A. (2004). Injectable bioactive glass/biodegradable polymer composite for bone and cartilage reconstruction: concept and experimental outcome with thermoplastic composites of poly (ϵ -caprolactone-co-D, L-lactide) and bioactive glass S53P4. *Journal of Materials Science: Materials in Medicine*, 15(10), 1165-1173.
95. Nykänen, V. P. S., Nykänen, A., Puska, M. A., Silva, G. G., & Ruokolainen, J. (2011). Dual-responsive and super absorbing thermally cross-linked hydrogel based on methacrylate substituted polyphosphazene. *Soft Matter*, 7(9), 4414-4424.
96. Logeart-Avramoglou, D., Anagnostou, F., Bizios, R., & Petite, H. (2005). Engineering bone: challenges and obstacles. *Journal of cellular and molecular medicine*, 9(1), 72-84.
97. Tas, A. C., Korkusuz, F., Timucin, M., & Akkas, N. (1997). An investigation of the chemical synthesis and high-temperature sintering behaviour of calcium hydroxyapatite (HA) and tricalcium phosphate (TCP) bioceramics. *Journal of Materials Science: Materials in Medicine*, 8(2), 91-96.
98. Kitamura, M., Ohtsuki, C., Ogata, S. I., Kamitakahara, M., & Tanihara, M. (2004). Microstructure and Bioresorbable Properties of α -TCP Ceramic

- Porous Body Fabricated by Direct Casting Method. *Materials Transactions*, 45(4), 983-988.
99. Hollinger, J. O., & Battistone, G. C. (1986). Biodegradable Bone Repair Materials Synthetic Polymers and Ceramics. *Clinical orthopaedics and related research*, 207, 290-306.
 100. Yu, X., Botchwey, E. A., Levine, E. M., Pollack, S. R., & Laurencin, C. T. (2004). Bioreactor-based bone tissue engineering: the influence of dynamic flow on osteoblast phenotypic expression and matrix mineralization. *Proceedings of the National Academy of Sciences of the United States of America*, 101(31), 11203-11208.
 101. Adachi, T., Osako, Y., Tanaka, M., Hojo, M., & Hollister, S. J. (2006). Framework for optimal design of porous scaffold microstructure by computational simulation of bone regeneration. *Biomaterials*, 27(21), 3964-3972.
 102. Descamps, M., Richart, O., Hardouin, P., Hornez, J. C., & Leriche, A. (2008). Synthesis of macroporous β -tricalcium phosphate with controlled porous architectural. *Ceramics International*, 34(5), 1131-1137.
 103. Vail, N. K., Swain, L. D., Fox, W. C., Aufdlemorte, T. B., Lee, G., & Barlow, J. W. (1999). Materials for biomedical applications. *Materials & design*, 20(2), 123-132.
 104. Duan, B., Wang, M., Zhou, W. Y., Cheung, W. L., Li, Z. Y., & Lu, W. W. (2010). Three-dimensional nanocomposite scaffolds fabricated via selective laser sintering for bone tissue engineering. *Acta Biomaterialia*, 6(12), 4495-4505.
 105. Williams, J. M., Adewunmi, A., Schek, R. M., Flanagan, C. L., Krebsbach, P. H., Feinberg, S. E., ... & Das, S. (2005). Bone tissue engineering using polycaprolactone scaffolds fabricated via selective laser sintering. *Biomaterials*, 26(23), 4817-4827.
 106. Tan, K. H., Chua, C. K., Leong, K. F., Cheah, C. M., Cheang, P., Bakar, M. A., & Cha, S. W. (2003). Scaffold development using selective laser sintering of polyetheretherketone–hydroxyapatite biocomposite blends. *Biomaterials*, 24(18), 3115-3123.
 107. Chua, C. K., Leong, K. F., Wiria, F. E., Tan, K. C., & Chandrasekara, M. (2004). Fabrication of poly (vinyl alcohol)/hydroxyapatite in tissue engineering. In *International conference on Competitive manufacturing*.

108. Das, S., Hollister, S. J., Flanagan, C., Adewunmi, A., Bark, K., Chen, C., ... & Widjaja, E. (2002). Computational design, freeform fabrication and testing of nylon-6 tissue engineering scaffolds. In *MRS Proceedings* (Vol. 758, pp. LL5-7). Cambridge University Press.
109. Rietzel, D., Drexler, M., Kühnlein, F., & Drummer, D. (2011). Influence of temperature fields on the processing of polymer powders by means of laser and mask sintering technology. In *Proceedings of the Solid Freeform Fabrication Symposium* (pp. 252-262).
110. Wiria, F. E., Leong, K. F., Chua, C. K., & Liu, Y. (2007). Poly- ϵ -caprolactone/hydroxyapatite for tissue engineering scaffold fabrication via selective laser sintering. *Acta biomaterialia*, 3(1), 1-12.
111. Salmoria, G. V., Klauss, P., Paggi, R. A., Kanis, L. A., & Lago, A. (2009). Structure and mechanical properties of cellulose based scaffolds fabricated by selective laser sintering. *Polymer Testing*, 28(6), 648-652.
112. Franco, A., & Romoli, L. (2012). Characterization of laser energy consumption in sintering of polymer based powders. *Journal of Materials Processing Technology*, 212(4), 917-926.
113. Chung, H., & Das, S. (2006). Processing and properties of glass bead particulate-filled functionally graded Nylon-11 composites produced by selective laser sintering. *Materials Science and Engineering: A*, 437(2), 226-234
114. Allen, N. S., & Edge, M. (1992). *Fundamentals of polymer degradation and stabilization*. Springer Science & Business Media
115. Evans, R. S., Bourell, D. L., Beaman, J. J., & Campbell, M. I. (2005, August). SLS materials development method for rapid manufacturing. In *16th Solid Free. Fabr. Symp. University of Texas at Austin, Austin, TX, USA* (pp. 184-196).
116. Olsen, F. O., & Alting, L. (1989). Cutting front formation in laser cutting. *CIRP Annals-Manufacturing Technology*, 38(1), 215-218.
117. Tolochko, N. K., Khlopkov, Y. V., Mozzharov, S. E., Ignatiev, M. B., Laoui, T., & Titov, V. I. (2000). Absorptance of powder materials suitable for laser sintering. *Rapid Prototyping Journal*, 6(3), 155-161.
118. Kruth, J. P., Wang, X., Laoui, T., & Froyen, L. (2003). Lasers and materials in selective laser sintering. *Assembly Automation*, 23(4), 357-371

119. Nelson, J. C., Xue, S., Barlow, J. W., Beaman, J. J., Marcus, H. L., & Bourell, D. L. (1993). Model of the selective laser sintering of bisphenol-A polycarbonate. *Industrial & Engineering Chemistry Research*, 32(10), 2305-2317.
120. Donaldson, R., & Gilchriese, M. G. D. (1990). Proceedings of the workshop on calorimetry for the Supercollider.
121. Harmon, J. P., & Gaynor, J. F. (1993). The effect of gamma irradiation on color center formation in optical polymers. *Journal of Polymer Science Part B: Polymer Physics*, 31(2), 235-236.
122. Prakash, S., & Kumar, S. (2015). Energy Based Analysis of Laser Microchanneling Process on Polymethyl Methacrylate (PMMA). In *Lasers Based Manufacturing* (pp. 239-253). Springer India.
123. Tadmor, Z., & Gogos, C. G. (1979). Principles of Polymer Processing John Wiley u. Sons, New York, Brisbane, Chichester, Toronto.
124. Askeland, D. R., & Phulé, P. P. (2003). The science and engineering of materials.
125. Dos Santos, W. N., de Sousa, J. A., & Gregorio, R. (2013). Thermal conductivity behaviour of polymers around glass transition and crystalline melting temperatures. *Polymer Testing*, 32(5), 987-994.
126. Orr, C. (1966). Particle Technology.
127. Yagi, S., & Kunii, D. (1957). Studies on effective thermal conductivities in packed beds. *AIChE Journal*, 3(3), 373-381.
128. Park, G. S., & Crank, J. (1968). Diffusion in polymers. *Academic Press*; 1968. p. 219–57.
129. Miller-Chou, B. A., & Koenig, J. L. (2003). A review of polymer dissolution. *Progress in Polymer Science*, 28(8), 1223-1270.
130. Kasemo, B., & Lausmaa, J. (1986). Surface science aspects on inorganic biomaterials. *CRC Crit. Rev. Clin. Neurobiol. ;(United States)*, 4.
131. Agarwala, M., Bourell, D., Beaman, J., Marcus, H., & Barlow, J. (1995). Direct selective laser sintering of metals. *Rapid Prototyping Journal*, 1(1), 26-36.
132. Saleh, B. E., Teich, M. C., & Saleh, B. E. (1991). *Fundamentals of photonics* (Vol. 22). New York: Wiley.

133. Williams, J. D., & Deckard, C. R. (1998). Advances in modeling the effects of selected parameters on the SLS process. *Rapid Prototyping Journal*, 4(2), 90-100.
134. General Scanning, Inc 500 Arsenal Street, Massachusetts D, E Series: 2000-3000, *Digital Electronics, User Manual*, 1992.
135. DTM Corporation, 1611 Headway Circle, Austin, Texas 78754, *DTM Sinterstation system 2000, User's guide*, 1996.
136. Tan, K. H., Chua, C. K., Leong, K. F., Cheah, C. M., Cheang, P., Bakar, M. A., & Cha, S. W. (2003). Scaffold development using selective laser sintering of polyetheretherketone–hydroxyapatite biocomposite blends. *Biomaterials*, 24(18), 3115-3123.
137. DeRosa, R. L., Schader, P. A., & Shelby, J. E. (2003). Hydrophilic nature of silicate glass surfaces as a function of exposure condition. *Journal of non-crystalline solids*, 331(1), 32-40.
138. Wang, Q., Xia, H., & Zhang, C. (2001). Preparation of polymer/inorganic nanoparticles composites through ultrasonic irradiation. *Journal of applied polymer science*, 80(9), 1478-1488.
139. Kaniappan, K., & Latha, S. (2011). Certain Investigations on the formulation and characterization of polystyrene/poly (methyl methacrylate) blends. *Int. J. Chem. Tech. Res*, 3(2), 708-717.
140. Caulfield, B., McHugh, P. E., & Lohfeld, S. (2007). Dependence of mechanical properties of polyamide components on build parameters in the SLS process. *Journal of Materials Processing Technology*, 182(1), 477-488.
141. Jang, D. W., Nguyen, T. H., Sarkar, S. K., & Lee, B. T. (2016). Microwave sintering and in vitro study of defect-free stable porous multilayered HAp–ZrO₂ artificial bone scaffold. *Science and Technology of Advanced Materials*.
142. Gregory, C. A., Gunn, W. G., Peister, A., & Prockop, D. J. (2004). An Alizarin red-based assay of mineralization by adherent cells in culture: comparison with cetylpyridinium chloride extraction. *Analytical biochemistry*, 329(1), 77-84.
143. Ma, R., Tang, S., Tan, H., Lin, W., Wang, Y., Wei, J., ... & Tang, T. (2014). Preparation, characterization, and in vitro osteoblast functions of a nano-

- hydroxyapatite/polyetheretherketone biocomposite as orthopedic implant material. *International journal of nanomedicine*, 9, 3949.
144. Schmittgen, T. D., & Livak, K. J. (2008). Analyzing real-time PCR data by the comparative CT method. *Nature protocols*, 3(6), 1101-1108.
 145. Schultz, J. P. (2004). *Modeling heat transfer and densification during laser sintering of viscoelastic polymers* (Doctoral dissertation, Virginia Polytechnic Institute and State University).
 146. Forderhase, P., McAlea, K., Michalewicz, M., Ganninger, M., & Firestone, K. (1994, September). SLS prototypes from nylon. In *Solid Freeform Fabrication Symposium Proceedings* (pp. 102-109).
 147. Moeskops, E., Kamperman, N., van de Vorst, B., & Knoppers, R. (2004). Creep behaviour of polyamide in selective laser sintering. *Proceedings of SFF, Austin USA*.
 148. Hague*, R., Mansour, S., & Saleh, N. (2004). Material and design considerations for rapid manufacturing. *International Journal of Production Research*, 42(22), 4691-4708.
 149. Shi, Y., Li, Z., Sun, H., Huang, S., & Zeng, F. (2004). Effect of the properties of the polymer materials on the quality of selective laser sintering parts. *Proceedings of the Institution of Mechanical Engineers, Part L: Journal of Materials Design and Applications*, 218(3), 247-252.
 150. Gibson, I., & Shi, D. (1997). Material properties and fabrication parameters in selective laser sintering process. *Rapid Prototyping Journal*, 3(4), 129-136.
 151. Ajoku, U., Hopkinson, N., & Caine, M. (2006). Experimental measurement and finite element modelling of the compressive properties of laser sintered Nylon-12. *Materials Science and Engineering: A*, 428(1), 211-216.
 152. Ajoku, U., Saleh, N., Hopkinson, N., Hague, R., & Erasenthiran, P. (2006). Investigating mechanical anisotropy and end-of-vector effect in laser-sintered nylon parts. *Proceedings of the Institution of Mechanical Engineers, Part B: Journal of Engineering Manufacture*, 220(7), 1077-1086.
 153. Partee, B., Hollister, S. J., & Das, S. (2006). Selective laser sintering process optimization for layered manufacturing of CAPA® 6501

- polycaprolactone bone tissue engineering scaffolds. *Journal of Manufacturing Science and Engineering*, 128(2), 531-540.
154. Schmidt, M., Pohle, D., & Rechtenwald, T. (2007). Selective laser sintering of PEEK. *CIRP Annals-Manufacturing Technology*, 56(1), 205-208.
 155. Rudin, A., & Choi, P. (2012). *The Elements of Polymer Science & Engineering*. Academic Press.
 156. Rantuch, P., Kačíková, D., & Nagypál, B. (2014). Investigation of activation energy of polypropylene composite thermooxidation by model-free methods. *European Journal of Environmental and Safety Sciences*, 2(1), 12-18.
 157. Hao, L., Savalani, M. M., Zhang, Y., Tanner, K. E., & Harris, R. A. (2006). Selective laser sintering of hydroxyapatite reinforced polyethylene composites for bioactive implants and tissue scaffold development. *Proceedings of the Institution of Mechanical Engineers, Part H: Journal of Engineering in Medicine*, 220(4), 521-531.
 158. Bryngelson, J. D., Onuchic, J. N., Socci, N. D., & Wolynes, P. G. (1995). Funnels, pathways, and the energy landscape of protein folding: a synthesis. *Proteins: Structure, Function, and Bioinformatics*, 21(3), 167-195.
 159. Borzacchiello, A., Ambrosio, L., Nicolais, L., Harper, E. J., Tanner, K. E., & Bonfield, W. (1998). Isothermal and non-isothermal polymerization of a new bone cement. *Journal of Materials Science: Materials in Medicine*, 9(6), 317-324.
 160. Vaidyanathan, J., Vaidyanathan, T. K., Wang, Y., & Viswanadhan, T. (1992). Thermoanalytical characterization of visible light cure dental composites. *Journal of oral rehabilitation*, 19(1), 49-64.
 161. Jancar, J., Wang, W., & Dibenedetto, A. T. (2000). On the heterogeneous structure of thermally cured bis-GMA/TEGDMA resins. *Journal of Materials Science: Materials in Medicine*, 11(11), 675-682.
 162. Eldiwany M, Powers JM, George LA. Mechanical properties of direct and post-cured composites. *Am J Dent* 1993; 6:222-4
 163. Manring, L. E., Sogah, D. Y., & Cohen, G. M. (1989). Thermal degradation of poly (methyl methacrylate). 3. Polymer with head-to-head linkages. *Macromolecules*

164. Rimell, J. T., & Marquis, P. M. (2000). Selective laser sintering of ultra-high molecular weight polyethylene for clinical applications. *Journal of biomedical materials research*, 53(4), 414-420.
165. Eyerer, P., Wagner, T., & Woicke, N. (2005). Carbon assisted laser sintering of thermoplastic polymers. In *ANTEC-CONFERENCE PROCEEDINGS-* (Vol. 7, p. 36).
166. Khumalo, V. M., Karger-Kocsis, J., & Thomann, R. (2010). Polyethylene/synthetic boehmite alumina nanocomposites: structure, thermal and rheological properties. *Express Polym. Lett*, 4, 264-274.
167. Di Silvio, L., Dalby, M. J., & Bonfield, W. (2002). Osteoblast behaviour on HA/PE composite surfaces with different HA volumes. *Biomaterials*, 23(1), 101-107.
168. Sichel, E. K. Carbon black-polymer composites: the physics of electrically conducting composites/edited by Enid Keil Sichel. *Plastics Engineering*; 3.
169. Vacanti, J. P., Morse, M. A., Saltzman, W. M., Domb, A. J., Perez-Atayde, A., & Langer, R. (1988). Selective cell transplantation using bioabsorbable artificial polymers as matrices. *Journal of pediatric surgery*, 23(1), 3-9.
170. Sarver, J. G., Fournier, R. L., Goldblatt, P. J., Phares, T. L., Mertz, S. E., Baker, A. R., ... & Selman, S. H. (1995). Tracer technique to measure in vivo chemical transport rates within an implantable cell transplantation device. *Cell transplantation*, 4(2), 201-217.
171. Boyan, B. D., Hummert, T. W., Dean, D. D., & Schwartz, Z. (1996). Role of material surfaces in regulating bone and cartilage cell response. *Biomaterials*, 17(2), 137-146.
172. Beruto, D. T., Mezzasalma, S. A., Capurro, M., Botter, R., & Cirillo, P. (2000). Use of α -tricalcium phosphate (TCP) as powders and as an aqueous dispersion to modify processing, microstructure, and mechanical properties of polymethylmethacrylate (PMMA) bone cements and to produce bone-substitute compounds. *Journal of biomedical materials research*, 49(4), 498-505.
173. Holland, B. J., & Hay, J. N. (2002). The effect of polymerisation conditions on the kinetics and mechanisms of thermal degradation of PMMA. *Polymer degradation and stability*, 77(3), 435-439.

174. Kolossov, S., Boillat, E., Glardon, R., Fischer, P., & Locher, M. (2004). 3D FE simulation for temperature evolution in the selective laser sintering process. *International Journal of Machine Tools and Manufacture*, 44(2), 117-123.
175. Baojun, Z. H. A. O., Fazhong, S., Tao, F. E. N. G., & Jianmin, S. (2002). Studies on numerical simulations of temperature field in selective laser sintering of polystyrene powders. *Laser J*, 23(9), 66-69.
176. Dai, K., & Shaw, L. (2002). Distortion minimization of laser-processed components through control of laser scanning patterns. *Rapid Prototyping Journal*, 8(5), 270-276.
177. Schnabel, W. (1981). Polymer degradation: principles and practical applications.
178. Liufu, S. C., Xiao, H. N., & Li, Y. P. (2005). Thermal analysis and degradation mechanism of polyacrylate/ZnO nanocomposites. *Polymer degradation and stability*, 87(1), 103-110.
179. Gomez, B., Ardakani, S., Ju, J., Jenkins, D., Cerelli, M. J., Daniloff, G. Y., & Kung, V. T. (1995). Monoclonal antibody assay for measuring bone-specific alkaline phosphatase activity in serum. *Clinical chemistry*, 41(11), 1560-1566.
180. Dinescu, S., Gălăţeanu, B., Albu, M., Lungu, A., Radu, E., Hermenean, A., & Costache, M. (2013). Biocompatibility assessment of novel collagen-sericin scaffolds improved with hyaluronic acid and chondroitin sulfate for cartilage regeneration. *BioMed research international*, 2013.
181. PUCHTLER, H., MELOAN, S. N., & TERRY, M. S. (1969). On the history and mechanism of alizarin and alizarin red S stains for calcium. *Journal of Histochemistry & Cytochemistry*, 17(2), 110-124.
182. Song, Y., Ju, Y., Song, G., & Morita, Y. (2013). In vitro proliferation and osteogenic differentiation of mesenchymal stem cells on nanoporous alumina. *International journal of nanomedicine*, 8, 2745-2756.
183. Muller, J., Huaux, F., Moreau, N., Misson, P., Heilier, J. F., Delos, M., ... & Lison, D. (2005). Respiratory toxicity of multi-wall carbon nanotubes. *Toxicology and applied pharmacology*, 207(3), 221-231.
184. Yokozeki, H., Hayashi, T., Nakagawa, T., Kurosawa, H., Shibuya, K., & Ioku, K. (1998). Influence of surface microstructure on the reaction of the

- active ceramics in vivo. *Journal of Materials Science: Materials in Medicine*, 9(7), 381-384.
185. Hao, L., Lawrence, J., & Chian, K. S. (2004). Effects of CO₂ laser irradiation on the surface properties of magnesia-partially stabilised zirconia (MgO-PSZ) bioceramic and the subsequent improvements in human osteoblast cell adhesion. *Journal of biomaterials applications*, 19(2), 81-105.
186. Tsang, V. L., & Bhatia, S. N. (2004). Three-dimensional tissue fabrication. *Advanced drug delivery reviews*, 56(11), 1635-1647.
187. Ziegelmeier, S., Wöllecke, F., Tuck, C. J., Goodridge, R. D., & Hague, R. J. (2014). Aging behavior of thermoplastic elastomers in the laser sintering process. *Journal of Materials Research*, 29(17), 1841-1851.
188. Wudy, K., Drummer, D., Kühnlein, F., & Drexler, M. (2014, May). Influence of degradation behavior of polyamide 12 powders in laser sintering process on produced parts. In *AIP Conference Proceedings* (Vol. 1593, pp. 691-695).
189. Oliani, W. L., Parra, D. F., & Lugão, A. B. (2010). UV stability of HMS-PP (high melt strength polypropylene) obtained by radiation process. *Radiation Physics and Chemistry*, 79(3), 383-387.
190. Duan, G., Zhang, C., Li, A., Yang, X., Lu, L., & Wang, X. (2008). Preparation and characterization of mesoporous zirconia made by using a poly (methyl methacrylate) template. *Nanoscale research letters*, 3(3), 118
191. Marois, Y., Guidoin, R., Roy, R., Vidovsky, T., Jakubiec, B., Sigot-Luizard, M. F., ... & King, M. (1996). Selecting valid in vitro biocompatibility tests that predict the in vivo healing response of synthetic vascular prostheses. *Biomaterials*, 17(19), 1835-1842.
192. Qin, T. W., Yang, Z. M., & Cai, S. (1999). [Interaction of cell adhesion to materials in tissue engineering]. *Chinese journal of reparative and reconstructive surgery*, 13(1), 31-37.
193. Heil, J., Reifferscheid, G., Waldmann, P., Leyhausen, G., & Geurtsen, W. (1996). Genotoxicity of dental materials. *Mutation Research/Genetic Toxicology*, 368(3), 181-194.

194. Matsuo, K., & Irie, N. (2008). Osteoclast–osteoblast communication. *Archives of biochemistry and biophysics*, 473(2), 201-209.
195. Wieslander, A. P., Nordin, M. K., Hansson, B., Baldetorp, B., & Kjellstrand, P. T. (1993). In vitro toxicity of biomaterials determined with cell density, total protein, cell cycle distribution and adenine nucleotides. *Biomaterials, Artificial Cells and Immobilization Biotechnology*, 21(1), 63-70.
196. Jain, S., Sharma, A., & Basu, B. (2013). In vitro cytocompatibility assessment of amorphous carbon structures using neuroblastoma and Schwann cells. *Journal of Biomedical Materials Research Part B: Applied Biomaterials*, 101(4), 520-531.
197. Tripathi, G., & Basu, B. (2012). A porous hydroxyapatite scaffold for bone tissue engineering: Physico-mechanical and biological evaluations. *Ceramics International*, 38(1), 341-349.
198. Afzal, M. A. F., Kesarwani, P., Reddy, K. M., Kalmudia, S., Basu, B., & Balani, K. (2012). Functionally graded hydroxyapatite-alumina-zirconia biocomposite: synergy of toughness and biocompatibility. *Materials Science and Engineering: C*, 32(5), 1164-1173.
199. Wilson, J. R., Mills, J. G., Prather, I. D., & Dimitrijevic, S. D. (2005). A toxicity index of skin and wound cleansers used on in vitro fibroblasts and keratinocytes. *Advances in skin & wound care*, 18(7), 373-378.
200. Declercq, H., Van den Vreken, N., De Maeyer, E., Verbeeck, R., Schacht, E., De Ridder, L., & Cornelissen, M. (2004). Isolation, proliferation and differentiation of osteoblastic cells to study cell/biomaterial interactions: comparison of different isolation techniques and source. *Biomaterials*, 25(5), 757-768.
201. Cerroni, L., Filocamo, R., Fabbri, M., Piconi, C., Caropreso, S., & Condo, S. G. (2002). Growth of osteoblast-like cells on porous hydroxyapatite ceramics: an in vitro study. *Biomolecular engineering*, 19(2), 119-124.
202. Di Silvio, L., Dalby, M., & Bonfield, W. (1998). In vitro response of osteoblasts to hydroxyapatite-reinforced polyethylene composites. *Journal of Materials Science: Materials in Medicine*, 9(12), 845-848.

203. Muhammad, K. B., Abas, W. A. B. W., Kim, K. H., Pinguan-Murphy, B., Zain, N. M., & Akram, H. (2012). In vitro comparative study of white and dark polycaprolactone trifumarate in situ cross-linkable scaffolds seeded with rat bone marrow stromal cells. *Clinics*, 67(6), 629-638.
204. Kim, S. S., Park, M. S., Jeon, O., Choi, C. Y., & Kim, B. S. (2006). Poly (lactide-co-glycolide)/hydroxyapatite composite scaffolds for bone tissue engineering. *Biomaterials*, 27(8), 1399-1409.
205. Anselme, K. (2000). Osteoblast adhesion on biomaterials. *Biomaterials*, 21(7), 667-681.
206. Anselme, K., Ponche, A., & Bigerelle, M. (2010). Relative influence of surface topography and surface chemistry on cell response to bone implant materials. Part 2: biological aspects. *Proceedings of the Institution of Mechanical Engineers, Part H: Journal of Engineering in Medicine*, 224(12), 1487-1507.
207. Jang, D. W., Nguyen, T. H., Sarkar, S. K., & Lee, B. T. (2016). Microwave sintering and in vitro study of defect-free stable porous multilayered HAp–ZrO₂ artificial bone scaffold. *Science and Technology of Advanced Materials*.
208. Lehmann, M. J., Sherer, N. M., Marks, C. B., Pypaert, M., & Mothes, W. (2005). Actin-and myosin-driven movement of viruses along filopodia precedes their entry into cells. *The Journal of cell biology*, 170(2), 317-325.
209. Khung, Y. L., Barritt, G., & Voelcker, N. H. (2008). Using continuous porous silicon gradients to study the influence of surface topography on the behaviour of neuroblastoma cells. *Experimental cell research*, 314(4), 789-800.
210. Meyer, U., Büchter, A., Wiesmann, H. P., Joos, U., & Jones, D. B. (2005). Basic reactions of osteoblasts on structured material surfaces. *Eur Cell Mater*, 9, 39-49.
211. Yang, J. M., Lu, C. S., & Hsu, Y. G. (1997). Effect of tricalcium phosphate, hydroxyethyl methacrylate, and ethylene glycol dimethacrylate on the mechanical properties of acrylic bone cement. *Die Angewandte makromolekulare Chemie*, 245(1), 49-62.

212. Dai, K., Li, X. X., & Shaw, L. L. (2004). Comparisons between thermal modeling and experiments: effects of substrate preheating. *Rapid Prototyping Journal*, 10(1), 24-34.
213. Gebhardt, A. (2007). Rapid Prototyping–Rapid Tooling–Rapid Manufacturing. *Carl Hanser, München*.
214. Pham, D. T., Dimov, S., & Lacan, F. (1999). Selective laser sintering: applications and technological capabilities. *Proceedings of the Institution of Mechanical Engineers, Part B: Journal of Engineering Manufacture*, 213(5), 435-449.
215. Ippolito, R., Iuliano, L., & Gatto, A. (1995). Benchmarking of rapid prototyping techniques in terms of dimensional accuracy and surface finish. *CIRP Annals-Manufacturing Technology*, 44(1), 157-160.
216. Shen, J., Steinberger, J., Göpfert, J., Gerner, R., Daiber, F., Manetsberger, K., & Ferstl, S. (2000, August). Inhomogeneous shrinkage of polymer materials in selective laser sintering. In *Proceedings of the 11th International Solid freeform fabrication symposium (SFF 2000)*, The University of Texas at Austin (pp. 298-305).
217. Yang, J., Bei, J., & Wang, S. (2002). Enhanced cell affinity of poly (D, L-lactide) by combining plasma treatment with collagen anchorage. *Biomaterials*, 23(12), 2607-2614.
218. Deshmane, C., Yuan, Q., & Misra, R. D. K. (2007). On the fracture characteristics of impact tested high density polyethylene–calcium carbonate nanocomposites. *Materials Science and Engineering: A*, 452, 592-601.
219. Chung, H., & Das, S. (2008). Functionally graded Nylon-11/silica nanocomposites produced by selective laser sintering. *Materials Science and Engineering: A*, 487(1), 251-257.